Title
Electron-Scale Processes in the Solar Wind and Magnetosphere

Author
Tong, Yuguang

Publication Date
2019

Peer reviewed|Thesis/dissertation

Electron-Scale Processes in the Solar Wind and Magnetosphere

by

Yuguang Tong

A dissertation submitted in partial satisfaction of the

requirements for the degree of

Doctor of Philosophy

in

Physics

in the

Graduate Division

of the

University of California, Berkeley

Committee in charge:

Professor Stuart D. Bale, Chair
Professor Forrest S. Mozer
Professor Eliot Quaertet

Summer 2019

Electron-Scale Processes in the Solar Wind and Magnetosphere

Abstract

Electron-Scale Processes in the Solar Wind and Magnetosphere

by

Yuguang Tong

Doctor of Philosophy in Physics

University of California, Berkeley

Professor Stuart D. Bale, Chair

Plasma, one of the four fundamental states of matter, prevails the universe and accounts for 90% of the known masses. Interaction between the solar wind, a space plasma with solar origin, and the terrestrial magnetic field shapes the space climate that is crucial for our modern society that heavily dependent on electricity, electronics and satellites. Waves ubiquitously grow, propagate, interact with other waves and plasmas, and eventually damps away in plasmas, significantly altering plasma dynamics and energy transport. Measurements of both plasma particles and electromagnetic fields allow probing wave-plasma interactions of interest.

Part one of the thesis presents a few new results relating to the electron heat flux in the solar wind. Electron heat flux is a poorly understood quantity in weakly collisional or collisionless astrophysical and space plasmas, but it is crucial to modeling large scale systems such as galaxy clusters and stellar winds. We present a statistical study of the electron heat flux in the solar wind and confirm that it is bounded from above by power laws of electron beta. We consider various collisionless processes that potentially reduce the heat flux. In particular, the whistler heat flux instability (WHFI) has long been considered to constrain heat flux in the high beta regime. We show for the first time local generation of whistler waves in the solar wind using high-cadence simultaneous particles and wave measurements onboard ARTEMIS spacecraft. We present the statistical properties of the whistler waves in the solar wind at 1 AU, with evidence supporting WHFIs generating the observed whistler waves. However, we argue that the wave amplitude is too small to effectively reduce the electron heat flux. Accompanied by the electron heat flux is measurable electron bulk drifts with respect to the solar wind protons, which significantly modify Landau resonance of kinetic Alfvén waves (KAWs). We consider the effects of potential KAW instabilities in the context of electron heat flux inhibition.

Part two of the thesis considers a type of electrostatic structure known as the electron phase space hole (EPSH). It is formed in the non-linear stage of plasma streaming instabilities and remains highly stable for long duration. We address for the first time 3D configuration of EPSHs by analyzing multi-spacecraft (using NASA MMS) passing of the same EPSH.

The length scale perpendicular to the background magnetic field is directly measured with significant implications to electron motions inside EPSHs. In addition, statistical study of such multi-spacecraft observation reveals strong correlation among parameters of fast EPSHs.

To Yue Pan, Xiaomu Yu and Jingou Tong

Contents

List of Figures

List of Tables

Acknowledgments

It took an incredible six years in graduate school before I could begin to write this piece of acknowledgement! There are so many ups and downs on the road that I know I would not be able to finish it without the supports from family, friends and colleagues.

My sincere gratitude goes to my advisor Professor Stuart Bale for his patience, guidance and immense knowledge. Stuart has encouraged me to develop my own taste of research and his open mind towards competition and collaboration in research has tremendous positive influence on me.

During the past six years, I have had great pleasure working with many collaborators in the Space Sciences Laboratory and from other institutions. I am especially grateful to Dr. Ivan Vasko. We started collaboration merely two years ago but it has been very fruitful! Ivan has provided me timely hands on guidance on how to formulate interesting questions and how to give interesting written / oral presentations, in addition of being a very good friend. I would also like to thank these collaborators for many deeply helpful discussions: Dr. Marc Pulupa (SSL), Dr. Chadi Salem (SSL), Professor Forrest Mozer (SSL), Dr. Chris Chen (Queen Mary), Dr. Daniel Vascharen (UCL), Dr. Jason TenBarge (Princeton) and Professor Kris Klein (Arizona), Dr. Anton Artemyev (UCLA) and Dr. Joe Borovsky (LANL).

Leaving home alone and living in a distant foreign country for six years is not easy. I feel fortunate that I have met many caring people and made many friends over the course. I especially thank Andy and Yumeng for a few years of companion at Berkeley and being supportive and caring during hard times.

Any success I have had are built upon the strong foundation provided by my family. My parents are biologists who study fishes. They are the role models that have motivated me and my brother to study science and to pursuit research trainings through PhDs. Finally, I would also like to thank my wonderful wife Yue for sharing and enriching my life during the past two years. Yue has saved me from eating takeout from Chipole or Lucky Thai house everyday.

Chapter 1

Introduction

1.1 The Sun

The Sun has been an integral part of human society. It has been worshipped as a deity in many religions and mythologies around the world since the early human history. The synodic rotation of Earth around the Sun form the basis of solar calendars, one of which most of us use today. Early scientific studies of the Sun date back as early as 1000 BC when Babylonian astronomers took note of the Sun's nonuniform motion along the ecliptic. Ancient Chinese astronomers maintained records of sunspot observations during the Han dynasty (206 BC - AD 220). However, establishing early scientific understanding of the sun still took a long time. Most of our current understanding of the sun and its influence on human have been developed in the past century, when several scientific and technology revolutions have dramatically accelerated the process of knowledge accumulation.

We now know the Sun is almost a perfect sphere of hot plasma with a diameter about $1.4 \times 10^6 km$ or about 100 times that of Earth. It was formed about 4.6 billion years ago by a large molecular cloud that collapsed under gravitational contraction and accounts for about 99.86% of the total mass of the solar system. The central mass became so hot that nuclear fusion was initiated. The Sun is a roughly middle-aged, G-type main-sequence star based on its spectral. Currently the Sun fuses an incredible 600 million tons of hydrogen into helium per second, in which process 4 million tons of matter is converted into energy per second. The emitted energy, carried by photons, typically takes tens to hundreds of thousand of years to travel from the solar core to the solar surface, and becomes the source of the Sun's light and heat. Within the next 5 billion years, the Sun will gradually run out of hydrogen and while its core density will markedly increase, the Sun's outer layer will expand making it a "red giant".

1.2 The solar wind, Earth's magnetosphere, and solar-terrestrial physics

Emergence of the modern scientific discipline of solar-terrestrial physics began with the invention of the telescope in the 17th century. But in the first hundred years, the sunspot study was slow since the solar activities were somewhat abnormal. It was not until 1851 that the 11-year period of the sunspot number was discovered by H. Schwabe.

The sunspot variation was quickly linked to geomagnetic activities. The great mathematician C. F. Gauss led the effort to make simultaneous observation of widely separated magnetometers. This allows the magnetic field contribution from the space to be separated from the geomagnetic field originated from below the surface of Earth. On September 1, 1859, R. Carrington sighted the first a solar transient event, a great white-light flare in his telescope that disappeared within a minute. 18 hours later, one of the strongest magnetic storms known as the solar storm of 1859 took place on Earth.

Around the beginning of the 20th century, the Norwegian physicist K. Birkeland realized the connection betwen the extensive data of the magnetic perturbations associated with auroras and then recent discovery of electrons by J. J. Thomson. He conducted the famous terralla (a small magnetized model ball representing the Earth) experiments which demonstrated that electrons incident on the terrella would produce patterns quite similar to the observation of the Auroral zone. Birkeland also suggested that the electrons come from the Sun.

The invention of radio transmitter and receiver at the turn of the 20th century provide powerful tools to probe the solar-terrestrial environment. Trans-Atlantic radio transmission led A. E. Kennelly and O. Heaviside to postulate the existence of highly electrically conducting layer known as the ionosphere. The ionosphere was verified in 1925 using short pulses of radio wave at vertical incidence to infer the altitude of the electrically reflecting layer.

In the 1930s, solar corona temperature was determined to be a million Kelvin from spectroscopy. This led S. Chapman to propose the "solar breeze" model which describes a steady state solar atmosphere that extends beyond Earth's orbit. However, Chapman's model was put into question by the observation that a comet tail lag behind the comet's radial direction by about 5°. In 1951, L. Biermann correctly interpreted the lag as a consequence of an interaction between the solar wind and the comet tail, therefore deducing the solar wind is flowing at about 450 km/s from the sun in all the places and all the time. In 1958, Eugene W. Parker provided the well known Parker solar wind model that properly explains the supersonic flow. In this theory, the competition between heat conduction and gravitation that weakens with distance enables the outer coronal atmosphere to accelerate and eventually escape supersonically into interstellar space. A year before Parker published his model, the Soviet Union launched the first artificial satellite into space, and marked the dawn of the space age. Within a few years, the Soviet and American space probes confirmed the existence of the solar wind and the interplanetary magnetic field with direct in-situ measurements.

Numerous satellite observations have resulted in our current understanding of the region

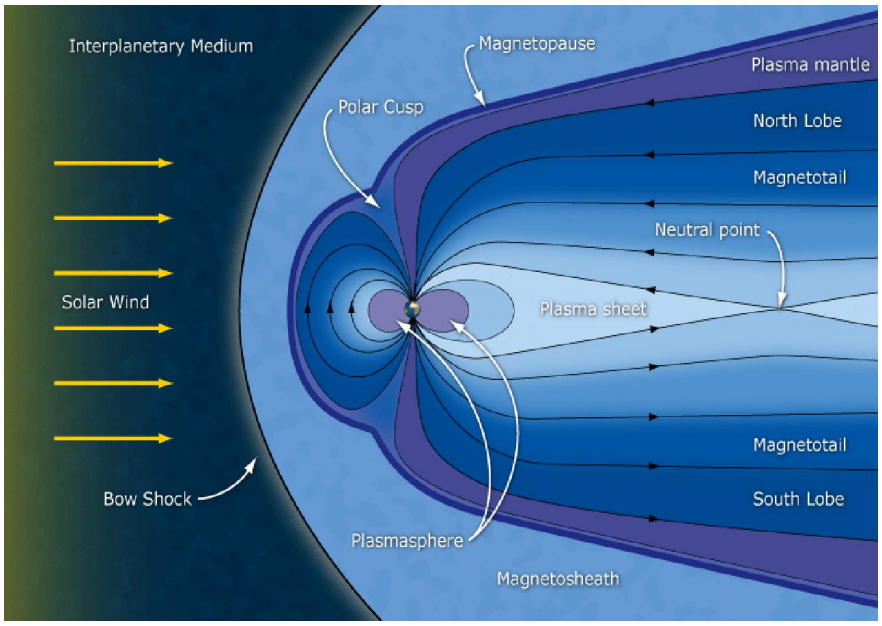

Figure 1.1: Diagram of Earth's magnetosphere.

of space surrounding Earth known as the magnetosphere. The Earth's dipole magnetic field is distorted by the supersonic solar wind and forms the structure shown in the simplified diagram in Figure 1.1.

The outermost layer of the magnetosphere is known as the bow shock, where the solar wind undergoes a collisionless shock to sharply reduce its speed. Eventually the solar wind dynamical pressure becomes sufficiently small to be balanced by the Earth's magnetic pressure at a boundary known as the magnetopause. The magnetopause is asymmetric, with the sunward side being about 10 Earth radii out but the other side stretching out as the so called magnetotail that extends beyond 200 Earth radii.

The region between the bow shock and the magnetopause is known as the magnetosheath, filled mainly by shocked solar wind. This region is featured by erratically varying magnetic field and high particle energy flux accompanied by strong particle thermalization. Inside the magnetosphere is a donut-shaped region above the ionosphere known as the plasmasphere with altitude between 60 km to a few Earth radii. It is filled up with low-energy plasma that rotates with Earth.

1.3 Solar wind and magnetosphere as plasma physics laboratories

The space plasma in the solar wind and the Earth's magnetosphere provide accessible natural environments to study plasma physics. Since 1957, about 8,100 satellites have been

launched into space, many of which carry scientific payload to make in-situ and remote sensing measurements. Such measurements provide access to time and length scales and energies unavailable in ground laboratories, therefore complement laboratory experiment to study plasma physics.

Within the solar wind and magnetosphere, many universal plasma processes are found and studied in an in-situ environment. This thesis pays special attention to plasma waves, microinstabilities and their interactions with plasma particles. Other example processes include magnetic reconnection, turbulence, shock and etc.

Recently, multi-point measurements by the four Magnetospheric Multiscale (MMS) spacecraft have enabled observation of electron-scale dynamics of the electron diffusion region in magnetic reconnections in space. The first observation of symmetric magnetic reconnection in Earth's magnetotail suggest that the dominant dynamics are laminar, despite presence of turbulence near the reconnection site (Torbert et al., 2018). Another recent MMS observation reveals the existence of a new type of electron magnetic reconnection without ion coupling in Earth's magnetosheath (Phan et al., 2018).

Plasma turbulence is a universal collective phenomena that occur in a diverse range of environments, including galaxy clusters, interstellar medium, accretion disks, stellar winds and planetary magnetospheres. Because of the wide range of scales excited, the solar wind and magnetospheres can be seen as very big laboratories to investigate turbulence in developing phase and in fully developed phase. In the past two decades, theories (Goldreich and Sridhar, 1995; Boldyrev, 2005) and solar wind observations have established the anisotropy nature in the strong Alfvénic turbulence (Horbury, Forman, and Oughton, 2008; Chen et al., 2010). Recent work using measurements of the polarization of electromagnetic field fluctuations and the density fluctuations in the solar wind show compelling evidence that supports the kinetic Alfvén turbulence in favor of the whistler turbulence in the kinetic range between ion and electron scales (Salem et al., 2012a; Chen et al., 2013a).

Spacecraft sampling plasmas at different stage of evolution shed lights on the effect of complex dynamics. A recent study of electrons in the low latitude solar wind combines electron measurements onboard Ulysses, WIND and Helios to give a global picture between 0.3 and 4 AU and show the scattering of beam electrons into isotropic populations in the course of solar wind expansion (Štverák et al., 2009).

Decades of continuous spacecraft measurements in the solar wind have resulted in some large datasets of solar wind parameters. Statistical studies of the pressure anisotropy and the wave power enhancement in the solar wind suggest that the mirror mode and firehose instabilities are likely to prevent the solar wind from developing extreme temperature anisotropies (Hellinger et al., 2006; Bale et al., 2009). We will present a couple of statistical studies of electrons and of waves in this thesis as well.

1.4 Social impacts of space weather

Research of the strong solar-terrestrial coupling in the past half century has naturally resulted in the realization of the vulnerability of our modern society that is built upon many powerful yet sensitive technologies. Such concern has brought space weather towards the center of space physics research in the 21st century. Space weather is a branch of space physics, that mainly concern with the time varying conditions on the Sun and in space that can influence the lives on Earth. Special attention has been paid to the space surrounding Earth, including the solar wind, magnetosphere and ionosphere.

A number of physical phenomena are associated with space weather, including coronal mass ejections (CMEs), geomagnetic storms and substorms, ionospheric disturbance, aurora, geomagnetically induced currents on Earth, etc. Understanding relevant physical processes in the solar wind and magnetosphere, and constant monitoring of space weather is crucial to prevent or alleviate potential negative impacts that solar activities have on Earth.

A National Academy of Sciences report (Board and Council, 2009) identified many cases of social impact associated with space weather events. Below we list several examples whose potential costs are billions of dollars.

1. Damage to satellites. Radiation damage and spacecraft charging are the two most common adverse space weather effects on spacecraft. High energy particles (radiation) penetrating the spacecraft skin may cause erroneous signals, change bits in memory or even destroy sections of the electronics in the extreme cases. 46 of the 70 satellite failures reported in 2003 took place during the great geomagnetic storm in October 2003. Accumulation of electrostatic charge on spacecraft may trigger electric discharge and mislead decisions by the spacecraft computer. Recent studies suggest that spacecraft charging is the major risk to satellites in geosynchronous orbit. In addition, low-Earth-orbit satellites may suffer from quick orbit changes due to geomagnetic storms, which heat and increase the volume of the thermalsphere. Increasing satellite drag and lacking capability to quickly maneuver orbits led to the satellite collision between the Iridium 33 and Cosmos 2251 in 2009.

2. Damage to electric power grids. Geomagnetic storm can induce electric field in Earth's lithosphere. The induced voltage difference is couple to electric electric power grids by ground connections, which drives interfering currents that may damage transformers or even cause blackouts. Such damage was exemplified by the complete collapse of the Quebec power grid triggered by the magnetic storm in March 1989. Nine million people lost power access temporarily in the incident.

3. Disruption of radio signal. Major geomagnetic storms can push disturbed ionosphere towards equator and cause large ionospheric gradient. Ionosphere disturbances can disrupt long-distance radio communications in the HF band (3-30 MHz). Transpolar flight routes are especially sensitive to small space weather, since reliable radio com-

munication over the entire flight is necessary for operation per regulation. Diverting such a flight costs about $100,000.

4. Degradation of GPS. GPS and similar positioning and navigation systems have played a huge role in modern society. They have essentially become a major part of the infrastructure behind modern transportation and telecommunication systems and beyond. GPS uses signals at 1.675 GHz and 1.228 GHz, at which frequency radio signals can still transit a disturbed ionosphere, but may get distorted beyond ground receivers' tracking capability. Severe space weather events that corrup GPS signals have high social impacts. For example, the navigation tool operated by the US Federal Aviation Administration (FAA) for North American commercial aviation is disabled by every major space weather events, causing outage up to days.

1.5 Goals of this thesis

This chapter has given an extremely brief and broad introduction to the Sun, the solar wind and magnetosphere, and provided a few reasons why studing this environment is interesting and useful. The particular areas of this large field with which this thesis is concerned are instabilities, waves and interaction with electrons. Chapter 2 introduces the basic concepts describing these phenomena. Chapter 3 describes the spacecraft and working principles of the instruments used to study them. Chapters 4-8 describe several new results on these topics.

Chapter 2

Plasma physics, linear waves and electron holes

2.1 Linear dispersion relation of a plasma wave

The propagation of small amplitude plasma waves is governed by linearized plasma equations of motions. In a homogeneous medium, we can construct the general solution to a system of linear equations by a superposition of plane waves

$$\mathbf{E}(\mathbf{r},t) = \mathbf{E}_{\mathbf{k}} e^{i(\mathbf{k}\cdot\mathbf{r}-\omega t)} \tag{2.1}$$

where $\mathbf{E}$ is the perturbed electric field, and the constant phase $\mathbf{k}\cdot\mathbf{r} - \omega t = \text{const}$ yields the phase velocity

$$\mathbf{v}_{ph} = \frac{\omega}{k}\hat{\mathbf{k}} \tag{2.2}$$

Analogous expression to Eq. (2.1) can be constructed for the perturbed magnetic field $\mathbf{B}(\mathbf{r},t)$ as well.

A wave mode can be specified by the relation between the wavenumber vector $\mathbf{k}$ and wave frequency ω. Such relation allows us to determine how a group of waves disperse due to their different phase velocities that depend on frequencies, hence giving the name "dispersion relation". The general framework to obtain dispersion relation is outlined below before we dive into a particular plasma model.

Substituting plane wave solutions Eq. (2.1) into two Maxwell equations, namely the Ampere's law and the Faraday equation yields

$$\mathbf{k}\times\mathbf{B} = -\frac{4\pi i}{c}\mathbf{j} - \frac{\omega}{c}\mathbf{E} \tag{2.3}$$

$$\mathbf{k}\times\mathbf{E} = \frac{\omega}{c}\mathbf{B} \tag{2.4}$$

The current density linearly relates to the electric field in linear theory by the generalized Ohm's law

$$\mathbf{j} = \sigma\cdot\mathbf{E} = -\frac{i\omega}{4\pi}\chi\cdot\mathbf{E} \tag{2.5}$$

where σ is the electric *conductivity tensor*, and χ is the *susceptibility tensor*. Once we have decided plasma equations, be it cold plasma fluid equations, MHD equations or kinetic equations, χ becomes uniquely determined. Eliminating the magnetic field from Eq. (2.3), (2.4) and (2.5) yields the wave equation

$$\left(\mathbf{nn} - n^2\mathbf{I} + \epsilon\right) \cdot \mathbf{E} = 0 \tag{2.6}$$

where

$$\mathbf{n} = \frac{c\mathbf{k}}{\omega} \tag{2.7}$$

is the refractive index and

$$\epsilon = \mathbf{I} + \chi \tag{2.8}$$

is the *dielectric tensor*.

Therefore, non-trivial wave solutions ($\mathbf{E} \neq \mathbf{0}$) are given by the dispersion relation

$$D(\omega, \mathbf{k}) \equiv \det(\mathbf{nn} - n^2\mathbf{I} + \epsilon) = 0 \tag{2.9}$$

Polarization

A right-handed circularly polarized wave propagating along z axis is characterized by electric field of the following form

$$E_x = A\cos(kz - \omega t) \tag{2.10}$$

$$E_y = -A\sin(kz - \omega t) \tag{2.11}$$

In terms of complex amplitudes,

$$E_x/E_y = -i \tag{2.12}$$

At fixed location, time varying electric field rotates circularly in the direction given by the right-hand rule. Similarly, a left-handed circularly polarized wave has

$$\frac{E_x}{E_y} = i \tag{2.13}$$

2.2 Fluid treatment

Cold plasma

Cold plasma equations describe waves that propagate in a plasma much faster than typical thermal velocities. The fluid velocity is identical to the particle velocity. However, the cold plasma model determines the electromagnetic fields self-consistently using the charge and current densities generated by the particle motions.

MHD

The Magnetic Hydrodynamic (MHD) model is a simple yet powerful model to understand many processes in the solar wind and magnetosphere. The MHD approximation treats the plasma as a fluid and deals only with the bulk properties: total plasma mass density ρ, center of mass velocity $\mathbf{V}$, magnetic field B, electric field E, and total plasma pressure $p = n_i k_B T_i + n_e k_B T_e$. Ideal MHD goes further to ignore resistive and viscous effects. MHD equations describe large-scale and relatively violent motions of strongly magnetized plasmas in time scale longer than the ion gyration time.

The ideal MHD equations write

$$\frac{d\rho}{dt} + \rho \nabla \cdot \mathbf{V} = 0 \qquad \text{Continuity} \tag{2.14}$$

$$\rho \frac{d\mathbf{V}}{dt} + \nabla p - \frac{(\nabla \times \mathbf{B}) \times \mathbf{B}}{\mu_0} = 0 \qquad \text{Momentum} \tag{2.15}$$

$$-\frac{\partial \mathbf{B}}{\partial t} + \nabla \times (\mathbf{V} \times \mathbf{B}) = 0 \qquad \text{Induction} \tag{2.16}$$

$$\frac{d}{dt}\left(\frac{p}{\rho^\gamma}\right) = 0 \qquad \text{Eq. of state} \tag{2.17}$$

where $\gamma = C_p/C_v$ is the ratio of the specific heat, and the usual adiabatic index. We have also used the ideal MHD assumption of perfect conduction $\mathbf{E} + \mathbf{V} \times \mathbf{B} = \mathbf{0}$ to eliminate electric field from equations.

2.3 Kinetic treatment

Kinetic plasma equations

While a plasma resembles a conducting fluid or multiple fluids, one for each particle species, in many ways, many interesting aspects of a hot plasma we are interested in only appear in its macroscopic behavior, such as collisionless damping, finite larmor-radius effect, plasma wave echoes, etc. The methods of *kinetic theory* takes into account the motions of all the particles. The most widely used formulation of kinetic theory is the Boltzmann equation

$$\frac{\partial f_s}{\partial t} + \mathbf{v} \cdot \frac{\partial f_s}{\partial \mathbf{r}} + \frac{q_s}{m_s}\left(\mathbf{E} + \frac{\mathbf{v} \times \mathbf{B}}{c}\right) \cdot \frac{\partial f_s}{\partial \mathbf{v}} = \left.\frac{df_s}{dt}\right|_{\text{collisions}} \tag{2.18}$$

where $f_s(\mathbf{r}, \mathbf{v}, t)$ is the particle distribution function for the s species. $\mathbf{E}$ and $\mathbf{B}$ are the electric fields and the magnetic field averaged over a spatial volume containing many particles but small compared to the Debye length. The right-hand side of the equation is a formal term for the collisional effects, which we ignore in this thesis. Therefore we restrict ourselves to the so called *Vlasov equations*

$$\frac{\partial f_s}{\partial t} + \mathbf{v} \cdot \frac{\partial f_s}{\partial \mathbf{r}} + \frac{q_s}{m_s}\left(\mathbf{E} + \frac{\mathbf{v} \times \mathbf{B}}{c}\right) \cdot \frac{\partial f_s}{\partial \mathbf{v}} = 0 \tag{2.19}$$

A complete set of equations describing collisionless plasams consist of Vlasov equation, Maxwell's equations and the defition of spatial charge density and current density:

$$\sigma = \sum q_s \int d^3\mathbf{v} f_s(\mathbf{r}, \mathbf{v}, t) \tag{2.20}$$

$$\mathbf{j} = \sum q_s \int d^3\mathbf{v}\mathbf{v} f_s(\mathbf{r}, \mathbf{v}, t) \tag{2.21}$$

Linear perturbations in hot magnetized plasmas

Let's focus on linear perturbations in kinetic theory assuming plasma is hot and a constant external magnetic field exists. First-order perturbation to the velocity distribution function can be expressed in terms of the first-order electric field and magnetic field. Taking moments allow one to obtain the charge and current density and also susceptibility tensors. We first provide susceptibilities for general velocity distribution then we consider two special cases in the non-relativistic limit.

Susceptibilities for arbitrary velocity distrbitution function

For arbitrary $f_0(p_\perp, p_\parallel)$, the susceptibility tensor is given by

$$\begin{aligned}\chi_s =& \frac{\omega_{p0,s}^2}{\omega\Omega_{0,s}} \int_0^\infty 2\pi p_\perp dp_\perp \int_{-\infty}^\infty dp_{||} \left[\hat{\mathbf{e}}_{||}\hat{\mathbf{e}}_{||} \frac{\Omega}{\omega} \left(\frac{1}{p_{||}} \frac{\partial f_0}{\partial p_{||}} - \frac{1}{p_\perp} \frac{\partial f_0}{\partial p_\perp} \right) p_{||}^2 \right. \\ &\left. + \sum_{n=-\infty}^{\infty} \frac{\Omega p_\perp U}{\omega - k_{||} v_{||} - n\Omega} \mathbf{T}_n \right]_s \end{aligned} \tag{2.22}$$

where

$$U = \frac{\partial f_0}{\partial p_\perp} + \frac{k_{||}}{\omega} \left(v_\perp \frac{\partial f_0}{\partial p_{||}} - v_{||} \frac{\partial f_0}{\partial p_\perp} \right) \tag{2.23}$$

and

$$\mathbf{T}_n = \begin{pmatrix} \frac{n^2 J_n^2}{z^2} & \frac{inJ_n^2 J_n'}{z} & \frac{nJ_n^2 p_{||}}{zp_\perp} \\ -\frac{inJ_n^2 J_n'}{z} & (J_n')^2 & -\frac{iJ_n J_n' p_{||}}{p_\perp} \\ \frac{nJ_n^2 p_{||}}{zp_\perp} & \frac{iJ_n J_n' p_{||}}{p_\perp} & \frac{J_n^2 p_\parallel^2}{p_\perp^2} \end{pmatrix} \tag{2.24}$$

Here $J_n = J_n(z)$ is the Bessel function of the first kind. The argument $z = k_\perp v_\perp/\Omega$. Ω is the relativistic cyclotron frequency

$$\Omega = \frac{qB_0}{\gamma m_s c} = \frac{\Omega_{cs}}{\gamma} \tag{2.25}$$

Susceptibilities for a shifting Maxwellian

Very often the velocity distribution of interest in space plasmas can be decomposed into a sum of shifting Maxwellian distributions and generalized Lorenzian (kappa) distributions. A shifting Maxwellian takes the following form

$$f_0(v_\perp, v_\parallel) = \frac{1}{\pi^{3/2} v_{T\perp}^2 v_{T||}} \exp\left(-\frac{v_{T\perp}^2}{v_{T\perp}^2} - \frac{(v_\parallel - V)^2}{v_{T\parallel}^2}\right) \tag{2.26}$$

where V is a drift along the quasi-static background magnetic field. $v_{T\perp}$ and $v_{T||}$ are the perpendicular and parallel thermal speed

$$v_{T_c}^2 = \frac{2k_B T_c}{m} \quad c = \perp, \parallel \tag{2.27}$$

The susceptibilitiy tensor for species s is

$$\chi_s = \left(\hat{\mathbf{e}}_\parallel \hat{\mathbf{e}}_\parallel \frac{2\omega_p^2 V}{\omega k_\parallel v_{T\perp}^2} + \frac{\omega_p^2}{\omega} \sum_{n=-\infty}^{\infty} e^{-\lambda} \mathbf{Y}_n(\lambda)\right)_s \tag{2.28}$$

$$\mathbf{Y}_n(\lambda) = \begin{pmatrix} \frac{n^2 I_n}{\lambda} A_n & -in(I_n - I_n') A_n & \frac{k_\perp}{\Omega} \frac{n I_n}{\lambda} B_n \\ in(I_n - I_n') A_n & \left(\frac{n^2}{\lambda} I_n + 2\lambda I_n - 2\lambda I_n^2\right) A_n & \frac{ik_\perp}{\Omega}(I_n - I_n') B_n \\ \frac{k_\perp}{\Omega} \frac{n I_n}{\lambda} B_n & -\frac{ik_\perp}{\Omega}(I_n - I_n') B_n & \frac{2(\omega - n\Omega)}{k_{||} v_{T\perp}^2} I_n B_n \end{pmatrix} \tag{2.29}$$

where $I_n = I_n(\lambda)$ is the modified Bessel function with argument $\lambda = k_\perp^2 v_{T\perp}^2 / 2\Omega^2 = k_\perp^2 \rho_L^2$. Here A_n and B_n are

$$A_n = \frac{1}{\omega} \frac{T_\perp - T_{||}}{T_{||}} + \frac{1}{k_{||} v_{T||}} \frac{(\omega - k_{||} - n\Omega) T_\perp + n\Omega T_{||}}{\omega T_{||}} Z_0 \tag{2.30}$$

$$B_n = \frac{1}{k_{||}} \frac{(\omega - n\Omega) T_\perp - (k_{||} V - n\Omega) T_{||}}{\omega T_{||}} + \frac{1}{k_{||}} \frac{\omega - n\Omega}{k_{||} v_{T||}} \frac{(\omega - k_{||} V - n\Omega) T_\perp + n\Omega T_{||}}{\omega T_{||}} Z_0 \tag{2.31}$$

where $Z_0 = Z_0(\xi_n)$ is the plasma dispersion function (Fried and Conte, 1961) with the argument

$$\xi_n = \frac{\omega - k_{||} - n\Omega}{k_{||} v_{T||}} \tag{2.32}$$

2.4 Some linear modes of interest

Whistler waves

Whistler waves were first discovered in the early days of radio communication. In 1918, Barkhausen (1919) reported unusual whistling tones whose frequencies drop with time, when

listening to signals from an antenna connected to a vacuum tube amplifier. It was not until thirty yeras later that Storey (1953) explained the origin of whistlers. Whistlers are produced by lightning at high altitudes as instantaneous radio pulses, travel along the Earth's dipolar magnetic field from one hemisphere to the other and eventually return to the ground.

In general, the whistler mode is an electromagnetic plasma wave whose frequency could vary between the lower hybrid frequency and electron cyclotron frequency. It is pervasive in ionosphere, magnetosphere and the solar wind. We will give a brief description of its dispersion relation and polarization in the cold-plsam framework.

The linearized cold plasma equations are

$$m_i n_e \frac{\partial \mathbf{V}}{\partial t} = \frac{\mathbf{j} \times \mathbf{B}_0}{c} \tag{2.33}$$

$$c\mathbf{E} = -\mathbf{V} \times \mathbf{B}_0 + \frac{\mathbf{j} \times \mathbf{B}_0}{n_e e} + \frac{m_e}{n_e e^2} \frac{\partial \mathbf{j}}{\partial t} \tag{2.34}$$

The dielectric tensor has a simple form

$$\epsilon_{\text{circ}} = \begin{pmatrix} R & 0 & 0 \\ 0 & L & 0 \\ 0 & 0 & P \end{pmatrix} \tag{2.35}$$

where

$$R = 1 - \frac{\omega_{pe}^2}{\omega^2 + \omega\Omega_{ce} + \Omega_{ce}\Omega_{ci}} \tag{2.36}$$

$$L = 1 - \frac{\omega_{pe}^2}{\omega^2 - \omega\Omega_{ce} + \Omega_{ce}\Omega_{ci}} \tag{2.37}$$

$$P = 1 - \frac{\omega_{pe}^2}{\omega^2} \tag{2.38}$$

R and L represent the permittivities for right-handed and left-handed circularly polarized waves; P represents the permittivity parallel to the magnetic field and is identical to that of an unmagnetized plasma.

For the special case of waves propagating parallel to the magnetic field, Eq. (2.9) has three solutions

$$P = 0 \tag{2.39}$$

$$c^2 k^2/\omega^2 = R \tag{2.40}$$

$$c^2 k^2/\omega^2 = L \tag{2.41}$$

Whistler wave arise from the solution of Eq. (2.40), whose characteristic electric vector is $(E_x, iE_x, 0)$. Hence whistler wave is evidently a right-handed circularly polarized wave. Figure 2.1 shows a schematic dispersion relation of whistler wave in cold plasma.

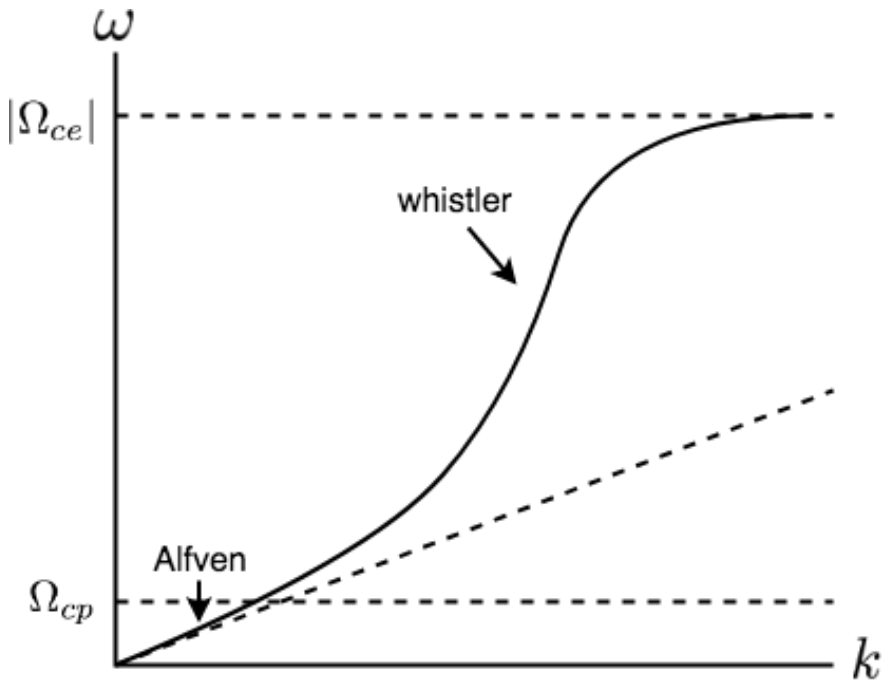

Figure 2.1: Schematic diagram showing the dispersion relation of whistler waves in a cold plasma.

At low frequencies ($\omega \ll \Omega_{ci}$), Eq. (2.40) yields Alfvén wave whose dispersion relation is

$$\omega = kv_A \tag{2.42}$$

where $v_A = \sqrt{B_0^2/\mu_0 n_i m_i}$ is the Alfvén speed. The continuation of the Alfvén wave above the ion cyclotron frequency is called the whistler wave, or sometimes, the electron cyclotron wave.

In the intermediate frequency, i.e., $\Omega_{ci} \ll \omega\Omega_{ce}$, the dispersion relation reduces to a simple expression

$$\omega \approx \left(\frac{kc}{\omega_{pe}}\right)^2 |\Omega_{ce}| \tag{2.43}$$

In this frequency range, a whistler wave packet propagate at the group velocity

$$v_g = \frac{d\omega}{dk} = 2c\frac{\sqrt{\omega|\Omega_{ce}|}}{\omega_{pe}} \tag{2.44}$$

that increases with wave frequency. Consequently, a whistler wave packet generated in the ionosphere has been stretched out temporally by the time it reaches receivers on the ground. Higher frequency components arrive earlier than its lower frequency components, hence whistler waves stand out in frequency-time spectrograms as lowering tones.

When the wave frequency approach the electron cyclotron frequency from below ($\omega \longrightarrow |\Omega_{ce}|$), a whistler wave excites electron cyclotron resonance ($R \longrightarrow \infty$). The transverse electric field associated with a whistler wave rotates with respect to the equilibrium magnetic field in the same direction as electrons gyration at the same velocity. As a result of continuous acceleration from electric field, the electrons gain perpendicular energy. Hence whistler waves are absorbed by electrons at the electron cyclotron frequency.

Above the cyclotron frequency, the solution to Eq. (2.40) is a plasma modified right-handed electromagnetic wave (i.e. light), and is not the focus of this thesis.

MHD waves

The linearized MHD equations give rise to three famous low frequency MHD wave modes: Alfvén wave, fast and slow magnetosonic waves. Their dispersion relations are

$$\omega = k v_A \cos\theta \qquad \text{Alfvén} \tag{2.45}$$

$$\omega = k v_+ \qquad \text{Fast} \tag{2.46}$$

$$\omega = k v_- \qquad \text{Slow} \tag{2.47}$$

$$\tag{2.48}$$

where

$$v_\pm = \sqrt{\frac{v_A^2 + c_s^2}{2} \pm \frac{1}{2}\sqrt{(v_A^2 + c_s^2)^2 - 4 v_A^2 c_s^2 \cos^2\theta}} \tag{2.49}$$

Here, v_A is the Alfvén speed and c_s is the sound speed

$$v_A = \sqrt{\frac{B_0^2}{\mu_0 \rho_0}} \tag{2.50}$$

$$c_s = \sqrt{\frac{\gamma p_0}{\rho_0}} \tag{2.51}$$

Obviously $v_+ > v_-$, hence the name of the two magnetosonic waves. Figure 2.2 shows the phase velocities of the MHD waves for the case $v_A > c_s$ (left) and the case $v_A < c_S$ (right). Here we assume that the external background magnetic field is along the z-axis and the wavenumber vector lies in the $x - z$ plane.

The density, pressure and magnetic field perturbations are given by

$$\delta\rho = \rho_0 \frac{\mathbf{k} \cdot \delta\mathbf{V}}{\omega} \tag{2.52}$$

$$\delta p = \gamma p_0 \frac{\mathbf{k} \cdot \delta\mathbf{V}}{\omega} \tag{2.53}$$

$$\delta B = \frac{(\mathbf{k} \cdot \delta\mathbf{V})\mathbf{B_0} - (\mathbf{k} \cdot \mathbf{B_0})\delta\mathbf{V}}{\omega} \tag{2.54}$$

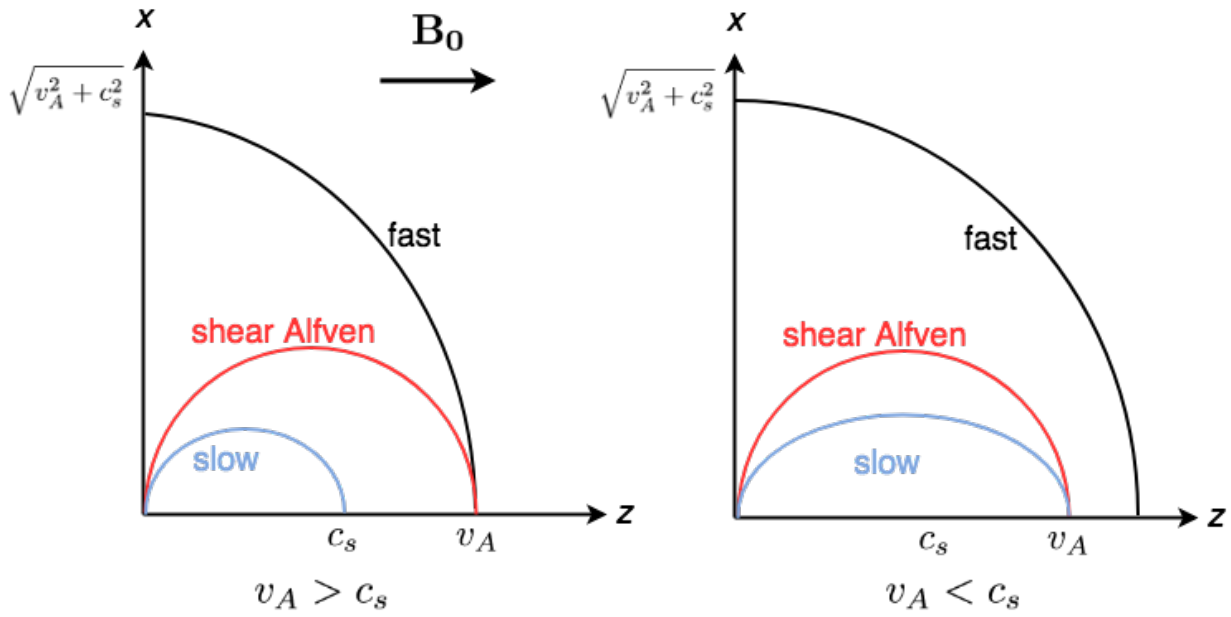

Figure 2.2: Phase velocities of three MHD modes.

The Alfvén mode is characterized by $\mathbf{k} \cdot \delta\mathbf{V} = 0$ and $\delta\mathbf{v} \cdot \mathbf{B_0} = 0$. The wave mode has no parallel magnetic field fluctuations and possesses no density or pressure perturbation. In other words, the Alfvén wave is incompressible. In contrast, the magnetosonic waves are strongly compressible: $\mathbf{k} \cdot \delta\mathbf{V} \neq 0$ and $\delta\mathbf{V} \cdot \mathbf{B_0} \neq 0$. In fact, the plasma pressure fluctuations linearly correlate with the parallel magnetic field fluctuations

$$\frac{\delta\mathbf{B} \cdot \mathbf{B_0}}{\mu_0} = \frac{v_A^2}{c_s^2}\left[1 - \left(\frac{kc_s \cos\theta}{\omega}\right)^2\right]\delta p \tag{2.55}$$

Since $v_+ > c_s \cos\theta$ and $v_- < c_s \cos\theta$, the plasma pressure and magnetic pressure fluctuations reinforce (oppose) each other in the fast (slow) magnetosonic wave.

Kinetic Alfvén waves

The Kinetic Alfvén wave (KAW) is obtained when the MHD shear Alfvén wave develops a large perpendicular wavenumber $k_\perp$. It deviates from the shear Alfvén waves in dispersion relation, polarization, field comprehensibility and other wave features.

The KAW is of particular interest in space plasma physics for a number of reasons. The finite parallel electric field associated with the KAW leads to Landau damping and particle acceleration (see e.g. Hollweg, 1999, and reference therein). Large-scale shear Alfvén waves naturally evolve into KAWs by the strong turbulence cascade (Goldreich and Sridhar, 1995). The dispersion or dissipation of KAWs are likely responsible for the dissipation range of the

turbulent interplanetary magnetic field at 1 AU (Leamon et al., 1999; Bale et al., 2005a; Howes et al., 2011; Salem et al., 2012a; Chen et al., 2013a).

To accurately obtain the dispersion relation and other wave properties, one needs to solve the full kinetic equations that include both electrons and ions, as we have outlined in Section 2.3. Analytic dispersion relation is available for some limiting cases.

Lysak and Lotko (1996) present a general analytic solution, which we summarize below. In the regime $\beta \ll 1$ and $k_\perp \rho_p \lesssim 1$, the fast mode decouples from the other two MHD mode. The KAW is a result of coupling between the shear Alfvén mode and the ion acoustic mode. The dispersion relation is given by the determinant

$$\det \begin{pmatrix} \frac{c^2}{v_A^2}\frac{1-\Gamma_0(\lambda_p)}{\lambda_p} - n_{||}^2 & n_{||}n_\perp \\ n_{||}n_\perp & \frac{\Gamma_0(\lambda_e)}{k_{||}^2\lambda_{De}^2}(1+\xi_e Z(\xi_e)) - n_\perp^2 \end{pmatrix} = 0 \tag{2.56}$$

where $\Gamma_0(\lambda) = e^{-\lambda} I_0(\lambda)$, $\lambda_{p,e} = k_\perp^2 \rho_{p,e}^2$, $n_{||,\perp} = k_{||,\perp} c/\omega$, $\xi_e = \omega/k_{||} v_{Te}$ Properties of KAW and Z is the plasma dispersion function. The above equation yields the dispersion relation

$$\frac{\omega^2}{k_{||}^2 v_A^2} = \frac{\lambda_p}{1-\Gamma_0(\lambda_p)} + \frac{\lambda_e}{\Gamma_0(\lambda_e)\left[1+\xi_e Z(\xi_e)\right]} \tag{2.57}$$

In the limit of hot electrons, $\xi_e \ll 1$ and small wave number $k_\perp \rho_e \ll 1$, the above expression reduces to the famous KAW dispersion relation

$$\omega^2 = k_{||}^2 v_A^2 \left[1 + k_\perp^2 \rho_p^2 \left(\frac{3}{4} + \frac{T_e}{T_p}\right)\right] \tag{2.58}$$

Eq. (2.58) was initially obtained when the KAW was first introduced to the space plasma community in Hasegawa and Chen (1976) to include the finite-gyroradius and the finite-electron-pressure effects.

The shear Alfvén wave is incompressible with no parallel magnetic field fluctuation $\delta B_{||}$. It also possesses no parallel electric field fluctuation $\delta E_{||}$. In contrast, the KAW develops $\delta E_{||}$, leading to Landau damping and plasma heating. KAW also becomes increasingly compressible (non-vanishing $\delta B_{||}$ and δn) with growing $k_\perp$, which implies non-negligible transit time damping.

Hollweg (1976) provides the analytic approximations for some wave properties of the KAW in the low beta regime. In particular, δn and $\delta B_{||}$ develop similar correlation as the MHD slow mode:

$$\frac{\delta B_{||}/B_0}{\delta n/n_0} = -\frac{v_s^2}{v_A^2} \tag{2.59}$$

where v_s is the sound speed with electron correction

$$v_s = \left(\frac{\gamma_p k_B T_p + \gamma_e k_B T_e}{m_p}\right)^{1/2} \tag{2.60}$$

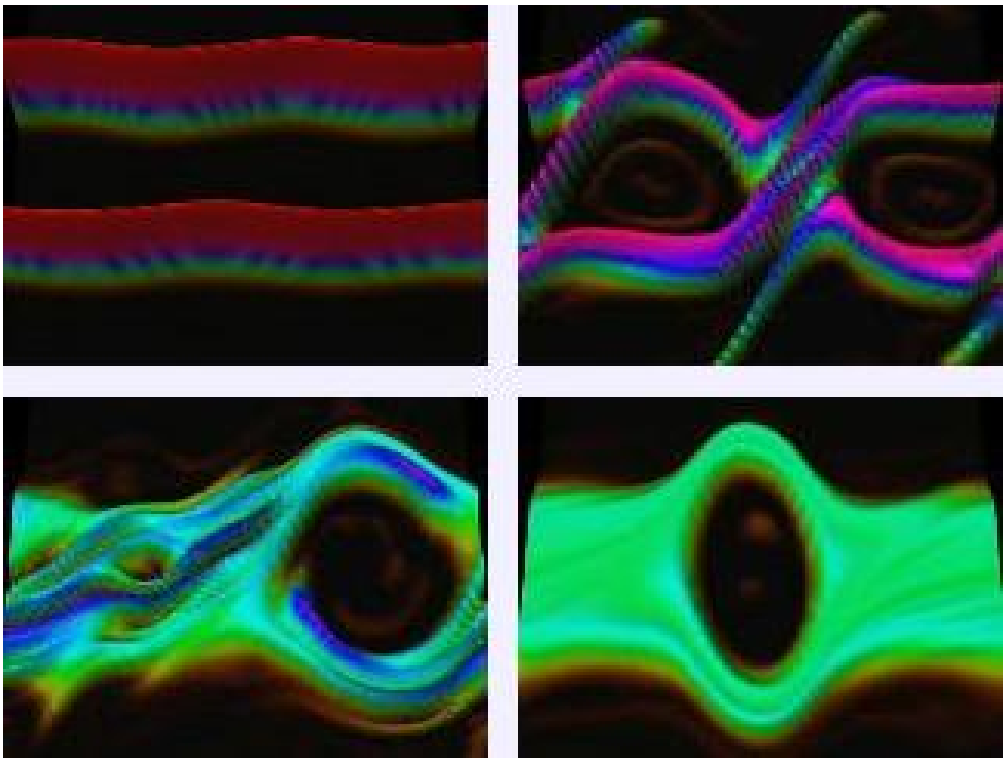

Figure 2.3: Example snapshots of the evolution of the phase space density $f(x, v_x)$ in a 1D PIC simulation of the two-stream instability. The simulation is described in Oppenheim, Newman, and Goldman (1999). The figure is accessed from `www.bu.edu/tech/support/research/visualization/gallery/epstornado`.

The electric field transverse to B_0 also becomes elliptically polarized and rotates in the electron sense

$$\frac{\delta E_x}{\delta E_y} \approx -i \frac{v_s^2}{v_A^2} \frac{\omega}{\Omega_{cp}} \tag{2.61}$$

2.5 Electron holes

An electron hole is a localized plasma region in which the electron density is lower than the ambient plasma due to reduced phase-space density on trapped electron orbits. Positive charge density and electric potential accompany the reduced electron density, and maintain the electron trapping self consistently. It has been referred to by many other names in the literature: "electron phase space hole", "electrostatic solitary wave", "phase space vortex", "time domain structures" and etc. Electron hole is a type of Bernstein, Green, and Kruskal (BGK) mode (Bernstein, Greene, and Kruskal, 1957).

Figure 2.3 gives an example of electron holes observed in a 1D PIC simulation of the

two-stream instability. The horizontal and the vertical axes represent the position x and velocity v_x; the color scale represent the logarithm of the phase space density. The two stream instability initially possesses small amplitude (panel (a)), then becomes nonlinear and start to trap electrons in two small electron holes (panel (b)). The nonlinear evolution merge the two small electron holes into a single big electron hole (panel (c)), which remains stable for thousands of electron gyro-period (panel (d)).

Electron holes frequently occur in simulations, laboratory plasmas and space plasmas. It was first observed in the earliest 1-D kinetic computer simulations of the two stream instability half a century ago (Morse and Nielson, 1969). The first observation in laboratory experiments happened ten years later in 1979 However, the first observation in space plasmas didn't take place until 1994 when fast sampling of the electric field waveform becomes available to resolve individual bipolar parallel electric fields which are signatures of electron holes (Omura, Kojima, and Matsumoto, 1994). Since then electron holes have been observed in many different space plasmas, e.g. the Earth's auroral region, bow shock, magnetopause, magnetosheath, plasma sheet, plasma sheet, free solar wind at interplanetary shocks and current sheets (see e.g. Hutchinson, 2017, for a review).

Since electron holes are predominantly electrostiatic, and are collisionless phenomenon requiring a kinetic description, the simplest set of equations governing the one dimensional electron hole are the Vlasov equation and Poisson's equation.

$$\frac{\partial f}{\partial \hat{t}} + v\frac{f}{\partial \hat{x}} - \frac{\partial \hat{\phi}}{\partial \hat{x}}\frac{\partial f}{\partial \hat{v}} = 0 \tag{2.62}$$

$$\frac{\partial^2 \hat{\phi}}{\partial \hat{x}^2} = \hat{n}_e - \hat{n}_i \tag{2.63}$$

Here several scaled dimensionless parameters are used to simplify the equations.

$$\begin{aligned} \hat{x} =& x/\lambda_{De} & \hat{t} =& \omega_{pe}t \\ \hat{n}_s =& n_s/n_\infty & \hat{\phi} =& e\phi/k_BT_e \\ \hat{v} =& v/\sqrt{k_BT_e/m_e} & \hat{u} =& v/\sqrt{2} \end{aligned} \tag{2.64}$$

where n_∞ is some fixed value representing the background plasma density. The hats are dropped hereafter for convenience. The Vlasov equation Eq. (2.62) is seldom solved explicitly. Instead, one generally only needs to use the fact that $f(v, x)$ is a constant along the particle orbits to find a solution for the electron hole model.

Assuming an electron hole remains steady shape and size in its rest frame, the distribution function is known at all orbits if it is known at the peak of the potential, i.e. f(u, x=0). Denoting $f(u, x = 0) = f_0(u)$ and $\psi = \phi(x = 0)$, then $f(u, x)$ and n_e become functions of

the potential and velocity

$$f(u,x) = f_0\left(\sqrt{u^2-\phi(x)+\psi}\right) \tag{2.65}$$

$$n_e(\phi) = \int f_0\left(\sqrt{u^2-\phi+\psi}\right) du \tag{2.66}$$

It is clear that an electron hole solution consist of a pair of self consistent $\phi(x)$ and $f_0(u)$ that satisfy Eqs (2.63) and (2.66).

The electron hole solutions can be obtained by two different approaches, the BGK approach (integral approach) and the Classical potential approach (differential approach). Both approaches are proposed in the original BGK paper (Bernstein, Greene, and Kruskal, 1957). The integral approach starts with a specified potential $\phi(x)$ which then define electron orbits in the phase space. Given the background distribution $f(u, x = \infty)$, then $f(u, x)$ everywhere can be obtained by solving an integral equation. The differential approach starts by specifying the distribution $f_0(u)$. Then solving the Poisson's equation (a differential equation) yields the potential profile and the particle orbits. The relative merits of the two approaches have been under debate over the years. The integral approach is more direct in terms of mathematical convenience, and the analysis starts with the observations of the potential shape and the background distribution. A key difference is that an electron hole of any spatial scale seems to be permitted by the integral approach, but very long electron hole is prevented by the differential approach. We refer to Hutchinson (2017) for more discussions on this topic.

Chapter 3

Spacecraft and Instruments

The results presented in this thesis are based on data from the plasma and fields instruments onboard WIND, THEMIS/ARTEMIS and MMS spacecraft. In this chapter we provide brief but self contained descriptions of the spacecraft and relevant instruments.

3.1 Missions

WIND

WIND is a single-spacecraft mission launched on November 1, 1994, as part of the International Solar Terrestrial Physics (ISTP) program. It was initially launched into a dual lunar swingby orbit, during which period the spacecraft made many crossings of the terrestrial bow shock and spent significant time in both the ion and electron foreshock regions upstream of the shock. Gravitational encounter with the Moon help pushing the apogee farther from the Earth to eventually reach L1 Lagrangian point between the Earth and the Sun. Since 2004, it has settled in a stable halo orbit around L1.

The main goal of the WIND mission is to provide complete measurement of plasma, energetic particle and magnetic field for magnetospheric and solar wind studies, and to provide baseline observations in the ecliptic plane at 1 AU for other missions in the inner and the outer heliosphere. To achieve this goal, the WIND spacecraft carries a full suite of instruments including: the Magnetic Field Investigation (MFI), the Solar Wind and Suprathermal Ion Composition Experiment (SMS), the Energetic Particles: Acceleration, Composition, and Transport (EPACT) investigation, the Solar Wind Experiment (SWE), a Three-Dimensional Plasma and Energetic Particle Investigation (3DP), and the Radio and Plasma Wave Investigation (WAVES).

By the time of writing, WIND has been working healthily in the space for a spectacular 25 years. It has resulted in more than four thousand peer-reviewed research papers and almost a hundred Master or PhD dissertations (Wilson III, 2017).

THEMIS / ARTEMIS

THEMIS, which is acronym for "Time History of Events and Macroscale Interactions during Substorms", is a NASA mid-Explore mission that consists of a constellation of five spacecraft (A to E). Its main science goal is to study substorms, the magnetic phenomena that drives violent eruptions of colorful auroras near Earth's poles.

The THEMIS spacecraft were launched on February 17, 2007. Each spacecraft carries identical science payload, including an electrostatic analyzer (ESA), a solid state telescope (SST), an electric field instrument (EFI), and fluxgate and search coil magnetometers (FGM and SCM). The spacecraft's orbits were chosen carefully so that their apogees line up about once every 4 days over an array of ground observatories in north America.

THEMIS successfully completed their mission in 2010. NASA repurposed two of THEMIS spacecraft to orbit around the Moon to study the interactions between the moon and the sun. The two spacecraft (THEMIS B and C or ARTEMIS 1 and 2) form the new mission ARTEMIS, which stands for "Acceleration, Reconnection, Turbulence and Electrodynamics of the Moons Interaction with the Sun.

The two spacecraft arrived in lunar orbit in 2011. ARTEMIS became the first mission ever to orbit the Moon's Lagrangian points, where the Moon's gravity perfectly balances that of Earth's. ARTEMIS have been contributing to Earth and lunar science, and to study of the solar wind since the arrival.

MMS

Magnetospheric Multiscale (MMS) is a NASA mission consisting of four identical spacecraft flying in a tetrahedral formation in near-equatorial orbits. The main science goal of MMS is to investigate magnetic reconnection, a process that magnetic fields connect and disconnect, in which energy is explosively transferred from one to another. Each of the four spacecraft carries the same instruments that measure plasmas, fields and energetic particles. The MMS spacecraft was launched on March 13, 2015.

MMS is built upon the success of the ESA CLUSTER mission, but well surpasses the latter in both the spatial and the temporal resolution, allowing for the time study of the elusively thin and transient electron diffusion region, where magnetic connection happens.

Each MMS spacecraft has an octagonal shape at a width of about 3.5 meters and height of 1.2 meter. Each satellite has 8 depolyable booms: four 60 meter wire booms in the spin plane and two 12.5 meter boom in the axial plane for electric field sensors, and two 5 meter booms in the spin plane for magnetometers. Each spacecraft carry identical suite of instrument that contain plasma analyzers, energetic particle detectors, magnetometers and electric field instrument. The plasma and fields instruments measure the particle distributions with an unprecedented millisecond time resolution.

3.2 Electrostatic Detectors

Wind, ARTEMIS and MMS all use some variants of the so called "top-hat" electrostatic analyzers (Carlson et al., 1982) to measure three-dimensional velocity distribution function of electrons and ions. Below we briefly describe how the most basic version work.

Figure 3.1 shows the top view and cross-section view of the most basic design following the original paper by Carlson et al. (1982). An ESA measures particle energy by applying a electrostatic potential across the outer and the inner section surfaces. Trajectories of charged particles are deflected and only those in certain range of velocities are allowed to go through the section, eventually hit microchannel plates (MCPs) on the exit that generates signals measurable by the instrument electronics. Top-hat ESAs have cylindrical symmetric spherical sections that give 360° field of view in the plane perpendicular to the cylindrical axis. Accordingly MCPs at section exits take cylindrical geometry and record entering solid angles of hitting particles. Mounted on a spinning spacecraft with appropriate orientation, an ESA can scan through the full 4π solid angles in a single spin period. The energy and angular resolutions of an ESA is determined by the analyzer geometry. With knowledge of energies and solid angles, measurements of particle counts can be transformed into 3D particle distribution function.

Table 3.1 summarize the performance of the ESAs onboard WIND, THEMIS/ARTEMIS and MMS (Lin et al., 1995; McFadden et al., 2008; Pollock et al., 2016).

3.3 Magnetometers

Magnetometers broadly fall into two categories, scalar magnetometers and vector magnetometers, the latter of which have been favored in space science. Among various types of vector magnetometers, search coil magnetometers (SCMs) and fluxgate magnetometers (FGMs) are the two most commonly used types in space missions. WIND, ARTEMIS and MMS all carry both SCMs and FGMs. A single magnetometer of either type can only measure a component of $\mathbf{B}$. Three magnetometers put in an orthogonal configuration allow measuring $\mathbf{B}$.

Search coil magnetometer

An SCM is essentially a coil of conducting wire wrapped around a high-magnetic-permeability material (core). External changing magnetic field are amplified by the core to induce voltage signals, which are measured as AC current. SCM is sensitive to AC magnetic field but has poor response to low frequency field. We show why this is the case below following Verscharen and Chandran (2013). The magnetic field inside the core is

$$\mathbf{B}_{\text{core}} = \mu_c \mathbf{B}_{\text{ext}} \tag{3.1}$$

Mission	instrument	FOV	angular resolution [°]	energy range	energy resolution	geometric factor [$cm^2 \cdot sr$]	3D time resolution	integration time
WIND	EESA-L	$180° \times 14°$	5.6-22.5	3 eV-30 keV	20%	0.013	1.5/3s	3ms
	EESA-H	$360° \times 90°$	5.6-22.5	0.1-30 keV	20%	0.1	1.5/3s	3ms
	PESA-L	$180° \times 14°$	5.6-22.5	3eV-30 keV	20%	$1.6 \cdot 10^{-4}$	1.5/3s	3ms
	PESA-H	$360° \times 14°$	5.6-22.5	0.1-30keV	20%	0.015	1.5/3s	3ms
ARTEMIS	ESA-e	$180° \times 6°$	22.5	2 eV-30 keV	17%	$6.6 \cdot 10^{-3}$	3s	-
	ESA-i	$180° \times 6°$	22.5	1.6 eV-30 keV	18%	$6.6 \cdot 10^{-3}$	3s	-
MMS	DES	$180° \times 34°$	9-15	0.01-30 keV	14-20%	$(1-7) \cdot 10^{-4}$	30ms	195μs
	DIS	$180° \times 34°$	≤ 15	0.01-30 keV	11-15%	$(1-2) \cdot 10^{-4}$	30ms	1ms

Table 3.1: Instrument performance summary of the ESAs onboard WIND, THEMIS/ARTEMIS and MMS.

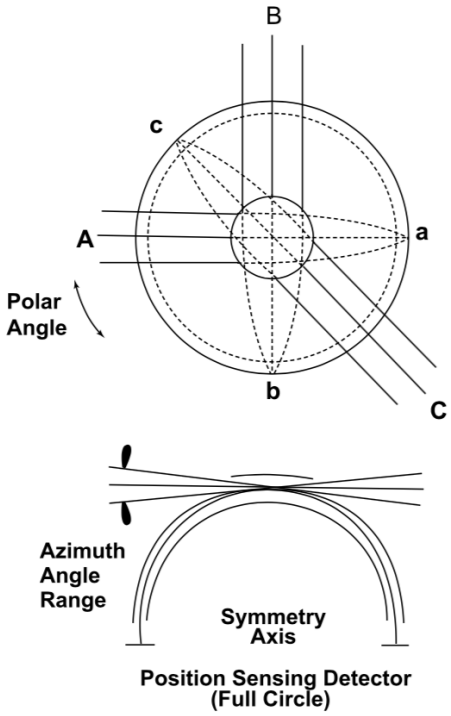

Figure 3.1: Top view and cross section view of the basic top hat plasma spectrometer first introduced by Carlson et al. (1982), who referred to it as a symmetric quadrisphere, this top hat ESA design has been used extensively in space missions. This illustration is adapted from Carlson et al. (1982)

where μ_c is the effective relative permeability of the core. By Faraday's law, the electromotive force (EMF) inside the coil is

$$\mathcal{E} = \frac{nA\mu_c}{c}\frac{dB_{ext,z}}{dt} \tag{3.2}$$

where we have assumed that the coil contains n turns, the core has a cross-sectional area A and the the core is orientated along the z-axis.

Consider an external magnetic field fluctuating at an angular frequency ω

$$B_{ext,z} = B_{z0}\sin(\omega t + \phi) \tag{3.3}$$

where B_{z0} is the peak amplitude. Then EMF becomes

$$\mathcal{E} = \frac{nA\mu_c B_{z0}\omega}{c}\cos(\omega t + \phi) \tag{3.4}$$

The above expression demonstrates that $\mathcal{E} \propto \omega$, i.e., SCM sensitivity increases with frequency. This explains why SCM is poorly sensitive in the low frequency range. In practice, SCM is used for the frequency range higher than a few hertz.

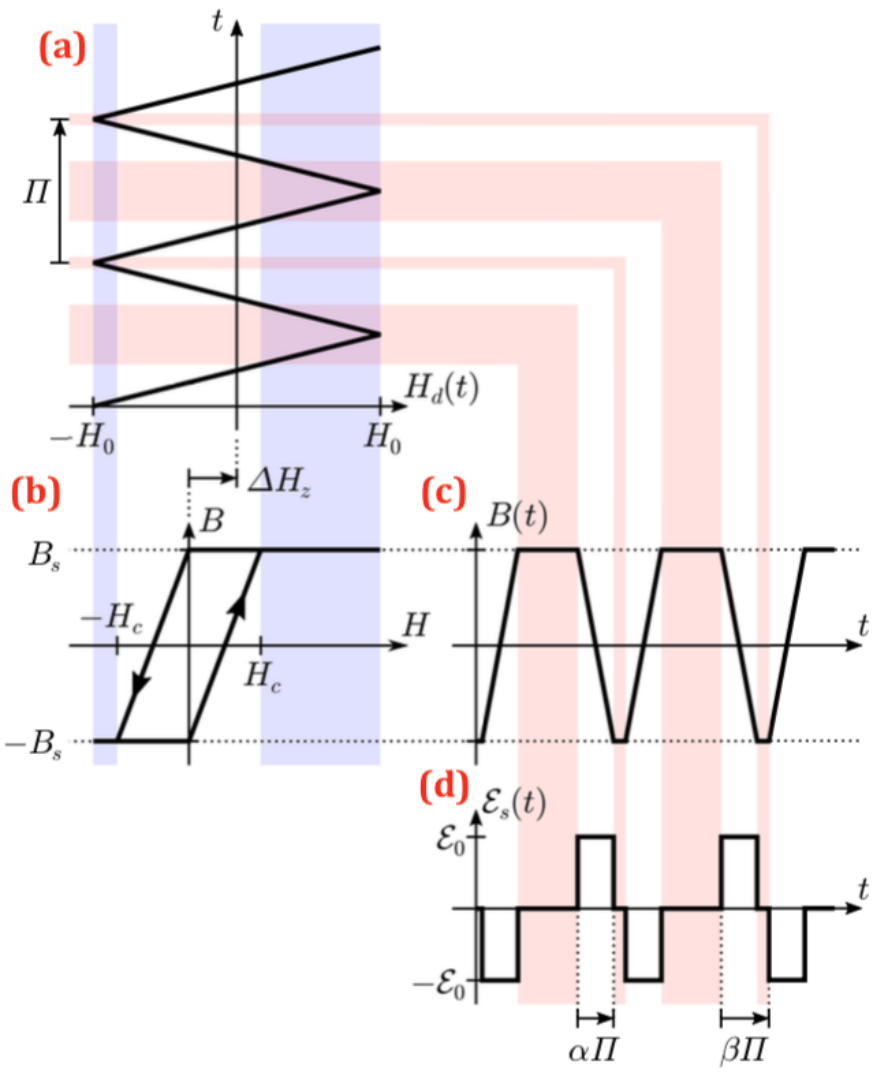

Figure 3.2: A schematic diagram illustrating the working principle of a basic fluxgate magnetometer. Taken from Verscharen, Klein, and Maruca (2019).

Fluxgate magnetometer

In contrast to SCM, FGM is suitable to measure quasi-static magnetic field or low frequency fluctuating magnetic field. We follow Verscharen, Klein, and Maruca (2019) to illustrate how the most basic FGM work.

FGM relies on the hysteresis of ferromagnetic materials. Figure 3.2(b) shows a simplified hysteresis curve. The magnetic field $\mathbf{B}$ depends on both the current external magnetic field $\mathbf{H}$ and some historical values $\mathbf{H}(t)$. However, $\mathbf{B}$ would saturate at $\pm B_s$ when $|\mathbf{H}|$ goes beyond some critical value H_c.

A basic FGM design includes a driver coil and a sensor coil. A periodic triangular current is applied on the driver coil to drive a triangular auxiliary field $H_d(t)$ as shown in figure 3.2(a). In the figure, H_0 is the amplitude and Π is the period. Assuming a constant external field ΔH is to be measured, the total auxiliary field in the ferromagnetic core is

$$H = H_d(t) + \Delta H_z \tag{3.5}$$

Here we have assumed that the core orient along z-axis. Figure 3.2(c) shows $B(t)$ inside the core as a function of time. Due to the saturation of the ferromagnetic core, $B(t)$ takes the form of truncated triangles. The uneven truncation arises as a result of the external field ΔH_z.

Figure 3.2(d) shows the time variation of EMF over the sensor coil $\mathcal{E}$ as irregular square pulses. The duration of positive pulses is denoted as $\alpha\Pi$, the time from the start of positive EMF to the start of negative EMF is denoted as $\beta\Pi$, as described in figure 3.2(d). From geometry, the two dimensionless parameters can be written as

$$\alpha = \frac{H_c}{4H_0} \tag{3.6}$$

$$\beta = \frac{1}{2} - \frac{\Delta H_z}{2H_0} \tag{3.7}$$

Notice α is fixed for a given FGM once H_0 has been chosen. Information of ΔH_z is contained in β. Typically H_0 is chosen to be very large so that $\alpha, \beta \ll 1$ and therefore the sensor EMF has the following Fourier expansion

$$\begin{aligned} \mathcal{E} &= \mathcal{E}_0 \sum_{k=0}^{\infty} \left(1 - e^{-i2\pi\beta k}\right) \frac{\sin(\pi\alpha k)}{\pi k} \cos\left(\frac{2\pi k t}{\Pi}\right) \\ \mathcal{E}_0 &= -\frac{2n_s A B_s}{c\alpha\Pi} \end{aligned} \tag{3.8}$$

where n_s is the number of turns in the sensor coil. Measuring the harmonics of EMF therefore inform the value of β and therefore of the external field ΔH_z. (3.8) also show that the amplitude of EMF are inversely proportional to the driving frequency. Therefore the FGM sensitivity drops with rising frequency.

3.4 Electric field

The double probe and the electron drift techniques are two most common techniques to measure electric fields or waveforms in space plasmas. WIND and THEMIS/ARTEMIS uses the former technique, whereas MMS uses both to measure the electric field. In this section, we briefly review both techniques.

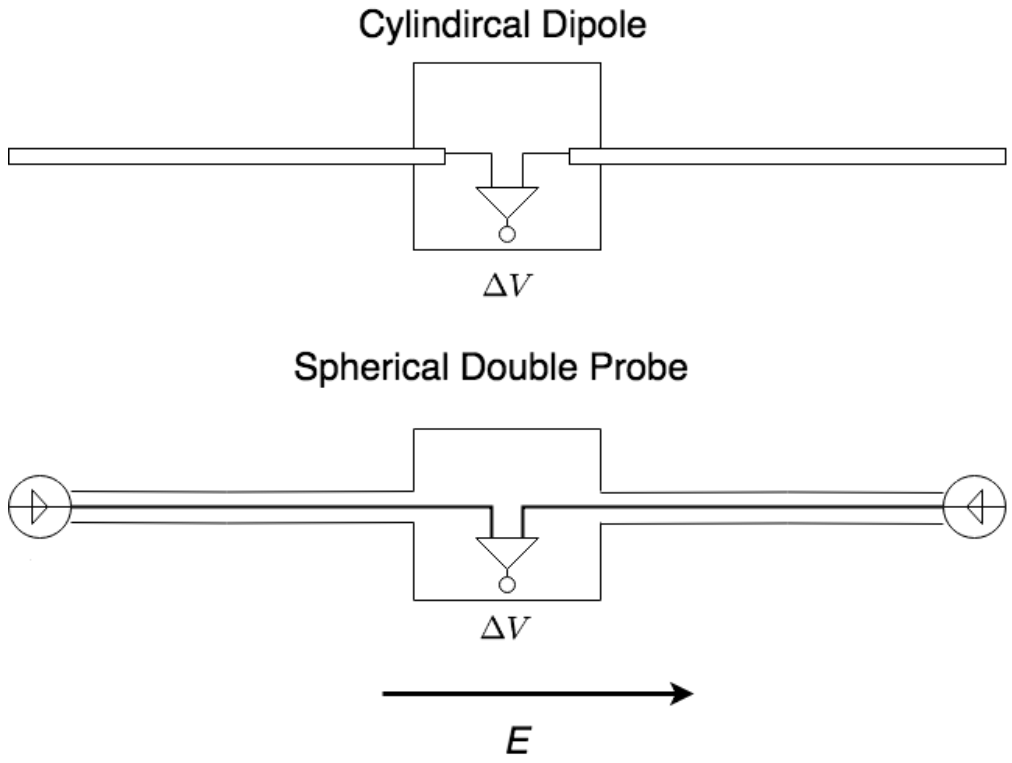

Figure 3.3: Schematic diagrams for cylindrical dipole antennas and spherical double probes.

Double Probe

The working principle of the double probe technique is direct potential measurement. In essence, the electric field instruments are sets of high-input-impedance, low-noise and broad-band digital voltmeters. External vector electric field can be estimated by measuring the potential difference between three pairs of electrodes separated along orthogonal directions, one can estimate the external vector electric field (Pedersen, Mozer, and Gustafsson, 1998).

Double probe techniques rely on dipole antennas, which have evolved over the years into two types, cylindrical dipoles and spherical double probes (Gurnett, 1998; Pedersen, Mozer, and Gustafsson, 1998; Maynard, 1998). Figure 3.3 shows the geometry of both types of antennas. The difference between the two are the active antenna elements. The active antenna elements are the cylindrical conductors at the tip of the boom (or simply the whole boom) in the case of cylindrical dipole antennas, whereas for a spherical double probe, the antenna booms are insulate and only two conducting spheres at the tips of the booms are active. In either case, the amplifier in the satellite body provides a voltage output that is proportional to the voltage difference between the antenna elements.

The response of an electric dipole antenna to electric field can be characterized as the effective length of the antenna L_{eff}, which relates the electric field E to the open circuit

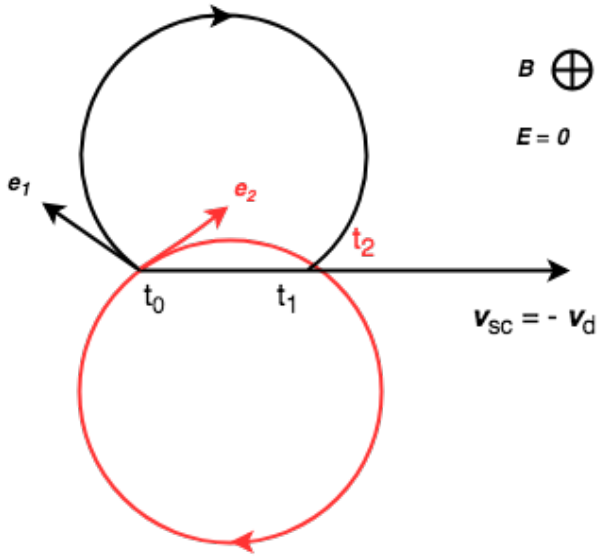

Figure 3.4: Schematic diagram illustrating the working principle of the electron drift technique.

potential difference between the antenna elements

$$\Delta V = EL_{eff} \tag{3.9}$$

In tenuous plasmas, the potential difference in the plasma Φ maybe different from the measured voltage difference between the two antenna elements ΔV if the dipole antenna is receiving signals passively (Paschmann et al., 1998). In such case, a suitably chosen bias current has to be applied over the antenna to force ΔV to stay close to Φ.

Electron Drift

The electron drift technique relies on the so called $E \times B$ drift. To zeroth order, the gyrocenter of charged particles drift perpendicular to both $\mathbf{E}$ and $\mathbf{B}$

$$\mathbf{v}_d = \frac{\mathbf{E} \times \mathbf{B}}{B^2} \tag{3.10}$$

We illustrate the basic working principle of an electron drift instrument below following (Paschmann et al., 1998; Vaith et al., 2013).

Figure 3.4 demonstrates a basic electron drift instrument. A frame in which no electric field exists is chosen to simplify the illustration. In this frame, the spacecraft moves at $\mathbf{v}_{sc} = -\mathbf{v}_d$. Two electron beams with known velocity v_e are launched in two directions $\mathbf{e}_1$ and $\mathbf{e}_2$ at t_0 and return to the spacecraft at t_1 and t_2. Assuming the chosen electron beam

	Double probes	Electron drift
Ambient B	no limitations	$B \geq B_c$
Frequency range	DC to MHz	$\leq$ 10 Hz (depending on beam nature)
Dimensionality	2D (spin plane) or 3D (if axial booms)	2D ($\perp$ **B**)
Sensitive to thermal/cold plasma	yes	no
Sensitive to SC-plasma interactions	yes	no
Sensitive to ambient keV electrons	low	May swamp signal
Sensitive to B-field variations	no	yes
Additional data products	SC potential, plasma density, waveform	$\|\mathbf{B}\|$
Alternative data products	density and temperature as a Langmuir probe	keV electron measurements at high time resolution

Table 3.2: Comparison of merits and drawbacks of the double probe and the electron drift techniques.

velocity is large $v_e \gg v_d$ then

$$t_1 - t_0 = T_g(1 - v_d/v_e) \tag{3.11}$$
$$t_2 - t_0 = T_g(1 + v_d/v_e) \tag{3.12}$$

where $T_g = 2\pi m_e/eB$ is the electron gyro-period. Hence the time of light measurements allow determining T_g and v_d which in turn yields $B = eT_g/2\pi m_e$ and $E_\perp = v_d B$.

To summarize, table 3.2 compares the characteristics of the double probe technique and the electron drift technique.

Chapter 4

Electron heat flux in the solar wind at 1 AU: WIND observation

Tong Y., Bale S. D., Salem C. S., Pulupa M. (2018). *arXiv*, preprint arXiv:1801.07694.

Electron heat flux in a collisionless mangetized plasma is not well understood. In this study, we report observations of the electron heat flux based on a large dataset of electron measurements in the solar wind at 1 AU. The electron heat flux in the collisionless solar wind generally deviates from the collisional values given by the Spitzer-Härm law with large spread. We confirm the strong beta dependence of the heat flux and show clear distinctions between low-beta and high-beta solar wind. In the low-beta solar wind ($\beta_{c||} \lesssim 1$, where $\beta_{c||} = 8\pi n_c k_B T_{c||}$ is the core electron parallel beta), q_e/q_0 shows an apparent upper bound of $\beta_{c||}^{-0.1}$ that only weakly varies with beta and has almost constant most probable values ~ 0.35. Here we normalize the electron heat flux q_e by the free streaming heat flux $q_0 = 3/2 n_e k_B T_{c||} v_{Tc||}$. In the high-beta solar wind, however, heat flux decreases quickly with beta. q_e/q_0 takes an upper bound of $2\beta_{c||}^{-0.8}$. The most probable heat flux takes the same beta scaling at lower values of $0.2\beta_{c||}^{-0.8}$. The heat flux values in the low beta plasma are consistent with values estimated from exospheric models, suggesting that heat flux may be controlled by the large-scale interplanetary electric field. In contrast, scattering of the suprathermal electrons is necessary to explain why the heat flux drop with beta. We discuss several collisionless mechanisms that might regulate the heat flux.

4.1 Introduction

The electron heat flux in a collisionless or weakly collisional plasma is poorly understood. While the collisional Spitzer-Härm law (Spitzer and Härm, 1953) is widely used in simulations

of space and astrophysical plasmas, it is thought to be inaccurate based on direct in-situ measurements in the solar wind (Feldman et al., 1975a; Scime et al., 1994; Salem et al., 2003; Bale et al., 2013) and remote observations of the temperature distribution of a hot gas in galaxy clusters (Cowie and McKee, 1977; Bertschinger and Meiksin, 1986; Zakamska and Narayan, 2003; Wagh, Sharma, and McCourt, 2014; Fang et al., 2018). Scudder (1992) argued that the Spitzer-Härm law may be inadequate for describing the heat conduction in the solar corona (see also Landi and Pantellini, 2001; Dorelli and Scudder, 2003). The heat flux suppression below the collisional value was recently established in the analysis of coronal loop oscillations (Wang et al., 2015).

The solar wind is a highly-ionized, weakly collisional plasma that expands super-Alfvénically from the solar corona into the heliosphere. Significant field aligned electron HF arises from the anisotropy in the electron velocity distribution function (eVDF), which is often modeled as a superposition of three gyrotropic populations: a cool dense 'core', a hotter tenuous 'halo', and a beam-like field-aligned 'strahl' (Feldman et al., 1975a; Feldman et al., 1976; Rosenbauer et al., 1977; Pilipp et al., 1987; Maksimovic, Pierrard, and Riley, 1997; Tong et al., 2019b). In the solar wind frame (here, we define the solar wind frame as the frame in which the total current of all solar wind ion species is zero), the core electrons drift sunward along the background magnetic field line, whereas the suprathermal (halo and strahl) electrons drift anti-sunward. The drift velocities of core and suprathermal electron populations are anti-correlated, maintaining near zero net electric current in the solar wind frame (Feldman et al., 1975a; Scime et al., 1994). The electron heat flux in the solar wind points anti-sunward and is predominately carried by the suprathermal halo and strahl.

The observations of the electron heat flux in the solar wind have been interpreted in terms of heat flux regulation by wave-particle interactions (Feldman et al., 1975a; Gary and Feldman, 1977; Scime et al., 1994), but the wave activity potentially regulating the electron heat flux is still under debate (e.g., Hollweg, 1978; Roberg-Clark et al., 2016; Tong et al., 2018a; Roberg-Clark et al., 2018b; Komarov et al., 2018; Vasko et al., 2019a). The alternative view is that wave-particle interactions may be not necessary to explain the observed heat flux values in the solar wind (Landi, Matteini, and Pantellini, 2012; Landi, Matteini, and Pantellini, 2014; Horaites et al., 2015). In this paper, we present new observations of the electron heat flux in the solar wind using a large dataset based on electron measurements onboard the WIND spacecraft, and compare with several collisionless processes that potentially regulate the heat flux.

The paper is organized as follows. Section 4.2 describes the data processing and introduces the dataset. Section 4.3 presents observations on the electron heat flux. Section 4.4 and 4.5 discuss collisionless processes in the high-beta and the low-beta solar wind in light of the observations. Section 4.6 conclude the discussions.

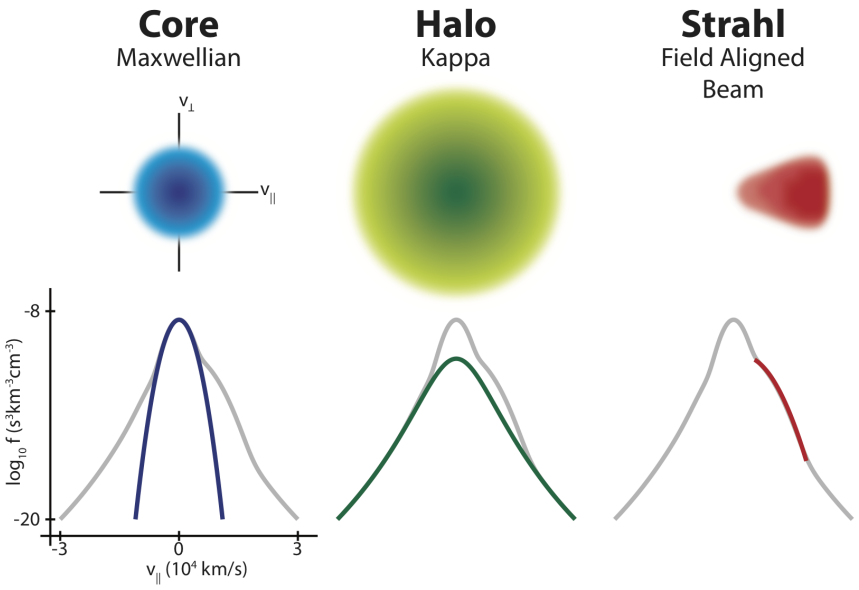

Figure 4.1: Schematic diagram for electron populations. Courtesy of Marc Pulupa.

4.2 Dataset

We use a solar wind electron dataset (Pulupa et al., 2014a) produced by nonlinear fits to the electron velocity distribution function (VDF), measured by two electron detectors (EESA-L and EESA-H (Lin et al., 1995)) onboard the WIND spacecraft. Spacecraft potential is corrected using independent measurements of electron density by the WIND/WAVES Thermal Noise Receiver (TNR) (Bougeret et al., 1995) using quasi-thermal noise analysis (Meyer-Vernet and Perche, 1989).

Each electron VDF is fitted to a two-component model

$$f_{fit}(v_{||}, v_{\perp}) = f_c(v_{||}, v_{\perp}) + f_h(v_{||}, v_{\perp}) \tag{4.1}$$

where f_c and f_h correspond to the core and halo electrons. The core distribution takes the form of a drifting, bi-Maxwellian

$$f_c(v_{||}, v_{\perp}) = A_c \exp\left[-\frac{(v_{||} - v_{0c})^2}{v_{Tc||}^2} - \frac{v_{\perp}^2}{v_{Tc\perp}^2}\right] \tag{4.2}$$

where $A_c = 2n_c v_{\perp}/\sqrt{\pi} v_{Tc\perp}^2 v_{Tc||}$ and $v_{Tcj} = \sqrt{2T_{cj}/m_e}$, $(j = ||, \perp)$. The halo distribution takes the form of a drifting, bi-kappa

$$f_h(v_{||}, v_{\perp}) = A_h B_h \left[1 + \frac{(v_{||} - v_{0h})^2}{v_{Th||}^2} + \frac{v_{\perp}^2}{v_{Th\perp}^2}\right]^{-\kappa-1} \tag{4.3}$$

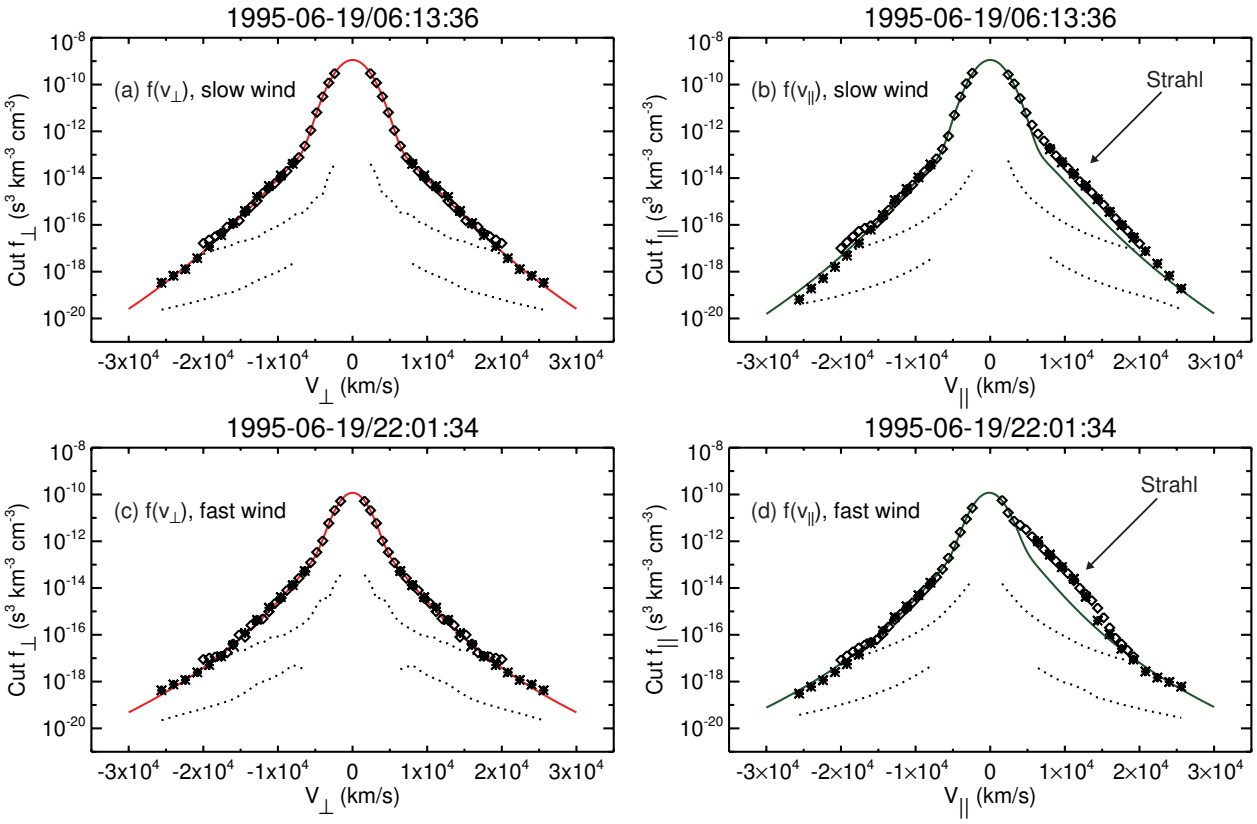

Figure 4.2: Measured solar wind electron distribution functions and fits. The top two panels show $f(v)$ in the slow solar wind ($v_{sw} \approx 381$ km/s), with $f(v_\perp)$ in panel (a) and $f(v_\parallel)$ in panel (b). Hollow squares show the EESA-L data, while asterisks mark the EESA-H data and small black dots mark the 1-count level for each detector. The red curve in panel (a) is the fit to the measured $f(v_\perp)$. The green curve in panel (b) is the fit to $f(v_\parallel)$. The strahl appears clearly as an enhanced field-aligned feature which is limited in energy. Panels (c) and (d) show the same features in the fast solar wind ($v_{sw} \approx 696$ km/s).

where $A_h = 2n_h v_\perp/\sqrt{\pi} v_{Th\perp}^2 v_{Th||}$, $B_h = \Gamma(\kappa+1)/\Gamma(\kappa-1/2)$ and the thermal velocities $v_{Thj} = \sqrt{(2\kappa-3)T_{hj}/m_e}$, $(j = ||, \perp)$.

The strahl electrons are characterized by the difference between the measured VDF and the fitted VDF: $f_s(v_{||}, v_\perp) = f(v_{||}, v_\perp) - f_{fit}(v_{||}, v_\perp)$. In this study we use the strahl density n_s and current j_s, as computed from the zeroth and first moments of f_s.

Figure 4.2 shows typical electron VDFs measured in the fast and slow solar wind; fast wind is characterized by hotter, more tenuous plasma than slow wind. The top panels show cuts through the perpendicular velocity distribution $f(v_\perp)$ and the parallel velocity distribution $f(v_\parallel)$ on the left and right, respectively, for an interval of slow solar wind. Data from EESA-L and EESA-H are included, shown as diamonds and stars respectively, and the 'one count' levels for each detector are shown as dotted black lines. The two detectors are

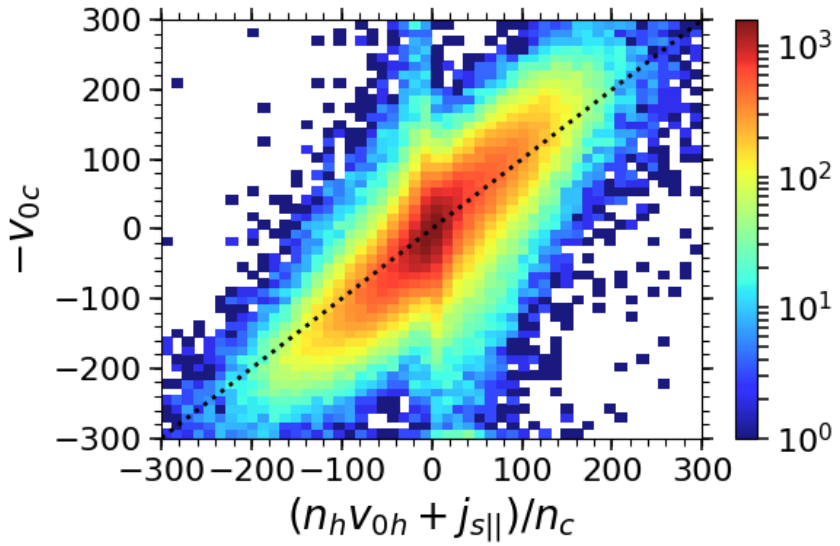

Figure 4.3: Frequency distribution of core electron drift with respect to suprathermal electron drift.

well inter-calibrated. The bottom panels show the same for an interval of fast wind.

Following the aforementioned procedure, we obtain 154,567 independent electron measurements from two, 2 year intervals: 1995-1997 (solar minimum) and 2001-2002 (solar maximum), and include only 'ambient' solar wind (no coronal mass ejections (CMEs), foreshock, etc.). Intervals of 'bidirectional' heat flux (usually associated with CMEs) are also excluded.

Figure 4.3 presents the distribution of $-v_{0c}$ and $(n_h v_{0h} + j_{s||})/n_c$ where the latter is the suprathermal electron drifts along the direction of background magnetic field. The black dotted line give reference to zero current. Overall the current due to the core electron drift balance the current of the suprathermal electrons very well, agreeing with existing knowledge that the net current is small in the solar wind (Feldman et al., 1975a; Scime et al., 1994; Artemyev et al., 2018). Spread of data along the zero-current line comes from either a real net current, the measurement uncertainty or the fitting uncertainty.

Notice that the sign of v_{0c} indicates the direction of the core bulk drift with respect to B_0. The core electrons predominately drift sunward in the frame of solar wind protons, but because the interplanetary magnetic field can take different polarities, v_{0c} can take either positive or negative values. For convenience of discussion, we define $\tilde{v}_{0c} \equiv v_{0c}\text{sign}(\mathbf{q}_e \cdot \mathbf{B}_0)$ so that a positive (negative) $\tilde{v}_{0c}$ indicate a sunward (an anti-sunward) core drift.

4.3 Electron heat flux observations

Early studies of the solar wind electrons indicate that the electron heat flux is often much smaller than the Spitzer-Härm heat flux (e.g. Scime et al., 1994; Salem et al., 2003). Figure 4.4 quantifies the difference between the solar wind heat flux and the collisional heat flux, and suggests that it enhances with the plasma beta. Panel (a) shows the histogram of q_e/q_{sh}, where q_{sh} is the collisional heat flux

$$q_{sh} = \sigma_{sh} \nabla_{||} T_e \tag{4.4}$$

defined in terms of the Spitzer-Härm thermal conductivity coefficient (Spitzer and Härm, 1953)

$$\begin{aligned} \sigma_{sh} =& \frac{3\sqrt{\pi}}{2} \frac{ne^2 \tau_{ep}}{m_e} \\ \nu_{ep} =& \frac{4\pi n e^4 \ln \Lambda}{m_e^2 v_{Te}^3} \end{aligned} \tag{4.5}$$

Here ν_{ep} is the electron-proton collision frequency, and $\ln \Lambda$ is the Coulomb logarithm. To estimate q_{sh}, we assume $T_e \sim r^{-\alpha}$ and approximate ∇T_e by $-T_e/\alpha$. While there is no consensus on the value of α, observations report values ranging from 0.4 to 0.8 (Le Chat et al., 2011, e.g.). We have assumed $\alpha = 0.6$, giving the most probable value of $q_e/q_{sh} \sim 0.5$. Taking a larger (smaller) value of α moves the whole histogram to the right (left). Nevertheless, the panel demonstrate clearly that the solar wind electron heat flux takes a broad range of values that are different from the collisional heat flux. Panel (b) shows the distribution of q_e/q_{sh} against $\beta_{c||}$. q_e/q_{sh} demonstrates strong negative correlation with $\beta_{c||}$. While q_e is comparable to or larger than $q_s h$ when $\beta_{c||} \lesssim 0.1$, q_e becomes an order of magnitude smaller than $q_s h$ when $\beta_{c||} \gtrsim 10$. The heat flux suppression compare to the collisional values is more pronounced in the high beta solar wind.

Panel (a) of figure 4.4 presents the frequency distribution of q_e/q_0 over $\beta_{c||}$. Scatter plots similar to this figure have been presented in literature in the context of heat flux regulation by the heat flux instabilities using the electron measurements onboard the Ulysses spacecraft (Gary et al., 1994; Gary et al., 1999; Gary, Skoug, and Daughton, 1999a). Those measurements imply a beta-dependent upper bound on q_e/q_0 but could not assert due to data scarcity, especially when $\beta_{c||} \lesssim 1$. With an unprecedentedly large number of independent particle measurements, figure 4.4(a) shows without ambiguity clear upper bound on electron heat flux for beta in the range $0.05 \lesssim \beta_{c||} \lesssim 50$. The upper bound takes the form of piece-wise power laws

$$q_e/q_0 = \begin{cases} \beta_{c||}^{-0.1} & \text{if } \beta_{c||} \lesssim 2 \\ 2\beta_{c||}^{-0.8} & \text{if } \beta_{c||} \gtrsim 2 \end{cases} \tag{4.6}$$

which are shown as the blue and red dotted lines in figure 4.4(a). The low-beta upper bound has very weak beta dependence since the power-law index is as small as -0.1. In the

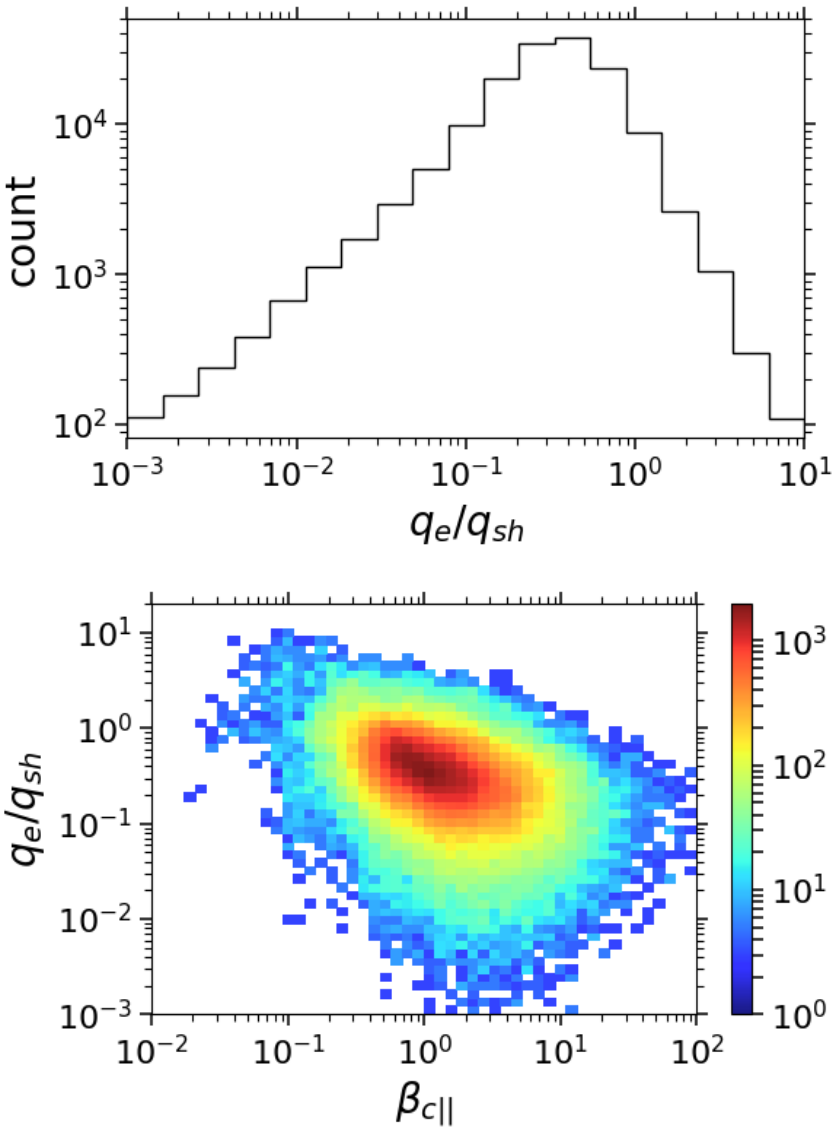

Figure 4.4: (a) Histogram of the ratio between the measured electron heat flux q_e over the Spitzer-Härm heat flux q_{sh}. (b) Frequency distribution of q_e/q_{sh} against core electron parallel beta $\beta_{c||}$.

higher-beta solar wind, the upper bound is much steeper with a power-law index of -0.8. The Ulysses measurements in the solar wind between 2 and 5 AU shows a similar power-law index of -0.82 (Gary et al., 1999) and -0.8 (Gary, Skoug, and Daughton, 1999a), suggesting that the upper bound on heat flux is real.

Figure 4.4(b) shows the normalized frequency of q_e/q_0 with respect to $\beta_{c||}$. For every $\beta_{c||}$ bin, the frequencies over q_e/q_0 bins are normalized by the largest frequencies among them, therefore giving normalized frequencies between 0 and 1. Essentially figure 4.4(b) demonstrates how the most probable values of heat flux depend on beta. Again different trends are observed in the low-beta solar wind and in the solar wind with order-unity-and-greater beta. The black and blue dashed lines in figure 4.4(b) provide the reference variation of the most probable q_e/q_0 with respect to $\beta_{c||}$ that roughly take the follow form

$$q_e/q_0 = \begin{cases} 0.35 & \text{if } \beta_{c||} \lesssim 0.5 \\ 0.2\beta_{c||}^{-0.8} & \text{if } \beta_{c||} \gtrsim 0.5 \end{cases} \tag{4.7}$$

In the low-beta solar wind, q_e/q_0 is most likely to take an almost constant value about 0.35. Interestingly, this value is very close to the collisionless electron heat flux suggested by Hollweg (1976) $q_c = 3/2 n_e k_B T_e v_{sw} \sim (1/3) 3/2 n_e k_B T_e v_{Te} = q_0/3$, assuming that $T_e \sim 10eV$

The distribution of $-\tilde{v}_{0c}/v_A$ with respect to $\beta_{c||}$ is presented in figure 4.6. It is striking that the maximum core electron drift in unit of the local Alfvén speed increases sharply with beta until unity beta then turns around and drops dramatically with beta.

The electron heat flux in the low-beta solar wind takes almost a constant fraction of the free streamng heat flux and is almost independent of beta. This behavior agrees with the collisionless heat flux that is controlled by the global interplanetary electric field, but a couple of other collisionless processes might be relevent as we shall see in Section 4.5. In the solar wind with intermediate or high beta, however, the electron heat flux develops strong negative correlation with the electron beta, which points to physical processes that scatter heat-carrying suprathermal electrons. The efficiency of such processes has to increase with electron beta. Several candidate collisionless processes are considered in Section 4.4

4.4 Collisionless processes in the high-beta solar wind

Whistler heat flux instability

The whistler heat flux instability (WHFI) is a circularly right-handed polarized electromagnetic whistler mode that may become unstable in case of large electron heat flux (Gary et al., 1975a). It propagates parallel to the magnetic field in the same direction as the electron heat flux. The WHFI is the fastest growing mode for a wide range of plasma parameters typical to the solar wind and therefore has long been considered a likely candidate to kick

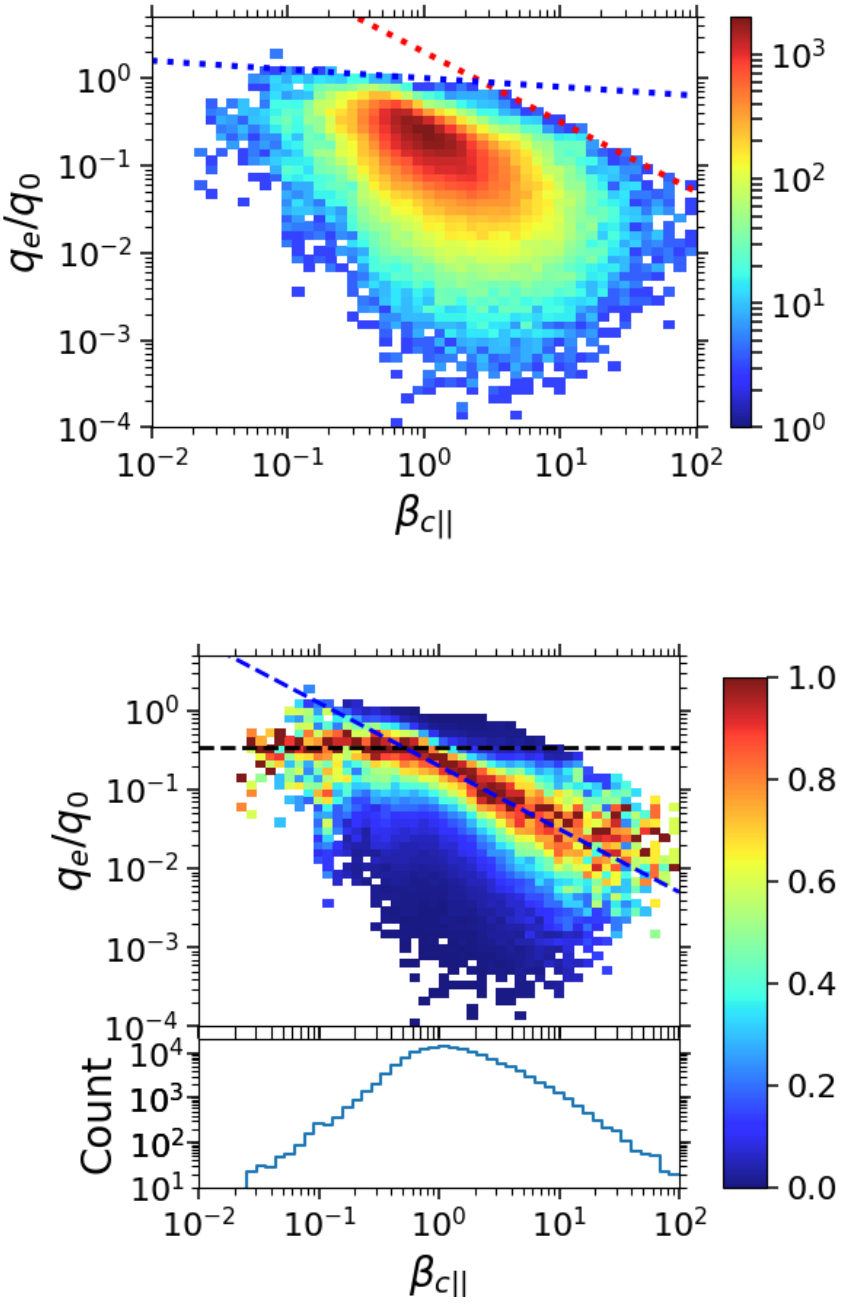

Figure 4.5: (a) Frequency distribution of normalized heat flux with respect to core electron parallel beta. (b) Normalized distribution of normalized heat flux with respect to core electron parallel beta.

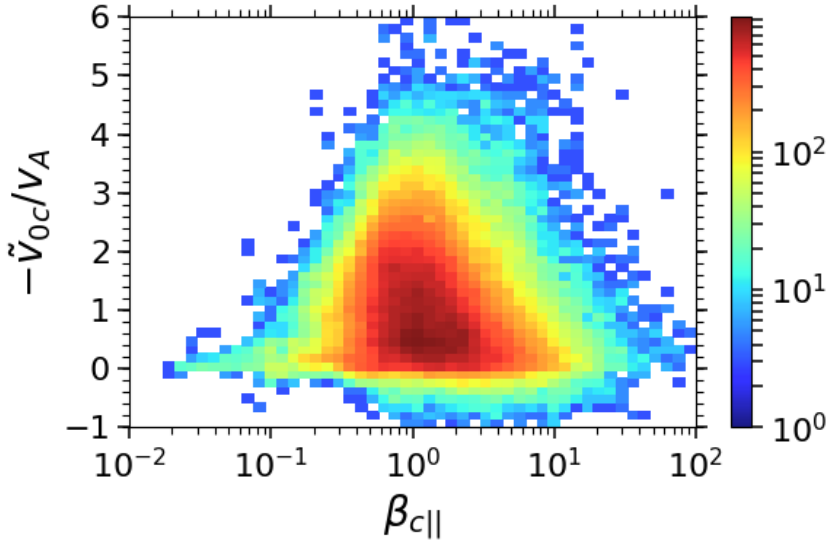

Figure 4.6: Distribution of normalized core electron drift versus core electron parallel beta.

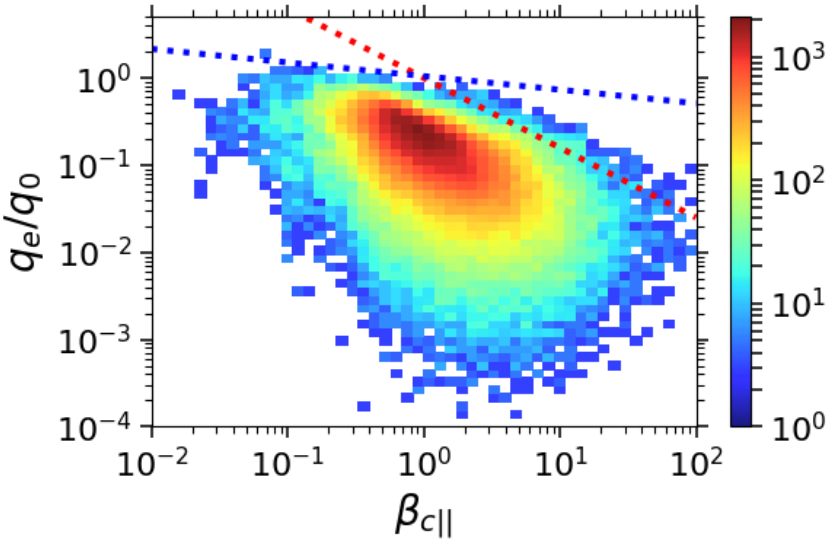

Figure 4.7: Distribution of electron heat flux against core electron parallel beta overplot with linear instability thresholds of KAW and WHFI.

in when electron heat flux in the solar wind exceeds its instability threshold (Feldman et al., 1976; Gary et al., 1994; Gary et al., 1999).

The WHFI cyclotron resonates with the tail of the halo electrons and its growth rate can be described by the kinetic framework outlined by Kennel and Petschek (1966). The halo electron density fraction, the halo temperature anisotropy and the halo drift speed together determine the growth rate of a WHFI. If the solar wind heat flux is predominately carried by the halo electrons, the WHFI growth rate develops dependence on the total electron heat flux.

The above considerations lead to parametric studies of the WHFI based on linear stability analysis. (Gary et al., 1999) use the Ulysses measurements of the solar wind electrons to calculate the linear dispersion relations of the WHFI, and report that the linear growth rate contour for $\gamma/\Omega_p = 10^{-2}$ scales with beta as $q_e/q_0 = \sqrt{2}\beta_{c||}^{-0.8}$ in the beta range $0.1 \leq \beta_{c||} \leq 5.0$. (Gary, Skoug, and Daughton, 1999a) use another set of Ulysses data and obtain a similar growth rate contour $q_e/q_0 = \sqrt{2} \cdot 0.85\sqrt{2}\beta_{c||}^{-0.82}$. Gary and Li (2000) conduct similar calculations for $\beta_{c||} < 10^3$, and find that proton Landau damping become non-negligible in high beta plasmas. However, the power-law index remains between 0.8 and 1.0. Figure 4.7 overlay the linear instability threshold $q_e/q_0 = \sqrt{2}\beta_{c||}^{-0.8}$ (red dotted line) on the WIND observation. The WIND heat flux measurement show with convincing statistics that the linear instability threshold agree with the observed heat flux upper bound quite well.

Unfortunately, the WIND spacecraft does not have reliable magnetic field measurements in the frequency range of the whistler waves, therefore it is difficult to correlate wave activities directly with the marginal instabilities. However, narrow band whistler waves of kinetic origins are quite often observed in the solar wind and are estimated to show up in as much as 10% of the clean solar wind at 1 AU (Lacombe et al., 2014). Very recently, simultaneous particle and electromagnetic waveform measurements onboard the ARTEMIS spacecraft are used to show for the first time of local narrow band whistler waves generated by WHFI (Tong et al., 2019b).

It is tempting to combine the particle measurements in this study with the prevalent whistler wave observations to conclude that the WHFI suppresses electron heat flux in the intermediate-and-high-beta solar wind. However, this mechanism has a key issue yet to be resolved. Since the WHFI propagates anti-sunward, it can only effectively interact with halo electrons on the tail of the distribution. If the WHFI can reduce electron heat flux, the reduction has to happen in the nonlinear stage of the instability. A very recent of particle-in-cell (PIC) simulation suggest that monochromatic WHFIs are incapable of reducing electron heat flux (Kuzichev et al., 2019 (submitted)). Therefore, the agreement between the linear instability threshold of the WHFI and the apparent upper bound on the electron heat flux might be a coincidence. Nevertheless, a large fraction of the whistler waves seem to be generated by WHFI (Tong et al., 2019a). The physical consequence of such whistler waves are still under active investigation.

Oblique electromagnetic whistler instabilities

Roberg-Clark et al. (2018a) recently report 2D PIC simulations that model the heat conduction in collisionless and weakly-magnetized (i.e. high beta) plasmas (see also Komarov et al., 2018; Roberg-Clark et al., 2018b). A hot and a cold temperature reservoirs at the two ends of a simulation box keep a temperature gradient along an ambient magnetic field. The simulations show that the temperature gradient destabilizes oblique whistler waves that grow to large wave amplitude, $\delta B/B \sim 1$, scattering heat-flux-carrying electrons thus reducing the heat flux significantly. Roberg-Clark et al. (2018a) show that the resultant heat flux is independent of the temperature gradient, and is instead controlled by the phase speed of whistler waves. The whistler-suppressed heat flux scales with $1/\beta_e$ in the PIC simulations, in rough agreement with the WIND observation in the high-beta solar wind.

However, direct observational evidence supporting the above mechanism operating in the solar wind is still lacking. There are two features of the whistler waves in the simulations that enable efficient heat flux reduction. First, the wave is quite oblique, very often around $40^\circ - 50^\circ$ (private communication with Roberg-Clark). Second, the waves possess large amplitude, $\delta B/B_0 \lesssim 1$.

Observations of strong and narrow-band electromagnetic whistler waves with relatively long duration in the solar wind at 1 AU suggest that they are predominately quasi-parallel propagating with $\theta_{kB} \leq 30^\circ$ (Lacombe et al., 2014; Kajdič et al., 2016a). Such whistler waves are quite often observed and estimated as much as 10% (Lacombe et al., 2014) in the clean solar wind. In addition, observation of significantly oblique whistler waves in the solar wind are rare (Tong et al., 2019a) and are often linked to shocks (Breneman et al., 2010; Wilson et al., 2013).

The whistler wave amplitude in the solar wind is likely much smaller than suggested by Roberg-Clark et al. (2018a). Tong et al. (2019a) study the wave amplitude of whistler waves in the solar wind at 1 AU using the magnetic field spectra processed onboard ARTEMIS, and conclude that $\delta B/B_0 \lesssim 0.01$. Note that the magnetic field spectra averaged over a few seconds may significantly underestimate the wave amplitude of very short-lived waves. This issue should be addressed with direct waveform captures in the future.

In short, existing evidence of the heat-flux-driven oblique electromagnetic whistler waves operating in the solar wind is still lacking. This specific heat flux suppression mechanism might be more relevant to astrophysical plasmas.

Whistler fan instability

Vasko et al. (2019a) consider self-inhibition of the electron heat flux by quasi-electrostatic whistler waves. A core-strahl velocity distribution is adopted to demonstrate that the strahl electrons could spontaneously generate highly oblique whistler waves via the so-called fan instability. Such whistler waves propagate about $70^\circ - 80^\circ$ to the strahl, have group velocities parallel to the strahl, and have wavelengths shorter or comparable to the electron gryoradius, therefore are likely to scatter the suprathermal electrons efficiently. The authors suggest that

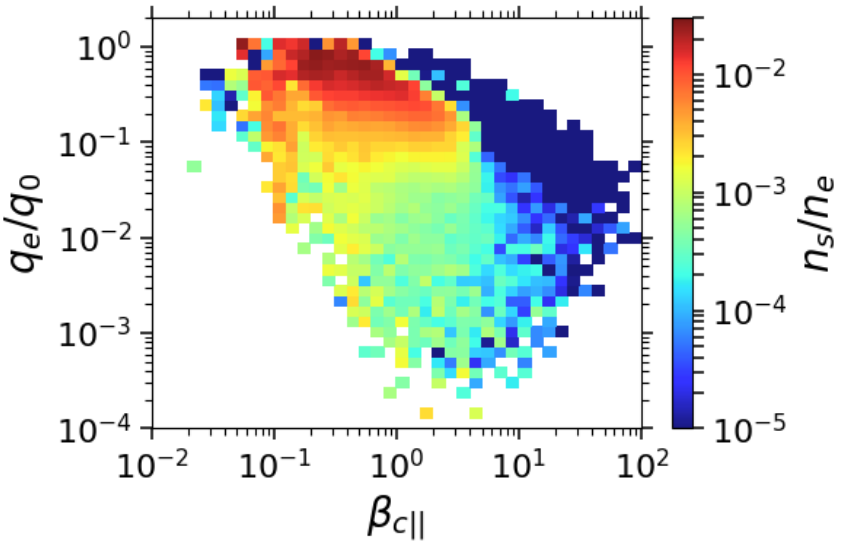

Figure 4.8: Median strahl electron density in the plane of normalized heat flux and core electron parallel beta.

these quasi-electrostatic whistler waves pitch-angle scatter the strahl electrons into the halo electrons and suppress the total electron heat flux to values below some beta-dependent threshold. Indeed, figure 4(b) in Vasko et al. (2019a) show qualitatively the same behavior as the observed heat flux upper bound in our figure 4.5.

However, it is unclear whether this mechanism could operate in the solar wind at 1 AU. Oblique whistler waves with weak magnetic field signature has not been actively sought after and reported.

The onset of the fan instability requires large disparity between the parallel and the anti-parallel VDF, which suggest a large strahl density fraction or a large strahl drift speed (Vasko et al., 2019a). However, such requirement may not be achieved in the solar wind at 1 AU. Figure 4.8 shows the WIND measurement of the median strahl density fraction n_s/n_e over every bin in the plane of q_e/q_0 and $\beta_{c||}$. The median n_s/n_e can be as large as about a few percent in the low-beta solar wind when q_e/q_0 is large. When $\beta_{c||} \gtrsim 1$, however, the median n_s/n_e becomes negligible, which suggests that the halo carry the majority of the electron heat flux. Note that the strahl population in this study is defined differently from Vasko et al. (2019a) (the latter includes some of the halo electrons in our study) therefore technically our strahl density fraction is not directly comparable to the values in Vasko et al. (2019a). But we suggest that the amount of strahl electrons is not likely to be sufficient to drive electrostatic whistler waves via the fan instability in local plasmas in the solar wind at 1 AU. Fitting WIND electron VDF measurement by the same model as Vasko et al. (2019a) could verify this statement.

Another possible scenario is that the fan instability kicks in much closer to the sun than

at 1 AU where the strahl density is presumably much larger. The heat flux suppression happens in the inner heliosphere and the solar wind just transport the suppressed heat flux to 1 AU. This more speculative scenario could be investigated with data from the Parker Solar Probe.

Whistler component temperature anisotropy instability

An electron VDF with a sufficiently large perpendicular temperature anisotropy generates whistler waves propagating both parallel and anti-parallel to $\mathbf{B}_0$ (Kennel and Petschek, 1966), among which the sunward propagating parallel whistler waves could potentially effectively scatter heat-carrying suprathermal electrons. The solar wind electrons seldom exhibit strong $T_{e\perp}/T_{e||}$ to drive the whistler temperature anisotropy instability (WTAI) (Lacombe et al., 2014). However, the temperature anisotropy of a electron population may also drive whistler waves. The whistler component temperature anisotropy instability (WCTAI) associated with the anisotropic core and halo populations is recently considered in literature (Lazar et al., 2018).

Panel (a) of figure 4.9 shows the distribution of $T_{h\perp}/T_{h||}$ with respect to $\beta_{e||}$. The red solid and dashed curves show for reference the WCTAI instability threshold for the growth rate $\gamma = 10^{-3}\Omega_{ce}$ and $\gamma = 10^{-2}\Omega_{ce}$ respectively. These thresholds are taken from Lazar et al. (2018)

$$T_{h\perp}/T_{h||} = \begin{cases} 1 + 0.081\beta_{h||}^{-0.566} & \text{if } \gamma = 10^{-3}\Omega_{ce} \\ 1 + 0.173\beta_{h||}^{-0.527} & \text{if } \gamma = 10^{-2}\Omega_{ce} \end{cases} \tag{4.8}$$

where the halo kappa is assumed $\kappa_h = 8$ and $n_c T_{c||}/n_h T_{h||} = 3.27$. (Another assumption of $\kappa_h = 3$ yield very similar thresholds.) We emphasize that $\gamma = 10^{-3}\Omega_{ce}$ is a very fast growth rate in the solar wind at 1 AU, corresponding to an e-folding growth time of one to a few second (Tong et al., 2019b). In comparison, the solar wind typically takes about a week to travel from the sun to the earth. Therefore, we expect the solar wind samples above the $\gamma/\Omega_{ce} = 10^{-3}$ threshold to generate parallel whistler waves locally.

Panel (b) of figure 4.9 shows the median value of q_e/q_0 in every bin in the $(T_{h\perp}/T_{h||}, \beta_{e||})$ plane. The same instability thresholds as in panel (a) are overplotted. q_e/q_0 show small variation around 0.1 in the plane except a strikingly drop out near the WCTAI threshold, where q_e/q_0 is suppressed by up to an order of magnitude. Recall that figure 4.8 show that the halo carry the majority of the heat flux in the solar wind when $\beta_{c||} \gtrsim 1$. The coincidence of solar wind unstable to the WCTAI and the heat flux dropout suggest that the WCTAI generates sunward whistler waves that effectively scatter anti-sunward part of the halo electrons.

Notice while the core electron perpendicular temperature anisotropy could also generates parallel whistler waves, our data does not reveal a correlation with the heat flux drop out as in the case of the halo electrons. Therefore, we conclude that the halo temperature anisotropy may contribute to the heat flux suppression when $\beta_{e||} \gtrsim 1$. We emphasize that

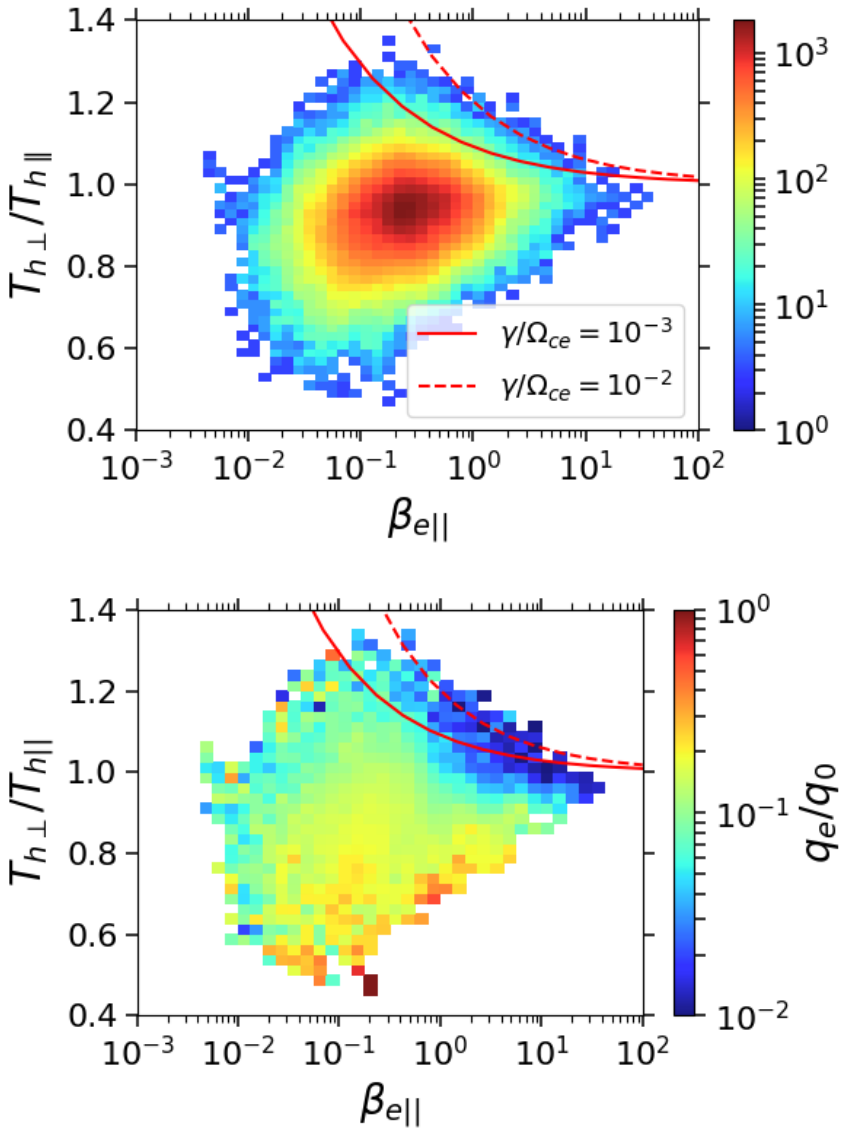

Figure 4.9: (a) Frequency distribution of halo electron temperature anisotropy with respect to halo parallel beta. (b) Median heat flux values as a function of halo electron temperature anisotropy and halo electron parallel beta.

this mechanism only partially solve the problem, because it does not operate when halo electrons show parallel temperature anisotropy.

parameters	linear calculation	dataset
n_h/n_e	0.05	0.04 ± 0.04
n_s/n_e	-	0.01 ± 0.01
T_h/T_c	6	5.6 ± 3.6
$T_{c\perp}/T_{c\parallel}$	1	0.98 ± 0.09
$T_{h\perp}/T_{h\parallel}$	0.9	0.91 ± 0.10
v_A/c	1.5×10^{-4}	$(1.6 \pm 0.8) \times 10^{-4}$

Table 4.1: Typical values of some dimensionless parameters in the WIND electron dataset ($\beta_{c\parallel} \in [0.1, 2]$). These parameters take fixed values in the linear stability analysis of KAWs.

4.5 Collisionless processes in the low beta solar wind

Unstable kinetic Alfvén wave

Linear stability analysis of plasmas consisting of drifting core-halo populations show that kinetic Alfvén waves (KAW) become unstable easily in the low-beta solar wind (Gary et al., 1975a). Gary et al. (1999) suggest that the KAW instability may constrain the heat flux in the low-beta solar wind while the WHFI constrain the heat flux in the high-beta solar wind. In this section, we present data supporting the potential role of KAWs.

The heat-flux-driven KAW instabilities in the solar wind is intimately related to the core electron drift. Since the core make the majority of the solar wind electron density, the bulk drift of the core with respect to the solar wind protons create a positive slope that drives unstable KAWs via Landau resonance. Since the phase speed of a KAW is comparable to the proton thermal velocity, the proton Landau damping is significant as well. It is hypothesized that the marginal instability of KAWs would impose an upper bound on the electron heat flux in the low-beta solar wind (Gary et al., 1999). The theoretical heat flux upper bound associated with the KAW instability has not been seriously investigated due to scarce particle measurements in low beta. The WIND electron dataset provide for the first time compelling measurement of the heat flux upper bound in the low-beta regime.

To obtain the marginal instability threshold on the core drift, we conduct a growth rate analysis over the beta range $\beta_{c||} \in [0.1, 2]$ using a core-halo electron model. Table 4.1 summarizes the mean values and the standard deviations of several dimensionless parameters in the WIND dataset over $\beta_{c||} \in [0.1, 2]$. To illustrate the instability threshold on the core drift, we fixed the value of n_h/n_e, T_h/T_c, $T_{c\perp}/T_{c||}$, $T_{h\perp}/T_{h||}$ and v_A/c to values close to their mean values in the WIND dataset. The proton population is simplified as a single Maxwellian population with a temperature T_p. Since the proton Landau damping is also strong, several values of T_c/T_p are considered. The only free parameters in the linear stability calculation are $\tilde{v}_{0c}/v_A$ and $\beta_{c||}$.

Figure 4.10 demonstrates that the beta-dependent KAW instability threshold on $\tilde{v}_{0c}/v_A$ well constrain the WIND observation. The red solid, dashed and dotted curves in the panels represent the instability thresholds for KAW instability at a growth rate $\gamma/\Omega_p = 10^{-2}$ and

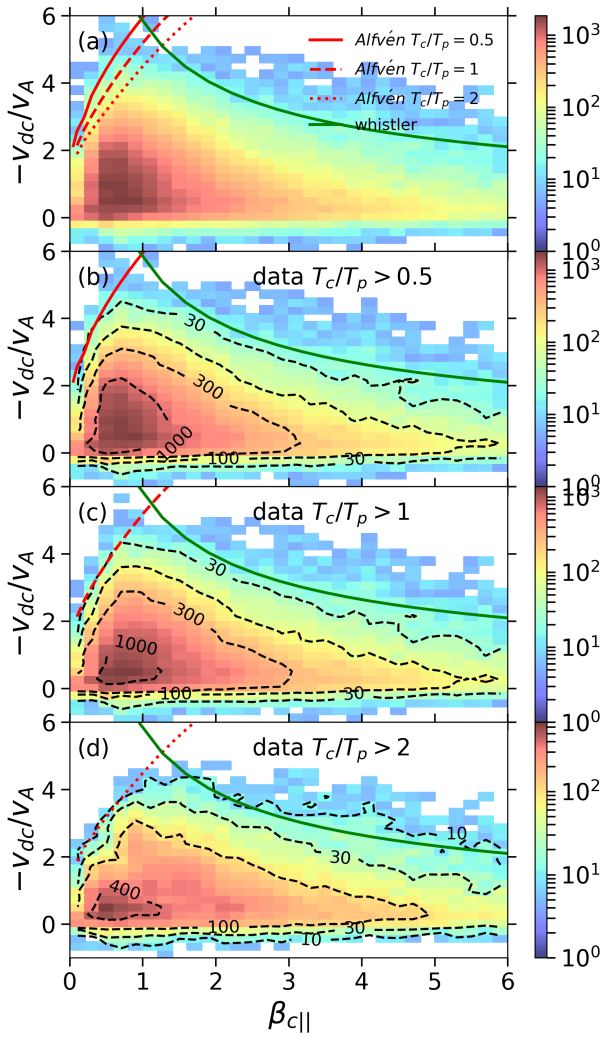

Figure 4.10: Constraint on drift velocity by marginal instabilities of KAWs.

$T_c/T_p = 0.5, 1$ and 2 respectively. Choosing a larger (smaller) growth rate imposes less (more) constraint on the the core drift. It turns out that $\gamma/\Omega_p = 10^{-2}$ fits the observation better as we will explain. Note when T_c/T_p increases from 0.5 to 2, the marginal core drift threshold increase as well, which is a consequence of an enhanced proton Landau damping. At proton gyroradius scale, the KAW phase speed is only slightly larger than the typical Alfvén speed therefore

$$\frac{v_{ph}}{v_{Tp}} \gtrsim \frac{v_A}{v_{Tp}} \approx \sqrt{\frac{1}{\beta_{c||}}\frac{T_c}{T_p}} \tag{4.9}$$

When $\beta_{c||} \ll 1$, increasing T_c/T_p from 0.5 to 2 makes the KAW phase speed become more comparable to the proton thermal speed, therefore enhancing the proton Landau damping

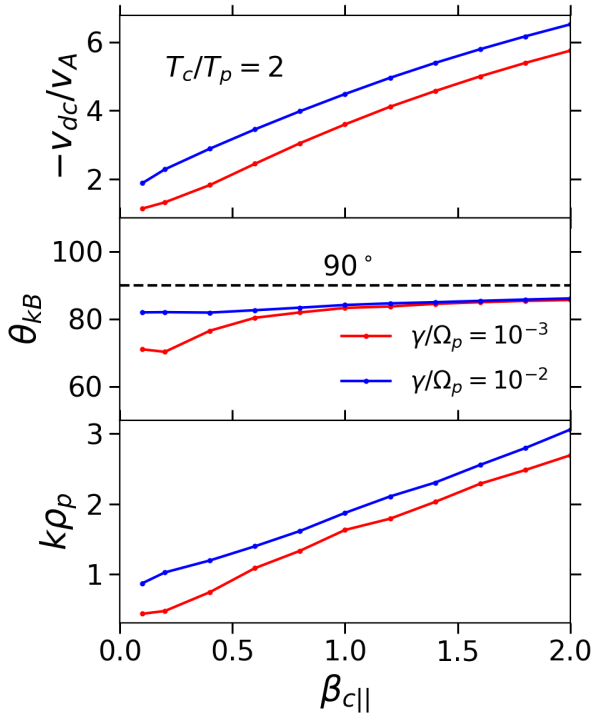

Figure 4.11: Dependence of the wavenumbers of the unstable KAW modes on core electron beta.

and reducing KAW growth rate.

The color plots in the panel (a) to (d) of figure 4.10 show the distribution of $-\tilde{v}_{0c}/v_A$ with respect to $\beta_{c||}$. The differences are the conditions on T_c/T_p. Panel (a) uses all the data, while panel (b)-(d) requires that $T_c/T_p > 0.5, 1$ and 2 respectively. The black dashed traces in panel (b)-(d) shows the distribution contours with frequency labels. The KAW instability thresholds strikingly lie on top of some distribution contours for each choice of T_c/T_p, suggesting that onset of heat flux driven KAWs may constrain the data distribution.

We could further convert the KAW marginal instability thresholds on the core drift to marginal instability thresholds on the heat flux. Fitting by a power law of beta we obtain

$$\frac{q_e}{q_0} = 1.05\beta_{c||}^{-0.156} \tag{4.10}$$

for the range $\beta_{c||} \in [0.1, 2]$ and $T_c/T_p = 0.5$. This theoretical upper bound is very close to the observed one given by Eq. (4.6) and is shown by the blue dotted traces in figure 4.7.

Figure 4.11 shows the properties of the most unstable KAWs. Their wavelengths are comparable or smaller than the proton gyroradius, propagating at very oblique angles around $80° - 90°$ with respect to B_0. Their group velocities have the same direction as the core electron drifts with respect to protons, that is in the sunward direction.

Roberg-Clark et al. (2018b) report KAW-like magnetic field fluctuations associated with double layers in their PIC simulations studying the heat flux suppression in low beta plasmas (also see Section 4.5) and suggest that these fluctuations does not suppress the heat flux. Note that the KAW structures in Roberg-Clark et al. (2018b) in fact have much smaller scale $k_\perp d_e \sim 1$, where $d_e = v_{Te}/\omega_{pe}$ is the electron inertial length. It is still unclear how the heat flux driven KAWs at ion scales can reduce the heat flux. While these KAWs are oblique and can interact with anti-sunward heat-carrying electrons by cyclotron resonance, the resonance would happen at very high energies comparable to the typical energy of suprathermal electrons at around 100-1000 eV:

$$\begin{aligned} v_{res} \approx & \frac{\Omega_{ce}}{k_{||}} = \frac{m_p}{m_e}\frac{v_{Tp}}{k_{||}\rho_p} \\ & \sim \frac{2000 \cdot 30}{k_{||}\rho_p} km/s \sim \frac{6 \cdot 10^4}{k_{||}\rho_p} km/s \\ & \sim \frac{10^4}{k_{||}\rho_p} eV \end{aligned} \tag{4.11}$$

Broadband turbulence has been suggested as possible alternative mechanism to effectively reduce heat flux (Vocks et al., 2005; Horaites et al., 2018). How does the nonlinear stage of the unstable KAWs interact with suprathermal electrons and the associated heat flux is an open problem for future studies to address.

Double layer

Roberg-Clark et al. (2018b) conduct a series of 2D PIC simulations to study the heat conduction in magnetized collisionless plasmas under imposed temperature gradient for $\beta_e \in [1/4, 32]$. They report a transition from a whistler-dominated heat flux suppression in high-beta plasmas to a double-layer-dominated heat flux suppression in low-beta plasmas. In the low-beta plasmas, the whistler wave suppression of heat flux saturates quickly as the whistler wave amplitude becomes small. The double layers are formed in the nonlinear stage of the Buneman instability driven by the cold electrons penetrating into the hot electrons to balance the current associated with the hot electrons. Roberg-Clark et al. (2018b) show that the double layers possess a potential drop $e\Phi_{DL} \sim 0.4 k_B T_h$ over tens of Debye length. Heat-carrying hot electrons with energy lower than the double layer potential are efficiently scattered by the double layers, suppressing the heat flux to $q_e/q_0 \sim 0.3$.

Despite the unrealistic temperature gradient, the series of PIC simulations by Roberg-Clark et al. (2018a) and Roberg-Clark et al. (2018b) reproduce some key features of our heat flux observation: the power-law scaling with electron beta in the high beta solar wind and the rollover to an almost constant fraction of the free streaming heat flux in the low beta solar wind (see figure 4.5 and Eq. (4.7)).

Mangeney et al. (1999) report observations of double layers in the solar wind using the electric field measurement onboard WIND. These double layers have a typical length scale

of 25 Debye length and very weak potential jump of $e\Delta\phi/k_BT_e \sim 3\times10^{-4}$. Therefore the double layers in the solar wind at 1 AU is likely to be too weak to affect the suprathermal electrons and the heat flux at all.

In fact, for the localized double layers to suppress heat flux to constant values in the solar wind at 1 AU, the average electric field associated with the double layer is

$$\begin{aligned}\langle E\rangle \sim & \frac{\Phi}{L}\sim\frac{k_BT_e}{10e\lambda_D}\\ \sim & \frac{10}{10\times10}\mathrm{V/m}\sim 100\mathrm{mV/m}\end{aligned} \tag{4.12}$$

where we have taken the typical electron temperature to be 10 eV and the typical Debye length to be 10 m. It is not unreasonable to assume the peak electric field to be a few times larger than the average electric field, therefore $E_{\max}\sim 1$V/m. It would be surprising to observe such huge electric field in the solar wind even inside 1 AU. An alternative to the localized electrostatic structure would be the large scale interplanetary electric field, which does imply beta-independent heat flux (Hollweg, 1976).

4.6 Conclusions

In this paper, we present new observations of the electron heat flux and the electron component drifting in the solar wind at 1 AU based on a statistically large dataset built upon particle measurements made by the WIND/3DP instrument. Our observations are summarized below.

1. The electron heat flux shows large variations. It can be either larger or smaller than the Spitzer-H arm heat flux in the low-beta solar wind, but become most likely smaller than the Spitzer-H arm value in the high-beta solar wind.

2. The electron heat flux show an apparent upper bound that can be divided into two power laws of beta: $q_e/q_0\sim\beta_{c||}^{-0.1}$ when $\beta_{c||}\lesssim 2$ and $q_e/q_0\sim 2\beta_{c||}^{-0.8}$ when $\beta_{c||}\gtrsim 2$

3. The most probable heat flux is about a constant fraction of the free streaming heat flux $q_e/q0\sim 0.35$ in the low-beta solar wind.

4. The distribution of core electron drift speed show an upper bound that increase with beta when $\beta_{c||}\lesssim 1$ but decrease with beta when $\beta_{c||}\gtrsim 1$.

The physics shaping the heat flux in the solar wind is likely a combination of multiple processes. We have compared the new observations with a few collisionless processes that may regulate the electron heat flux. Below are our suggestions.

1. The whistler heat flux instability (WHFI) yields an upper bound on the heat flux that is comparable to the observed one. But its anti-sunward propagation direction and the small wave amplitude prevent efficient interactions with the heat-carrying electrons.

2. Recent PIC simulations of collisionless plasmas with a temperature gradient along an ambient magnetic field reproduce the transition of the heat flux at around unity beta. They suggest that the large amplitude oblique whistler waves and the double layers with large potential drops are responsible for the heat flux suppression in the high-beta and the low-beta plasmas. However, neither have been observed in the solar wind so far. We suggest that the large scale interplanetary electric field might play a role instead.

3. A large strahl population may drive very oblique and quasi-electrostatic whistler waves that could effectively scatter anti-sunward suprathermal electrons and reduce the heat flux. However, our observation show that the strahl density is likely too low in the high-beta plasmas. Such mechanism might be active much closer to the sun.

4. Kinetic Alfvén waves (KAWs) become unstable as a consequence of the core electrons drifting sunward with respect to the protons. We show some observational evidence that marginal instabilities of KAWs might regulate the core electron drift and as a result the electron heat flux. Since the KAWs can only interact with electrons at very high or very low energies, the heat flux regulation, if any, must happen in the nonlinear stage of the evolution.

In this study, we have left out the Coulomb collision in our discussion. While we know Coulomb collisions are rare in the solar wind, there is evidence that they may affect electron heat flux. Two collisional parameters, the collisonal age and the Knudsen number have been shown to order the heat flux and the core electron drift speed very well (Salem et al., 2003; Bale et al., 2013; Pulupa et al., 2014a). Particle simulation can reproduce the qualitative dependence of the heat flux on the Knudsen number by incorporating some form of collisions and the solar wind expansion effect (Landi, Matteini, and Pantellini, 2014). How does the collisional suppression of the electron heat flux happen? It has been suggested that the strahl electrons are scattered into the halo electrons as distance from the sun increases (Maksimovic et al., 2005a). Recently Horaites et al. (2018) use measurements from the WIND strahl detector to show that the energy-dependent angular width of the strahl is dominated by the Coulomb collisions up to 200 eV in the fast solar wind. Therefore, it is possible that the collisional broadening of the strahl might significantly reduce the strahl electron density and therefore reducing the total heat flux. This interpretation is consistent with figure 4.8 that shows the heat flux regulation (in high beta) is accompanied by the significant reduction in the strahl.

Chapter 5

Effects of Electron Drift on the Collisionless Damping of Kinetic Alfvén Waves in the Solar Wind

Tong Y., Bale S. D., Chen, C. H. K., Salem C. S., Verscharen D. (2019). *Astrophys. J. Lett.*, 804(2), L36.

The collisionless dissipation of anisotropic Alfvénic turbulence is a promising candidate to solve the solar wind heating problem. Extensive studies examined the kinetic properties of Alfvén waves in simple Maxwellian or bi-Maxwellian plasmas. However, the observed electron velocity distribution functions in the solar wind are more complex. In this study, we analyze the properties of kinetic Alfvén waves in a plasma with two drifting electron populations. We numerically solve the linearized Maxwell-Vlasov equations and find that the damping rate and the proton-electron energy partition for kinetic Alfvén waves are significantly modified in such plasmas, compared to plasmas without electron drifts. We suggest that electron drift is an important factor to take into account when considering the dissipation of Alfvénic turbulence in the solar wind or other $\beta \sim 1$ astrophysical plasmas.

5.1 Introduction

One major question in space physics is how collisionless plasmas in the extended corona and in the solar wind are heated. Observations in the solar wind reveal that the fluctuations of the electric and magnetic fields show a turbulent spectrum similar to the power-law spectrum of fluid turbulence as described by Kolmogorov (Tu and Marsch, 1995; Bale et al., 2005b; Bruno and Carbone, 2013a; Alexandrova et al., 2013). The turbulence in the solar wind

shows mainly Alfvénic polarization (Belcher and Davis, 1971) and becomes more anisotropic during the cascade to higher wavenumbers k (Goldreich and Sridhar, 1995; Horbury, Forman, and Oughton, 2008; Chen et al., 2010), resulting in $k_\perp \gg k_\parallel$ at short wavelengths. At the proton scale, the turbulence is thought to transition into a kinetic Alfvén wave (KAW) cascade (Schekochihin et al., 2009; Sahraoui et al., 2010; Howes et al., 2011; Salem et al., 2012a; Boldyrev and Perez, 2012; Chen et al., 2013a), which gradually dissipates energy to the particles (Leamon et al., 1999; Howes et al., 2011).

Despite the nonlinear nature of turbulence, linear theory has been used in studies of solar wind turbulence (see, for instance, Howes, Klein, and TenBarge (2014) for review). These studies analyze turbulent fluctuations by means of the linear propagation and damping characteristics of KAWs to help to understand the dissipation of the turbulence and the heating of the solar wind. The vast majority of these studies rely on representing the velocity distribution functions (VDFs) by an isotropic or bi-Maxwellian background (e.g., Quataert, 1998; Leamon et al., 1999; Cranmer and van Ballegooijen, 2003). In this work, we investigate how more realistic VDFs modify the damping of KAWs. In the solar wind, both ions and electrons can be modeled by several populations drifting with respect to each other. Recent studies show that the differential flow between ions affects ion heating by both ion-cyclotron waves (Kasper et al., 2013) and low-frequency KAWs (Chandran et al., 2013).

The solar-wind electron VDF can be modeled as a superposition of three electron populations: a cool and dense "core", a hot and less dense "halo" (Feldman et al., 1975b) and a beam-like one-sided "strahl" (Maksimovic et al., 2005b). In the proton frame, core (halo and strahl) electrons drift sunward (anti-sunward) along the background magnetic field. Empirically, the solar wind fulfills quasi-neutrality and the zero-current condition (Feldman et al., 1975b; Pulupa et al., 2014b). The uncertainty in the fitting parameters for electron core properties is smaller than the uncertainty in the fitting parameters for halo and strahl properties. A drifting bi-Maxwellian population models core electrons very well. In particular, the core electron bulk drift speed is usually comparable to or larger than the Alfvén speed and shows a clear statistical dependence on collisional age (Pulupa et al., 2014b). In the extrapolated asymptotic limit of no collisions, the core drift is as large as three to four times the Alfvén speed.

In this letter, we examine how the drift between electron core and halo affects the linear damping of KAWs. We model the solar wind electrons by a superposition of a Maxwellian core and a Maxwellian halo drifting against each other in the proton frame. Choosing a set of parameters typical for the solar wind, we solve the full hot-plasma dispersion relation of KAWs in the framework of Vlasov-Maxwell theory and identify the contribution to wave damping from each plasma component. We show that, in the linear approximation, electron drifts can lead to significant variations in both the KAW damping rates and the relative energy transfer from the waves to protons and electrons, the latter of which is another important unsolved problem in turbulent plasma heating.

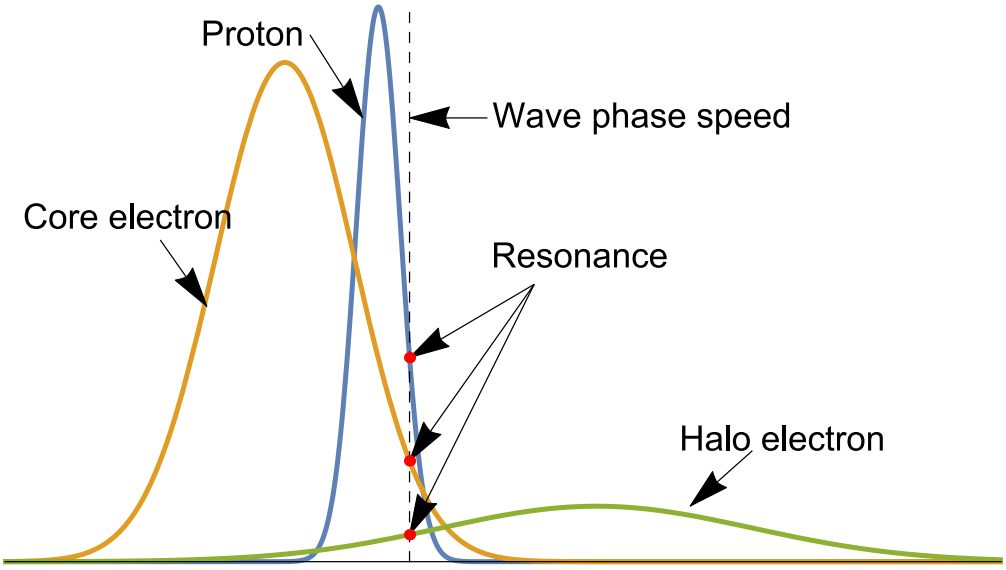

Figure 5.1: Schematic diagram for the plasma considered in this letter. We annotate the parallel wave phase speed $v_{\rm res} = \omega_r/k_\parallel$ for our resonance analysis in Section 5.3.

5.2 Theory and method

Motivated by observed solar wind electron VDFs, we consider a collisionless, homogeneous, and warm proton-electron plasma in a constant uniform background magnetic field. The proton temperature and density are denoted as T_p and n_p; the electron distribution consists of two shifted Maxwellian populations, a cool (T_c) "core" and a hot (T_h) "halo." As an initial step to study the effects of core electron drifts on resonant damping, we use isotropic temperatures for all plasma components. Both electron populations drift along the background magnetic field $\mathbf{B}_0 = B_0\hat{\mathbf{z}}$ with $\mathbf{v}_c = v_c\hat{\mathbf{z}}$ and $\mathbf{v}_h = v_h\hat{\mathbf{z}}$ in the proton frame. The halo electron drift adjusts to the core electron drift to guarantee the absence of net currents in the plasma: $v_h = -v_c n_c/n_h$, where n_c and n_h denote core and halo electron densities. Figure 5.1 shows the plasma described above schematically.

Under the assumption of strong anisotropy in kinetic scale fluctuations in the solar wind, we consider KAWs with wavevectors at a large angle with respect to the magnetic field. We use constant values for the angle between $\mathbf{k}$ (wavenumber vector) and $\mathbf{B}_0$ (89° or 91°), plasma beta, the electron-core-to-proton temperature ratio and the core-to-halo density ratio, so that the only free parameters are $\mathbf{k}$, $\mathbf{v}_c$ and $\mathrm{sign}(\mathbf{k}\cdot\mathbf{B}_0)$. In particular, we allow $\mathbf{B}_0$ to be either parallel or anti-parallel to $\mathbf{v}_c$, and $\mathbf{k}$ has a finite component along $\mathbf{B}_0$. In principle, each configuration $(\mathbf{v}_c, \mathbf{k}, \mathbf{B}_0)$ requires a separate treatment; however, changing the direction of $\mathbf{B}_0$ only inverts the direction of propagation and does not produce a new dispersion relation. Therefore, we introduce the dimensionless core electron drift $\delta v_c \equiv |v_c/v_A|\mathrm{sign}(\mathbf{k}\cdot\mathbf{v}_c)$, where

Quantity	Value
Proton plasma beta β_p	0.4
Temperature ratio T_c/T_p	2
T_h/T_p	10
Density ratio n_c/n_h	9
Proton bulk drift v_p/v_A	0
Angle between $\mathbf{k}$, $\mathbf{B}_0$	89° or 91°

Table 5.1: Values of fixed plasma parameters in our study.

$v_A \equiv \sqrt{B_0^2/4\pi n_p m_p}$ is the proton Alfvén speed. The values of the remaining parameters are given in Table 5.1.

We study the dispersion relations of KAWs by numerically solving the full set of the linear Maxwell-Vlasov equations. Linear Maxwell-Vlasov theory has been described in detail in the literature (see, for instance, Swanson, 1989 and Stix, 1992). We summarize the relevant results here. Linear plasma waves are eigenmodes of the wave equation:

$$\mathbf{k} \times (\mathbf{k} \times \mathbf{E}) + \frac{\omega^2}{c^2} \boldsymbol{\epsilon} \cdot \mathbf{E} = 0, \tag{5.1}$$

where $\mathbf{E}$ is the fluctuating electric field in Fourier space. The dielectric tensor $\boldsymbol{\epsilon}$ incorporates contributions from each plasma component: $\boldsymbol{\epsilon} = \mathbf{1} + \Sigma_s \boldsymbol{\chi}_s$, where $\boldsymbol{\chi_s}$ is the susceptibility tensor for species s. We obtain $\boldsymbol{\chi_s}$ from the linearized and Fourier-transformed Vlasov equation and Maxwell's equations.

To study the contribution to wave damping (growth) from each component, we calculate the relative particle heating rates as (Stix, 1992)

$$P_s \equiv \mathbf{E}^* \cdot \boldsymbol{\chi}_s^a|_{\omega=\omega_r} \cdot \mathbf{E}/4W. \tag{5.2}$$

where $\boldsymbol{\chi}_s^a \equiv \left(\boldsymbol{\chi_s} - \boldsymbol{\chi}_s^\dagger\right)/2i$ is the anti-Hermitian part of $\boldsymbol{\chi_s}$, $\omega_r \equiv \Re(\omega)$ and W is the wave energy.

In the weak damping limit, P_s gives the fraction of wave energy damped by plasma component s during one wave period. The total heating rate $P_{total} \equiv \sum_s P_s$ corresponds to the wave energy dissipation rate directly calculated from the damping rate, i.e., $1 - e^{2\omega_i T}$, where $\omega_i \equiv \Im(\omega)$ and $T \equiv 2\pi/\omega_r$ is the wave period, as long as ω_i is small compared to ω_r. In this letter, we focus on the linear damping of KAWs. Electron drifts may, however, alter wave–particle interactions to such a degree that the corresponding waves become unstable, which we note for the sake of completeness. Notice that P_s may become negative, corresponding to cooling of species s.

5.3 Results

Figures 5.2(a)-(b) show dispersion relations of KAWs in plasmas with $\delta v_c \in [-4, 4]$. Panel (a) demonstrates that electron drifts have little effect on the real part of the KAW frequencies,

consistent with Gary et al., 1975b. Indeed, the protons rather than the electrons mainly determine the dynamics of low-frequency KAWs. Panel (b) compares damping rates of KAWs in plasmas with different electron drifts. Negative (positive) δv_c lead to an enhancement (reduction) of the KAW damping at all wavenumbers. Panel (b) shows that $\delta v_c \sim -4$ leads to an increase in the damping rate by $\sim 50\%$ compared to the case without electron drifts. For sufficiently large positive δv_c, KAWs become unstable in certain wavenumber ranges. This instability is an example of a "heat flux instability" (Gary et al., 1975b). The two-population electrons in our model introduce an electron heat flux (third moment of the electron VDF), which may provide energy to drive certain wave modes (e.g., whistler, Alfvén, and magnetosonic) unstable (Gary et al., 1975b; Gary et al., 1998; Gary, Skoug, and Daughton, 1999b). These heat flux instabilities, in return, regulate the electron heat flux and hence the electron drifts. We note that there is no conflict between the damping and growth of KAWs and other wave modes. For instance, parallel whistler waves, whose instability threshold is much lower than that of the Alfvénic instability, are unstable even if $\delta v_c > -4$. Therefore, the Alfvénic instability cannot regulate the electron heat flux in the solar wind and is more of academic interest under typical solar-wind conditions since the instability with the lowest threshold constrains the electron heat flux once triggered. Figure 5.2(c) compares the total particle heating rate (solid) with the wave energy dissipation rate (dotted). When $1 - e^{2\omega_i T} \lesssim 0.5$, *i.e.*, the wave retains more than half of its energy after a wave period, $P_{total} \approx 1 - e^{2\omega_i T}$. Hence we show that P_s is a good measure of energy flow as long as damping is weak.

Figures 5.3 (a)-(d) present heating rates for protons, all electrons (core + halo), as well as separately for core electrons and halo electrons. Recall that positive P_s indicates heating for species s, and that negative P_s indicates cooling. Panel (a) shows that protons are always heated, although electron drifts can slightly modify the values of the proton heating rate. On the other hand, panels (b)-(d) show that an electron population can experience both cooling and heating depending on δv_c. While both core and halo are heated in the absence of bulk drifts, sufficiently large positive δv_c lead to core cooling and at the same time significantly enhance halo heating. Negative δv_c have the opposite effect on electron heating. In general, electron drifts have a larger effect on electron heating than on proton heating. Electron drifts modify the damping rates of KAWs by changing the efficiency of wave–particle interactions for the different electron populations.

Figure 5.4 shows how the energy partition depends on electron drifts at $k_\perp \rho_p = 1$. P_c/P_p and P_h/P_p vary wildly with δv_c. However, since electron drifts affect core heating and halo heating in opposite ways, the total electron heating and consequently the electron-proton energy partition reveal a more moderate dependence on electron drifts. Nevertheless, a core drift of $\delta v_c \sim -4$ increases P_e/P_p by $\sim 25\%$. Without electron drifts, electron heating dominates over proton heating in hydrogen plasmas at $k_\perp \rho_p \sim 1$ for $\beta \sim 1$ (Quataert, 1998). We see in Figure 5.4 that positive δv_c significantly reduces electron-to-proton heating ratio. At $\delta v_c \sim 3$, electron heating becomes negligible compared to proton heating. We note at this point that the dependence of energy partition on electron drifts is qualitatively the same at other wavenumbers, which can be inferred from Figure 5.3.

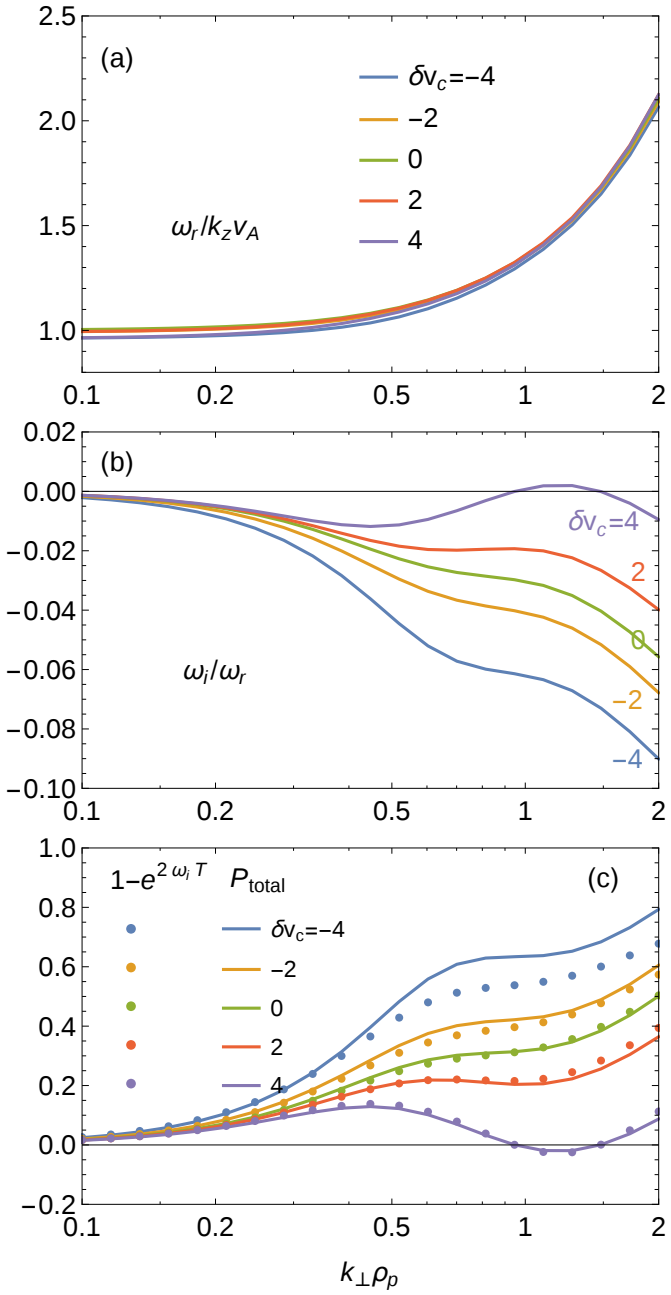

Figure 5.2: (a)-(b): Dispersion relation of KAWs in plasmas for different δv_c. ω_r and ω_i are the real and imaginary parts of the wave frequency. $\rho_p \equiv v_{Tp}/\Omega_p$ is the proton gyro-radius, $v_{Tp} \equiv \sqrt{2k_B T_p/m_p}$ is the proton thermal speed, and $\Omega_p \equiv eB_0/m_p c$ is the proton gyro-frequency. (c): Total particle heating rates (P_{total}, solid lines) and wave energy dissipation rates ($1 - e^{2\omega_i T}$, dots) as functions of wavenumber.

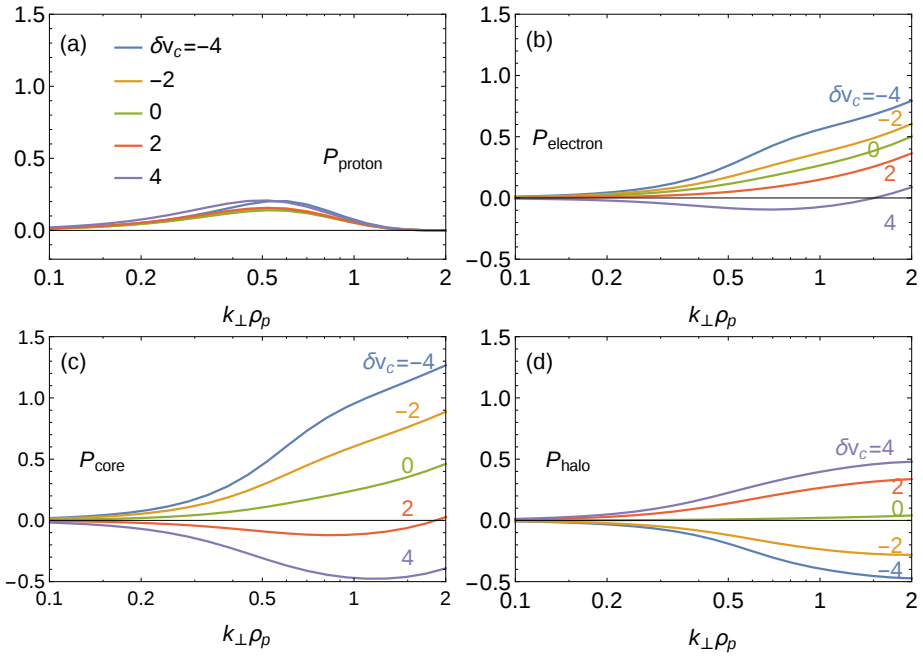

Figure 5.3: Dependence of P_{proton} (a), $P_{electron}$ (b), P_{core}(c) and P_{halo} (d) on $k_\perp \rho_p$ in plasmas with varying δv_c.

We interpret the dependence of wave damping and particle heating on electron drifts in terms of a simplified resonance analysis. Since ω_r is almost independent of electron drifts, the proton heating rate shows only a small variation. However, core and halo electron bulk drifts significantly change the value and the gradient of the eVDF at the resonance speed,

$$v_{\rm res} \equiv \frac{\omega_r - n\Omega_e}{k_\parallel}, \tag{5.3}$$

where Ω_e is the electron gyro-frequency and n is an integer depending on the polarization properties of the wave mode (Marsch, 2006).

In our case, the most relevant resonance for wave–particle interactions with KAWs is the Landau resonance with $n = 0$. Electrons with the (field-parallel) speed $v_{\rm res}$ interact resonantly with the corresponding wave mode. We illustrate the case for negative δv_c schematically in Figure 5.1.

The gradient of the distribution functions at the resonance speed determines if the particle species gains or loses energy, i.e., the signs of P_p, P_c, and P_h. In the example shown in Figure 5.1, the resonance occurs where the halo VDF has a positive gradient, and hence the KAW removes energy from the halo electrons, leading to a negative value for P_h. In contrast, core electrons and protons have resonances where the gradients of their VDFs are negative, leading to positive values for P_c and P_p. Similarly, the dependence of P_s on δv_c

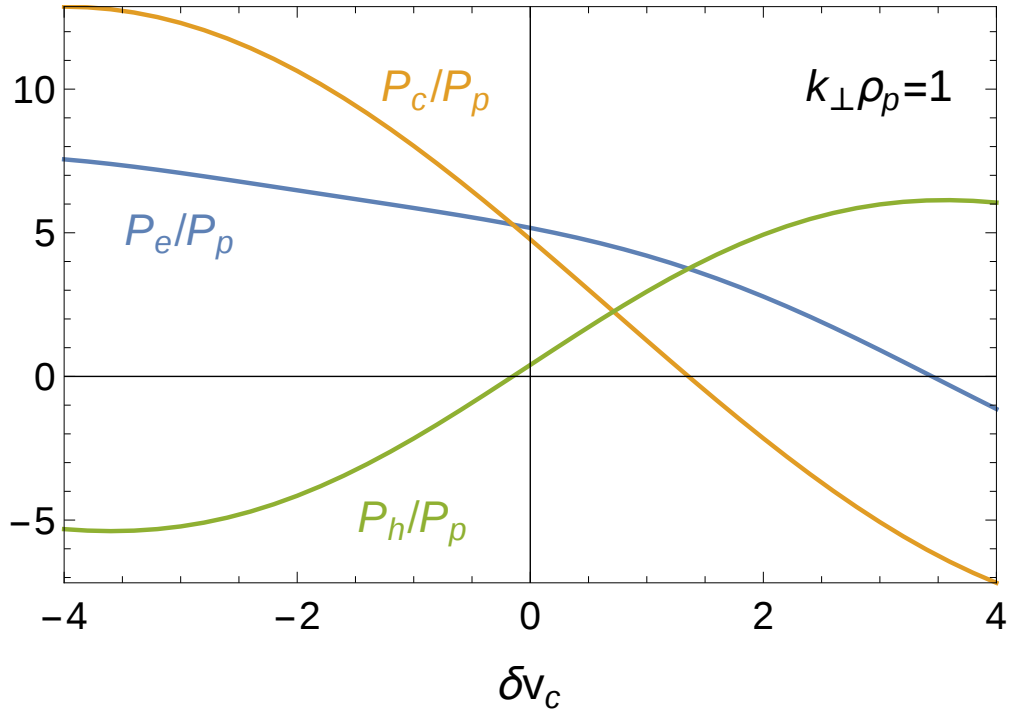

Figure 5.4: Ratio of energy partition between electrons and protons as a function of electron drift.

can also be inferred from the positions of the resonance points with respect to the VDFs. However, a qualitative resonance analysis cannot provide a thorough comparison across the plasma components. We find that P_s, defined in Eq. (5.2), gives a better understanding of the energy transfer between waves and different plasma components.

It is worth noting that electron drifts seem to provide a collisionless energy coupling between core and halo electrons (see the case with $\delta v_c = -2$ for instance). Figure 5.2(c) shows that $1 - e^{2\omega_i T} \approx P_c + P_h + P_p$. With $P_c, P_p > 0$ and $P_h < 0$ (from Figure 5.3), $\left(1 - e^{2\omega_i T}\right) + (-P_h) \approx P_c + P_p$, meaning that energy flows from damped waves and halo electrons into core electrons and protons. A similar energy transport among electron components was suggested by Gary, Newbury, and Goldstein (1998). According to this study, the Alfvénic heat-flux instability transfers energy from the drifting halo into the electron core through the Landau-resonant absorption of the waves, leading to a lower limit for β_c.

5.4 Discussion and conclusion

For the sake of clarity, we present results for a single propagation angle in this letter. A careful analysis shows that other oblique angles do not lead to any qualitative differences. Given a fixed KAW power spectrum, we anticipate that the presence of electron drifts changes the

wave-energy dissipation rate, particle heating rates, and the proton-electron energy partition ratio significantly.

In the context of the solar wind, since core electrons are nearly always observed to drift sunward in the proton frame, positive (negative) δv_c correspond to KAWs propagating sunward (anti-sunward). Therefore, anti-sunward KAWs experience stronger damping in the presence of electron drifts and lead to a stronger core heating, halo electron cooling, and a stronger total electron heating. Since the total energy flux typically points anti-sunward in the solar wind, we suggest that electron drifts lead to stronger electron heating than expected from previous calculations (Quataert, 1998; Leamon et al., 1999). An interesting corollary of this work is that, since the core electron drift speed depends on the collisionality of the solar wind (Pulupa et al., 2014b), the heating rate as calculated here may therfore also indirectly depend on solar wind Couloumb collisions.

Our model includes relative drifts in the electron VDF, while it ignores several additional features of solar wind electrons, namely the presence of superthermal electrons, one-sided beams (strahl) and temperature anisotropies. By using a Maxwellian halo, we ignore high energy tails in the electron VDF. However, this assumption does not significantly affect the gradients of the electron distribution function at $v_{\rm res} \sim v_A$ which mainly determine the damping. We can apply a similar argument to strahl electrons, which also occupy a different region in the velocity space. Regarding temperature anisotropies, Gary et al., 1975b studied the dependence of the core drift threshold for the Alfvénic instability on electron temperature anisotropy and found that the dependence is weak in plasmas with $\beta_p < 0.25$. We expect a similar weak relation in our case, since Landau-resonant instabilities show such a weak dependence in general (Verscharen and Chandran, 2013), since the strength of this type of resonant interaction is determined by the parallel gradients of the electron distribution function. If the parallel temperature is kept constant, the introduction of temperature anisotropy only changes the perpendicular gradients of the VDF and therefore does not significantly alter the wave–particle interaction.

In this letter, we choose a fiducial set of representative solar wind plasma parameters to demonstrate the effects of electron drifts on the damping of KAWs. In order to fully account for all of the relevant effects in the solar wind, it is important to conduct a full scan of the corresponding parameter space. This endeavor is beyond the scope of this work and will be presented in a future paper.

Our work shows that, despite our limiting assumption of a superposition of Maxwellians to represent the electron distribution function, its fine-structure has a strong influence on the propagation and damping properties of KAWs. Therefore, our work is of relevance in the broader context of all collisionless astrophysical plasmas in which non-Maxwellian electron distributions can develop and persist. Considering that most astrophysical plasmas are in a turbulent state and that KAW-turbulence is believed to be the dominant type of plasma turbulence on small scales, our work suggests that the effects of non-Maxwellian electron distributions be carefully accounted for in studies of collisionless astrophysical plasmas in general. *We are grateful to Christopher C. Chaston, Marc P. Pulupa, Eliot Quataert and*

Kristopher G. Klein for helpful discussions. Y. Tong is supported by NASA grant APL-975268 and Charles K. Kao Scholarship. S. D. Bale is supported by NASA grant APL-975268. C. H. K. Chen is supported by an Imperial College Junior Research Fellowship. C. Salem is supported by NASA grant NNX14AC07G. D. Verscharen is supported by NASA grant NNX12AB27G.

Chapter 6

Whistler Wave Generation by Halo Electrons in the Solar Wind

Tong Y., Vasko I. V., Pulupa M., Mozer F. S., Bale S. D., Artemyev A. V. and Krasnoselskikh V. (2019). *Astrophys. J. Lett.*, 870(1), L6.

We present an analysis of simultaneous particle and field measurements from the ARTEMIS spacecraft which demonstrate that quasi-parallel whistler waves in the solar wind can be generated locally by a bulk flow of halo electrons (whistler heat flux instability). ARTEMIS observes quasi-parallel whistler waves in the frequency range $\sim 0.05 - 0.2 f_{ce}$ simultaneously with electron velocity distribution functions that are a combination of counter-streaming core and halo populations. A linear stability analysis shows that the plasma is stable when there are no whistler waves, and unstable in the presence of whistler waves. In the latter case, the stability analysis shows that the whistler wave growth time is from a few to ten seconds at frequencies and wavenumbers that match the observations. The observations clearly demonstrate that the temperature anisotropy of halo electrons crucially affects the heat flux instability onset: a slight anisotropy $T_\parallel/T_\perp > 1$ may quench the instability, while a slight anisotropy $T_\parallel/T_\perp < 1$ may significantly increase the growth rate. These results demonstrate that heat flux inhibition is strongly dependent on the microscopic plasma properties.

6.1 Introduction

The mechanisms controlling the heat flux in collisionless or weakly-collisional plasmas are of high interest in astrophysics (Cowie and McKee, 1977; Pistinner and Eichler, 1998; Roberg-Clark et al., 2018a). In-situ measurements in the solar wind indicate that the heat flux is generally different from the classical Spitzer-Härm prediction (Feldman et al., 1975a; Scime et al., 1994; Bale et al., 2013) and apparently constrained by a threshold dependent on local plasma parameters (Gary, Skoug, and Daughton, 1999a; Gary and Li, 2000; Tong et al.,

2018b). Such observations have motivated many studies on the detailed physics of heat flux inhibition in the solar wind.

In the slow solar wind ($v_{sw} \lesssim 400$ km/s) the electron velocity distribution function can often be approximated by a bi-Maxwellian thermal dense core and a tenuous, suprathermal halo (Feldman et al., 1975a; Maksimovic, Pierrard, and Riley, 1997). The heat flux is predominantly parallel to the magnetic field and carried by suprathermal electrons. Linear stability analysis shows that the counter-streaming core and halo electrons are capable of driving whistler waves propagating quasi-parallel to the bulk flow of the halo population via the so-called heat flux instability (Gary et al., 1975a; Gary et al., 1994; Gary and Li, 2000). The quasi-linear theory (Gary and Feldman, 1977; Pistinner and Eichler, 1998) and numerical simulations (Roberg-Clark et al., 2018a; Komarov et al., 2018; Roberg-Clark et al., 2018b) suggest that the scattering of halo electrons by the whistler waves should suppress the heat flux below some threshold value that is in general agreement with the heat flux constraints observed in the solar wind (Gary et al., 1994; Gary, Skoug, and Daughton, 1999a; Tong et al., 2018b). However, the aforementioned experimental studies did not provide measurements of whistler waves accompanying the electron heat flux measurements, and are therefore insufficient to firmly establish the heat flux inhibition by whistler waves in the solar wind.

It is not until recently that careful studies of whistler waves presumably generated by the heat flux instability in freely expanding solar wind have been reported with measurements on Cluster and ARTEMIS spacecraft. Lacombe et al. (2014) reported whistler waves observed along with the heat flux values close to the theoretical threshold given by Gary, Skoug, and Daughton (1999a). Stansby et al. (2016) presented observations of similar whistler waves on ARTEMIS and determined the dependence of the whistler wave dispersion relation on β_e. However, neither study showed that the whistler waves were indeed generated by the heat flux instability in the local plasma, leaving the possibility that whistler waves were generated in a very different plasma by an alternative mechanism and propagated to the spacecraft location. We note that whistler waves in the solar wind can be associated with shocks and stream interaction regions (Lengyel-Frey et al., 1996; Lin et al., 1998; Breneman et al., 2010; Wilson et al., 2013), while we focus on whistler waves in the freely expanding solar wind.

In this study we analyze simultaneous particle and wave measurements for data intervals presented by Stansby et al. (2016) and carry out linear stability analysis on electron velocity distribution functions. We find that the observed whistler waves are indeed generated locally by the heat flux instability on a time scale of a few seconds. In this letter we present one of those events, which also demonstrates crucial features of the heat flux instability.

6.2 Observations

We consider observations of ARTEMIS (Angelopoulos, 2011) on November 9, 2010 for ten minutes around 10:17:00 UT as the spacecraft was in the pristine solar wind about 40 Earth radii upstream of the Earth's bow shock. We use measurements of the following instruments aboard ARTEMIS: the magnetic fields with 3 second resolution provided by the Flux Gate

Magnetometer (Auster et al., 2008), the electron velocity distribution function (32 log-spaced energy bins from a few eV up to 25 keV and 88 angular bins) and particle moments (density, bulk velocity and temperatures) with 3 second time resolution provided by the Electrostatic Analyzer (McFadden et al., 2008), measurements of three magnetic and electric field components at 128 Hz sampling rate provided by the Search Coil Magnetometer (Le Contel et al., 2008) and Electric Field Instrument (Bonnell et al., 2008).

Figure 6.1 shows that the solar wind was streaming at about $v_{sw} \sim 320$ km/s, the quasi-static magnetic field was gradually decreasing from $B_0 \sim 5$ nT to 3 nT, the plasma density was $n_0 \sim 5$ cm^{-3}, and the electron temperature was $T_e \sim 15$ eV. The ion temperature was $T_i \sim 5$ eV (from the OMNI dataset and not shown). The electron cyclotron frequency f_{ce} was varying from 150 to 90 Hz, the Alfvén speed $v_A = B_0/(4\pi n_0 m_i)^{1/2}$ from 90 to 30 km/s, while $\beta_{i,e} = 8\pi n_0 T_{i,e}/B_0^2 \sim 0.5-2$. Over the ten minute interval, continuous electric and magnetic field measurements at 128 samples per second were available. Panel (e) presents the wavelet power spectrum of one of the magnetic field components perpendicular to the quasi-static magnetic field. The enhancement of spectral power density from a few Hz up to about 0.2 f_{ce} corresponds to whistler waves (Stansby et al., 2016). Since the power spectra above 64 Hz cannot be obtained from the search coil magnetic field time series, we also checked the on board FFT power spectra of search coil magnetic fields (not shown) covering 8 Hz-4 kHz and verified that there was no significant power between 64 Hz and f_{ce}. Panel (f) presents the spectral coherence between the two magnetic field components perpendicular to the quasi-static magnetic field and indicates a high coherence of the whistler waves. We carry out a spectral polarization analysis following Santolik, Parrot, and Lefeuvre (2003) to determine the obliqueness of whistler waves to the quasi-static magnetic field. Panel (g) presents the cosine of the propagation angle and confirms that whistler waves propagate almost parallel or anti-parallel to the quasi-static magnetic field in accordance with the conclusions of Stansby et al. (2016). The amplitude of whistler waves ranges from 0.05-2 nT in the ten-minute interval in this study, and is small compared to B_0.

Figure 6.2 presents example wave forms around 10:16:19 UT. Panel (a) shows the band-pass filtered magnetic field fluctuations in the field aligned coordinate (FAC). Panel (b) shows the electric field counterpart. Both wave forms are band-pass filtered between 5 and 15 Hz. The two perpendicular magnetic field components have comparable amplitude, obviously shifted by about 90 degrees in phase, and are significantly stronger than the parallel magnetic field component. This is clearly signatures of circularly polarized waves propagating parallel to the background magnetic field, as Figure 6.1 (g) has already suggested.

The electric field wave form is much noisier than the magnetic field wave form since the spacecraft antenna is not very long compare to the spacecraft main body. Nevertheless, the approximately 90-degree phase shift between the two perpendicular components is still apparent. Minimal Variance Analysis (MVA) is performed to determine more accurately the direction of the maximum variance (M), the direction of intermediate variance (L), and the direction of minimal variance (N). Panel (c) and (d) presents E_M versus B_L and E_L versus B_M, the ratios of which yield the wave phase speed in spacecraft's frame. Linear regression determines that the wave phase speed is $1400 km/s$, which falls in the range of whistler waves'

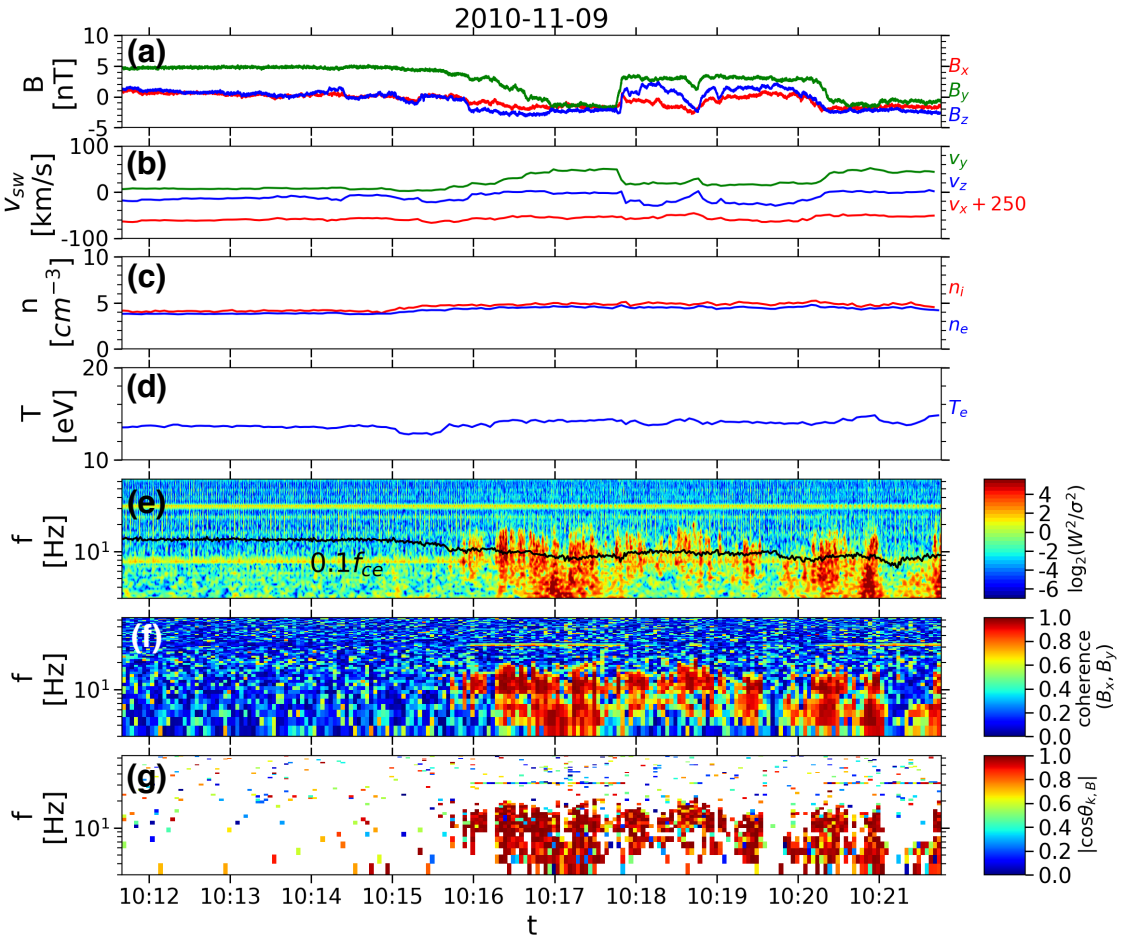

Figure 6.1: ARTEMIS observations in the pristine solar wind on November 9, 2010 about 40 Earth radii upstream of the Earth's bow shock: (a) quasi-static magnetic field; (b) ion bulk velocity in the GSM coordinate system; (c,d) electron and ion densities and temperatures; (e) wavelet power spectrum of one of the magnetic field components perpendicular to the quasi-static magnetic field; we use a Morlet wavelet with center frequency $\omega_0 = 32$ as the mother wavelet and normalize the wavelet power (W^2) by the white noise power (σ^2); (f) the coherence coefficient between magnetic field components B_x and B_y perpendicular to the quasi-static magnetic field; (g) $|\cos\theta_{\mathbf{kB}}|$ indicating obliqueness of the whistler waves ($\mathbf{k}$ and $\mathbf{B}$ are the wave vector and the quasi-static magnetic field). In panel (g) domains with coherence smaller than 0.6 have been masked out for clarity. 2D maps (e)-(g) are computed using the magnetic field measured at 128 Hz sampling rate.

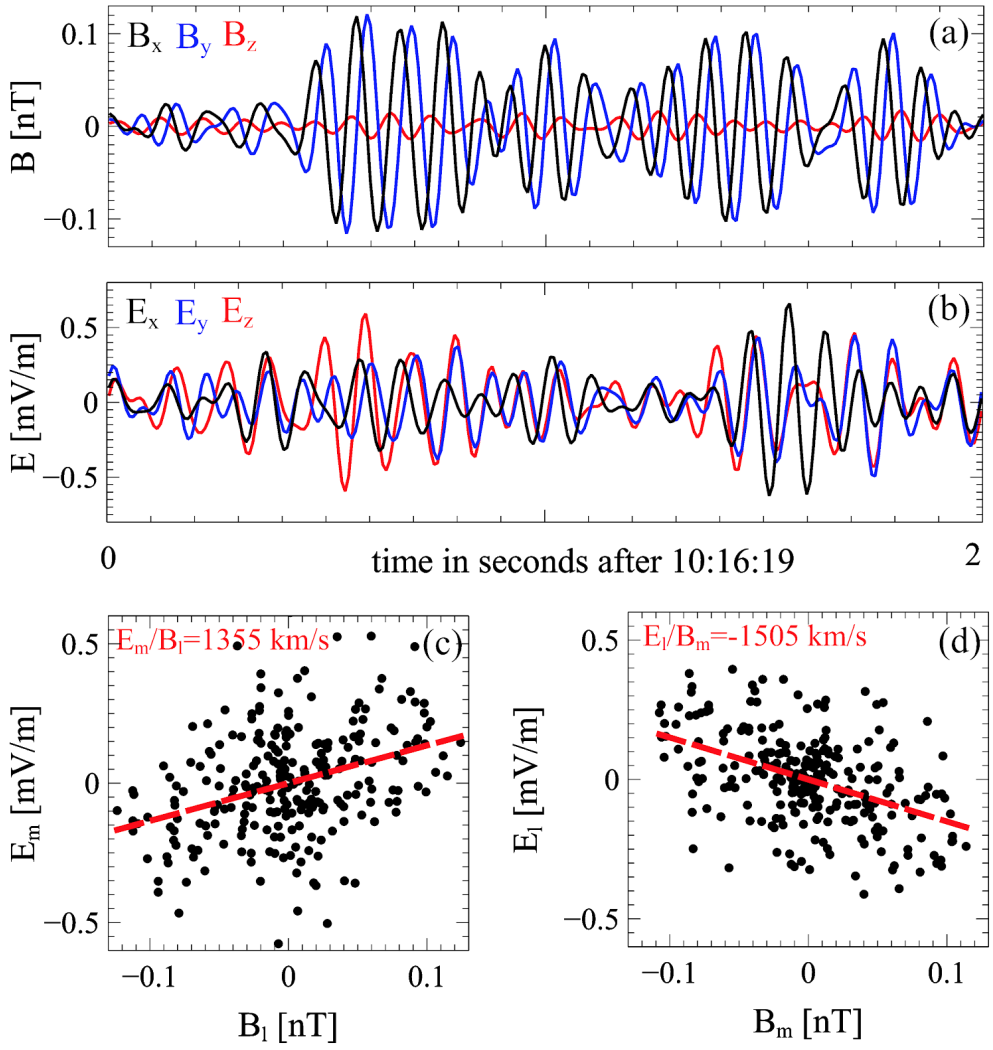

Figure 6.2: Wave forms and phase speed diagnostics. (a) Band passed filtered magnetic field fluctuations in field aligned coordinate (FAC). (b) Band passed filtered electric field fluctuations in FAC. (c) E_M versus B_L. (d) E_L versus B_M. The subscript M, L denotes two orthogonal directions in the plane of maximum variance.

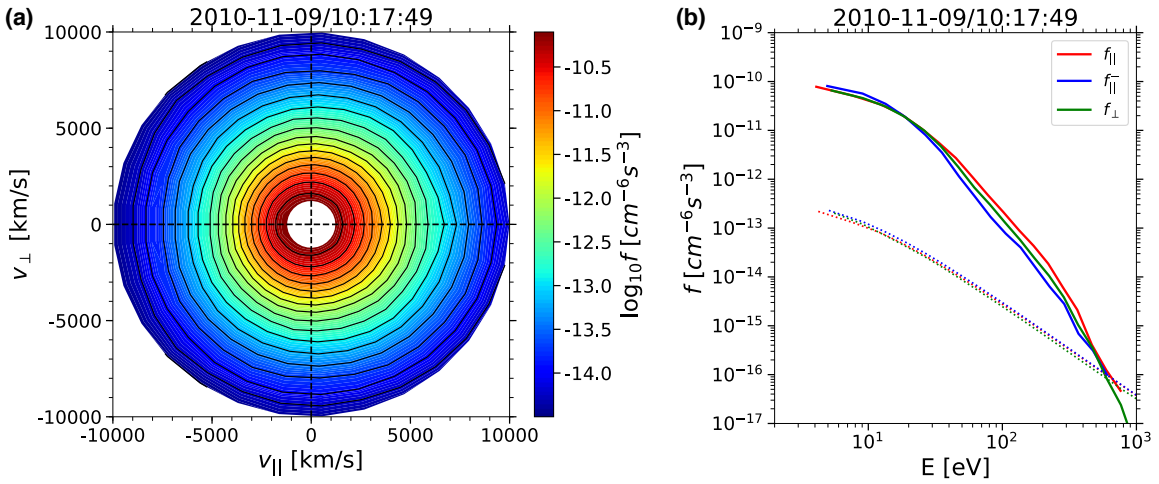

Figure 6.3: Example of an electron VDF that has been transformed into the solar wind frame and calibrated for the spacecraft potential: (a) gyrophase averaged $f(v_{||}, v_\perp)$, where $v_{||}$ and $v_\perp$ are parallel and perpendicular to the magnetic field; (b) VDF cuts plotted vs. electron energy and corresponding to electrons streaming parallel ($f_{||} = f(v_\parallel > 0, v_\perp = 0)$), perpendicular ($f_\perp = f(v_\parallel = 0, v_\perp)$) and anti-parallel ($f_{||}^- = f(v_\parallel < 0, v_\perp = 0)$) to the quasi-static magnetic field.

phase speeds in the local plasma.

Figure 6.3 presents an example of the processed electron velocity distribution function (VDF). The raw electron VDF measured around 10:17:49 UT is corrected for the effect of spacecraft potential and transformed from the spacecraft frame into the solar wind frame using the ion bulk velocity measurements. Panel (a) shows the processed VDF $f(v_{||}, v_\perp)$ averaged over the gyrophase, where $v_{||}$ and $v_\perp$ correspond to velocities parallel and perpendicular to the background magnetic field. The VDF is asymmetric in the direction parallel to the magnetic field with opposite asymmetries below and above a few thousand km/s, indicating counter-streaming of cold and hot electrons. Panel (b) shows VDF cuts $f_{||}$, $f_\perp$ and $f_{||}^-$ corresponding to electrons streaming parallel (pitch angles $\alpha \sim 0°$), perpendicular ($\alpha \sim 90°$) and anti-parallel ($\alpha \sim 180°$) to the quasi-static magnetic field. Below ~30 eV, $f_{||}^- > f_{||}$, consistent with core electrons streaming anti-parallel to the magnetic field. At higher energies, $f_{||} > f_{||}^-$ shows that the hotter electrons are streaming in the opposite direction.

The counter-streaming cold and hot electrons persist through the whole ten minutes in Figure 6.1. Is this plasma indeed capable of generating the observed whistler waves? How fast is the instability? What controls the absence of whistler waves before 10:16:00 UT and their later appearance? To address these questions we fit the processed electron VDFs and carry out a linear kinetic stability analysis using the previously developed numerical code (Tong et al., 2015).

6.3 Analysis

During this slow solar wind interval, the electron VDFs are well described by a combination of core and halo populations $f = f_c + f_h$. The core and halo are modelled respectively with drifting bi-Maxwellian and bi-kappa distributions

$$f_c = A_c \exp\left[-\frac{m_e\left(v_{||}-v_{0c}\right)^2}{2T_{||c}} - \frac{m_e v_\perp^2}{2T_{\perp c}}\right],$$

$$f_h = A_h B_\kappa \left[1 + \frac{m_e(v_{||}-v_{0h})^2}{(2\kappa-3)T_{||h}} + \frac{m_e v_\perp^2}{(2\kappa-3)T_{\perp h}}\right]^{-(\kappa+1)},$$

where $A_s = n_s(m_e/2\pi T_{\perp s}^{2/3} T_{||s}^{1/3})^{3/2}$, $B_\kappa = \Gamma(\kappa+1)/(\kappa-3/2)^{3/2}\Gamma(\kappa-1/2)$ and n_s, v_{0s}, $T_{\perp s}$, $T_{||s}$ are densities, bulk velocities and temperatures (parallel and perpendicular to the quasi-static magnetic field $\mathbf{B}_0$) of the core and halo populations ($s = c, h$). These parameters are estimated by fitting the model to VDF cuts $f_{||}$, $f_\perp$ and $f_{||}^-$ using the standard χ^2 minimization method. Following Feldman et al. (1975a) the electron current in the solar wind frame is kept zero by restricting the parameters to $n_c v_{0c} + n_h v_{0h} = 0$.

Figures 6.4 (a) and (c) illustrate the fitting procedure, using an electron VDF measured in absence of whistler wave activity at 10:12:11 UT and another VDF in presence of whistler waves at 10:17:49 UT. Panels (a) and (c) present the VDF cuts, the model fits and the best fit parameters. Only data points above the one count level have been used in the fitting procedure. Core electrons make up about 80-85% of the total electron density, the bulk velocity is 100-200 km/s (anti-parallel to $\mathbf{B}_0$ in the solar wind frame), or about four times larger than the local Alfvén speed, the temperature is around 9 eV, and the parallel and perpendicular temperatures are slightly different, $T_{\perp c}/T_{||c} \sim 1.06$. The halo bulk velocity is about 500-1000 km/s (parallel to $\mathbf{B}_0$) and the temperature is about 30 eV. The halo population is rather anisotropic in (a) with $T_{\perp h}/T_{\|,h} \sim 0.8$ and essentially isotropic in (c) with $T_{\perp h}/T_{\|,h} \sim 1.0$.

We address the whistler wave generation by carrying out a linear stability analysis. In the computations we use the model electron VDF with the best fit parameters and isotropic Maxwellian protons with a temperature of 5 eV. The precise shape of the ion distribution function is not critical, because thermal ions do not interact resonantly with the observed whistler waves. We have restricted computations to parallel propagating whistler waves, because counter-streaming core and halo electrons with parameters realistic to the solar wind are known to generate whistler waves propagating only quasi-parallel to the bulk flow of the halo population (Gary et al., 1975a; Gary et al., 1994), which is parallel to $\mathbf{B}_0$ in our case.

Figures 6.4 (b) and (d) present growth rates and dispersion curves of parallel propagating whistler waves computed for electron VDFs in (a) and (c). In agreement with observations we find whistler waves to be stable for VDF (a), but unstable for VDF (c). In the latter case the linear stability analysis predicts the fastest growing whistler waves at the frequency of

0.05 f_{ce}. Although it is in general agreement with the whistler wave spectrum in Figure 6.1e, a careful comparison requires Doppler shifting the plasma frame frequency of 0.05 f_{ce} into the spacecraft frame (see below). Panel (d) shows that the maximum growth rate is about $10^{-3} f_{ce}$ or 0.5 s^{-1} in physical units, which corresponds to an e-folding time of about a second. During this time, whistler waves can only propagate a few hundred kilometers, because the phase velocity of the whistler waves is about $c(f/f_{ce})^{1/2} f_{ce}/f_{pe}$ ∼500 km/s, where f and f_{pe} are whistler and plasma frequencies (see also Stansby et al. (2016)). This indicates that the observed whistler waves were likely generated locally.

In order to uniquely identify the free energy source driving the whistler waves, we computed growth rates for electron VDFs (a) and (c), but with either 1) core and halo bulk velocities set to zero or 2) temperature-isotropic core and halo. Panels (b) and (d) show that the electron VDFs with zero bulk velocities (blue curves) are stable and can not generate whistler waves. The free energy driving the observed whistler waves is hence provided by the bulk motions of the core and halo or, in other words, by the electron heat flux. The assumption of isotropic core and halo makes VDF (a) unstable, demonstrating thereby that $T_{||h}/T_{\perp h} > 1$ acts to suppress and possibly quench the instability (Gary and Feldman, 1977).

Figures 6.5 (a)-(d) summarize the results of the fitting of all 183 electron VDFs available over the ten-minute interval. Panel (a) demonstrates that the total electron density derived from the fitting matches (within 5%) the calibrated electron moment densities shown previously in Figure 6.1 (a). Panel (b) shows that the core and halo parallel temperatures are steady. Panel (c) demonstrates that the core temperature anisotropy $T_{\perp c}/T_{||c}$ is steady and around 1.1, while the halo is temperature-anisotropic with $T_{\perp h}/T_{||h} \sim 0.8$ before 10:15:00 UT, gradually becoming isotropic at 10:16:00 UT, and remaining nearly isotropic until the end of the interval. Panel (d) shows that the bulk velocity of the core population varies between 2 and $7v_A$. We perform the linear stability analysis on every electron VDF and determine the growth rate γ_m, frequency f_m and wavenumber k_m of the fastest growing whistler wave. In the spacecraft frame the whistler wave will be observed at a Doppler-shifted frequency $f_m + \mathbf{k}_m \mathbf{v}_{sw}$, where $\mathbf{k}_m$ is parallel to the quasi-static magnetic field $\mathbf{B}_0$.

Panel (e) demonstrates that the Doppler-shifted frequency of the fastest growing whistler wave indeed traces the observed whistler waves. There are no whistler waves before about 10:16:00 UT, while the plasma is stable. Whistler waves suddenly appear around 10:16:00 UT, when the plasma becomes unstable. Around 10:21:00 UT the plasma is stable for a short time interval, and the coherent whistler waves disappear over this interval. The strong correlation between whistler waves and the local plasma stability/instability indicates that the whistler waves are indeed generated locally. Panel (f) strengthens this conclusion by demonstrating that the e-folding time γ_m^{-1} of the fastest growing whistler wave is from 1 to 10 seconds.

The abrupt transition from stable to unstable plasma around 10:16:00 UT coincides with the halo population becoming more isotropic. As we demonstrated in Figure 6.4, the reason is that the halo temperature anisotropy quenches the whistler heat flux instability. The crucial role of the temperature anisotropy is further demonstrated in Figure 6.6. Panel (a) presents the electron heat flux q_e normalized to the free streaming heat flux $q_0 = 1.5 n_e T_e (T_e/m_e)^{1/2}$

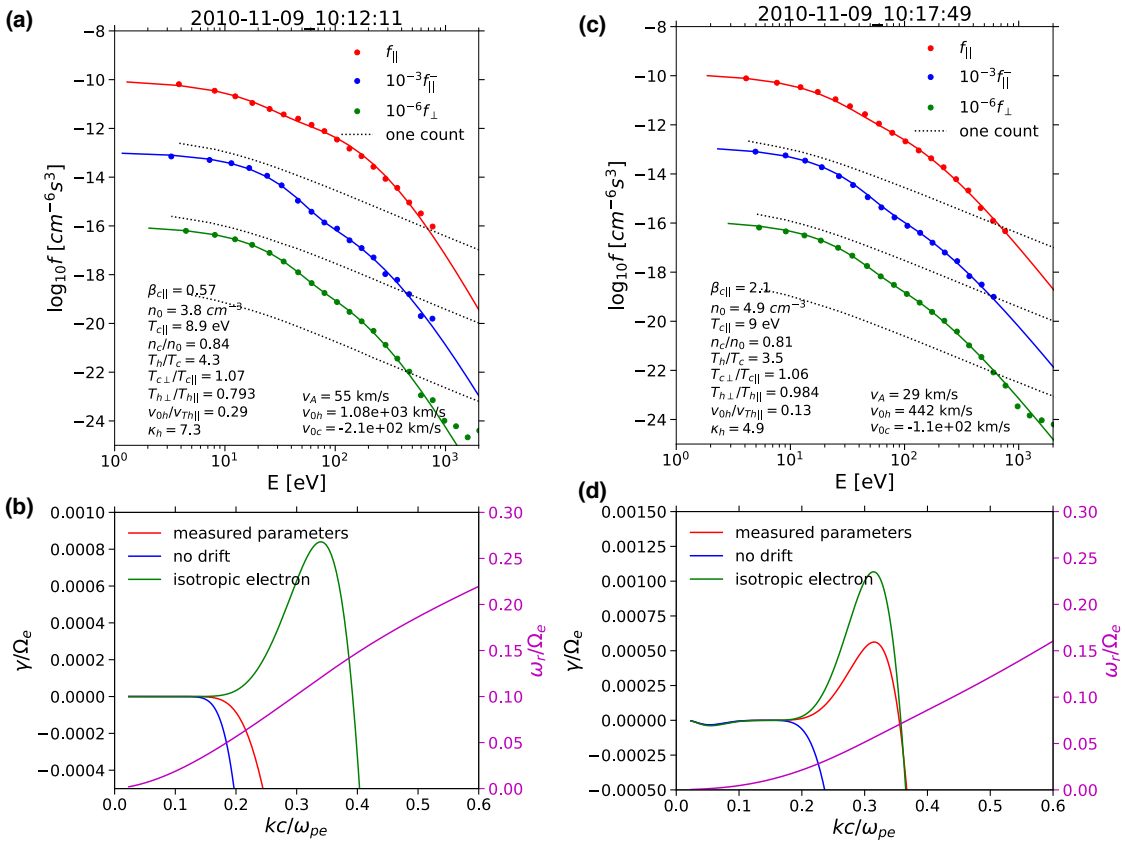

Figure 6.4: Illustration of the fitting procedure and linear stability analysis of VDFs associated with negligible and noticeable whistler wave activity observed around 10:12:11 and 10:17:49 UT: (a,c) the VDF cuts $f_{||}$, $f_{\perp}$ and $f_{||}^{-}$ corresponding to electrons with pitch angles around 0°, 90° and 180° are shown with dots; the VDF cuts are shifted vertically with respect to each other for visual clarity; only VDF values above one count level (dashed curves) have been used in the fitting procedure; the model fits are presented with solid curves and the fitting parameters are indicated in the panels; (b,d) the growth rate and dispersion curves of parallel propagating whistler waves; the growth rate computations are carried out for (red) the measured electron VDFs and for the measured VDF with either (blue) core and halo bulk velocities set to zero or (green) temperature-isotropic core and halo.

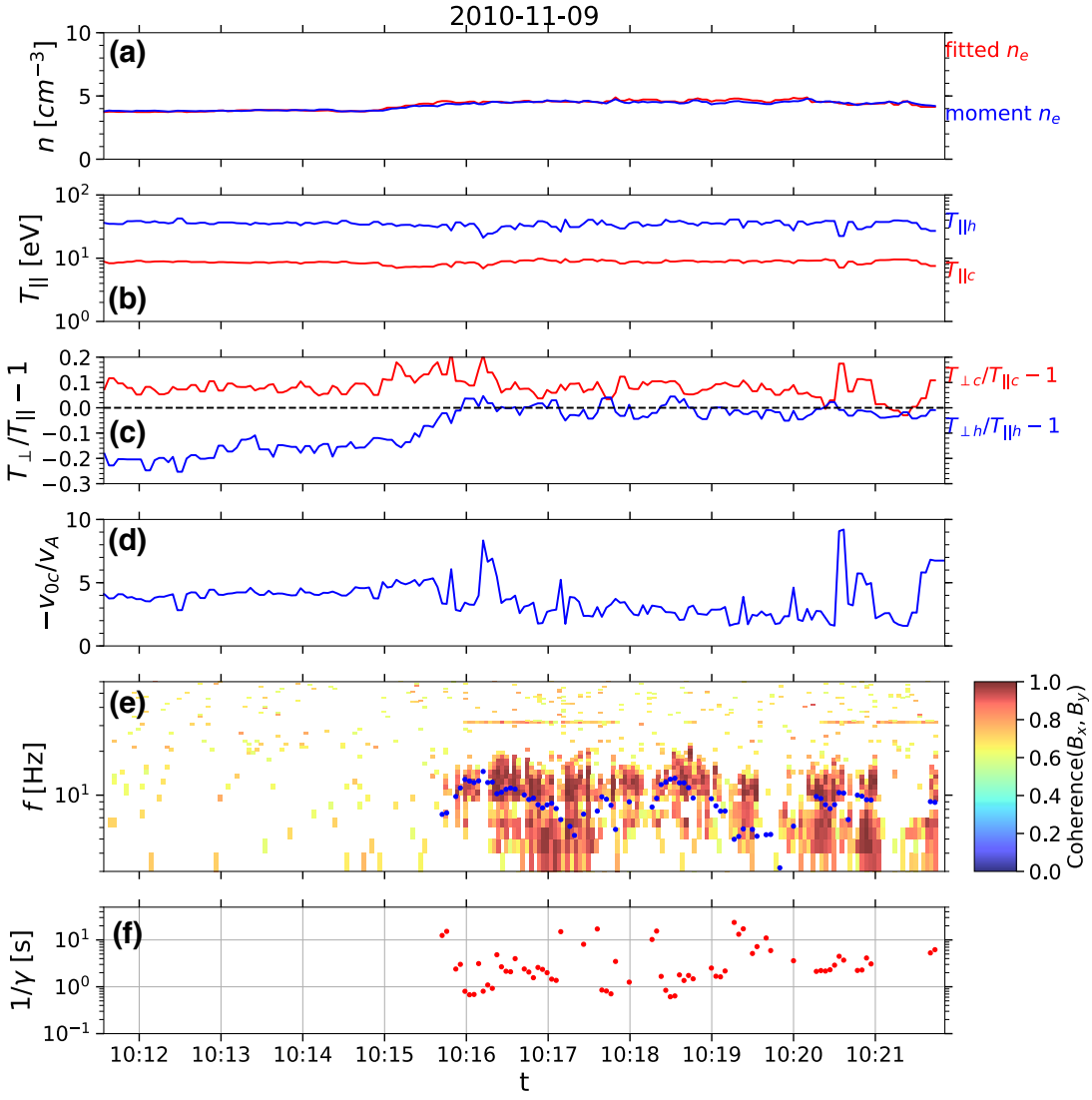

Figure 6.5: The results of the fitting of 183 electron VDFs: (a) the total electron densities from the fitting and the electron density calibrated on the ground; (b,c) parallel temperatures and temperature anisotropies of the core and halo population; (d) the bulk velocity of core population v_{0c} with respect to the local Alfvén speed v_A. Panel (e) repeats Figure 6.1g that shows the coherence between the two magnetic field components perpendicular to the quasi-static magnetic field (domains with coherence smaller than 0.6 have been masked out for visual clarity). The spacecraft frame frequency of the fastest growing whistler mode is indicated in panel (e) with dots. Panel (f) presents the e-folding time (inverse of the growth rate) of the fastest growing whistler wave. The absence of dots in some intervals implies that the plasma was stable.

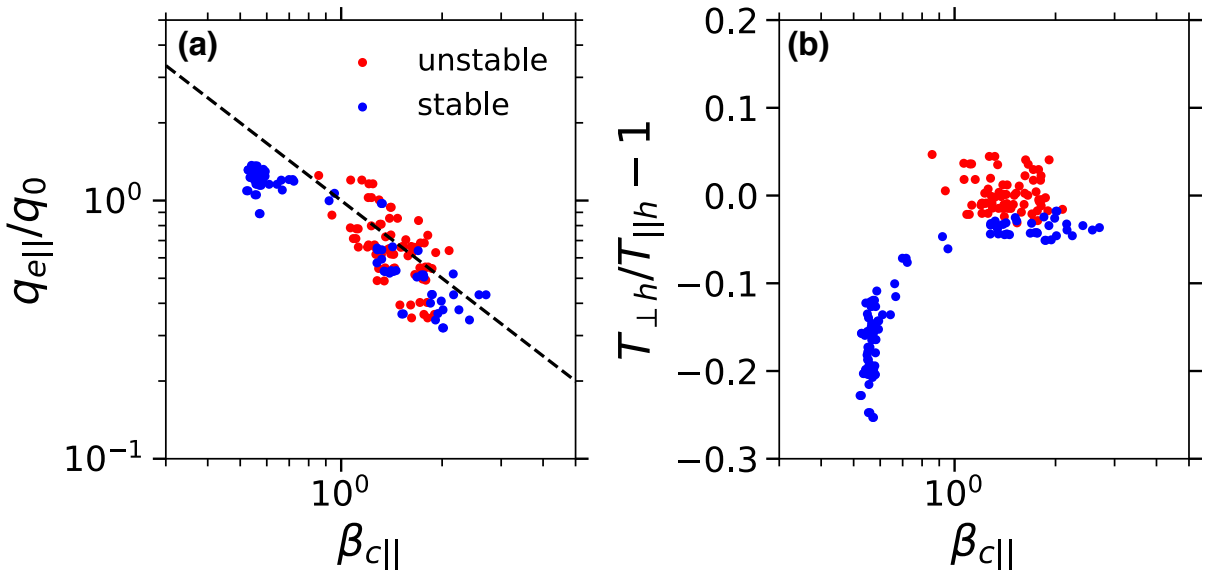

Figure 6.6: The demonstration of the crucial effect of the halo temperature anisotropy on the whistler heat flux instability. Panel (a) presents the electron heat flux q_e normalized to the free-streaming heat flux $q_0 = 1.5 n_e T_e (T_e/m_e)^{3/2}$ versus core electron beta parameter $\beta_{c||}$ computed for all 183 VDFs available over the ten-minute interval. $q_e/q_0 = 1/\beta_{c||}$ is plotted in dashed line for reference. Panel (b) presents the temperature anisotropy of the halo population versus $\beta_{c||}$. Unstable (stable) VDFs are labeled with red (blue) dots.

versus $\beta_{c||} = 8\pi n_c T_{||c}/B_0^2$. At any given $\beta_{c||}$ the heat flux is clearly below a threshold given by $q_e/q_0 \sim 1/\beta_{c||}$, that is similar to the marginally stable values in literature (Gary et al., 1999; Pistinner and Eichler, 1998; Roberg-Clark et al., 2018a; Komarov et al., 2018; Roberg-Clark et al., 2018b). However, at a given q_e/q_0 both stable and unstable VDFs are observed, indicating thereby that some other parameter controls the onset of the whistler wave generation. Panel (b) shows that the halo temperature anisotropy separates stable and unstable VDFs with a similar heat flux value. This re-emphasizes the crucial effect of the halo temperature anisotropy on the heat flux constraints in the solar wind.

6.4 Discussion and Conclusion

In-situ observations indicated that whistler waves generated by the heat flux instability highly likely constrain the heat flux in the solar wind (Feldman et al., 1975a; Gary, Skoug, and Daughton, 1999a; Tong et al., 2018b). However, there have been no previous analyses that would prove that whistler waves in the solar wind are actually produced locally by the whistler heat flux instability. In this letter we have presented a careful analysis of simultaneous particle and wave measurements for one of the time intervals in Stansby et al.

(2016). We have performed similar analysis for other Stansby et al. (2016) time intervals and confirmed that whistler waves are generated locally by the heat flux instability in those intervals as well. The presented event has shown that the e-folding growth time of whistler waves can be as short as one second and clearly demonstrated the crucial effect of the halo temperature anisotropy $T_{\perp h}/T_{||h} < 1$. In some of the Stansby et al. (2016) events the halo population has $T_{\perp h}/T_{||h} > 1$. The linear stability analysis has shown that even a slight $T_{\perp h}/T_{||h} > 1$ significantly enhances the growth rate of the heat flux instability, but we stress that the observed temperature anisotropies are insufficient to drive whistler waves purely via the temperature-anisotropy (without core and halo bulk motion) (Sagdeev and Shafranov, 1960; Kennel and Petschek, 1966).

Other parameters such as plasma beta are also crucial to the onset of whistler waves. The work to find the most critical parameter to whistler heat flux instabilities by statistical studies is under active investigation at this moment and beyond the scope of this letter. The presented analysis indicates that the sporadic occurrence of whistler waves in the solar wind pointed out by Lacombe et al. (2014) may be due to an interplay between the electron heat flux and the halo temperature anisotropy that may easily quench or enhance the instability. Future statistical studies should carefully address the halo temperature anisotropy in any analysis of the source of whistler waves in the solar wind.

Up to this point we have been focused on the electron heat flux constrained by wave-particle interactions. In fact, Coulomb electron-electron collisions can also affect solar wind electrons and constrain the electron heat flux (Salem et al., 2003; Bale et al., 2013; Pulupa et al., 2014a; Landi, Matteini, and Pantellini, 2014). The Knudsen number for the observed solar wind $K_n \sim 1 - 1.5$ falls into the collisionless regime (c.f. Figure 2 in Bale et al., 2013). Consistently, the observed heat flux is 30-50% lower than the Spitzer-Härm prediction. This implies that the observed heat flux constraint and deviation from the Sptizer-Härm prediction are due to electron scattering by the whistler waves.

Finally, the presented whistler waves are observed in the slow solar wind, where the electron VDF is satisfactorily described by counter-streaming core and halo (Feldman et al., 1975a; Maksimovic, Pierrard, and Riley, 1997). In the fast solar wind there is an additional anti-sunward propagating strahl population (Pilipp et al., 1987; Štverák et al., 2009) that do not directly interact with parallel whistler waves driven by whistler heat flux instabilities. Hence we expect the whistler heat flux instabilities to operate in the fast wind as well.

We acknowledge the THEMIS team for the use of data. We thank T. A. Bowen, J. W. Bonnel, J. M. McTiernan and A. Hull for useful discussions. Y. T. and S. D. B. were supported in part by NASA contract NNN06AA01C. I. V. and F. M. were supported by Johns Hopkins University/Applied Physics Lab Contract No. 922613 (Radiation Belt Storm Probes-Electric Fields and Waves).

Chapter 7

Statistical Study of Whistler Waves in the Solar Wind at 1 AU

Tong Y., Vasko I. Y., Artemyev A. V., Bale S. D., Mozer F. S. (2019). *Astrophys. J.* 878(1), 41.

Whistler waves are intermittently present in the solar wind, while their origin and effects are not entirely understood. We present a statistical analysis of magnetic field fluctuations in the whistler frequency range (above 16 Hz) based on about 801,500 magnetic field spectra measured over three years aboard ARTEMIS spacecraft in the pristine solar wind. About 13,700 spectra (30 hours in total) with intense magnetic field fluctuations satisfy the interpretation in terms of quasi-parallel whistler waves. We provide estimates of the whistler wave occurrence probability, amplitudes, frequencies and bandwidths. The occurrence probability of whistler waves is shown to strongly depend on the electron temperature anisotropy. The whistler waves amplitudes are in the range from about 0.01 to 0.1 nT and typically below 0.02 of the background magnetic field. The frequencies of the whistler waves are shown to be below an upper bound that is dependent on β_e. The correlations established between the whistler wave properties and local macroscopic plasma parameters suggest that the observed whistler waves can be generated in local plasmas by the whistler heat flux instability. The whistler wave amplitudes are typically small, which questions the hypothesis that quasi-parallel whistler waves are capable to regulate the electron heat flux in the solar wind. We show that the observed whistler waves have sufficiently wide bandwidths and small amplitudes, so that effects of the whistler waves on electrons can be addressed in the frame of the quasi-linear theory.

7.1 Introduction

Whistler waves, electromagnetic emissions between ion and electron cyclotron frequencies, are potentially regulating several fundamental processes in the collisionless or weakly-collisional solar wind. In particular, spacecraft observations of the electron heat flux values below a threshold dependent on β_e were interpreted in terms of the heat flux regulation by the whistler heat flux instability (Feldman et al., 1975a; Feldman et al., 1976; Scime et al., 1994; Gary, Skoug, and Daughton, 1999a; Tong et al., 2018b) and whistler fan instability (Vasko et al., 2019b). The observed radial evolution of the angular width of suprathermal field-aligned electron population (strahl electrons) in the solar wind (e.g., Hammond et al., 1996; Graham et al., 2017) requires pitch-angle scattering that can be potentially provided by whistler waves (Vocks et al., 2005; Shevchenko and Galinsky, 2010; Vocks, 2012; Kajdič et al., 2016b; Vasko et al., 2019b). Whistler waves may also suppress the electron heat flux in collisionless or weakly-collisional astrophysical plasma (Pistinner and Eichler, 1998; Gary and Li, 2000; Roberg-Clark et al., 2016; Roberg-Clark et al., 2018b; Komarov et al., 2018). The necessity of a heat flux suppression mechanism is suggested by observations of the temperature profile of hot gases in galaxy clusters (e.g., Cowie and McKee, 1977; Bertschinger and Meiksin, 1986; Zakamska and Narayan, 2003; Wagh, Sharma, and McCourt, 2014; Fang et al., 2018). The understanding of whistler wave origins and effects requires statistical analysis of whistler wave occurrence and properties in the solar wind.

The magnetic field fluctuations with power-law spectra in various frequency ranges are persistently observed in the solar wind and referred to as turbulence (see, e.g., Bruno and Carbone, 2013b, for review). Early studies associate the magnetic field turbulence in the whistler frequency range with whistler waves, their power was shown to decrease with increasing radial distance from the Sun and enhance around interplanetary shocks and high-speed stream interfaces (e.g., Beinroth and Neubauer, 1981; Coroniti et al., 1982; Lengyel-Frey et al., 1996; Lin et al., 1998). However, later studies show that the whistler frequency range of the magnetic field turbulence is dominated by kinetic-Alfvén and slow ion-acoustic waves Doppler-shifted into the whistler frequency range (e.g., Bale et al., 2005a; Salem et al., 2012b; Chen et al., 2013b; Lacombe, Alexandrova, and Matteini, 2017). The whistler wave contribution to the magnetic field turbulence spectrum is still under debate (e.g., Gary, 2015; Narita et al., 2016; Kellogg, Goetz, and Monson, 2018).

The modern spacecraft measurements have recently shown that whistler waves are intermittently present in the pristine (not disturbed by shocks or the Earth's foreshock) solar wind (Lacombe et al., 2014; Stansby et al., 2016; Tong et al., 2019c). Whistler waves have been identified by a local peak superimposed on a power-law spectrum of the magnetic field turbulence background. Therefore, these whistler waves should be produced by kinetic instabilities (free energy in the plasma), rather than by the turbulence cascade (see Gary, 2015, for discussion). In addition to the pristine solar wind, whistler waves have been reported around interplanetary shock waves (e.g., Breneman et al., 2010; Wilson et al., 2013) and in the Earth's foreshock (e.g., Hoppe and Russell, 1980; Zhang, Matsumoto, and Kojima, 1998).

The focus of this paper is the statistical analysis of whistler waves produced by kinetic instabilities in the pristine solar wind. The detailed analysis of whistler waves in the pristine solar wind has become possible only recently due to simultaneous wave and particle measurements aboard Cluster and ARTEMIS spacecraft (Lacombe et al., 2014; Stansby et al., 2016; Tong et al., 2019c). In contrast to WIND and Stereo spacecraft, wave measurements aboard Cluster and ARTEMIS are available almost continuously, rather than triggered by high-amplitude events, which typically occur around interplanetary shocks (e.g., Breneman et al., 2010; Wilson et al., 2013). Lacombe et al., 2014 have selected about twenty 10-minute intervals with whistler wave activity observed aboard Cluster in the pristine solar wind. The analysis of the magnetic field cross-spectra has shown that whistler waves propagate quasi-parallel to the background magnetic field. The simultaneous measurements of the electron heat flux have been presented to argue that the whistler waves are produced by the whistler heat flux instability (WHFI) (see, e.g., Gary et al., 1994, for the WHFI theory). Stansby et al., 2016 have selected several 10-minute intervals of ARTEMIS measurements to test the whistler wave dispersion relation in dependence on β_e. Tong et al., 2019c have carried out a detailed analysis of wave and particle measurements for Stansby et al., 2016 events and demonstrated that the whistler waves were produced locally on a time scales of seconds and indeed by the WHFI. The analysis by Tong et al., 2019c has proved that the WHFI may indeed operate in the solar wind and clearly demonstrated the critical role of the electron temperature anisotropy: the parallel temperature anisotropy may quench the WHFI instability, while the perpendicular temperature anisotropy favors the instability onset.

In spite of some recent progress, the parameters controlling the occurrence and properties of whistler waves in the solar wind have not been considered on a statistical basis. In this paper we present analysis of several hundred days of ARTEMIS observations in the solar wind (two spacecraft orbiting the Moon, see Angelopoulos, 2011, for details). The whistler wave selection produced a dataset of about 13,700 whistler wave spectra ($>$ 30 hours in total) in the pristine solar wind that is the most representative dataset up to date. The paper is organized as follows. We describe instrument characteristics, methodology and data selection criteria in Section 7.2. The results of the statistical study are presented in Sections 7.3, 7.4 and 7.5. We discuss the statistical results in light of whistler wave generation mechanism, electron heat flux regulation and recent particle-in-cell simulations in Section 7.6. The conclusions are summarized in Section 7.7.

7.2 Data and Methodology

We use ARTEMIS spacecraft measurements from 2011 to 2013 and select observations in the pristine solar wind, that is excluding the Earth's foreshock and the lunar wake. The Search Coil Magnetometer instrument provides Fast Fourier Transform (FFT) magnetic field spectra with 8s cadence and covers 64 piecewise linearly-spaced frequency channels between 8 to 4096 Hz (Roux et al., 2008). We use the spectral power density $\mathrm{SPD}_{\perp}$ of the magnetic field in the spacecraft spin plane (almost ecliptic plane), the spectral power density $\mathrm{SPD}_{||}$

of the magnetic field component along the spin axis (almost perpendicular to the ecliptic plane) and, the total spectral power density SPD = $\mathrm{SPD}_{||} + 2\ \mathrm{SPD}_{\perp}$. The Flux Gate Magnetometer (FGM) provides the quasi-static magnetic field measurements at 4 vectors per second (Auster et al., 2008), which we downsample by averaging to 8s cadence of the magnetic field spectra. The electron velocity distribution function (VDF) is measured every 3s by the Electrostatic Analyzer (McFadden et al., 2008), and transmitted to the ground every 3 or 96s depending on the telemetry mode. We use the ground calibrated particle moments (density, bulk velocity and temperatures)[1] and the electron heat flux parallel to the magnetic field computed by integrating the electron VDF[2]

$$q_e = \frac{1}{2} m_e \int \left(v_{||} - \langle v_{||} \rangle\right) \left(\mathbf{v} - \langle \mathbf{v} \rangle\right)^2 \mathrm{VDF}(\mathbf{v})\ d\mathbf{v} \tag{7.1}$$

where m_e is the electron mass, $v_{||}$ is the electron velocity parallel to the magnetic field and $\langle \mathbf{v} \rangle$ is the electron bulk velocity. The particle moments available at 96s are upsampled to 8s cadence of the magnetic field spectra via the linear interpolation. In total we have analyzed 801,527 magnetic field spectra, spanning 1,803 hours and 359 days in 2011-2013 [3]. In the rest of this paper, we will refer to each magnetic field spectrum as an independent event. Note that we did not filter out interplanetary shocks, but looking through the list of interplanetary shocks observed on Wind[4], we found only several days in our dataset with listed shocks. Therefore, our dataset is dominated by observations in the pristine solar wind. In what follows, we clarify criteria for whistler wave selection and demonstrate the data analysis techniques.

Figure 7.1 presents the magnetic field spectrum and particle moments for a particular day (July 29, 2011) in our dataset. Panel (a) shows the total spectral power density from 16 to 300 Hz. The SPD enhancements between 20 and 60 Hz appear first around 14:25 UT and continue intermittently thereafter before about 16:30 UT. In terms of a local electron cyclotron frequency f_{ce}, the observed SPD enhancements are between 0.1 and 0.3 f_{ce} which is in the whistler frequency range. The wave activity can be characterized by the total magnetic field power in the frequency range between 16 and 300 Hz

$$P_B \equiv \int_{16\ \mathrm{Hz}}^{300\ \mathrm{Hz}} \mathrm{SPD}(f)\ df \tag{7.2}$$

Panel (b) demonstrates that P_B well traces the SPD enhancements. In the absence of clear wave activities, P_B is a mixture of the inherent turbulence background and instrument noise between 16 and 300 Hz. We divide the magnetic field spectra into two-hour chunks and define the background power P_g as the 20th percentile of P_B within every chunk. Panel

[1]Ground-calibrated particle moments are accessed via two data products, `THB_L2_ESA` and `THC_L2_ESA` which can be found in `https://cdaweb.gsfc.nasa.gov/`.

[2]The electron VDF is accessed from `http://themis.ssl.berkeley.edu/data/themis/` and then processed by the open-source SPEDAS software (Angelopoulos et al., 2019).

[3]The data intervals are provided in `https://doi.org/10.5281/zenodo.2652949`

[4]`www.cfa.harvard.edu/shocks/wi_data`

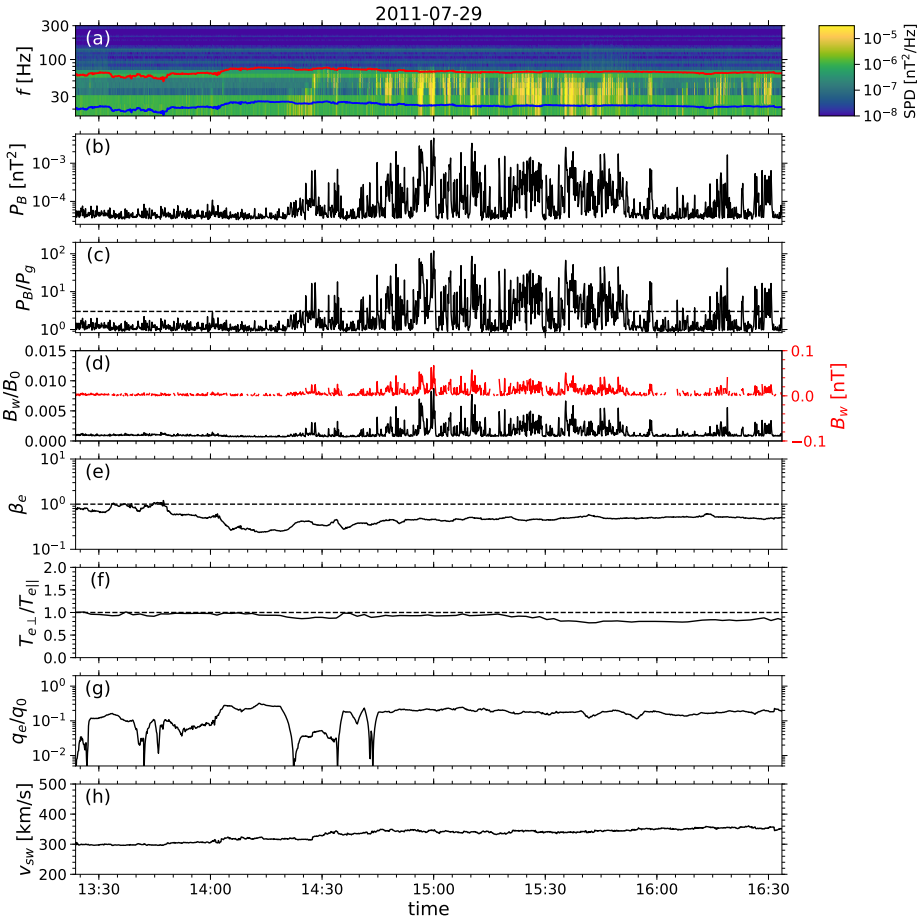

Figure 7.1: The wave activity in the whistler frequency range observed aboard ARTEMIS on July 29, 2011 (one day from our dataset): (a) magnetic field spectral power density, 0.1 f_{ce} and 0.3 f_{ce} are indicated with green and red curves, where f_{ce} is a local electron cyclotron frequency; (b) the magnetic field power P_B in the frequency range between 16 and 300 Hz determined by Eq. (7.2); (c) the magnetic field power P_B normalized to the background turbulence power P_g determined every 2 hours as 20th percentile of P_B; the visual inspection of our dataset showed that $P_B > 3\ P_g$ (dashed line) is a reasonable criterion for selecting the wave activity events in the whistler frequency range and filtering out variations of the turbulence background; (d) the amplitude of magnetic field fluctuations evaluated as $B_w = (P_B - P_g)^{1/2}$ (red trace) and B_w/B_0 (black trace) that is the amplitude with respect to the local background magnetic field B_0; (e)-(h) $\beta_e = 8\pi n_e T_{e||}/B_0^2$, electron temperature anisotropy $T_{e\perp}/T_{e||}$, the electron heat flux q_e normalized to the free-streaming heat flux $q_0 = 1.5 n_e T_e (T_e/m_e)^{1/2}$, solar wind velocity v_{sw}.

(c) presents P_B/P_g, demonstrating thereby that the wave activity corresponds to P_B significantly exceeding P_g. The amplitude of magnetic field fluctuations associated with the wave activity is characterized by $B_w = (P_B - P_g)^{1/2}$. Panel (d) shows that the amplitude of the magnetic field fluctuations reaches 0.05 nT, while B_w/B_0, that is the amplitude of the magnetic field fluctuations with respect to the background magnetic field, does not exceed 0.01. We emphasize that B_w is the amplitude averaged over 8s, while the actual peak amplitude may be larger due to intermittent appearance of the magnetic field fluctuations over 8s. Panels (e) to (h) present a few plasma parameters: $\beta_e = 8\pi n_e T_{e||}/B_0^2$, $T_{e\perp}/T_{e||}$ is the electron temperature anisotropy, q_e/q_0 is the electron heat flux normalized to the free-streaming heat flux $q_0 = 1.5\ n_e T_e\ (2T_e/m_e)^{1/2}$, v_{sw} is the solar wind proton velocity. In the above parameters, n_e is the electron density, $T_{e\perp}$ and $T_{e||}$ are the perpendicular and parallel electron temperature, B_0 is the magnitude of the quasi-static magnetic field. Note we have used a natural unit system in which temperature has the unit eV. The Boltzmann constant is dropped throughout the paper.

Visual inspections of the magnetic field spectra from our dataset show that SPD enhancements in the whistler frequency range are always below 300 Hz. The wave power P_B in the frequency range between 16 and 300 Hz is found to be a good indicator of the wave activity. The spectral power density in the first (8 Hz) frequency channel is excluded from P_B computation, because it provides strong and noisy contribution to P_B, so that the wave activity at $f \geq 16$ Hz could not be identified in P_B. Another reason for excluding the first channel is that it is more likely to be contaminated by low-frequency magnetic field fluctuations different from whistler waves (see below). Visual inspections show that $P_B > 3P_g$ is a reasonable empirical criterion for selecting noticeable wave activities between 16 and 300 Hz and filtering out spectra corresponding to variations of the turbulence background. The criterion $P_B > 3P_g$ selects 17,050 magnetic field spectra that is about 38 hours and about 2% of the original dataset.

Although the selected wave activities are in the whistler frequency range, they do not necessarily represent whistler waves (see Section 7.1 for discussion). The routinely available ARTEMIS measurements include only two component of spectral power densities that are not sufficient to determine wave vectors and polarizations of the selected wave activity events. Nevertheless, these components, namely, spectral power densities $\mathrm{SPD}_\perp$ and $\mathrm{SPD}_{||}$, along with results of the previous observations enable us to filter out events contradicting the whistler wave interpretation and provide a basis to argue that the major part of the selected events are whistler waves. The technique relies on the previous analysis of the magnetic field spectral matrix (spectra and cross-spectra up to 400 Hz) measurements provided by Cluster (Lacombe et al., 2014) and the analysis of magnetic field waveforms (frequencies up to 64 Hz resolved) provided by ARTEMIS (Stansby et al., 2016; Tong et al., 2019c), which both showed that whistler waves in the pristine solar wind propagate quasi-parallel to the background magnetic field $\mathbf{B}_0$. The observations of quasi-parallel whistler waves are consistent with theoretical predictions of potential instabilities operating in the solar wind (Gary et al., 1994; Gary, Chang, and Wang, 2012). Oblique whistler waves may be present in the solar wind, but they are predicted to be electrostatic and, hence, not identifiable in

the magnetic field spectra (Vasko et al., 2019b).

The whistler wave propagation parallel to the magnetic field results in a specific relation between $\mathrm{SPD}_{||}$ and $\mathrm{SPD}_{\perp}$ that is dependent on $\mathbf{B}_0$ orientation with respect to the spin axis (see Figure 7.2 for schematics). A whistler wave at frequency f propagating parallel to $\mathbf{B}_0$ is a circularly-polarized wave with the magnetic field along $\mathbf{b}_1 \cos(2\pi f t) + \mathbf{b}_2 \sin(2\pi f t)$, where $\mathbf{b}_{1,2}$ are unit vectors in the plane perpendicular to $\mathbf{B}_0$. This wave would produce $\mathrm{SPD}_{||}(f) \propto \sin^2\chi$ and $\mathrm{SPD}_{\perp}(f) \propto (1+\cos^2\chi)/2$, where χ is the angle between $\mathbf{B}_0$ and the spin axis (Fig. 7.2), so that the ratio

$$R \equiv \frac{\mathrm{SPD}_{||}(f)}{\mathrm{SPD}(f)} \tag{7.3}$$

would equal to $R_0 = 0.5\sin^2\chi$. A reasonable agreement between the observed R and expected R_0 may allow filtering out events corresponding to plasma modes different from quasi-parallel whistler waves.

Figure 7.3 presents the analysis of the nature of the wave activity shown in Figure 7.1. Panel (a) presents angle χ (Figure 7.2) computed using the quasi-static magnetic field measurements. Panels (b) and (c) present $\mathrm{SPD}_{||}$ and $\mathrm{SPD}_{\perp}$. For every magnetic field spectrum with $P_B > 3P_g$ we identify the frequency channel f_w with the largest total spectral power density, SPD in Figure 7.1a, and compute R using $\mathrm{SPD}_{||}(f_w)$ and $\mathrm{SPD}(f_w)$ in Eq. (7.3). Panel (d) shows that R is well consistent with $R_0 = 0.5\sin^2\chi$, supporting thereby the interpretation of the wave activity in terms of quasi-parallel whistler waves.

Figure 7.4 presents results of the comparison between R and R_0 evaluated for all 17,050 magnetic field spectra with $P_B > 3P_g$. Panel (a) shows that $R/(R+R_0)$ are clustered around 0.5, that is $R \approx R_0$. Most of the events with $R/(R+R_0)$ significantly deviating from 0.5 are in the three lowest frequency channels at 16, 24 and 32 Hz, where low-frequency modes are expected most likely to appear due to the Doppler effect. Panel (b) shows that the events with $R/(R+R_0)$ significantly deviating from 0.5 have frequencies from 0.02 to 0.5 f_{ce}, demonstrating thereby that the whistler frequency range may be populated by plasma modes different from quasi-parallel whistler waves. We introduce a quantitative criterion $0.4 < R/(R+R_0) < 0.6$ to select the events not contradicting the interpretation of quasi-parallel whistler waves. The probability and cumulative distribution functions in panels (c) and (d) show that this selection criterion filters out about 20% of the events leaving about 13,700 magnetic field spectra. In accordance with Lacombe et al., 2014 this shows that whistler waves identified in the magnetic field spectra in the pristine solar wind are predominantly quasi-parallel. In what follows we use the selected 13,700 events to clarify how the occurrence and properties of whistler waves depend on macroscopic plasma parameters.

The selected whistler wave SPD enhancements spread over several frequency channels. To quantify the frequency bandwidth of the whistler waves, we determine first the background spectral power density $\mathrm{SPD}_g(f)$ at frequency f as the 20th percentile of $\mathrm{SPD}(f)$ at that frequency every two hours. Similarly to P_g, $\mathrm{SPD}_g(f)$ is a combination of the magnetic field turbulence background and intrinsic instrument noise level. The whistler wave spectrum

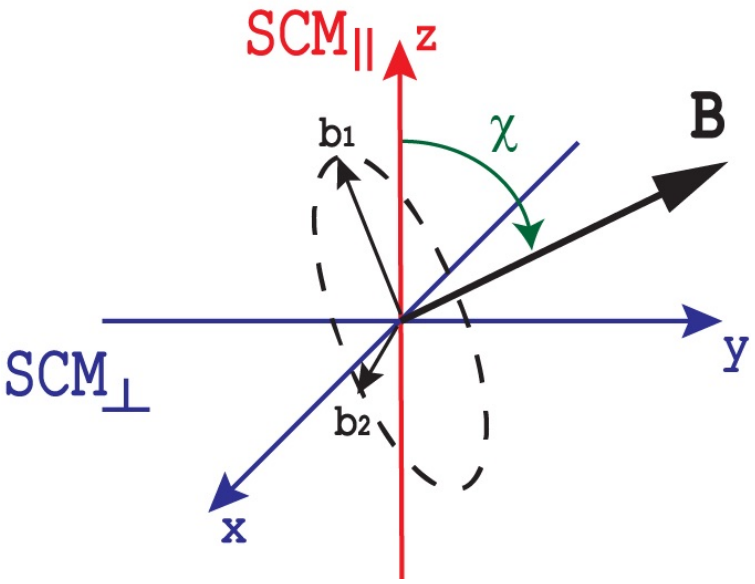

Figure 7.2: Schematics of the ARTEMIS search coil magnetometer antennas. The instrument provides spectral power densities $\mathrm{SPD}_{||}$ and $\mathrm{SPD}_{\perp}$ of magnetic field fluctuations along the spacecraft spin axis and in the plane perpendicular to the spin axis. The total spectral power density (Figure 7.1a) of the magnetic field fluctuations is computed as $\mathrm{SPD}=\mathrm{SPD}_{||}+2\ \mathrm{SPD}_{\perp}$. For a whistler wave propagating parallel to the quasi-static magnetic field B_0 there is a particular relation between $\mathrm{SPD}_{||}$ and $\mathrm{SPD}_{\perp}$ that depends on angle χ (see Section 7.2 for details).

$\mathrm{SPD}(f)$-$\mathrm{SPD}_g(f)$ is fitted to the Gaussian model with the peak at f_w

$$\mathrm{SPD}(f) - \mathrm{SPD}_g(f) = A \exp\left[-\frac{(f-f_w)^2}{2\sigma^2}\right], \tag{7.4}$$

where A and σ are the best fit parameters. The frequency bandwidth Δf is estimated as the full width at half maximum

$$\Delta f = 2\sigma(2\ln 2)^{1/2} \sim 2.35\ \sigma$$

Figure 7.5 presents the analysis of the frequency bandwidth of a particular whistler wave spectrum with the peak at $f_w \sim 40$ Hz measured at 15:35:33 UT on July 29, 2011 (one spectrum from Figure 7.1). The whistler wave SPD enhancement is about two orders of magnitude larger than $\mathrm{SPD}_g(f_w)$. The Gaussian fit to $\mathrm{SPD}(f) - \mathrm{SPD}_g(f)$ yields the frequency bandwidth $\Delta f \sim 21$ Hz. We restrict the statistical analysis of the frequency bandwidth to whistler wave events with $f_w > 16$ Hz, because only in those events we could guarantee that the peak of the Gaussian is at f_w, rather than at some frequency below 16 Hz. The criterion $f_w > 16$ Hz leaves 5,800 spectra for the frequency bandwidth analysis that is 42% of the selected 13,700 whistler wave spectra.

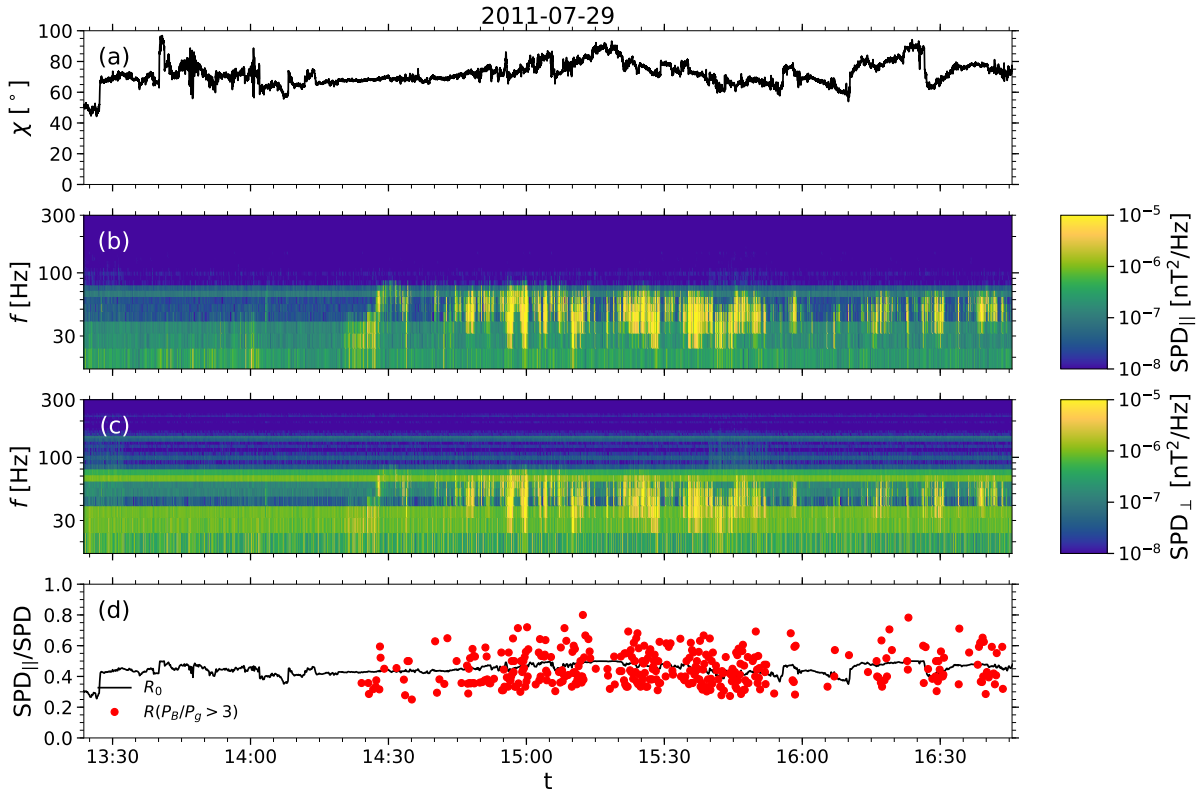

Figure 7.3: The test of the nature of the wave activity observed on July 29, 2011: (a) the angle χ between the magnetic field and the spin axis shown in Figure 7.2 and computed using the quasi-static magnetic field measurements; (b, c) spectra $\mathrm{SPD}_{||}$ and $\mathrm{SPD}_{\perp}$ of magnetic field fluctuations along the spin axis and in the plane perpendicular to the spin axis; (d) the ratio $R = \mathrm{SPD}_{||}(f_w)/\mathrm{SPD}(f_w)$ at the frequency channel f_w corresponding to the largest SPD, only points at the moments of time with $P_B > 3P_g$ are indicated (red dots); the ratio R_0 expected for a whistler wave propagating parallel to the background magnetic field is shown by the black curve.

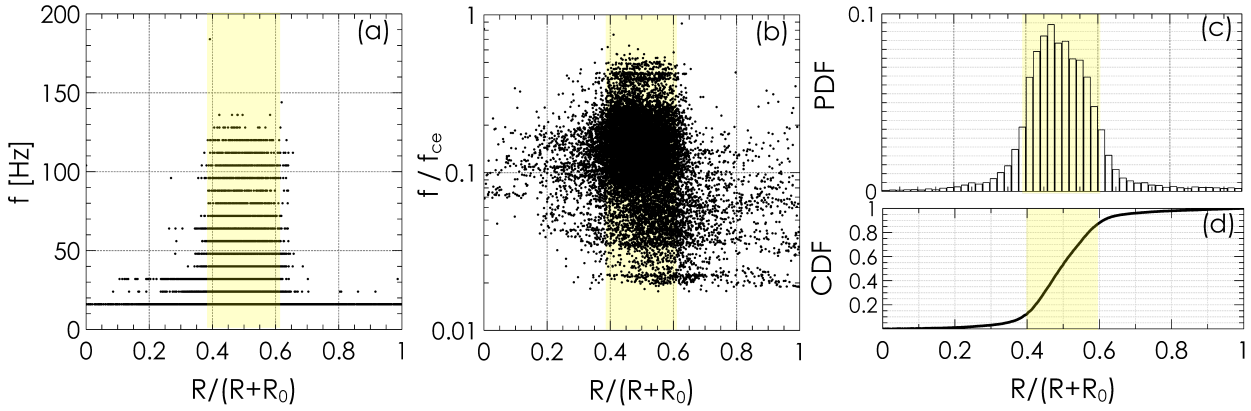

Figure 7.4: Results of testing the nature of the selected ∼17,050 magnetic field spectra through comparison of the observed $R = \mathrm{SPD}_{||}(f_w)/\mathrm{SPD}(f_w)$, where f_w is the frequency channel with the maximum SPD=$\mathrm{SPD}_{||}$+2 $\mathrm{SPD}_{\perp}$, and R value (denoted as R_0) expected for a whistler wave propagating parallel to the background magnetic field: (a,b) $R/(R+R_0)$ vs. frequency f_w and f_w/f_{ce}; (c,d) the probability and cumulative distribution functions of $R/(R+R_0)$. The data points within the shaded region, $0.4 < R/(R+R_0) < 0.6$, correspond to wave activity events non-contradicting to the hypothesis of quasi-parallel whistler waves. Panel (d) shows that exclusion of the data points outside of the shaded region filters out less than 20% of the data points.

7.3 Whistler wave occurrence

Out of about 8×10^5 spectra we have associated about 13,700 spectra with quasi-parallel whistler waves that yields a total occurrence probability of whistler waves of 1.7%. We emphasize that this is the probability of sufficiently intense whistler waves ($P_B > 3P_g$) above 16 Hz, i.e. whistler waves that are less intense and at lower frequencies have been excluded. The overall occurrence of whistler waves in the pristine solar wind is certainly higher. We demonstrate below that the occurrence probability of the selected whistler waves depends on macroscopic plasma parameters.

Figure 7.6 presents the analysis of effects of the electron heat flux q_e/q_0 and β_e on the occurrence probability of whistler waves. Panel (a) shows the distribution of all $\sim 8 \times 10^5$ magnetic field spectra in $(q_e/q_0, \beta_e)$ parameter plane. The electron heat flux at $\beta_e \gtrsim 1$ is below a threshold $q_e/q_0 \sim 1/\beta_e$ that is in agreement with previous spacecraft observations (Gary, Skoug, and Daughton, 1999a; Tong et al., 2018b). This heat flux threshold was previously considered as the evidence for the heat flux regulation by the whistler heat flux instability (Feldman et al., 1976; Gary, Skoug, and Daughton, 1999a). Panel (b) shows the distribution of $\sim 13,700$ magnetic field spectra associated with quasi-parallel whistler waves. Combining the distributions shown in panels (a) and (b) we evaluate the occurrence probability of whistler waves at various $(q_e/q_0, \beta_e)$. Panel (c) shows that the occurrence

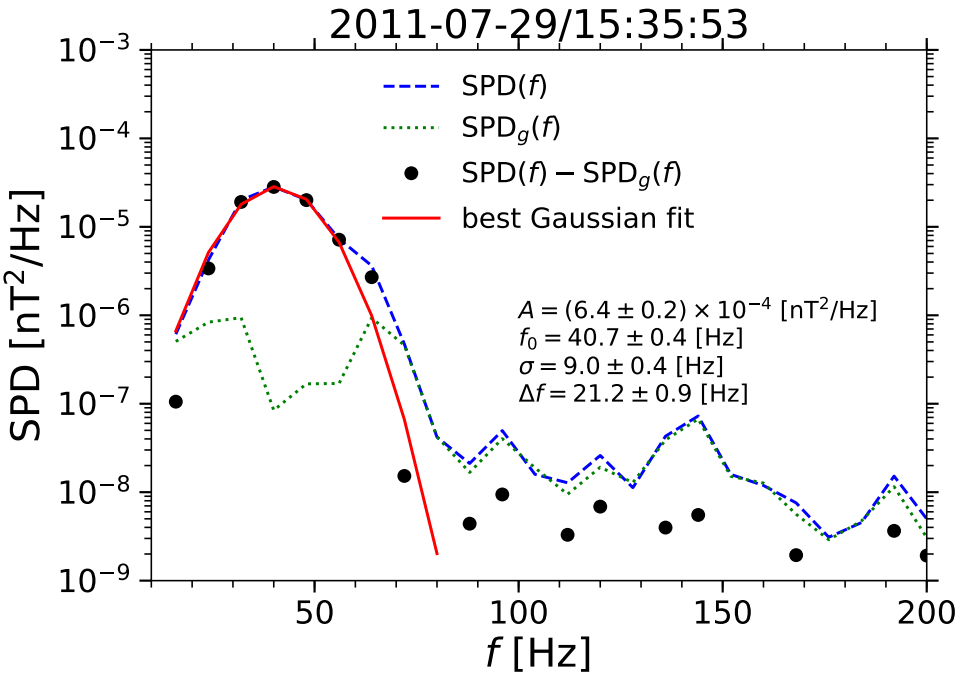

Figure 7.5: The analysis of the frequency bandwidth of a particular whistler wave spectrum on July 29, 2011. The measured spectral power density at 15:35:33 UT (blue), the background spectral power density SPD$_g(f)$ (green) that is computed at each frequency f as the 20th percentile of SPD(f) at that frequency every two hours. Black dots represent SPD(f)-SPD$_g(f)$ that is the whistler wave spectrum. The best-fit Gaussian (7.4) to the whistler wave spectrum is given by the red curve. The best fit parameters A and σ are indicated along with the frequency bandwidth estimated as the width at half maximum, $\Delta f = 2\sigma(2\ln 2)^{1/2}$.

probability does not favor the parameter space near the threshold $q_e/q_0 \sim 1/\beta_e$ and, instead, somewhat enhances at low heat flux values.

Figure 7.7 presents the analysis of effects of the electron heat flux q_e/q_0 and electron temperature anisotropy $T_{e\perp}/T_{e||}$ on the whistler wave occurrence probability. Panels (a) and (b) present distributions of all events and whistler wave events in $(q_e/q_0, T_{e\perp}/T_{e||})$ parameter plane. In accordance with previous statistical studies (e.g., Štverák et al., 2008; Artemyev, Angelopoulos, and McTiernan, 2018) solar wind electrons at 1 AU most often exhibit parallel temperature anisotropy, $T_{e\perp}/T_{e||} < 1$. Panels (a) and (b) are combined to compute the occurrence probability in $(q_e/q_0, T_{e\perp}/T_{e||})$ parameter plane. Panel (c) clearly demonstrates that the temperature anisotropy quite critically affects the whistler wave occurrence probability. At any given q_e/q_0 the occurrence probability increases with increasing $T_{e\perp}/T_{e||}$. The occurrence probability is less than a few percent at $T_{e\perp}/T_{e||} \lesssim 1$, but increases up to 10-60% at $T_{e\perp}/T_{e||} > 1$. In addition, panel (b) shows for whistler waves to occur

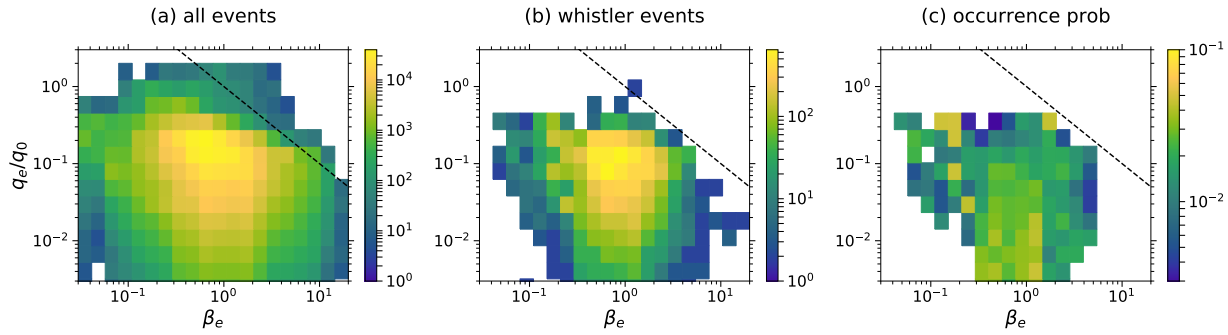

Figure 7.6: The analysis of whistler wave occurrence in dependence on the electron heat flux q_e/q_0 and β_e: (a) distribution of all $\sim 8 \times 10^5$ magnetic field spectra in $(q_e/q_0, \beta_e)$ parameter plane; (b) distribution of the selected ∼13,700 spectra associated with quasi-parallel whistler waves; (c) the occurrence probability of whistler waves that is computed by dividing a number of events with whistler waves shown in panel (b) over a total number of events shown in panel (a). The dashed line in the panels represent $q_e/q_0 = 1/\beta_e$ for reference.

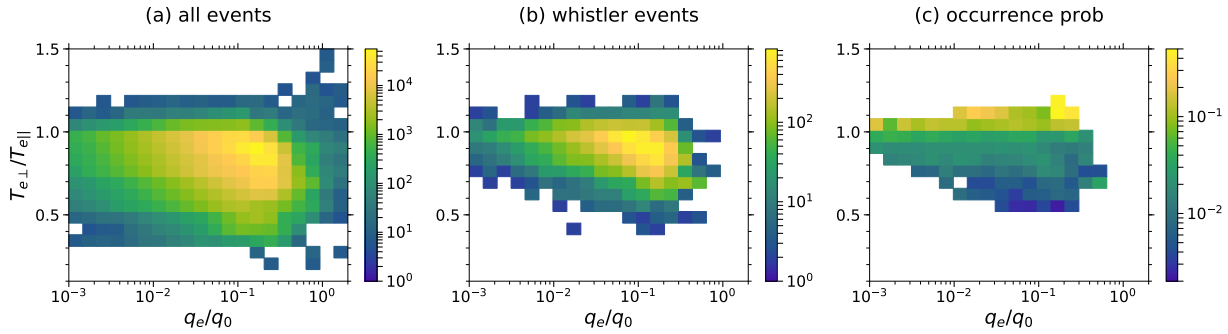

Figure 7.7: The analysis of whistler wave occurrence in dependence on the electron heat flux q_e/q_0 and $T_{e\perp}/T_{e||}$: (a) distribution of all $\sim 8 \times 10^5$ magnetic field spectra in $(q_e/q_0, T_{e\perp}/T_{e||})$ parameter plane; (b) distribution of the selected ∼13,700 spectra associated with quasi-parallel whistler waves; (c) the occurrence probability of whistler waves that is computed by dividing a number of events with whistler waves shown in panel (b) over a total number of events shown in panel (a).

the temperature anisotropy should be above a threshold that increases as the electron heat flux decreases: at $q_e/q_0 \lesssim 10^{-2}$ the temperature anisotropy should be above 0.75, while at $q_e/q_0 \gtrsim 3 \times 10^{-2}$ whistler waves may occur at $T_{e\perp}/T_e||$ as low as 0.5. In addition to the 2D occurrence probabilities, we have computed whistler wave occurrence probabilities in dependence on individual macroscopic plasma parameters.

Figure 7.8 presents the occurrence probability of whistler waves in dependence on q_e/q_0, β_e, v_{sw} and $T_{e\perp}/T_{e||}$. The occurrence probability $P(\xi)$ of whistler waves in dependence on

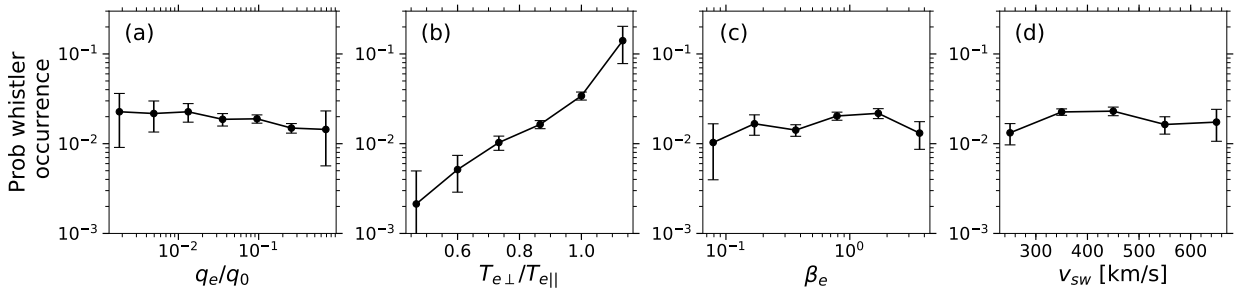

Figure 7.8: The occurrence probability of whistler waves in dependence on individual macroscopic plasma parameters.

a macroscopic plasma parameter A is determined as $P(\xi) = N_W(\xi)/N(\xi)$, where $N_W(\xi)$ is the number of whistler wave events with A in the range $(\xi - \Delta\xi/2, \xi + \Delta\xi/2)$, while $N(\xi)$ is the total number of events with A in the same range. The bin width $\Delta\xi$ is chosen so that the number of events within each bin would be sufficiently large. The uncertainties of $P(\xi)$ are estimated with the assumption that each particle measurement is independent [5]. Panels (a), (c) and (d) demonstrate that the electron heat flux, β_e and solar wind velocity do not significantly affect the occurrence probability of whistler waves. Panel (b) confirms that the whistler wave occurrence probability is critically dependent on the electron temperature anisotropy. The probability is less than 2% at $T_{e\perp}/T_{e||} < 0.9$, but increases from 5 to 15% as $T_{e\perp}/T_{e||}$ varies from 0.95 to 1.2.

7.4 Whistler wave intensity

Figure 7.9 presents the probability distribution functions of whistler wave amplitudes B_w and B_w/B_0 for the slow ($v_{sw} \lesssim 400$ km/s) and fast ($v_{sw} > 500$ km/s) solar wind. Our dataset is dominated by the slow solar wind events, fast solar wind events constitute less than 12% of the dataset. Panels (a) and (b) show that whistler waves amplitude B_w is typically below 0.02 B_0 or in physical units in the range from 0.01 up to 0.1 nT. We recall that B_w is the amplitude averaged over 8s, so that the actual peak amplitudes of magnetic field fluctuations could be in principle larger due to intermittent presence of whistler wave over 8s. However, these amplitudes are consistent with previous measurements of whistler waveforms aboard ARTEMIS spacecraft (Stansby et al., 2016; Tong et al., 2019c), indicating thereby that quite likely whistler waves in the pristine solar wind have amplitudes B_w much smaller than B_0. Panels (a) and (b) also demonstrate that there is a bit higher chance to observe intense whistler waves in the slow solar wind than in the fast solar wind.

[5] Assuming that each particle measurement has the same probability to have a whistler companion, and that n measurements estimate the probability to be p. Then the standard error of p is $s_p = \sqrt{p(1-p)/n}$. We estimate the uncertainty of p as the uncertainty at the 95% level of confidence $\delta p = 2s_p$.

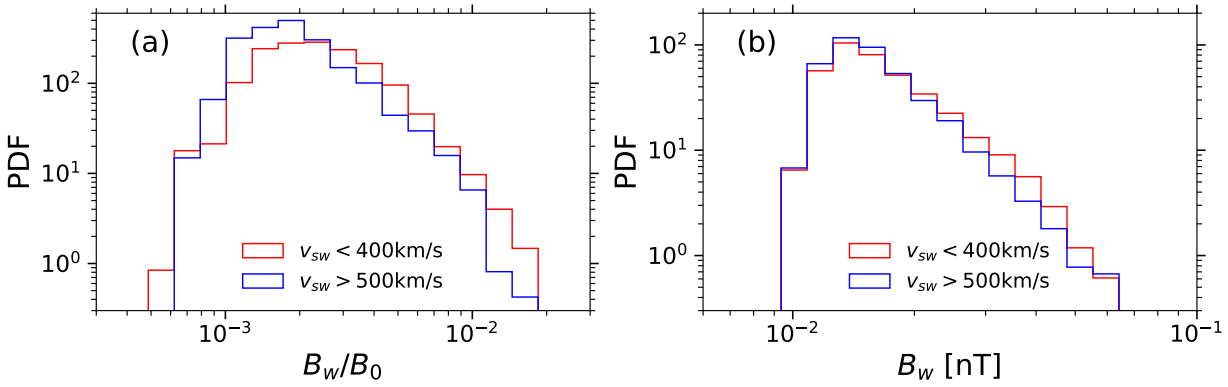

Figure 7.9: Probability distribution functions of whistler wave amplitudes B_w and B_w/B_0 in the slow ($v_{sw} < 400$ km/s) and fast ($v_{sw} > 500$ km/s) solar wind.

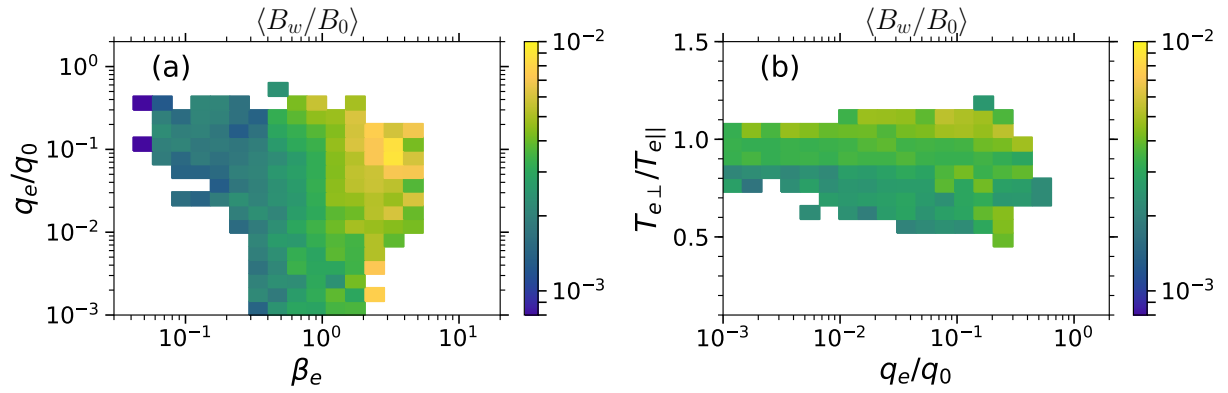

Figure 7.10: The whistler wave amplitude $\langle B_w/B_0 \rangle$ averaged over bins in (a) $(q_e/q_0, \beta_e)$ and (b) $(T_{e\perp}/T_{e||}, q_e/q_0)$ parameter planes.

Figure 7.10 presents the distribution of the averaged whistler wave amplitude $\langle B_w/B_0 \rangle$ in $(q_e/q_0, \beta_e)$ and $(T_{e\perp}/T_{e||}, q_e/q_0)$ parameter planes. Panel (a) demonstrates that $\langle B_w/B_0 \rangle$ is strongest, when both β_e and q_e/q_0 are high. As a result, the averaged whistler wave amplitude is enhanced in the parameter space around to the threshold $q_e/q_0 \sim 1/\beta_e$. It is interesting to note that the whistler wave occurrence probability doesn't favor this region in the parameter space (Figure 7.6). The reason is that the occurrence of whistler waves is most critically controlled by the temperature anisotropy, rather than q_e/q_0 or β_e. Panel (b) shows that $\langle B_w/B_0 \rangle$ enhances with increasing $T_{e\perp}/T_{e||}$ at fixed q_e/q_0, while the positive correlation between $\langle B_w/B_0 \rangle$ and q_e/q_0 is noticeable only at $T_{e\perp}/T_{e||} \gtrsim 1$.

Figure 7.11 presents the distribution of whistler wave amplitudes B_w/B_0 in dependence on individual macroscopic parameters. The upper panels indicate the mean and median B_w/B_0

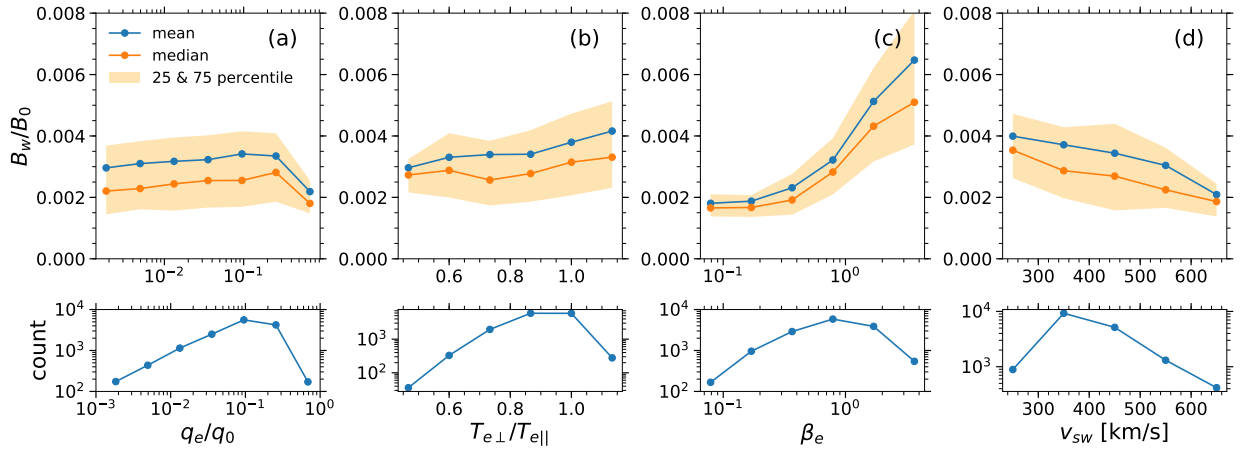

Figure 7.11: The whistler wave amplitude B_w/B_0 versus (a) the electron heat flux, (b) electron temperature anisotropy, (c) β_e, and (d) the solar wind velocity. The curves represent the median and mean values of B_w/B_0, while the shaded regions cover from 25th to 75th percentile of B_w/B_0.

values in dependence on q_e/q_0, $T_{e\perp}/T_{e||}$, β_e and v_{sw}, while the shaded regions cover from the 25th percentile to the 75th percentile of B_w/B_0. The bottom panels present the number of events within bins used to compute the B_w/B_0 distributions in the upper panels. Panels (a) and (b) show that the mean and median values of B_w/B_0 are positively correlated with q_e/q_0 and $T_{e\perp}/T_{e||}$, though the overall variation of these values is about 30%. The negative correlation between B_w/B_0 and the heat flux at $q_e/q_0 \gtrsim 0.3$ is likely physical effect, because the number of events in the corresponding bins is sufficiently large. Panel (c) shows that the median and mean values of B_w/B_0 are most strongly correlated with β_e, both values increase by about a factor of three as β_e increases from 0.1 to 5. Panel (d) shows that the whistler wave amplitude is negatively correlated with the solar wind velocity, varying by a factor of two from the slow to fast solar wind.

7.5 Whistler wave frequency

Observations

We consider the frequency channel f_w with the largest SPD(f) or largest enhancement SPD(f) − SPD$_g$(f) (both provide the same frequency channel) as the frequency of a whistler wave event. We could consider the frequency channel with the largest relative SPD enhancement, SPD(f)/SPD$_g$(f), as the whistler wave frequency estimate. Because SPD$_g$(f) is a monotonically decreasing function of the frequency, this approach provides frequencies higher than f_w, but we have found that the difference is less than 50%. We use f_w as the

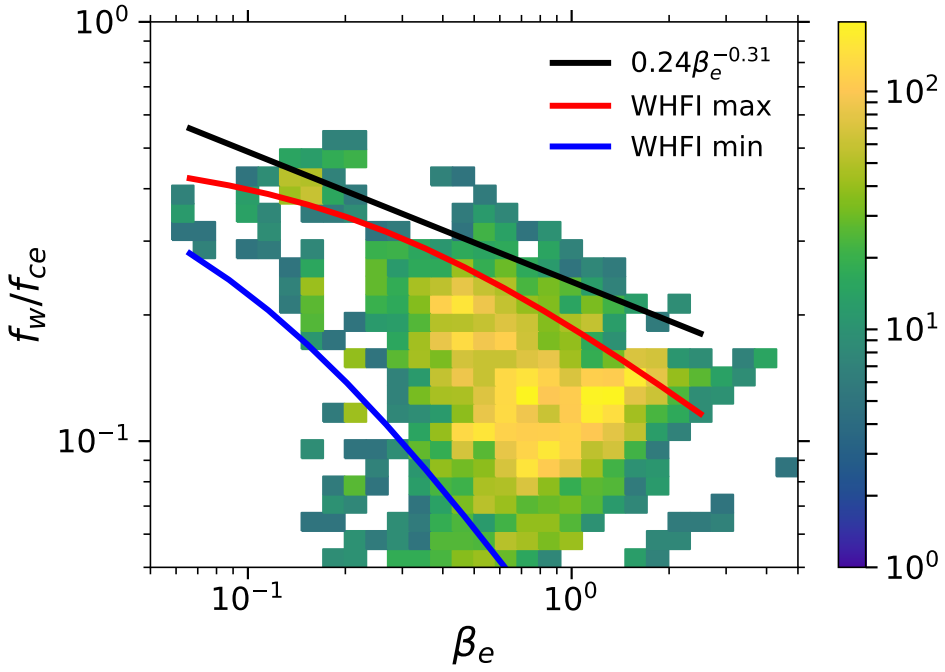

Figure 7.12: Whistler wave frequency f_w, determined as the frequency channel with the largest SPD(f), normalized to the electron cyclotron frequency f_{ce} versus β_e. The black curve represent the the best power-law fit to the 10% of the highest frequency events at various β_e. The red and blue curves represent the maximum and minimum frequencies of whistler waves that can be generated by the whistler heat flux instability (see Section 7.5 for details). The presented frequencies f_w are measured in the spacecraft frame, but the estimates of the Doppler-shift have shown that these frequencies differ from the plasma frame frequencies by less than 30% (see Section 7.5 for details).

whistler wave frequency estimate, while the use of the other frequency would not affect any of our conclusions. We have found that among various macroscopic plasma parameters only β_e correlates strongly with the normalized frequency f_w/f_{ce}.

Figure 7.12 demonstrates that there are apparent upper and lower frequency bounds that decrease with increasing β_e. Below we compare these bounds to theoretical predictions of the whistler heat flux instability. To quantify the negative correlation between the upper bound on f_w/f_{ce} and β_e we bin all the whistler wave events according to β_e and select 10% of the highest frequency events within each bin. These highest frequency events are fitted to a power-law of β_e. The best fit (black curve) shown in Figure 7.12 demonstrates that we generally have $f_w/f_{ce} \lesssim 0.24\ \beta_e^{-0.31}$. The whistler wave frequencies in Figure 7.12 are measured in the spacecraft frame and differ from those in the plasma frame by the Doppler-shift, $\Delta f_D = \mathbf{k}\mathbf{v}_{sw}/2\pi$, where $\mathbf{k}$ is the whistler wave vector. We have estimated

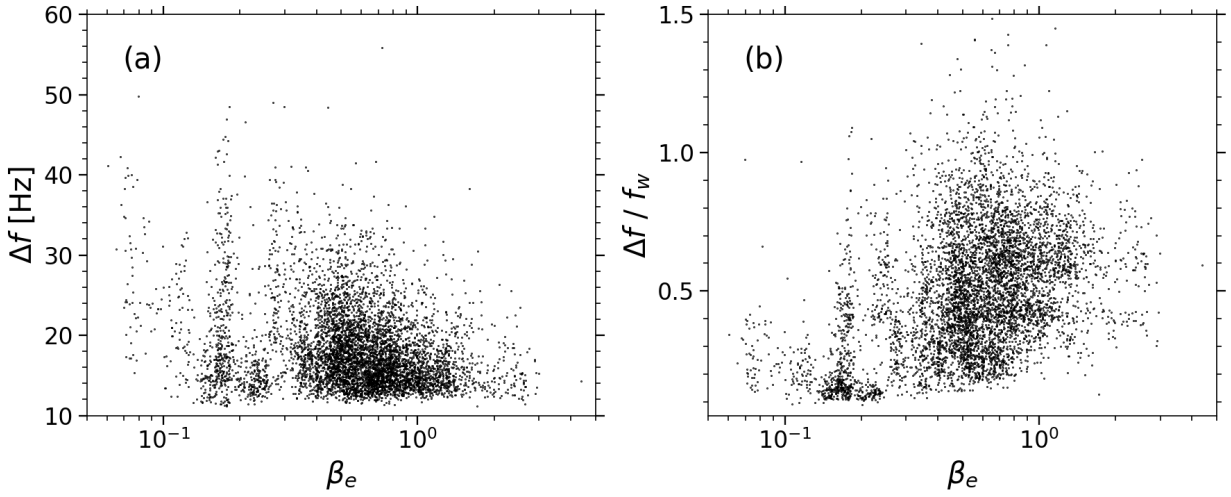

Figure 7.13: The frequency bandwidth, in physical units and normalized to f_w, of 5,800 whistler wave events, whose frequency f_w is above 16 Hz. The frequency bandwidth is presented versus β_e.

the Doppler-shift for all whistler waves events using the wave vector estimate from the cold dispersion relation, $f/f_{ce} = k^2 d_e^2/(1 + k^2 d_e^2)$, where $d_e = c/\omega_{pe}$ is the electron inertial length and ω_{pe} is the electron plasma frequency (e.g., Stix, 1962). We have found that $\Delta f_D/f_w$ is less than 0.3, so that the measured frequency can be considered as a good estimate of the whistler wave frequency in the plasma frame.

Figure 7.13 presents the frequency bandwidth Δf of about 5,800 whistler wave events with $f_w > 16$ Hz. Panel (a) shows that Δf is typically about 15 Hz, though can be as large as 50 Hz. Panel (b) shows that the frequency bandwidth normalized to the whistler wave frequency f_w is typically in the range between 0.1 and 1. There is a clear positive correlation between $\Delta f/f_w$ and β_e: at $\beta_e \ll 1$ whistler waves typically exhibit $\Delta f/f_w \sim 0.2$, while $\Delta f/f_w$ is typically about 0.5 at $\beta_e \sim 1$. The implications of the frequency width estimates will be discussed in Section 7.6.

WHFI predictions

The linear theory of the WHFI suggests that the electron velocity distribution function (VDF) consisting of bi-Maxwellian core and halo populations, counter-streaming in the plasma rest frame, can be unstable to whistler wave generation at sufficiently large core and halo bulk velocities (Gary et al., 1975a; Gary et al., 1994). Tong et al., 2019c have recently shown for several events that the WHFI indeed generates whistler waves in the pristine solar wind. In this section we evaluate the maximum and minimum frequencies of whistler waves expected to be produced by the WHFI in dependence on β_e. We consider the simplest electron VDFs consisting of isotropic core and halo populations ($T_\perp = T_{||}$) and

variable	values
T_c/T_p	1
n_c/n_0	$\{0.75, 0.8, 0.9, 0.95\}$
T_h/T_c	$\{3, 5, 7, 9, 11\}$
$\Delta v_c/v_A$	$\{-i/2 \vert i = 0, 1, 2....20\}$

Table 7.1: Parameter ranges used for the analysis of the maximum and minimum frequencies of whistler waves that can be generated by the whistler heat flux instability (see Section 7.5 for details).

assume a zero net electron current in the plasma rest frame, $n_c\Delta v_c + n_h\Delta v_h = 0$, where $n_{c,h}$ and $\Delta v_{c,h}$ are densities and bulk velocities of the core and halo populations. Because the bulk velocities are much smaller than the corresponding thermal velocities (e.g., Feldman et al., 1975a; Tong et al., 2019c), we have $\beta_e \approx \beta_c + \beta_h$, where $\beta_c = 8\pi n_c T_c/B_0^2$, $\beta_h = 8\pi n_h T_h/B_0^2$ and $T_{c,h}$ are core and halo temperatures.

The linear growth rate of the WHFI normalized to f_{ce} depends on n_c/n_0, T_h/T_c, T_p/T_c, and $\Delta v_c/v_A$, where n_0 is the total electron density which is also assumed equal to the proton density, $T_{c,h}$ are the core and the halo temperatures, T_p is the proton temperature, and $v_A = B_0/(4\pi n_0 m_p)^{1/2}$ is the Alfvén velocity , and m_p is the proton mass. The growth rate is almost independent of the proton to core electron temperature ratio, because in realistic conditions protons do not resonate with whistler waves produced by the WHFI (Gary et al., 1975a). In what follows we keep $T_p/T_c = 1$ which is a reasonable assumption at 1 AU (e.g., Newbury et al., 1998; Artemyev, Angelopoulos, and McTiernan, 2018). To evaluate the maximum and minimum frequencies of whistler waves that can be generated by the WHFI instability, we fix β_e and vary n_c/n_0, T_h/T_c and $\Delta v_c/v_A$ in the ranges typical for the solar wind at 1 AU (Table 7.1). For each combination of these three parameters we compute the linear growth rate using the numerical code developed by Tong et al., 2015 and identify the frequency of the fastest growing whistler wave. Then, for each fixed β_e we identify the maximum and minimum frequencies of whistler waves that can be generated by the WHFI. At a fixed β_e the minimum frequency decreases with decreasing threshold value on the growth rate. Different threshold values result in different minimum frequency bounds, but these bounds are of similar shape and almost parallel to each other in the $(\beta_e, f/f_{ce})$ plane. The maximum and minimum frequency bounds are well fitted to modified power-laws

$$f/f_{ce} = a(\beta_e + b)^c \tag{7.5}$$

Table 7.2 presents the best fit parameters a, b and c for the maximum frequency bound at zero growth rate and for the minimum frequency bounds derived for several growth rate thresholds, $\gamma/\omega_{ce} > 10^{-5}$ and 10^{-6}, where $\omega_{ce} = 2\pi f_{ce}$.

Figure 7.12 overlays the theoretical maximum and minimum frequency bounds upon the measured whistler wave frequencies. The presented minimum frequency bound is derived for $\gamma/\omega_{ce} > 10^{-6}$. The frequencies of the major part of the observed whistler waves fall

	γ/ω_{ce}	a	b	c
$f_{\max}/f_{ce}$	> 0	0.19	0.22	-0.58
$f_{\min}/f_{ce}$	$> 10^{-5}$	0.046	0.058	-0.95
$f_{\min}/f_{ce}$	$> 10^{-6}$	0.034	0.09	-1.1

Table 7.2: Values of parameters a, b and c in Eq. (7.5) that gives fitting to the maximum and minimum frequencies of whistler waves that can be generated by the whistler heat flux instability at various β_e. The maximum frequency quickly converges to some asymptotic value as the growth rate tends to zero, whereas the minimum frequency bound depends on the growth rate threshold. We present parameters for the maximum frequency bound at zero growth rate, and the minimum frequency bounds computed for $\gamma/\omega_{ce} > 10^{-5}$ and 10^{-6}, where $\omega_{ce} = 2\pi f_{ce}$.

between the minimum and the maximum theoretical bounds, demonstrating thereby that the observed whistler waves could be in principle generated by the WHFI. Moreover, the generation can be local that is the whistler waves are generated in a local plasma, rather than generated in some other region and propagated to the spacecraft location.

7.6 Discussion

We have carried out statistical analysis of whistler waves observed in the pristine solar wind using the most representative dataset collected up to date. We have focused on whistler waves identified by a local peak in the spectral power density of the magnetic field fluctuations, that is why these whistler waves are produced by free energy in a plasma, rather than by the turbulence cascade. Out of 801,527 magnetic field spectra measured at 1 AU aboard ARTEMIS, we have selected about 17,050 intense wave activity events in the whistler frequency range and associated 13,700 of them with quasi-parallel whistler waves. Thus, about 80% of the intense events in the whistler frequency range are consistent with quasi-parallel whistler wave interpretation. This conclusion is in agreement with results of the previous less extensive studies of waveform and cross-spectra measurements (Lacombe et al., 2014; Stansby et al., 2016; Tong et al., 2019c). The other $\sim$20% of the intense events are highly likely low-frequency plasma modes Doppler-shifted into the whistler frequency range, because they are predominantly observed in the three lowest frequency channels. The overall occurrence of quasi-parallel whistler waves in our dataset is about 1.7%, but the actual occurrence of whistler waves is certainly higher, because we selected only sufficiently intense whistler waves above 16 Hz.

We have shown that the occurrence probability of whistler waves most critically depends on the electron temperature anisotropy. There is no any drastic dependence of the whistler wave occurrence on the electron heat flux, solar wind velocity or β_e. The occurrence probability is less than 2% when $T_{e\perp}/T_{e||} \lesssim 0.9$, but varies from 5 to 15% as $T_{e\perp}/T_{e||}$ increases from 0.95 to 1.2. This correlation is consistent with the recent analysis by Tong et al., 2019c

of several whistler wave events measured in the burst mode (waveform available) aboard ARTEMIS. Tong et al., 2019c have shown that whistler waves in those events were generated locally by the WHFI, while the temperature anisotropy of the halo population $T_{h\perp}/T_{h||}$ critically affects the instability onset: $T_{h\perp}/T_{h||}$ sufficiently smaller than unity quenches the instability, while $T_{h\perp}/T_{h||} > 1$ significantly enhances the growth rate. In the present statistical analysis we did not compute temperature anisotropies of the core and halo electron populations, but we expect that the increase of the full anisotropy $T_{e\perp}/T_{e||}$ corresponds to the increase of the halo temperature anisotropy, because temperature anisotropies of core and halo populations are positively correlated (Feldman et al., 1976; Pierrard et al., 2016).

We have shown that whistler waves in the solar wind have amplitudes B_w typically below 0.02 B_0 or in physical units below 0.1 nT. These amplitude estimates are consistent with the previous less extensive studies, where waveform measurements were analyzed (Lacombe et al., 2014; Stansby et al., 2016; Tong et al., 2019c), but more extensive waveform analysis should be carried out in the future to verify this result. The averaged whistler wave amplitude B_w/B_0 is found to be negatively correlated with the solar wind velocity. The average B_w/B_0 correlates positively with the electron heat flux and electron temperature anisotropy, but the strongest positive correlation is found with β_e. The variation of q_e/q_0 and $T_{e\perp}/T_{e||}$ over the observed range results in variation of B_w/B_0 by about 30%, while the variation of β_e from 0.1 to 5 results in variation of B_w/B_0 by a factor of three. The presented amplitude estimates and correlations between B_w/B_0 and macroscopic parameters should be useful for future theoretical studies of origin and effects of whistler waves in the solar wind. At the moment, we note that the whistler wave amplitudes observed at 1 AU are much smaller than whistler wave amplitudes $B_w \sim B_0$ reported in recent Particle-In-Cell simulations (Roberg-Clark et al., 2016; Roberg-Clark et al., 2018b), indicating thereby that the simulations are initialized with electron VDFs unrealistic for the solar wind at 1 AU. The fact that the whistler wave amplitudes are rather small calls into question their role in the electron heat flux regulation in the solar wind, though this question deserves a separate study.

We have estimated the frequencies of the observed whistler waves and bandwidths of the whistler wave spectra. The only electrons that can drive and efficiently interact with quasi-parallel whistler waves are those in the first normal cyclotron resonance (e.g., Shklyar and Matsumoto, 2009)

$$v_{||} = \frac{\omega - \omega_{ce}}{k}, \tag{7.6}$$

where $v_{||}$ is electron velocity parallel to the quasi-static magnetic field, $\omega = 2\pi f$, $\omega_{ce} = 2\pi f_{ce}$ and k is the whistler wavenumber. The minimum energy of the cyclotron resonant electrons (e.g., Kennel and Petschek, 1966)

$$E_R = \frac{B_0^2}{8\pi n_0} \frac{f_{ce}}{f} \left(1 - \frac{f}{f_{ce}}\right)^3, \tag{7.7}$$

where we have used cold dispersion relation of whistler waves, $f/f_{ce} = k^2 d_e^2/(1 + k^2 d_e^2)$ (e.g, Stix, 1962). Figure 7.14 presents the minimum resonant energy evaluated using Eq. (7.7)

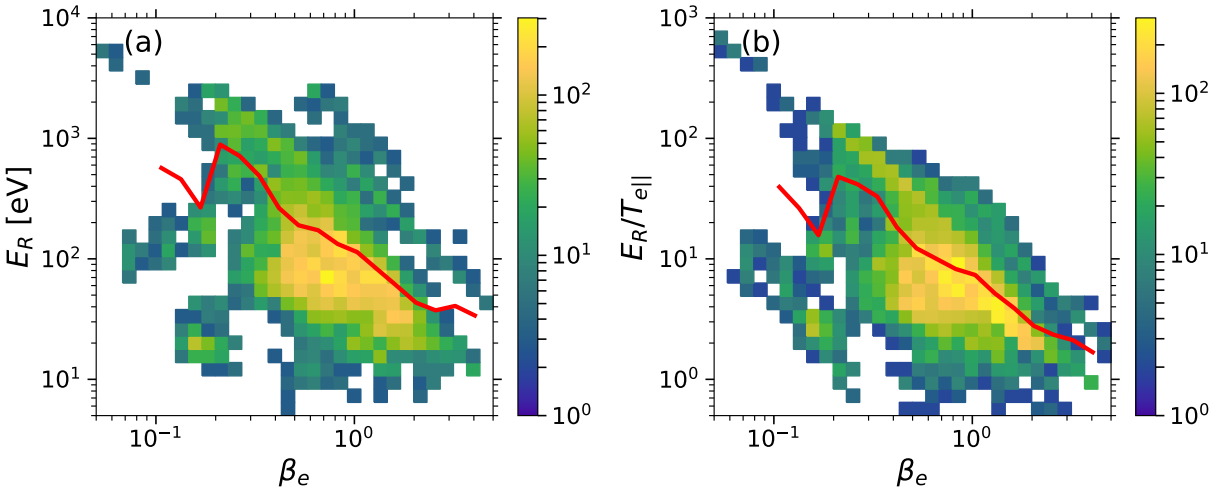

Figure 7.14: The minimum energy of electrons to be in the first normal cyclotron resonance with the observed whistler waves. It is given by Eq. (7.7) with the whistler wave frequencies adopted from Figure 7.12a. Panel (a) presents the minimum resonant energy in physical units, while panel (b) presents this energy with respect to the electron temperature $T_{e||}$. The averaged resonant energies are presented by the red curves.

with whistler wave frequencies adopted from Figure 7.12a. The minimum resonant energy is negatively correlated with β_e, because $E_R \propto B_0^2$, while $\beta_e \propto 1/B_0^2$. Panel (a) shows that the minimum resonant energy is of a few tens of eV at $\beta_e \sim 1$ and above a few hundred eV at low β_e. Panel (b) shows that in terms of thermal energies the resonant energy is about $3\,T_e$ at $\beta_e \sim 1$ and a few tens of T_e at low β_e. We conclude that the observed quasi-parallel whistler waves should be driven by the halo electron population in accordance with previous theoretical (Gary et al., 1975a; Gary et al., 1994) and experimental (Tong et al., 2019c) studies.

The estimated bandwidths of the whistler wave spectra allow us to evaluate whether the effect of the observed whistler waves on electrons could be addressed within the quasi-linear theory (QLT) (e.g., Sagdeev and Galeev, 1969). The QLT is applicable for a sufficiently wide frequency width of a whistler wave spectrum (e.g., Karpman, 1974): $\Delta f/f_w \gg (B_w/B_0)^{1/2}\ (kv_\perp/\omega_{ce})^{1/2}$, where $v_\perp$ is the electron velocity perpendicular to the magnetic field. Because the whistler waves interact efficiently with halo electrons, we can assume that $v_\perp$ is a few times larger than the electron thermal velocity. Using the cold dispersion relation for whistler waves we rewrite the QLT applicability criterion

$$\frac{\Delta f}{f_w} \gg \left(\frac{B_w}{B_0}\right)^{1/2} \left(\beta_e \frac{f_w/f_{ce}}{1 - f_w/f_{ce}}\right)^{1/4} \tag{7.8}$$

Figure 7.15 presents the test of the QLT applicability and shows that $\Delta f/f_w$ is always above the right-hand side of Eq. (7.8). The inset panel shows the probability distribution

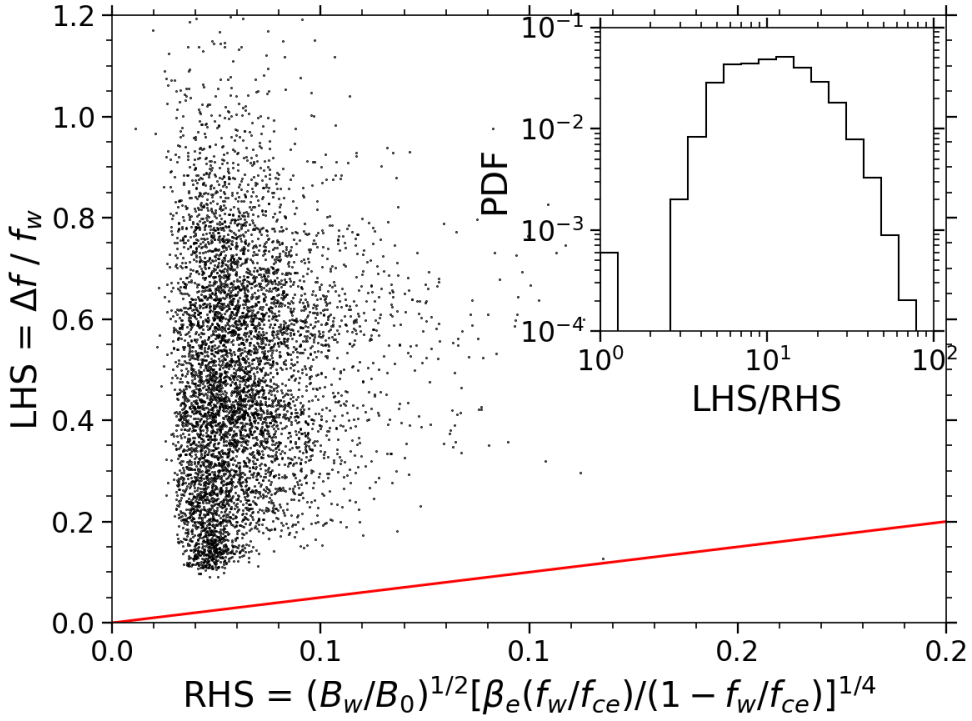

Figure 7.15: Estimated values of the left hand side (LHS) and the right hand side (RHS) of Eq. (7.8) using ARTEMIS measurements. The red line references equality between LHS and RHS. The probability density function of the ratio LHS/RHS is shown in the inset panel.

function of the ratio of $\Delta f/f_w$ to the right-hand side and confirms that in the majority of the events $\Delta f/f_w$ is about five times larger than the right-hand side. We conclude that the quasi-linear theory is likely a good approximation for analysis of effects of the observed whistler waves on electrons. At the same time, we stress that an extensive statistical analysis of waveform measurements should be carried out in the future to verify that whistler wave amplitudes B_w inferred from 8s magnetic field spectra do not significantly underestimate the actual peak amplitudes of whistler waves. The statement of the QLT applicability concerns only whistler waves in the pristine solar wind. Whistler waves observed in interplanetary shock waves may be rather narrow-band and large-amplitude for the QLT to be applicable (e.g., Breneman et al., 2010; Wilson et al., 2013).

Figure 7.16 presents order of magnitude estimates of the quasi-linear relaxation time of unstable electron VDFs by the observed whistler waves. The relaxation time is given by the following expression (e.g., Karpman, 1974)

$$\tau \approx \frac{1}{2\pi f_w \beta_e} \left(\frac{\Delta f}{f_w}\right)^3 \frac{B_0^2}{B_w^2}, \tag{7.9}$$

where in deriving this formula we have assumed that $f_w \ll f_{ce}$. The typical relaxation

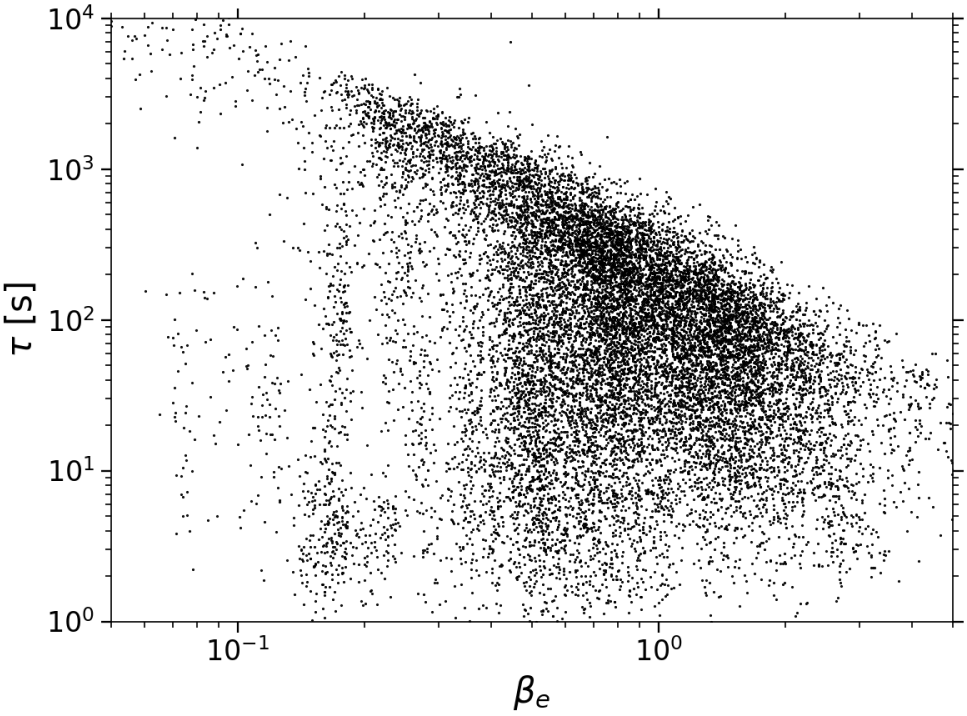

Figure 7.16: The quasi-linear relaxation time of unstable electron VDFs by the observed whistler waves presented versus β_e.

time is a few tens of minutes at low β_e to about a minute at $\beta_e \sim 1$. In principle the relaxation can be as fast as a few seconds. The strong negative correlation between τ and β_e is due to explicit dependence of τ on β_e according to Eq. (7.9) and due to a strong positive correlation between B_w/B_0 and β_e. During the relaxation time whistler waves may cover spatial distances of a few tens of thousands kilometers implying that low-frequency density and magnetic field fluctuations may affect the relaxation process of the WHFI (see, e.g., Voshchepynets et al., 2015, for relaxation of a beam instability in nonuniform solar wind plasma).

We have shown that the frequency upper bound of the observed whistler waves is negatively correlated with β_e and demonstrated that the frequencies are in effect consistent with the theoretical predictions of the WHFI. Thus, in accordance with conclusions of Tong et al., 2019c whistler waves observed in the pristine solar wind can be indeed generated by the WHFI operating in a local plasma. We have compared the observed frequencies to predictions of the WHFI theory with electron VDFs consisting of core and halo electron populations. The presence of the anti-sunward strahl population typical for the fast solar wind (Pilipp et al., 1987; Štverák et al., 2009) would not affect any characteristics of the WHFI, because whistler waves produced by the WHFI propagate anti-sunward and do not resonate with the strahl (e.g., Vasko et al., 2019b, for discussion).

The original WHFI theory assumed both core and halo electron populations to be temperature isotropic (Gary et al., 1975a). The unstable whistler waves were shown to propagate parallel to the halo bulk velocity or, equivalently, parallel to the electron heat flux. In the realistic solar wind both core and halo populations exhibit some temperature anisotropies (Feldman et al., 1976; Štverák et al., 2008; Pierrard et al., 2016). Even a slight temperature anisotropy $T_{h\perp}/T_{h||} > 1$ of the halo population increases the growth rate of whistler waves propagating parallel to the heat flux (Tong et al., 2019c). At sufficiently high $T_{h\perp}/T_{h||} > 1$ whistler waves propagating anti-parallel to the electron heat flux can be unstable as expected for the classical temperature anisotropy instability (TAI) (Sagdeev and Shafranov, 1960; Kennel and Petschek, 1966; Gary, Chang, and Wang, 2012), which may drive whistler waves propagating both parallel and anti-parallel to the electron heat flux at any negligible or zero heat flux value. We cannot rule out that some of the whistler waves in the solar wind are driven by the TAI of the halo population and propagate opposite to the electron heat flux. At the moment, we can point out that our statistical results support the WHFI scenario, so that the major part of the whistler waves in our dataset is likely produced by the WHFI. The analysis of the TAI in the solar wind requires very careful fitting of electron VDFs and analysis of whistler waveforms (not available continuously) that is left for future studies.

Finally, we notice that whistler waves considered in this paper are electromagnetic waves that have been identified in the magnetic field spectra. We have definitely missed electrostatic whistler waves potentially present in the solar wind (Vasko et al., 2019b), but not visible in the magnetic field spectra. The results of this statistical study will be useful for the future analysis of whistler wave origin and effects, e.g., heat flux regulation and supratheramal electron scattering, in the solar wind.

7.7 Conclusion

In this section we summarize the results of our statistiscal analysis of whistler waves at 1 AU:

1. The intense wave activity in the whistler frequency range is shown to be dominated (80%) by quasi-parallel whistler waves. The overall occurrence of quasi-parallel whistler waves in the pristine solar wind is found to be about 1.7%. We emphasize that only intense whistler waves above 16 Hz have been considered in this study, so that the actual occurrence is certainly higher.

2. The occurrence probability of whistler waves in the pristine solar wind is strongly dependent on the electron temperature anisotropy $T_{e\perp}/T_{e||}$. The occurrence probability is less than 2% at $T_{e\perp}/T_{e||} \lesssim 0.9$, but varies from 5 to 15% as $T_{e\perp}/T_{e||}$ increases from 0.95 to 1.2. There is no apparent dependence of the whistler wave occurrence on the electron heat flux q_e/q_0, the solar wind velocity v_{sw} or β_e.

3. Whistler waves in the solar wind have amplitudes typically below 0.02 B_0, where B_0 is the magnitude of the quasi-static magnetic field. In physical units the amplitudes are in the range from about 0.01 to 0.1 nT.

4. The average normalized whistler wave amplitude B_w/B_0 correlates positively with q_e/q_0 and $T_{e\perp}/T_{e||}$, but the strongest positive correlation is found with β_e. The variation of q_e/q_0 and $T_{e\perp}/T_{e||}$ over the observed range results in variation of B_w/B_0 by about 30%, while variation of β_e from 0.1 to 5 results in variation of B_w/B_0 by a factor of three. The whistler wave amplitude negatively correlates with the solar wind velocity, varying by a factor of two from slow to fast solar wind.

5. Whistler wave frequencies f_w/f_{ce} fall between some upper and lower bounds dependent on β_e. The upper bound on the whistler wave frequency is approximately given by 0.24 $\beta_e^{-0.31}$. The frequency bandwidth Δf of the whistler waves is determined and $\Delta f/f_w$ is shown to be positively correlated with β_e.

6. We show that the observed whistler wave frequencies are consistent with the theoretical predictions of the whistler heat flux instability, indicating thereby that whistler waves in the pristine solar wind can be generated by the WHFI. The generation of some of the whistler waves by the temperature anisotropy instability can not be ruled out.

7. We have shown that the frequency width of the whistler waves is sufficiently wide so that the quasi-linear theory is likely applicable to describe effects of the whistler waves on electrons. The typical quasi-linear relaxation time in a uniform plasma would be from a minute at $\beta_e \sim 1$ to a few tens of minutes at low β_e. In principle the relaxation can be as fast as a few seconds.

8. We have estimated the energies of electrons resonating the whistler waves and shown that the whistler waves should be driven by suprathemral electrons, whose minimum energy E_R is negatively correlated with β_e. E_R is about a few tens of eV, or equivalently, about three times the thermal energy at $\beta_e \sim 1$, and about a few hundred eV or about ten times the thermal energy at at low β_e.

We acknowledge the THEMIS team for the use of data. The initial data access and processing was done using SPEDAS V3.1 (Angelopoulos et al., 2019). We thank Trevor A. Bowen, Marc Pulupa, Vladimir Krasnoselskikh and Lynn B. Wilson III for useful discussions. Y. T. and S. D. B. were supported in part by NASA contract NNN06AA01C.

Chapter 8

Multi-spacecraft Observation of Electron Phase Space Holes

Tong Y., Vasko I. Y., Mozer F. S., Bale S. D., Roth I., Artemyev A. V., Ergun R., Giles B., Lindqvist P., Russell C. T., Strangeway R. and Torbert R. (2018). *Geophys. Rev. Lett.*, 45(21), pp.11,513-11,519.

We present a series of electron holes observed simultaneously on four Magnetospheric Multiscale spacecraft in the plasma sheet boundary layer. The mutli-spacecraft probing shows that the electron holes propagated quasi-parallel to the local magnetic field with velocities of a few thousand km/s with parallel spatial scales of a few kilometers (a few Debye lengths). The simultaneous mutli-spacecraft probing allows analyzing the 3D configuration of the electron holes. We estimate the electric field gradients and charge densities associated with the electrons holes. The electric fields are fit to simple 3D electron hole models to estimate their perpendicular scales and demonstrate that the electron holes were generally not axially-symmetric with respect to the local magnetic field. We emphasize that most of the electron holes had a complicated structure not reproduced by the simple models widely used in single-spacecraft studies.

8.1 Introduction

Electron phase space holes (EHs) are electrostatic solitary waves with a bipolar parallel electric field, whose existence is due to phase space density deficit of electrons trapped by the bipolar electric field (e.g., review by Schamel, 1986). Simulations suggest that EHs are formed in a nonlinear stage of various streaming instabilities and can be stable for thousands of plasma periods (e.g., Omura et al., 1996). They were originally observed in the plasma sheet boundary layer (Matsumoto et al., 1994) and later in reconnecting current sheets (Cattell et al., 2005; Graham et al., 2016), auroral region (Mozer et al., 1997; Ergun et al.,

1998), inner magnetosphere (Mozer et al., 2015; Malaspina et al., 2015), flow braking region (Ergun et al., 2015) and many other regions of the near-Earth space (e.g., Pickett et al., 2004; Pickett et al., 2008). Similar EHs were reproduced in laboratory plasma experiments (e.g., Fox et al., 2008). Numerical simulations and theoretical analyses showed that EHs can efficiently scatter electrons, thereby contributing to anomalous dissipation processes (e.g., Drake et al., 2003; Vasko et al., 2018).

EHs in the auroral region (Ergun et al., 1998; Franz et al., 2000), inner magnetosphere (Vasko et al., 2017; Malaspina et al., 2018) and flow braking region (Ergun et al., 2015) exhibit noticeable perpendicular electric fields with essentially unipolar profiles. The perpendicular electric fields indicate that EHs are intrinsically three-dimensional structures localized in directions perpendicular to the local magnetic field. Single-spacecraft measurements showed that the perpendicular and parallel spatial scales of EHs statistically satisfy the gyrokinetic scaling relation (Franz et al., 2000) : $d_\perp/d_\parallel \sim (1+\omega_p^2/\omega_c^2)^{1/2}$, where ω_p and ω_c are electron plasma and cyclotron frequencies. The laboratory experiments reported EHs with similar perpendicular and parallel spatial scales in the regime $\omega_p \gg \omega_c$, indicating that the gyrokinetic scaling relation may not be universal (Fox et al., 2008).

Most of EH studies have been limited to single-spacecraft crossings through intrinsically three-dimensional structures. In this Letter we present a series of EHs observed simultaneously at four Magnetospheric Multiscale (MMS) spacecraft in the plasma sheet boundary layer. The simultaneous multi-spacecraft probing allows analysis, for the first time, of the 3D configuration of EHs.

8.2 Observations

We consider MMS measurements on September 27, 2016 around 01:19:00 UT. The spacecraft were located in the plasma sheet boundary layer at $\mathbf{r}_{GSM} \sim (-2.6, 9.8, 0.6)\ R_E$ on field lines mapping to the southern auroral zone. The separation between the spacecraft was a few kilometers during the considered time interval. We use measurements of the DC-coupled magnetic field (128 samples/s) provided by Digital and Analogue Fluxgate Magnetometers (Russell et al., 2016), AC-coupled electric field (8192 samples/s) provided by Axial Double Probe (Ergun et al., 2016) and Spin-Plane Double Probe (Lindqvist et al., 2016), electron and ion moments provided by the Fast Plasma Instrument (Pollock et al., 2016). The electric fields are presented in the field-aligned coordinate system (x, y, z) with the z-axis along the local magnetic field, the x-axis in the plane of a dipole magnetic field line and the y-axis generally in the westward direction.

Figure 8.1 provides a global context for the intense electric field fluctuations that we analyze in detail. Panel (a) presents the quasi-static magnetic field $\mathbf{B}$ in the GSM coordinate system measured aboard MMS#4 for a few minutes around 01:19:00 UT and the magnetic field B_L in the lobes computed using the vertical pressure balance, $B_L^2 = B^2 + 8\pi n_e(T_e + T_p)$, where n_e is the electron density, T_e and T_p are electron and ion temperatures (not shown). We use four-spacecraft measurements to compute the current density by the curlometer

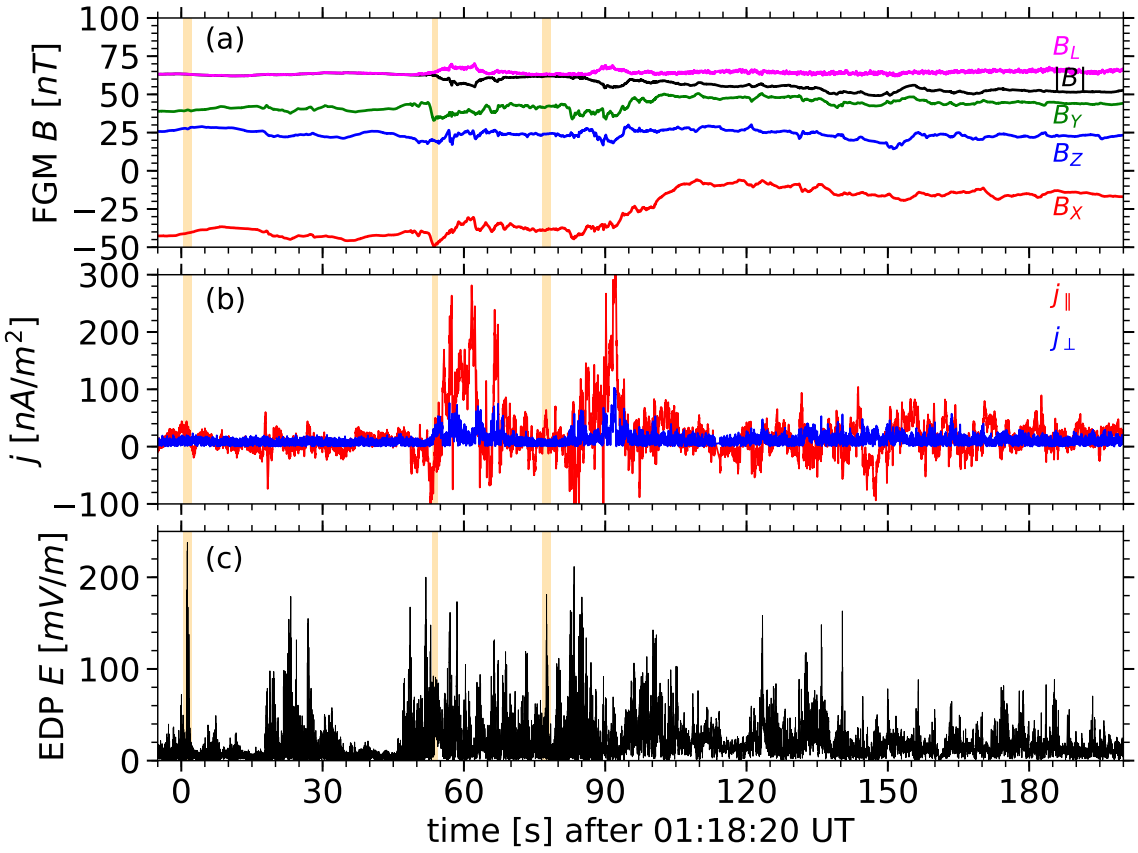

Figure 8.1: MMS observations on September 27, 2016 around 01:19:00 UT: (a) DC-coupled magnetic field measured aboard MMS#4 in the GSM coordinate system; B_L is an estimate of the magnetic field in the lobes; (b) current density parallel to the magnetic field and magnitude of the current density perpendicular to the magnetic field; (c) magnitude of AC-coupled electric field measured by MMS#4. Highlighted intervals indicate observations of electrostatic solitary waves. Two of the intervals are expanded in Figure 8.2 for further analysis.

technique (e.g., Chanteur, 2000) and determine current densities parallel and perpendicular to the magnetic field. Panels (a) and (b) show that the spacecraft were in the plasma sheet boundary layer ($B \sim B_L$) and became closer to the neutral sheet after 01:19:20 and 01:19:50 UT as $|B_x|$ decreased. The decreases of $|B_x|$ were associated with up to 300 nA/m^2 parallel currents, indicating (along with reversed plasma flows that are not shown), temporal variations of the magnetic field configuration in the plasma sheet. Panel (c) presents electric

field fluctuations with amplitudes up to 200 mV/m observed around the intense parallel current regions, although there was no strict correlation between the current density and electric field intensity. Series of electrostatic solitary waves (ESW) were observed during the three highlighted intervals. The rather noisy low-frequency electric field complicates analysis of ESW for the middle interval and, therefore, we focus on the two other highlighted intervals characterized by the following background plasma parameters: $n_e \lesssim 0.1$ cm^{-3}, $T_e \sim 1$ keV and $\omega_p/\omega_c \sim 1-2$.

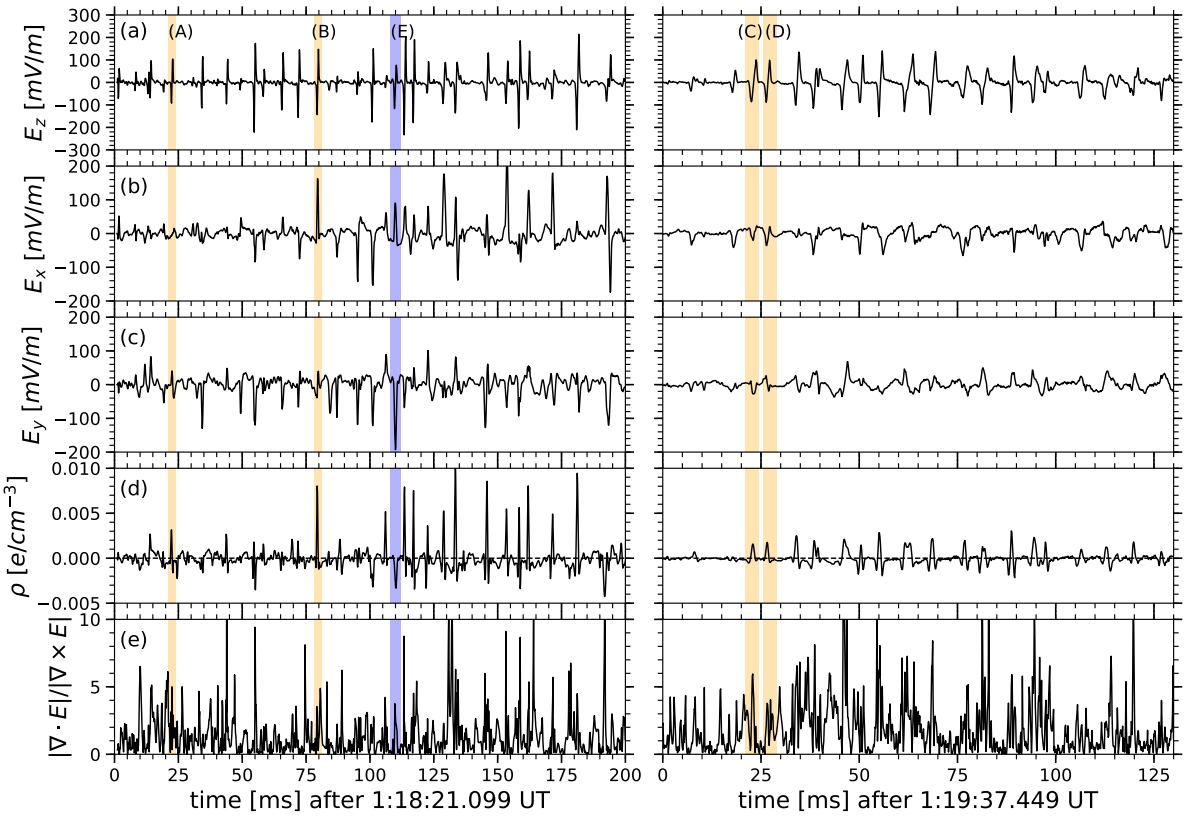

Figure 8.2: The expanded view of a few hundred millisecond intervals highlighted in Figure 8.1: (a) parallel and (b), (c) perpendicular electric fields measured aboard MMS#4; (d) the charge density estimate $\rho = \nabla \cdot \mathbf{E}/4\pi$ computed using electric fields measured at four MMS spacecraft; (e) parameter $|\nabla \cdot \mathbf{E}|/|\nabla \times \mathbf{E}|$ indicating a general consistency with the electrostatic nature of the solitary waves. The highlighted solitary waves (A)–(D) are presented in Figure 8.4.

Figure 8.2 covers a few hundred milliseconds around the two highlighted time intervals. Panels (a)–(c) present the electric fields measured aboard MMS#4 in the field-aligned coordinate system and show that the electric field fluctuations are produced by solitary waves with bipolar parallel and mostly unipolar perpendicular electric fields. The solitary waves

are associated with ~ 10 pT magnetic field fluctuations (not shown), which is why they are ESW ($\delta E \gg c\delta B$). The perpendicular magnetic field fluctuations appear due to the Lorentz transformation (Andersson et al., 2009) and provide the ESW velocity estimates of a few thousand km/s. Remarkably, the ESW are observed simultaneously at four MMS spacecraft (shown below). We use multi-spacecraft interferometry, i.e. analysis of time lags between observations of the same ESW at different spacecraft, to estimate the ESW velocity and direction of propagation. The ESW propagate with velocities 3000-10000 km/s anti-parallel to $\mathbf{B}$ within about ten degrees (see Appendix B for details). It would be difficult to estimate the ESW velocities using the interferometry between voltage-sensitive probes separated by about 120 m antennas because the ESW propagate too fast for the time lags between the probes to be determined reliably.

The electron phase space density measured during the ESW observation (see Appendix B) shows that there is a plateau in the phase space density of electrons with $\sim 180^\circ$ pitch angles in the energy range 100 -1000 eV (that is 6000-20000 km/s in terms of electron velocities). The fact that these energies correspond to the ESW propagation velocities indicates that the ESW are likely produced in a nonlinear stage of an instability driven by a few hundred eV electrons streaming anti-parallel to $\mathbf{B}$. The instability is the bump-on-tail type (e.g., Omura et al., 1996), rather than the Buneman-type, because the latter can only produce slow solitary waves propagating at $(m_e/m_i)^{1/3} j_\parallel/en_e$ (e.g., Drake et al., 2003) which is less than ~ 1500 km/s because, in our event, $j_{||} \lesssim 300$ nA/m^2. Because the ESW propagate anti-parallel to $\mathbf{B}$ and the parallel electric field of each ESW is first negative and then positive according to panel (a), the ESW have positive electrostatic potentials. Along with the plateau in the phase space density and numerous numerical simulations (e.g., Omura et al., 1996), this indicates that the ESW are electron phase space holes. Schematics of EH is presented in Figure 8.3.

Simultaneous probing of EH at four MMS spacecraft allows estimating electric field gradients ∇E_x, ∇E_y and ∇E_z by assuming that they are uniform over the MMS tetrahedron (the method is similar to the curlometer technique, see, e.g., Chanteur, 2000). The combinations of the gradients are used to compute $\nabla \cdot \mathbf{E}$ and $\nabla \times \mathbf{E}$. The charge density estimate $\rho = \nabla \cdot \mathbf{E}/4\pi$ presented in panel (d) shows that the EHs are associated with either tripolar ($-$ + $-$) charge densities expected for one-dimensional EHs or purely negative charge densities (see, e.g., EHs A-E). These charge densities correspond to different crossings of the four MMS spacecraft through the intrinsically three-dimensional EHs. The tripolar/negative charge densities correspond to crossings near/far from the EH center (Figure 8.3). Panel (e) shows that $|\nabla \cdot \mathbf{E}|/|\nabla \times \mathbf{E}| \sim 3 - 5$ within EHs, that is generally consistent with the electrostatic nature of these structures. The analysis by Robert et al. (1998) of the accuracy of the curlometer technique suggests that $|\nabla \cdot \mathbf{E}|/|\nabla \times \mathbf{E}|$ correlates with the accuracy of $\nabla \cdot \mathbf{E}$ estimate only statistically. Therefore, the accuracy of the charge density estimates is difficult to evaluate, but we stress that these estimates are consistent with those derived from the model used to fit the observed electric fields (shown below).

Figure 8.4 presents expanded views of EHs (A)–(D) and demonstrates that EHs are observed simultaneously at four MMS spacecraft. The velocities computed using the multi-

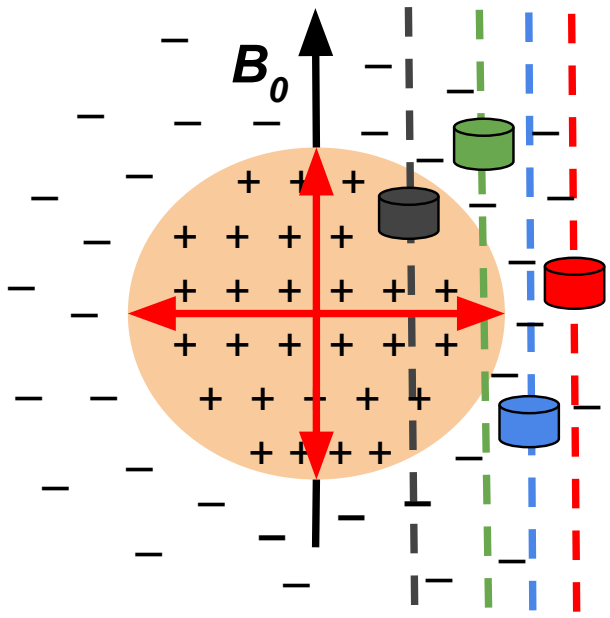

Figure 8.3: The schematic of an EH (red arrows indicate electric fields) and spacecraft crossings (dashed lines) due to quasi-parallel propagation of the EH with respect to the magnetic field. EHs are structures with a positive electrostatic potential localized in directions parallel and perpendicular to a local magnetic field. The plus/minus signs indicate the charge density: The EH is effectively a positively charged cloud screened by a negatively charged cloud.

spacecraft interferometry are indicated in the panels. The typical parallel scale of EH is computed as $d_{\parallel} = v_h \cdot \Delta t/2$, where v_h is the EH velocity and Δt is the time lag between observing minimum and maximum of E_z (Δt is averaged over the four spacecraft). The parallel scales of EHs are indicated in the panels. Because the Debye length and electron thermal gyroradius are both about one kilometer, the parallel scales of EHs are just a few Debye lengths or a few electron thermal gyroradii. The typical electric field amplitudes are about 100 mV/m, so the amplitudes of the maximum electrostatic potential along the spacecraft crossings are a few hundred Volts.

8.3 3D electron hole configuration

The theory does not pose significant restrictions on the 3D distribution of the electrostatic potential of EHs (e.g., Chen et al., 2005). In single-spacecraft studies, EHs are often assumed axially-symmetric with respect to a local magnetic field (e.g., Chen et al., 2005; Vasko et al., 2017). Statistical arguments have been invoked to estimate perpendicular scales of EHs based on numerous single spacecraft crossings (Franz et al., 2000). The mutli-spacecraft

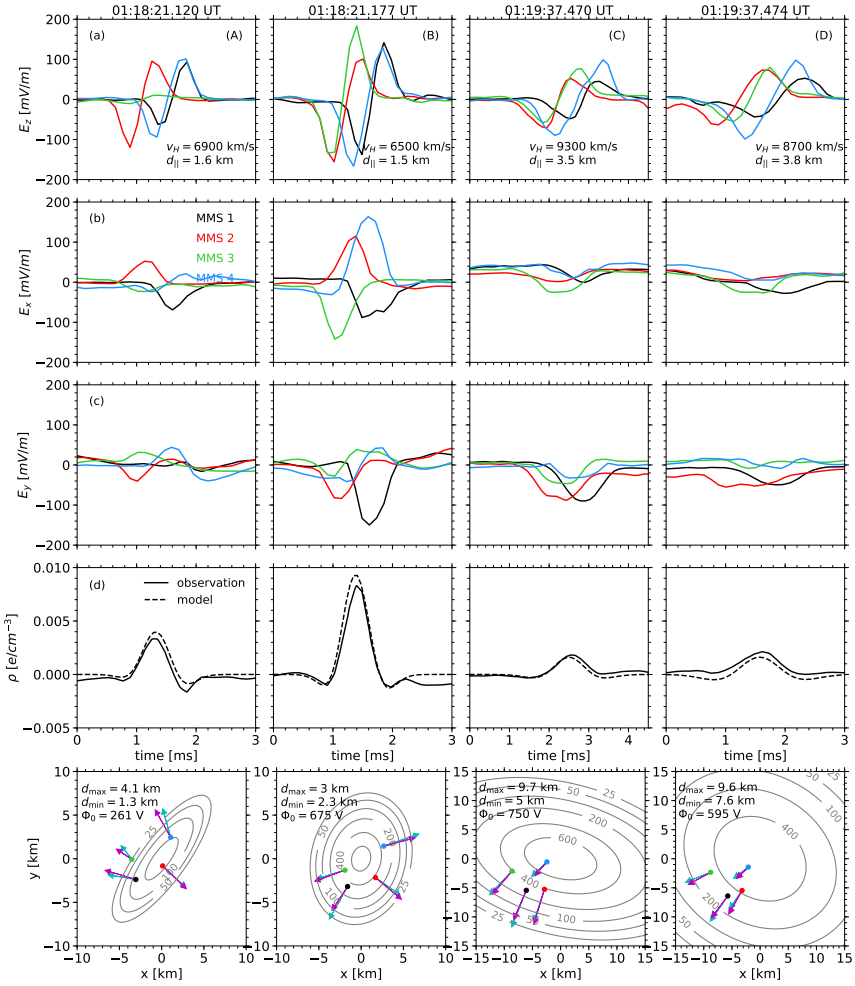

Figure 8.4: The simultaneous measurements of EHs (A)–(D) at four MMS spacecraft: (a)–(c) the electric field in the field-aligned coordinate system ; (d) the charge density computed using the electric field measurements at four spacecraft (solid) and the charge density computed using the electric fields at four spacecraft according to the best-fit model distribution (Eq. (8.1)) (dashed). The bottom panels present observed and best fit model electric fields (cyan and magenta arrows) in the plane perpendicular to the magnetic field, where $E_z = 0$. The equipotential contours (in unit of Volts) of the best fit model are shown and the best fit parameters d_{min}, d_{max} and Φ_0 are indicated. The field-aligned coordinate system is used in the bottom panels.

probing allows analyzing the 3D configuration of EHs.

The axial symmetry of EHs (A)–(D) is tested by fitting the observed electric fields to a model distribution of the electrostatic potential

$$\Phi(\mathbf{r},t) = \Phi_0 \exp\left[-(z-v_h t)^2/2d_\parallel^2\right] \cdot \mathcal{H}(\mathcal{R}), \quad \mathcal{R}^2 = x'^2/d_{min}^2 + y'^2/d_{max}^2, \tag{8.1}$$
$$x' = (x-x_0)\cos\psi + (y-y_0)\sin\psi, \quad y' = -(x-x_0)\sin\psi + (y-y_0)\cos\psi$$

where v_h and $d_\parallel$ have been evaluated, Φ_0 is the peak amplitude of the electrostatic potential, x_0 and y_0 determine the position of the EH center, angle ψ determines the orientation of minor and major axes of the elliptic cross section with respect to the field-aligned coordinates, and d_{min} and d_{max} are perpendicular scales corresponding to the minor and major axes. We have tried to fit the observed electric fields to various models and found the best fit to be provided by the Gaussian model, $\mathcal{H} = \exp(-\mathcal{R}^2/2)$. Origianlly we have used the axially-symmetric model with four parameters (Φ_0, x_0, y_0 and $d_{min} = d_{max}$) and found that the fitting procedure converges to a global minimum. Then we have used the non axially-symmetric model with six free parameters and searched for the best fit parameters around this global minimum (see Appendix C for details).

The bottom panels of Figure 8.4 present the observed and best fit model electric fields in the plane perpendicular to the magnetic field, where $E_z = 0$. The spacecraft positions and electric fields are in the field-aligned coordinate system with the origin in the EH center (x_0, y_0). Also shown are the best fit parameters and equipotential curves of the model electrostatic potential. The electric field of EHs (B) and (D) is satisfactorily fitted to almost axially-symmetric models with d_{min} and d_{max} different by a factor of less than 1.3. On the other hand, EHs (A) and (C) are clearly non axially-symmetric, because d_{min} and d_{max} differ by a factor of two to three. The perpendicular scales are larger than the parallel scales by a factor of two to three in agreement with the gyrokinetic scaling relation $d_\perp/d_\parallel \sim (1+\omega_p^2/\omega_c^2)^{1/2}$, where $\omega_p \sim 1-2\ \omega_c$. The amplitudes of the electrostatic potentials are 250-750 V, which is quite comparable to ~ 1 keV electron temperature.

Panel (d) presents the charge densities computed using the technique similar to the curlometer technique (see the previous section) using the electric fields observed at four spacecraft and those given by the best fit models. These charge densities are in satisfactory agreement. The best fit models also reproduce the observed electric fields (see Appendix C). On the time scales of the fast EHs, ions are essentially immobile, so the estimated charge densities are due to electron density deficiencies. Panel (d) indicates that the electron density deficiencies may reach values of $\sim 10^{-2}$ cm^{-3} which is about ten percent of the background electron density.

We note that the analysis of the 3D configuration of EHs requires simultaneous observations of the electric fields at four spacecraft with sufficiently high signal-to-noise ratio. EHs (A)-(D) are good examples satisfying this criterion. We couldn't fit the electric fields of EH (E) to the 3D model, because the electric fields observed at two of the spacecraft were too small (these spacecraft probed the EH rather far from the EH center). We have also failed to model many other EHs from the two selected intervals. Quite often the EH velocities had

large uncertainties that may have been due to either EH evolution during propagation from one spacecraft to another and/or complicated 3D configurations different from the simple model (8.1).

8.4 Discussion and Conclusions

We have presented observations of EHs observed simultaneously at four MMS spacecraft in a region with intense parallel currents and fast plasma flows in the plasma sheet boundary layer. Similar EHs associated with intense parallel currents in the plasma sheet boundary layer have been recently reported by Le Contel et al., 2017, but the spacecraft separation of about 50 km did not allow simultaneous observations of the EHs at four MMS spacecraft. We have used multi-spacecraft interferometry to estimate the EH velocities and direction of propagation. Previous multi-spacecraft interferometry analyses have been restricted to two spacecraft and required assumptions on the direction of EH propagation (Pickett et al., 2008; Norgren et al., 2015). Using the multi-spacecraft interferometry we have found that the EHs propagate quasi-parallel to the magnetic field with velocities of a few thousands km/s and have parallel spatial scales of a few Debye lengths.

Multi-spacecraft probing has allowed analysis, for the first time, of the 3D configuration of the EHs. We have estimated the charge densities associated with the EHs to find that they are consistent with the three-dimensional EH configuration: EH is effectively a positively charged cloud screened by a negatively charged cloud. For several of the EHs we have demonstrated that their 3D configuration is adequately described by Gaussian distributions with elliptic cross-section and two perpendicular scales that can differ by as much as a factor of three. Thus, in contrast to the assumption often invoked in single-spacecraft studies (e.g., Chen et al., 2005; Vasko et al., 2017; Le Contel et al., 2017), the EHs are generally not axially-symmetric. EHs exhibit $d_{max}/d_{\parallel} \sim 2-3$ and $d_{min}/d_{\parallel} \sim 1-2$ that is in satisfactory agreement with the gyrokinetic scaling relation (Franz et al., 2000) predicting $d_{\perp}/d_{\parallel} \sim 1.4 - 2.2$ for $\omega_p \sim 1$–$2\ \omega_c$.

In this Letter we have presented detailed analysis of the 3D configuration only for several EHs. In many other cases from the selected intervals, analyses have shown that EHs can either evolve in the course of propagation from one spacecraft to another and/or the 3D configuration of the EHs is more complicated than that given by a simple Gaussian model. For these EHs we could not obtain a reliable estimate of velocity and could not infer the 3D configuration. The approach presented in this Letter will be valuable for analyses of properties of EHs observed in space plasmas.

The work was supported by NASA MMS Guest Investigator grant No. 80NSSC18K0155. We thank the MMS teams for the excellent data.

The data are publicly available at https://lasp.colorado.edu/mms/public.

Bibliography

Torbert, R. B. et al. (2018). "Electron-scale dynamics of the diffusion region during symmetric magnetic reconnection in space". In: *Science* 362, pp. 1391–1395. DOI: 10.1126/science.aat2998. arXiv: 1809.06932 [physics.space-ph].

Phan, T. D. et al. (2018). "Electron magnetic reconnection without ion coupling in Earth's turbulent magnetosheath". In: *Nature* 557, pp. 202–206. DOI: 10.1038/s41586-018-0091-5.

Goldreich, P. and S. Sridhar (1995). "Toward a theory of interstellar turbulence. 2: Strong alfvenic turbulence". In: *ApJ* 438, pp. 763–775. DOI: 10.1086/175121.

Boldyrev, S. (2005). "On the Spectrum of Magnetohydrodynamic Turbulence". In: *ApJ* 626, pp. L37–L40. DOI: 10.1086/431649. eprint: astro-ph/0503053.

Horbury, T. S., M. Forman, and S. Oughton (2008). "Anisotropic Scaling of Magnetohydrodynamic Turbulence". In: *Phys. Rev. Lett.* 101.17, 175005, p. 175005. DOI: 10.1103/PhysRevLett.101.175005. arXiv: 0807.3713 [physics.plasm-ph].

Chen, C. H. K. et al. (2010). "Anisotropy of Solar Wind Turbulence between Ion and Electron Scales". In: *Phys. Rev. Lett.* 104.25, 255002, p. 255002. DOI: 10.1103/PhysRevLett.104.255002. arXiv: 1002.2539 [physics.space-ph].

Salem, C. S. et al. (2012a). "Identification of Kinetic Alfvén Wave Turbulence in the Solar Wind". In: *ApJ* 745, L9, p. L9. DOI: 10.1088/2041-8205/745/1/L9.

Chen, C. H. K. et al. (2013a). "Nature of Subproton Scale Turbulence in the Solar Wind". In: *Phys. Rev. Lett.* 110.22, 225002, p. 225002. DOI: 10.1103/PhysRevLett.110.225002. arXiv: 1305.2950 [physics.space-ph].

Štverák, Š. et al. (2009). "Radial evolution of nonthermal electron populations in the low-latitude solar wind: Helios, Cluster, and Ulysses Observations". In: *Journal of Geophysical Research (Space Physics)* 114, A05104, A05104. DOI: 10.1029/2008JA013883.

Hellinger, P. et al. (2006). "Solar wind proton temperature anisotropy: Linear theory and WIND/SWE observations". In: *Geophys. Res. Lett.* 33, L09101, p. L09101. DOI: 10.1029/2006GL025925.

Bale, S. D. et al. (2009). "Magnetic Fluctuation Power Near Proton Temperature Anisotropy Instability Thresholds in the Solar Wind". In: *Physical Review Letters* 103.21, 211101, p. 211101. DOI: 10.1103/PhysRevLett.103.211101. arXiv: 0908.1274 [astro-ph.SR].

Board, Space Studies, National Research Council, et al. (2009). *Severe space weather events: Understanding societal and economic impacts: A workshop report*. National Academies Press.

Fried, B. D. and S. D. Conte (1961). *The Plasma Dispersion Function*.

Barkhausen, H. (1919). "Zwei mit Hilfe der neuen Verstrker entdeckte Erscheinungen." In: *Phys. Ztschr.* 20 S.401.

Storey, LRO (1953). "An investigation of whistling atmospherics". In: *Philosophical Transactions of the Royal Society of London. Series A, Mathematical and Physical Sciences* 246.908, pp. 113–141.

Hollweg, J. V. (1999). "Kinetic Alfvén wave revisited". In: *J. Geophys. Res.* 104, pp. 14811–14820. DOI: 10.1029/1998JA900132.

Leamon, R. J. et al. (1999). "Dissipation range dynamics: Kinetic Alfvén waves and the importance of β_e". In: *J. Geophys. Res.* 104, pp. 22331–22344. DOI: 10.1029/1999JA900158.

Bale, S. D. et al. (2005a). "Measurement of the Electric Fluctuation Spectrum of Magnetohydrodynamic Turbulence". In: *Physical Review Letters* 94.21, 215002, p. 215002. DOI: 10.1103/PhysRevLett.94.215002. eprint: physics/0503103.

Howes, G. G. et al. (2011). "Gyrokinetic Simulations of Solar Wind Turbulence from Ion to Electron Scales". In: *Phys. Rev. Lett.* 107.3, 035004, p. 035004. DOI: 10.1103/PhysRevLett.107.035004. arXiv: 1104.0877 [astro-ph.SR].

Lysak, R. L. and W. Lotko (1996). "On the kinetic dispersion relation for shear Alfvén waves". In: *J. Geophys. Res.* 101, pp. 5085–5094. DOI: 10.1029/95JA03712.

Hasegawa, A. and L. Chen (1976). "Kinetic processes in plasma heating by resonant mode conversion of Alfven wave". In: *Physics of Fluids* 19, pp. 1924–1934. DOI: 10.1063/1.861427.

Hollweg, J. V. (1976). "Collisionless electron heat conduction in the solar wind". In: *J. Geophys. Res.* 81, pp. 1649–1658. DOI: 10.1029/JA081i010p01649.

Bernstein, I. B., J. M. Greene, and M. D. Kruskal (1957). "Exact Nonlinear Plasma Oscillations". In: *Physical Review* 108, pp. 546–550. DOI: 10.1103/PhysRev.108.546.

Oppenheim, M., D. L. Newman, and M. V. Goldman (1999). "Evolution of Electron Phase-Space Holes in a 2D Magnetized Plasma". In: *Physical Review Letters* 83, pp. 2344–2347. DOI: 10.1103/PhysRevLett.83.2344.

Morse, R. L. and C. W. Nielson (1969). "One-, Two-, and Three-Dimensional Numerical Simulation of Two-Beam Plasmas". In: *Physical Review Letters* 23, pp. 1087–1090. DOI: 10.1103/PhysRevLett.23.1087.

Omura, Y., H. Kojima, and H. Matsumoto (1994). "Computer simulation of electrostatic solitary waves: A nonlinear model of broadband electrostatic noise". In: *Geophys. Res. Lett.* 21, pp. 2923–2926. DOI: 10.1029/94GL01605.

Hutchinson, I. H. (2017). "Electron holes in phase space: What they are and why they matter". In: *Physics of Plasmas* 24.5, 055601, p. 055601. DOI: 10.1063/1.4976854.

Wilson III, Lynn B (2017). "Wind 2017 senior review proposal". In: *Executive Summary*.

Carlson, C. W. et al. (1982). "An instrument for rapidly measuring plasma distribution functions with high resolution". In: *Advances in Space Research* 2, pp. 67–70. DOI: 10.1016/0273-1177(82)90151-X.

Lin, R. P. et al. (1995). "A Three-Dimensional Plasma and Energetic Particle Investigation for the Wind Spacecraft". In: *Space Sci. Rev.* 71, pp. 125–153. DOI: 10.1007/BF00751328.

McFadden, J. P. et al. (2008). "THEMIS ESA First Science Results and Performance Issues". In: *Space Sci. Rev.* 141, pp. 477–508. DOI: 10.1007/s11214-008-9433-1.

Pollock, C. et al. (2016). "Fast Plasma Investigation for Magnetospheric Multiscale". In: *Space Sci. Rev.* 199, pp. 331–406. DOI: 10.1007/s11214-016-0245-4.

Verscharen, D. and B. D. G. Chandran (2013). "The Dispersion Relations and Instability Thresholds of Oblique Plasma Modes in the Presence of an Ion Beam". In: *ApJ* 764, 88, p. 88. DOI: 10.1088/0004-637X/764/1/88. arXiv: 1212.5192 [physics.space-ph].

Verscharen, Daniel, Kristopher G. Klein, and Bennett A. Maruca (2019). *The multi-scale nature of the solar wind*. eprint: arXiv:1902.03448.

Pedersen, A., F. Mozer, and G. Gustafsson (1998). "Electric Field Measurements in a Tenuous Plasma with Spherical Double Probes". In: *Washington DC American Geophysical Union Geophysical Monograph Series* 103, p. 1. DOI: 10.1029/GM103p0001.

Gurnett, D. A. (1998). "Principles of Space Plasma Wave Instrument Design". In: *Washington DC American Geophysical Union Geophysical Monograph Series* 103, p. 121. DOI: 10.1029/GM103p0121.

Maynard, N. C. (1998). "Electric Field Measurements in Moderate to High Density Space Plasmas with Passive Double Probes". In: *Washington DC American Geophysical Union Geophysical Monograph Series* 103, p. 13. DOI: 10.1029/GM103p0013.

Paschmann, Götz et al. (1998). "The electron drift technique for measuring electric and magnetic fields". In:

Vaith, H. et al. (2013). "Electron Gyro Time Measurement Technique for Determining Electric and Magnetic Fields". In: *Measurement Techniques in Space Plasmas*. American Geophysical Union (AGU), pp. 47–52. ISBN: 9781118664391. DOI: 10.1002/9781118664391.ch5. eprint: https://agupubs.onlinelibrary.wiley.com/doi/pdf/10.1002/9781118664391.ch5. URL: https://agupubs.onlinelibrary.wiley.com/doi/abs/10.1002/9781118664391.ch5.

Spitzer, L. and R. Härm (1953). "Transport Phenomena in a Completely Ionized Gas". In: *Physical Review* 89, pp. 977–981. DOI: 10.1103/PhysRev.89.977.

Feldman, W. C. et al. (1975a). "Solar wind electrons". In: *J. Geophys. Res.* 80, pp. 4181–4196. DOI: 10.1029/JA080i031p04181.

Scime, E. E. et al. (1994). "Regulation of the solar wind electron heat flux from 1 to 5 AU: ULYSSES observations". In: *J. Geophys. Res.* 99, p. 23. DOI: 10.1029/94JA02068.

Salem, C. et al. (2003). "Electron Properties and Coulomb Collisions in the Solar Wind at 1 AU: Wind Observations". In: *The Astrophysical Journal* 585.2, p. 1147. URL: http://stacks.iop.org/0004-637X/585/i=2/a=1147.

Bale, S. D. et al. (2013). "Electron Heat Conduction in the Solar Wind: Transition from Spitzer-Härm to the Collisionless Limit". In: *ApJ* 769, L22, p. L22. DOI: 10.1088/2041-8205/769/2/L22. arXiv: 1303.0932 [astro-ph.SR].

Cowie, L. L. and C. F. McKee (1977). "The evaporation of spherical clouds in a hot gas. I - Classical and saturated mass loss rates". In: *ApJ* 211, pp. 135–146. DOI: 10.1086/154911.

Bertschinger, E. and A. Meiksin (1986). "The role of heat conduction in the cooling flows of galaxy clusters". In: *ApJ* 306, pp. L1–L5. DOI: 10.1086/184692.

Zakamska, N. L. and R. Narayan (2003). "Models of Galaxy Clusters with Thermal Conduction". In: *ApJ* 582, pp. 162–169. DOI: 10.1086/344641. eprint: astro-ph/0207127.

Wagh, B., P. Sharma, and M. McCourt (2014). "Thermal conduction and multiphase gas in cluster cores". In: *MNRAS* 439, pp. 2822–2827. DOI: 10.1093/mnras/stu138. arXiv: 1310.2242.

Fang, X.-E. et al. (2018). "On the Efficiency of Thermal Conduction in Galaxy Clusters". In: *ApJ* 863, 177, p. 177. DOI: 10.3847/1538-4357/aad1f6. arXiv: 1801.02160 [astro-ph.HE].

Scudder, J. D. (1992). "Why all stars should possess circumstellar temperature inversions". In: *ApJ* 398, pp. 319–349. DOI: 10.1086/171859.

Landi, S. and F. G. E. Pantellini (2001). "On the temperature profile and heat flux in the solar corona: Kinetic simulations". In: *A&A* 372, pp. 686–701. DOI: 10.1051/0004-6361:20010552.

Dorelli, J. C. and J. D. Scudder (2003). "Electron heat flow in the solar corona: Implications of non-Maxwellian velocity distributions, the solar gravitational field, and Coulomb collisions". In: *Journal of Geophysical Research (Space Physics)* 108, 1294, p. 1294. DOI: 10.1029/2002JA009484.

Wang, T. et al. (2015). "Evidence of Thermal Conduction Suppression in a Solar Flaring Loop by Coronal Seismology of Slow-mode Waves". In: *ApJ* 811, L13, p. L13. DOI: 10.1088/2041-8205/811/1/L13. arXiv: 1509.00920 [astro-ph.SR].

Feldman, W. C. et al. (1976). "Evidence for the regulation of solar wind heat flux at 1 AU". In: *J. Geophys. Res.* 81, pp. 5207–5211. DOI: 10.1029/JA081i028p05207.

Rosenbauer, H. et al. (1977). "A survey on initial results of the HELIOS plasma experiment". In: *Journal of Geophysics Zeitschrift Geophysik* 42, pp. 561–580.

Pilipp, W. G. et al. (1987). "Characteristics of electron velocity distribution functions in the solar wind derived from the HELIOS plasma experiment". In: *J. Geophys. Res.* 92, pp. 1075–1092. DOI: 10.1029/JA092iA02p01075.

Maksimovic, M., V. Pierrard, and P. Riley (1997). "Ulysses electron distributions fitted with Kappa functions". In: *Geophys. Res. Lett.* 24, pp. 1151–1154. DOI: 10.1029/97GL00992.

Tong, Y. et al. (2019b). "Whistler Wave Generation by Halo Electrons in the Solar Wind". In: *ApJ* 870, L6, p. L6. DOI: 10.3847/2041-8213/aaf734.

Gary, S. P. and W. C. Feldman (1977). "Solar wind heat flux regulation by the whistler instability". In: *J. Geophys. Res.* 82, pp. 1087–1094. DOI: 10.1029/JA082i007p01087.

Hollweg, J. V. (1978). "Some physical processes in the solar wind". In: *Reviews of Geophysics and Space Physics* 16, pp. 689–720. DOI: 10.1029/RG016i004p00689.

Roberg-Clark, G. T. et al. (2016). "Suppression of Electron Thermal Conduction in the High β Intracluster Medium of Galaxy Clusters". In: *ApJ* 830, L9, p. L9. DOI: 10.3847/2041-8205/830/1/L9. arXiv: 1606.05261 [astro-ph.HE].

Tong, Y. et al. (2018a). "Observed instability constraints on electron heat flux in the solar wind". In: *arXiv e-prints*. arXiv: 1801.07694 [physics.space-ph].

Roberg-Clark, G. T. et al. (2018b). "Wave Generation and Heat Flux Suppression in Astrophysical Plasma Systems". In: *The Astrophysical Journal* 867.2, p. 154. URL: http://stacks.iop.org/0004-637X/867/i=2/a=154.

Komarov, S. et al. (2018). "Self-inhibiting thermal conduction in a high-beta, whistler-unstable plasma". In: *Journal of Plasma Physics* 84.3, p. 905840305. DOI: 10.1017/S0022377818000399.

Vasko, I. Y. et al. (2019a). "Whistler Fan Instability Driven by Strahl Electrons in the Solar Wind". In: *ApJ* 871, L29, p. L29. DOI: 10.3847/2041-8213/ab01bd.

Landi, S., L. Matteini, and F. Pantellini (2012). "On the Competition Between Radial Expansion and Coulomb Collisions in Shaping the Electron Velocity Distribution Function: Kinetic Simulations". In: *ApJ* 760, 143, p. 143. DOI: 10.1088/0004-637X/760/2/143.

— (2014). "Electron Heat Flux in the Solar Wind: Are We Observing the Collisional Limit in the 1 AU Data?" In: *ApJ* 790, L12, p. L12. DOI: 10.1088/2041-8205/790/1/L12.

Horaites, K. et al. (2015). "Self-Similar Theory of Thermal Conduction and Application to the Solar Wind". In: *Physical Review Letters* 114.24, 245003, p. 245003. DOI: 10.1103/PhysRevLett.114.245003.

Pulupa, M. P. et al. (2014a). "Spin-modulated spacecraft floating potential: Observations and effects on electron moments". In: *Journal of Geophysical Research (Space Physics)* 119, pp. 647–657. DOI: 10.1002/2013JA019359.

Bougeret, J.-L. et al. (1995). "Waves: The Radio and Plasma Wave Investigation on the Wind Spacecraft". In: *Space Sci. Rev.* 71, pp. 231–263. DOI: 10.1007/BF00751331.

Meyer-Vernet, Nicole and Claude Perche (1989). "Tool kit for antennae and thermal noise near the plasma frequency". In: *J. Geophys. Res.* 94.A3, pp. 2405–2415.

Artemyev, A. V. et al. (2018). "Dynamics of Intense Currents in the Solar Wind". In: *ApJ* 859, 95, p. 95. DOI: 10.3847/1538-4357/aabe89.

Le Chat, G. et al. (2011). "Large-Scale Variation of Solar Wind Electron Properties from Quasi-Thermal Noise Spectroscopy: Ulysses Measurements". In: *Sol. Phys.* 271, pp. 141–148. DOI: 10.1007/s11207-011-9797-3.

Gary, S. P. et al. (1994). "The whistler heat flux instability: Threshold conditions in the solar wind". In: *J. Geophys. Res.* 99, p. 23. DOI: 10.1029/94JA02067.

Gary, S. P. et al. (1999). "Solar wind electrons: Parametric constraints". In: *J. Geophys. Res.* 104, pp. 19843–19850. DOI: 10.1029/1999JA900244.

Gary, S. P., R. M. Skoug, and W. Daughton (1999a). "Electron heat flux constraints in the solar wind". In: *Physics of Plasmas* 6, pp. 2607–2612. DOI: 10.1063/1.873532.

Gary, S. P. et al. (1975a). "Heat flux instabilities in the solar wind". In: *J. Geophys. Res.* 80, pp. 4197–4203. DOI: 10.1029/JA080i031p04197.

Kennel, C. F. and H. E. Petschek (1966). "Limit on Stably Trapped Particle Fluxes". In: *J. Geophys. Res.* 71, p. 1. DOI: 10.1029/JZ071i001p00001.

Gary, S. P. and H. Li (2000). "Whistler Heat Flux Instability at High Beta". In: *ApJ* 529, pp. 1131–1135. DOI: 10.1086/308294.

Lacombe, C. et al. (2014). "Whistler Mode Waves and the Electron Heat Flux in the Solar Wind: Cluster Observations". In: *ApJ* 796, 5, p. 5. DOI: 10.1088/0004-637X/796/1/5. arXiv: 1410.6187 [astro-ph.SR].

Kuzichev, I. V. et al. (2019 (submitted)). "PIC simulation of heat flux instability". In: *ApJ*, submitted. DOI: submitted.

Tong, Y. et al. (2019a). "Statistical study of whistler waves in the solar wind at 1 AU". In: *ApJ*, Accepted. DOI: Accepted.

Roberg-Clark, G. T. et al. (2018a). "Suppression of Electron Thermal Conduction by Whistler Turbulence in a Sustained Thermal Gradient". In: *Phys. Rev. Lett.* 120 (3), p. 035101. DOI: 10.1103/PhysRevLett.120.035101. URL: https://link.aps.org/doi/10.1103/PhysRevLett.120.035101.

Kajdič, P. et al. (2016a). "Suprathermal Electron Strahl Widths in the Presence of Narrowband Whistler Waves in the Solar Wind". In: *ApJ* 833, 172, p. 172. DOI: 10.3847/1538-4357/833/2/172. arXiv: 1701.04819 [physics.space-ph].

Breneman, A. et al. (2010). "Observations of large-amplitude, narrowband whistlers at stream interaction regions". In: *Journal of Geophysical Research (Space Physics)* 115, A08104, A08104. DOI: 10.1029/2009JA014920.

Wilson, L. B. et al. (2013). "Electromagnetic waves and electron anisotropies downstream of supercritical interplanetary shocks". In: *Journal of Geophysical Research (Space Physics)* 118, pp. 5–16. DOI: 10.1029/2012JA018167. arXiv: 1207.6429 [physics.space-ph].

Lazar, M. et al. (2018). "Temperature anisotropy instabilities stimulated by the interplay of the core and halo electrons in space plasmas". In: *Physics of Plasmas* 25.2, 022902, p. 022902. DOI: 10.1063/1.5016261.

Vocks, C. et al. (2005). "Electron Halo and Strahl Formation in the Solar Wind by Resonant Interaction with Whistler Waves". In: *ApJ* 627, pp. 540–549. DOI: 10.1086/430119.

Horaites, K. et al. (2018). "Stability analysis of core-strahl electron distributions in the solar wind". In: *MNRAS* 480, pp. 1499–1506. DOI: 10.1093/mnras/sty1808. arXiv: 1805.04603 [astro-ph.SR].

Mangeney, Anne et al. (1999). "WIND observations of coherent electrostatic waves in the solar wind". In: *Annales Geophysicae*. Vol. 17. 3. Springer, pp. 307–320.

Landi, S, L Matteini, and F Pantellini (2014). "Electron Heat Flux in the Solar Wind: Are We Observing the Collisional Limit in the 1 AU Data?" In: *The Astrophysical Journal Letters* 790.1, p. L12.

Maksimovic, M. et al. (2005a). "Radial evolution of the electron distribution functions in the fast solar wind between 0.3 and 1.5 AU". In: *Journal of Geophysical Research (Space Physics)* 110, A09104, A09104. DOI: 10.1029/2005JA011119.

Tu, C.-Y. and E. Marsch (1995). "MHD structures, waves and turbulence in the solar wind: Observations and theories". In: *Space Sci. Rev.* 73, pp. 1–210. DOI: 10.1007/BF00748891.

Bale, S. D. et al. (2005b). "Measurement of the Electric Fluctuation Spectrum of Magnetohydrodynamic Turbulence". In: *Phys. Rev. Lett.* 94.21, 215002, p. 215002. DOI: 10.1103/PhysRevLett.94.215002. eprint: physics/0503103.

Bruno, R. and V. Carbone (2013a). "The Solar Wind as a Turbulence Laboratory". In: *Living Reviews in Solar Physics* 10, p. 2. DOI: 10.12942/lrsp-2013-2.

Alexandrova, O. et al. (2013). "Solar Wind Turbulence and the Role of Ion Instabilities". In: *Space Sci. Rev.* 178, pp. 101–139. DOI: 10.1007/s11214-013-0004-8. arXiv: 1306.5336 [astro-ph.SR].

Belcher, J. W. and L. Davis Jr. (1971). "Large-amplitude Alfvén waves in the interplanetary medium, 2". In: *J. Geophys. Res.* 76, p. 3534. DOI: 10.1029/JA076i016p03534.

Schekochihin, A. A. et al. (2009). "Astrophysical Gyrokinetics: Kinetic and Fluid Turbulent Cascades in Magnetized Weakly Collisional Plasmas". In: *ApJS* 182, pp. 310–377. DOI: 10.1088/0067-0049/182/1/310. arXiv: 0704.0044.

Sahraoui, F. et al. (2010). "Three Dimensional Anisotropic k Spectra of Turbulence at Subproton Scales in the Solar Wind". In: *Phys. Rev. Lett.* 105.13, 131101, p. 131101. DOI: 10.1103/PhysRevLett.105.131101.

Boldyrev, S. and J. C. Perez (2012). "Spectrum of Kinetic-Alfvén Turbulence". In: *ApJ* 758, L44, p. L44. DOI: 10.1088/2041-8205/758/2/L44. arXiv: 1204.5809 [astro-ph.SR].

Howes, G. G., K. G. Klein, and J. M. TenBarge (2014). "The Quasilinear Premise for the Modeling of Plasma Turbulence". In: *ArXiv e-prints*. arXiv: 1404.2913 [astro-ph.SR].

Quataert, E. (1998). "Particle Heating by Alfvénic Turbulence in Hot Accretion Flows". In: *ApJ* 500, pp. 978–991. DOI: 10.1086/305770. eprint: astro-ph/9710127.

Cranmer, S. R. and A. A. van Ballegooijen (2003). "Alfvénic Turbulence in the Extended Solar Corona: Kinetic Effects and Proton Heating". In: *ApJ* 594, pp. 573–591. DOI: 10.1086/376777. eprint: astro-ph/0305134.

Kasper, J. C. et al. (2013). "Sensitive Test for Ion-Cyclotron Resonant Heating in the Solar Wind". In: *Phys. Rev. Lett.* 110.9, 091102, p. 091102. DOI: 10.1103/PhysRevLett.110.091102.

Chandran, B. D. G. et al. (2013). "Stochastic Heating, Differential Flow, and the Alpha-to-proton Temperature Ratio in the Solar Wind". In: *ApJ* 776.1, p. 45. URL: http://stacks.iop.org/0004-637X/776/i=1/a=45.

Feldman, W. C. et al. (1975b). "Solar wind electrons". In: *J. Geophys. Res.* 80, pp. 4181–4196. DOI: 10.1029/JA080i031p04181.

Maksimovic, M. et al. (2005b). "Radial evolution of the electron distribution functions in the fast solar wind between 0.3 and 1.5 AU". In: *J. Geophys. Res.* 110, A09104, p. 9104. DOI: 10.1029/2005JA011119.

Pulupa, M. P. et al. (2014b). "Spin-modulated spacecraft floating potential: Observations and effects on electron moments". In: *J. Geophys. Res.* 119, pp. 647–657. DOI: 10.1002/2013JA019359.

Swanson, D. G. (1989). *Plasma waves*. Academic Press.

Stix, T. H. (1992). *Waves in plasmas*. American Institute of Physics.

Gary, S. P. et al. (1975b). "Heat flux instabilities in the solar wind". In: *J. Geophys. Res.* 80, pp. 4197–4203. DOI: 10.1029/JA080i031p04197.

Gary, S. P. et al. (1998). "Proton resonant firehose instability: Temperature anisotropy and fluctuating field constraints". In: *J. Geophys. Res.* 103, pp. 14567–14574. DOI: 10.1029/98JA01174.

Gary, S. P., R. M. Skoug, and W. Daughton (1999b). "Electron heat flux constraints in the solar wind". In: *Physics of Plasmas* 6, pp. 2607–2612. DOI: 10.1063/1.873532.

Marsch, E. (2006). "Kinetic Physics of the Solar Corona and Solar Wind". In: *Living Reviews in Solar Physics* 3, p. 1. DOI: 10.12942/lrsp-2006-1.

Gary, S. P., J. A. Newbury, and B. E. Goldstein (1998). "Lower bound for electron core beta in the solar wind". In: *J. Geophys. Res.* 103, pp. 14559–14566. DOI: 10.1029/98JA01172.

Pistinner, S. L. and D. Eichler (1998). "Self-inhibiting heat flux". In: *MNRAS* 301, pp. 49–58. DOI: 10.1046/j.1365-8711.1998.01770.x. eprint: astro-ph/9807025.

Tong, Y. et al. (2018b). "Observed instability constraints on electron heat flux in the solar wind". In: *ArXiv e-prints*. arXiv: 1801.07694 [physics.space-ph].

Stansby, D. et al. (2016). "Experimental Determination of Whistler Wave Dispersion Relation in the Solar Wind". In: *ApJ* 829, L16, p. L16. DOI: 10.3847/2041-8205/829/1/L16. arXiv: 1609.03039 [physics.space-ph].

Lengyel-Frey, D. et al. (1996). "Ulysses observations of whistler waves at interplanetary shocks and in the solar wind". In: *J. Geophys. Res.* 101, pp. 27555–27564. DOI: 10.1029/96JA00548.

Lin, N. et al. (1998). "Very low frequency waves in the heliosphere: Ulysses observations". In: *J. Geophys. Res.* 103, pp. 12023–12036. DOI: 10.1029/98JA00764.

Angelopoulos, V. (2011). "The ARTEMIS Mission". In: *Space Sci. Rev.* 165, pp. 3–25. DOI: 10.1007/s11214-010-9687-2.

Auster, H. U. et al. (2008). "The THEMIS Fluxgate Magnetometer". In: *Space Sci. Rev.* 141, pp. 235–264. DOI: 10.1007/s11214-008-9365-9.

Le Contel, O. et al. (2008). "First Results of the THEMIS Search Coil Magnetometers". In: *Space Sci. Rev.* 141, pp. 509–534. DOI: 10.1007/s11214-008-9371-y.

Bonnell, J. W. et al. (2008). "The Electric Field Instrument (EFI) for THEMIS". In: *Space Sci. Rev.* 141, pp. 303–341. DOI: 10.1007/s11214-008-9469-2.

Santolik, O., M. Parrot, and F. Lefeuvre (2003). "Singular value decomposition methods for wave propagation analysis". In: *Radio Science* 38, 1010, p. 1010. DOI: 10.1029/2000RS002523.

Tong, Y. et al. (2015). "Effects of Electron Drifts on the Collisionless Damping of Kinetic Alfvén Waves in the Solar Wind". In: *ApJ* 804, L36, p. L36. DOI: 10.1088/2041-8205/804/2/L36. arXiv: 1505.02328 [astro-ph.SR].

Sagdeev, R. Z. and V. D. Shafranov (1960). "On the Instability of a Plasma with an Anisotropic Distribution of Velocities in a Magnetic Field ". In: *Soviet JETP* 39, pp. 181–184.

Vasko, I. Y. et al. (2019b). "Whistler Fan Instability Driven by Strahl Electrons in the Solar Wind". In: *ApJ* 871, L29, p. L29. DOI: 10.3847/2041-8213/ab01bd.

Hammond, C. M. et al. (1996). "Variation of electron-strahl width in the high-speed solar wind: ULYSSES observations." In: *A&A* 316, pp. 350–354.

Graham, G. A. et al. (2017). "The evolution of solar wind strahl with heliospheric distance". In: *Journal of Geophysical Research (Space Physics)* 122, pp. 3858–3874. DOI: 10.1002/2016JA023656.

Shevchenko, V. I. and V. L. Galinsky (2010). "Stability of the strahl electron distribution function and its dynamics". In: *Nonlinear Processes in Geophysics* 17, pp. 593–597. DOI: 10.5194/npg-17-593-2010.

Vocks, C. (2012). "Kinetic Models for Whistler Wave Scattering of Electrons in the Solar Corona and Wind". In: *Space Sci. Rev.* 172, pp. 303–314. DOI: 10.1007/s11214-011-9749-0.

Kajdič, P. et al. (2016b). "Suprathermal Electron Strahl Widths in the Presence of Narrowband Whistler Waves in the Solar Wind". In: *ApJ* 833, 172, p. 172. DOI: 10.3847/1538-4357/833/2/172. arXiv: 1701.04819 [physics.space-ph].

Bruno, R. and V. Carbone (2013b). "The Solar Wind as a Turbulence Laboratory". In: *Living Reviews in Solar Physics* 10, 2, p. 2. DOI: 10.12942/lrsp-2013-2.

Beinroth, H. J. and F. M. Neubauer (1981). "Properties of whistler mode waves between 0.3 and 1.0 AU from HELIOS observations". In: *J. Geophys. Res.* 86, pp. 7755–7760. DOI: 10.1029/JA086iA09p07755.

Coroniti, F. V. et al. (1982). "Whistler mode turbulence in the disturbed solar wind". In: *J. Geophys. Res.* 87, pp. 6029–6044. DOI: 10.1029/JA087iA08p06029.

Salem, C. S. et al. (2012b). "Identification of Kinetic Alfvén Wave Turbulence in the Solar Wind". In: *ApJ* 745, L9, p. L9. DOI: 10.1088/2041-8205/745/1/L9.

Chen, C. H. K. et al. (2013b). "Nature of Subproton Scale Turbulence in the Solar Wind". In: *Physical Review Letters* 110.22, 225002, p. 225002. DOI: 10.1103/PhysRevLett.110.225002. arXiv: 1305.2950 [physics.space-ph].

Lacombe, C., O. Alexandrova, and L. Matteini (2017). "Anisotropies of the Magnetic Field Fluctuations at Kinetic Scales in the Solar Wind: Cluster Observations". In: *ApJ* 848, 45, p. 45. DOI: 10.3847/1538-4357/aa8c06. arXiv: 1710.02341 [physics.space-ph].

Gary, S. P. (2015). "Short-wavelength plasma turbulence and temperature anisotropy instabilities: recent computational progress". In: *Philos Trans A Math Phys Eng Sci.* 373, 2041. DOI: 10.1098/rsta.2014.0149.

Narita, Y. et al. (2016). "On Electron-scale Whistler Turbulence in the Solar Wind". In: *ApJ* 827, L8, p. L8. DOI: 10.3847/2041-8205/827/1/L8.

Kellogg, P. J., K. Goetz, and S. J. Monson (2018). "3D Electric Waveforms of Solar Wind Turbulence". In: *ApJ* 853, 14, p. 14. DOI: 10.3847/1538-4357/aa93df.

Tong, Y. et al. (2019c). "Whistler Wave Generation by Halo Electrons in the Solar Wind". In: *ApJ* 870, L6, p. L6. DOI: 10.3847/2041-8213/aaf734.

Hoppe, M. and C. T. Russell (1980). "Whistler mode wave packets in the earth's foreshock region". In: *Nature* 287, pp. 417–420. DOI: 10.1038/287417a0.

Zhang, Y., H. Matsumoto, and H. Kojima (1998). "Bursts of whistler mode waves in the upstream of the bow shock: Geotail observations". In: *J. Geophys. Res.* 103, pp. 20529–20540. DOI: 10.1029/98JA01371.

Roux, A. et al. (2008). "The Search Coil Magnetometer for THEMIS". In: *Space Sci. Rev.* 141, pp. 265–275. DOI: 10.1007/s11214-008-9455-8.

Angelopoulos, V. et al. (2019). "The Space Physics Environment Data Analysis System (SPEDAS)". In: *Space Sci. Rev.* 215, 9, p. 9. DOI: 10.1007/s11214-018-0576-4.

Gary, S. P., O. Chang, and J. Wang (2012). "Forward Cascade of Whistler Turbulence: Three-dimensional Particle-in-cell Simulations". In: *ApJ* 755, 142, p. 142. DOI: 10.1088/0004-637X/755/2/142.

Štverák, Š. et al. (2008). "Electron temperature anisotropy constraints in the solar wind". In: *Journal of Geophysical Research (Space Physics)* 113, A03103, A03103. DOI: 10.1029/2007JA012733.

Artemyev, A. V., V. Angelopoulos, and J. M. McTiernan (2018). "Near-Earth Solar Wind: Plasma Characteristics From ARTEMIS Measurements". In: *Journal of Geophysical Research (Space Physics)* 123, pp. 9955–9962. DOI: 10.1029/2018JA025904.

Stix, T. H. (1962). *The Theory of Plasma Waves*.

Newbury, J. A. et al. (1998). "Electron temperature in the ambient solar wind: Typical properties and a lower bound at 1 AU". In: *J. Geophys. Res.* 103, pp. 9553–9566. DOI: 10.1029/98JA00067.

Pierrard, V. et al. (2016). "The Electron Temperature and Anisotropy in the Solar Wind. Comparison of the Core and Halo Populations". In: *Sol. Phys.* 291, pp. 2165–2179. DOI: 10.1007/s11207-016-0961-7. arXiv: 1603.08392 [physics.space-ph].

Shklyar, D. and H. Matsumoto (2009). "Oblique Whistler-Mode Waves in the Inhomogeneous Magnetospheric Plasma: Resonant Interactions with Energetic Charged Particles". In: *Surveys in Geophysics* 30, pp. 55–104. DOI: 10.1007/s10712-009-9061-7.

Sagdeev, R. Z. and A. A. Galeev (1969). *Nonlinear Plasma Theory*.

Karpman, V. I. (1974). "Nonlinear Effects in the ELF Waves Propagating along the Magnetic Field in the Magnetosphere". In: *Space Sci. Rev.* 16, pp. 361–388. DOI: 10.1007/BF00171564.

Voshchepynets, A. et al. (2015). "Probabilistic Model of Beam-Plasma Interaction in Randomly Inhomogeneous Plasma". In: *ApJ* 807, 38, p. 38. DOI: 10.1088/0004-637X/807/1/38.

Schamel, H. (1986). "Electron holes, ion holes and double layers. Electrostatic phase space structures in theory and experiment". In: *Phys. Rep.* 140, pp. 161–191. DOI: 10.1016/0370-1573(86)90043-8.

Omura, Y. et al. (1996). "Electron beam instabilities as generation mechanism of electrostatic solitary waves in the magnetotail". In: *J. Geophys. Res.* 101, pp. 2685–2698. DOI: 10.1029/95JA03145.

Matsumoto, H. et al. (1994). "Electrotastic Solitary Waves (ESW) in the magnetotail: BEN wave forms observed by GEOTAIL". In: *Geophys. Res. Lett.* 21, pp. 2915–2918. DOI: 10.1029/94GL01284.

Cattell, C. et al. (2005). "Cluster observations of electron holes in association with magnetotail reconnection and comparison to simulations". In: *Journal of Geophysical Research (Space Physics)* 110, A01211, p. 1211. DOI: 10.1029/2004JA010519.

Graham, D. B. et al. (2016). "Electrostatic solitary waves and electrostatic waves at the magnetopause". In: *Journal of Geophysical Research (Space Physics)* 121, pp. 3069–3092. DOI: 10.1002/2015JA021527.

Mozer, F. S. et al. (1997). "New Features of Time Domain Electric-Field Structures in the Auroral Acceleration Region". In: *Physical Review Letters* 79, pp. 1281–1284. DOI: 10.1103/PhysRevLett.79.1281.

Ergun, R. E. et al. (1998). "Debye-Scale Plasma Structures Associated with Magnetic-Field-Aligned Electric Fields". In: *Physical Review Letters* 81, pp. 826–829. DOI: 10.1103/PhysRevLett.81.826.

Mozer, F. S. et al. (2015). "Time domain structures: What and where they are, what they do, and how they are made". In: *Geophys. Res. Lett.* 42, pp. 3627–3638. DOI: 10.1002/2015GL063946.

Malaspina, D. M. et al. (2015). "Electric field structures and waves at plasma boundaries in the inner magnetosphere". In: *Journal of Geophysical Research (Space Physics)* 120, pp. 4246–4263. DOI: 10.1002/2015JA021137.

Ergun, R. E. et al. (2015). "Large-amplitude electric fields associated with bursty bulk flow braking in the Earth's plasma sheet". In: *Journal of Geophysical Research (Space Physics)* 120, pp. 1832–1844. DOI: 10.1002/2014JA020165.

Pickett, J. et al. (2004). "Isolated electrostatic structures observed throughout the Cluster orbit: relationship to magnetic field strength". In: *Annales Geophysicae* 22, pp. 2515–2523. DOI: 10.5194/angeo-22-2515-2004. eprint: physics/0402122.

Pickett, J. S. et al. (2008). "Furthering our understanding of electrostatic solitary waves through Cluster multispacecraft observations and theory". In: *Advances in Space Research* 41, pp. 1666–1676. DOI: 10.1016/j.asr.2007.05.064.

Fox, W. et al. (2008). "Laboratory Observation of Electron Phase-Space Holes during Magnetic Reconnection". In: *Physical Review Letters* 101.25, 255003, p. 255003. DOI: 10.1103/PhysRevLett.101.255003.

Drake, J. F. et al. (2003). "Formation of Electron Holes and Particle Energization During Magnetic Reconnection". In: *Science* 299, pp. 873–877. DOI: 10.1126/science.1080333.

Vasko, I. Y. et al. (2018). "Scattering by the broadband electrostatic turbulence in the space plasma". In: *Physics of Plasmas* 25.7, p. 072903. DOI: 10.1063/1.5039687. eprint: https://doi.org/10.1063/1.5039687. URL: https://doi.org/10.1063/1.5039687.

Franz, J. R. et al. (2000). "On the perpendicular scale of electron phase-space holes". In: *Geophys. Res. Lett.* 27, pp. 169–172. DOI: 10.1029/1999GL010733.

Vasko, I. Y. et al. (2017). "Electron holes in the outer radiation belt: Characteristics and their role in electron energization". In: *Journal of Geophysical Research (Space Physics)* 122, pp. 120–135. DOI: 10.1002/2016JA023083.

Malaspina, David M. et al. (2018). "A Census of Plasma Waves and Structures Associated With an Injection Front in the Inner Magnetosphere". In: *Journal of Geophysical*

Research: Space Physics 123.4, pp. 2566–2587. DOI: 10.1002/2017JA025005. eprint: https://agupubs.onlinelibrary.wiley.com/doi/pdf/10.1002/2017JA025005. URL: https://agupubs.onlinelibrary.wiley.com/doi/abs/10.1002/2017JA025005.

Russell, C. T. et al. (2016). "The Magnetospheric Multiscale Magnetometers". In: *Space Sci. Rev.* 199, pp. 189–256. DOI: 10.1007/s11214-014-0057-3.

Ergun, R. E. et al. (2016). "The Axial Double Probe and Fields Signal Processing for the MMS Mission". In: *Space Sci. Rev.* 199, pp. 167–188. DOI: 10.1007/s11214-014-0115-x.

Lindqvist, P.-A. et al. (2016). "The Spin-Plane Double Probe Electric Field Instrument for MMS". In: *Space Sci. Rev.* 199, pp. 137–165. DOI: 10.1007/s11214-014-0116-9.

Chanteur, G. (2000). "Accuracy of Fields Gradient Estimations by Cluster: Explanation of its Dependency upon Elongation and Planarity of the Tetrahedron". In: *Cluster-II Workshop Multiscale / Multipoint Plasma Measurements*. Ed. by R. A. Harris. Vol. 449. ESA Special Publication, p. 265.

Andersson, L. et al. (2009). "New Features of Electron Phase Space Holes Observed by the THEMIS Mission". In: *Physical Review Letters* 102.22, 225004, p. 225004. DOI: 10.1103/PhysRevLett.102.225004.

Robert, P. et al. (1998). "Accuracy of Current Density Determination". In: *ISSI Scientific Reports Series* 1, pp. 395–418.

Chen, L.-J. et al. (2005). "On the width-amplitude inequality of electron phase space holes". In: *Journal of Geophysical Research (Space Physics)* 110, A09211, A09211. DOI: 10.1029/2005JA011087.

Le Contel, O. et al. (2017). "Lower Hybrid Drift Waves and Electromagnetic Electron Space-Phase Holes Associated With Dipolarization Fronts and Field-Aligned Currents Observed by the Magnetospheric Multiscale Mission During a Substorm". In: *Journal of Geophysical Research (Space Physics)* 122.A11, p. 12. DOI: 10.1002/2017JA024550.

Norgren, C. et al. (2015). "Slow electron phase space holes: Magnetotail observations". In: *Geophys. Res. Lett.* 42, pp. 1654–1661. DOI: 10.1002/2015GL063218.

Appendix A

ARTEMIS Intervals

day	probe	start	end
2011-01-01	b	06:00	16:59
2011-01-02	b	18:00	23:59
2011-01-03	b	18:00	23:59
2011-01-04	b	18:00	23:59
2011-01-08	b	02:00	12:59
2011-01-09	b	18:00	23:59
2011-01-10	b	18:02	23:59
2011-01-11	b	18:02	23:59
2011-01-12	b	18:02	23:59
2011-01-13	b	18:02	23:59
2011-01-26	b	18:02	23:59
2011-01-27	b	18:02	23:59
2011-01-28	b	18:02	23:59
2011-01-29	b	20:11	23:59
2011-01-30	b	00:00	07:59
2011-01-31	b	18:00	23:59
2011-02-01	c	18:02	23:59
2011-02-02	c	18:02	23:59
2011-02-04	c	06:00	16:56
2011-02-05	c	18:00	23:59
2011-02-06	c	18:02	23:59
2011-02-08	c	08:08	19:59
2011-02-09	c	18:02	23:59
2011-02-10	c	18:02	23:59
2011-02-11	c	18:02	23:59
2011-02-12	c	18:00	23:59
2011-02-23	c	18:02	23:59

2011-02-24	c	18:02	23:59
2011-02-25	c	18:02	23:59
2011-02-26	c	18:16	23:59
2011-02-27	c	13:00	23:59
2011-02-28	c	00:00	11:59
2011-03-01	c	18:02	23:59
2011-03-05	c	18:02	23:59
2011-03-06	c	20:02	23:59
2011-03-07	c	00:00	05:59
2011-03-08	c	12:02	23:59
2011-03-09	c	00:00	16:59
2011-03-10	c	06:01	23:59
2011-03-11	c	00:00	05:59
2011-03-13	c	18:02	23:59
2011-03-14	c	18:02	23:59
2011-03-23	c	18:02	23:59
2011-03-24	c	18:01	23:59
2011-03-25	c	18:02	23:59
2011-03-26	c	18:02	23:59
2011-03-27	c	18:02	23:59
2011-03-28	c	10:00	23:59
2011-03-29	c	00:00	09:47
2011-03-31	b	00:01	17:59
2011-04-01	b	18:02	23:59
2011-04-02	b	18:02	23:59
2011-04-03	b	18:02	23:59
2011-04-04	b	06:31	11:59
2011-04-08	c	10:01	23:59
2011-04-09	c	00:00	08:59
2011-04-10	b	18:02	23:59
2011-04-11	b	18:02	23:59
2011-04-12	b	18:02	23:59
2011-04-23	b	18:02	23:59
2011-04-24	b	18:02	23:59
2011-04-26	c	20:00	23:59
2011-04-27	c	00:00	14:59
2011-07-01	c	16:02	23:52
2011-07-02	c	16:02	23:52
2011-07-03	c	16:02	23:53
2011-07-04	c	10:00	20:59
2011-07-05	c	16:02	23:52
2011-07-06	c	16:02	23:47

2011-07-07	c	16:02	23:52
2011-07-08	c	16:02	23:52
2011-07-09	c	16:02	23:52
2011-07-21	c	08:11	11:59
2011-07-23	c	00:00	03:59
2011-07-24	c	16:00	19:50
2011-07-25	b	18:11	20:59
2011-07-26	c	08:00	10:59
2011-07-29	c	13:23	16:46
2011-07-30	b	09:00	11:59
2011-07-31	c	04:00	06:59
2011-08-03	c	04:06	06:59
2011-08-04	c	16:42	19:59
2011-08-07	c	18:00	20:59
2011-08-21	c	03:11	06:36
2011-08-23	c	17:03	19:59
2011-08-24	b	17:00	19:57
2011-08-25	c	00:00	02:47
2011-08-26	c	06:00	08:59
2011-08-27	c	12:00	14:59
2011-08-28	c	18:23	20:59
2011-08-29	b	04:00	08:46
2011-08-30	c	01:14	03:59
2011-09-01	c	15:14	17:59
2011-09-02	b	17:15	19:59
2011-09-04	b	14:00	17:59
2011-09-05	c	11:00	14:59
2011-09-06	b	11:00	14:48
2011-09-19	b	02:00	05:59
2011-09-20	c	16:00	19:59
2011-09-21	c	20:00	23:59
2011-09-22	c	18:00	23:59
2011-09-23	c	00:00	03:59
2011-09-24	c	14:00	17:59
2011-09-25	c	06:00	09:59
2011-09-27	c	13:02	18:59
2011-09-28	c	02:00	03:59
2011-09-29	c	18:00	23:59
2011-09-30	c	00:00	05:55
2011-10-02	c	04:10	09:59
2011-10-03	c	04:00	11:59
2011-10-04	c	11:10	22:59

2011-10-18	c	07:12	12:59
2011-10-24	b	10:00	14:59
2011-10-25	b	10:00	20:59
2011-10-27	b	00:00	04:59
2011-10-29	b	15:00	19:38
2011-10-30	b	21:00	23:59
2011-11-16	b	12:00	15:59
2011-11-18	c	11:00	14:57
2011-11-19	c	15:00	18:47
2011-11-20	c	19:00	21:59
2011-11-21	b	14:00	16:59
2011-11-23	c	03:00	06:33
2012-01-13	b	09:17	12:52
2012-01-14	c	00:00	02:59
2012-01-15	c	02:01	06:59
2012-01-16	c	06:20	11:57
2012-01-17	c	10:05	13:59
2012-01-20	c	20:16	23:59
2012-01-21	b	00:00	03:46
2012-01-22	b	06:00	09:32
2012-01-23	c	03:00	06:42
2012-01-24	b	17:15	20:54
2012-01-24	c	06:00	09:59
2012-01-25	b	09:00	13:52
2012-01-26	c	11:12	17:32
2012-01-27	b	15:00	20:59
2012-01-28	c	19:06	22:56
2012-01-29	b	18:00	21:21
2012-01-30	c	00:00	04:59
2012-01-31	b	00:00	05:59
2012-02-12	b	11:00	17:59
2012-02-13	b	15:11	22:59
2012-02-14	b	19:00	21:59
2012-02-15	c	02:00	05:59
2012-02-16	b	06:00	11:59
2012-02-17	b	01:00	04:48
2012-02-18	c	04:00	07:09
2012-02-19	c	07:00	09:54
2012-02-20	b	03:20	12:59
2012-02-22	b	12:15	21:44
2012-02-23	b	16:25	23:59
2012-02-24	b	20:00	23:39

2012-02-25	b	02:00	04:59
2012-02-26	c	00:00	01:59
2012-02-27	c	01:35	04:59
2012-02-28	b	04:10	07:59
2012-02-29	b	08:00	11:18
2012-03-01	b	02:00	06:59
2012-03-02	b	08:21	15:59
2012-03-13	b	12:41	21:40
2012-03-14	b	18:00	23:59
2012-03-15	b	00:00	01:59
2012-03-16	b	00:00	07:37
2012-03-17	b	04:00	11:59
2012-03-18	c	07:09	10:31
2012-03-19	b	10:09	13:56
2012-03-20	b	13:18	16:59
2012-03-21	b	02:22	06:59
2012-03-22	b	08:00	12:48
2012-03-23	b	14:00	17:59
2012-03-24	b	19:00	23:59
2012-03-25	c	02:00	04:54
2012-03-30	c	17:43	20:59
2012-03-31	c	22:00	23:59
2012-04-01	b	07:00	11:34
2012-04-12	b	11:16	15:59
2012-04-13	b	19:00	22:50
2012-04-14	c	12:30	16:44
2012-04-15	b	00:09	04:59
2012-04-16	b	06:18	11:07
2012-04-17	b	12:18	16:59
2012-04-18	b	18:00	22:50
2012-04-20	b	00:00	03:59
2012-04-25	b	00:00	02:59
2012-04-26	b	04:18	08:59
2012-04-28	b	20:11	20:59
2012-04-29	c	09:03	11:59
2012-04-30	c	12:12	15:59
2012-05-11	b	01:19	04:59
2012-05-12	b	07:10	11:59
2012-05-13	b	13:01	16:59
2012-05-14	b	19:00	23:36
2012-05-16	b	00:18	04:59
2012-05-17	b	06:00	09:59

2012-05-18	b	11:00	14:59
2012-05-19	b	16:00	19:59
2012-05-26	c	18:00	22:46
2012-05-27	b	01:00	04:59
2012-05-28	b	07:00	11:28
2012-05-29	b	12:18	16:59
2012-05-30	c	04:38	08:59
2012-06-11	c	19:00	22:59
2012-06-12	b	01:00	04:59
2012-06-13	b	07:00	10:56
2012-06-14	b	12:00	15:59
2012-06-15	b	16:23	20:59
2012-06-16	c	06:53	06:59
2012-06-18	b	02:35	07:51
2012-06-28	b	00:00	03:59
2012-07-15	b	03:13	08:31
2012-07-16	b	08:23	13:41
2012-07-17	b	14:00	18:59
2012-07-18	b	19:13	23:59
2012-07-19	c	10:03	14:59
2012-07-20	c	14:00	19:06
2012-07-21	c	17:25	21:59
2012-07-23	b	21:06	22:59
2012-08-08	b	17:35	22:56
2012-08-09	c	00:00	04:44
2012-08-16	b	01:00	05:59
2012-08-17	b	06:42	11:48
2012-08-18	b	12:30	17:35
2012-08-19	b	18:22	22:59
2012-08-20	c	10:12	14:59
2012-08-21	b	00:10	04:59
2012-08-22	b	05:40	10:50
2012-08-23	b	11:00	20:59
2012-08-25	c	00:00	03:59
2012-09-07	b	04:31	18:56
2012-09-09	b	15:00	19:58
2012-09-10	c	00:00	03:59
2012-09-11	c	03:00	07:44
2012-09-17	b	01:00	04:59
2012-09-18	c	00:00	03:59
2012-09-19	b	12:00	15:59
2012-09-23	c	16:00	20:59

2012-10-05	c	02:00	06:49
2012-10-06	c	05:10	09:59
2012-10-07	c	09:00	13:47
2012-10-08	c	12:20	16:59
2012-10-09	c	16:00	20:54
2012-10-10	c	19:31	23:59
2012-10-11	b	12:42	16:59
2012-10-12	b	19:51	22:59
2012-10-13	c	02:21	07:27
2012-10-21	b	09:00	13:58
2012-10-22	b	14:01	18:59
2012-10-23	b	19:30	23:59
2012-11-07	c	05:00	09:54
2012-11-08	b	19:00	22:59
2012-11-09	c	12:00	16:37
2012-11-10	c	15:00	19:48
2012-11-11	b	09:41	10:59
2012-11-12	b	12:00	16:59
2012-11-13	b	18:00	21:59
2012-11-14	c	00:00	05:30
2012-11-21	b	01:00	06:59
2012-12-04	b	12:00	19:59
2012-12-05	b	18:00	23:59
2012-12-06	c	14:45	16:59
2012-12-07	c	18:00	20:51
2012-12-08	c	19:28	22:59
2012-12-09	b	12:00	16:58
2012-12-10	b	17:35	21:59
2012-12-16	b	16:00	20:59
2012-12-18	c	14:00	14:59
2012-12-19	c	16:05	19:38
2012-12-20	b	06:00	11:57
2012-12-21	b	10:16	15:59
2012-12-22	b	14:15	20:59
2013-02-02	b	03:00	07:57
2013-02-03	b	06:10	10:59
2013-02-04	b	10:00	13:59
2013-02-05	b	13:00	17:57
2013-02-06	b	16:00	20:55
2013-02-07	b	19:00	23:58
2013-02-08	c	10:00	14:59
2013-02-09	c	13:00	16:59

2013-02-10	c	15:00	19:57
2013-02-11	b	03:15	07:59
2013-02-12	b	06:10	10:59
2013-02-14	c	00:00	03:38
2013-02-15	c	01:12	05:59
2013-02-16	c	03:00	06:59
2013-02-17	c	04:00	08:50
2013-03-03	b	11:15	15:59
2013-03-04	b	15:00	19:43
2013-03-13	b	15:00	18:59
2013-03-14	b	18:00	22:52
2013-03-15	c	09:10	13:59
2013-03-16	c	11:00	14:59
2013-03-17	c	12:00	16:57
2013-03-18	c	13:10	17:59
2013-03-19	b	07:00	11:58
2013-04-03	c	07:10	11:59
2013-04-14	b	08:15	11:48
2013-04-15	b	12:00	14:59
2013-04-16	b	15:05	18:38
2013-04-17	c	00:00	03:37
2013-05-01	c	15:00	19:59
2013-05-02	c	13:00	20:59
2013-05-08	c	06:00	08:59
2013-05-09	b	09:00	11:59
2013-05-10	b	12:00	14:59
2013-05-11	b	15:05	18:42
2013-05-12	b	19:00	21:59
2013-05-13	c	04:21	08:59
2013-05-14	c	05:30	10:38
2013-06-03	b	12:25	15:59
2013-06-04	b	16:00	19:28
2013-06-05	b	19:16	22:53
2013-06-08	b	01:28	04:58
2013-06-09	b	04:26	07:39
2013-06-17	b	03:00	06:28
2013-06-18	b	06:26	15:15
2013-06-30	b	18:00	21:31
2013-07-01	c	12:00	16:48
2013-07-02	c	13:10	17:59
2013-07-03	c	15:00	19:37
2013-07-04	c	16:00	20:47

2013-07-05	c	17:00	21:59
2013-07-15	b	11:15	16:53
2013-07-16	b	16:00	19:59
2013-07-17	b	18:10	22:59
2013-07-28	c	19:00	22:59
2013-08-01	b	11:03	15:59
2013-08-02	b	14:21	18:59
2013-08-03	b	18:00	21:59
2013-08-14	c	14:00	18:46
2013-08-15	c	15:00	19:59
2013-08-29	b	16:00	20:59
2013-08-30	b	19:10	23:59
2013-08-31	c	08:05	12:59
2013-09-01	c	09:05	13:59
2013-09-02	c	10:00	14:59
2013-09-03	c	11:00	15:59
2013-09-13	b	08:00	12:58
2013-10-08	b	02:23	06:59
2013-10-09	c	17:00	20:59
2013-10-10	c	17:35	20:59
2013-10-31	b	20:00	23:59
2013-11-02	c	14:16	17:53
2013-11-03	c	13:15	18:39
2013-11-04	c	14:25	19:29
2013-11-05	c	15:20	19:59
2013-11-28	c	17:12	21:59
2013-11-29	c	18:27	22:59
2013-11-30	b	03:11	07:59
2013-12-01	b	06:00	10:59
2013-12-02	b	09:00	13:59
2013-12-03	b	12:20	17:26
2013-12-04	b	16:00	20:49
2013-12-29	b	11:00	15:58
2013-12-30	b	14:00	18:59
2013-12-31	b	17:10	21:59

Appendix B

Electron Hole Velocity Measurement

The observed electron holes often exhibit perpendicular electric fields with unipolar profiles that can be suggested to be due to quasi-parallel propagation to the magnetic field lines. Figure B.1 presents an exemplary electron hole. In this appendix, we propose a new approach to measure the electron hole velocity with simultaneous electric field measurements at four spacecraft. We also compare the result with existing velocity measurement or diagnostic techniques.

B.1 Two spacecraft interferometry

Propagation parallel to the magnetic field is often assumed in literature to estimate the velocity of solitary waves. The standard procedure is to choose a pair of spacecraft, determine their separation δz along the magnetic field direction, and determine the time lag δt by cross-correlating bipolar electric fields E_z measured at the two spacecraft. Then the propagation velocity associated with the electron hole is estimated as $v_h = \delta z/\delta t$. Figure B.2 demonstrates the cross-correlation analysis of E_z measured by MMS 1 and MMS 2. Before calculating cross-correlation, we have upsampled the time series by a factor of 10. This allows resolving time lags at ~ 0.01 ms accuracy (alternatively, one could interpolate the cross-correlation function, but the resultant time lags agree within 0.01 ms). We perform the cross-correlation analysis for all pairs of spacecraft and obtain Table B.1 that shows time lags and phase speed estimates. MMS 2 and MMS 3 are located very close to each other, so that δt is comparable to the accuracy of ~ 0.01 ms. However, other spacecraft pairs also provide rather different velocity estimates ranging from 3.6 to 15.5 km/ms, which may imply oblique propagation of the electron hole.

B.2 Four spacecraft interferometry

To resolve the inconsistency between speed measured by each pair of spacecraft, we propose a four-spacecraft-interferometry approach to measure electron hole velocity. The key of this

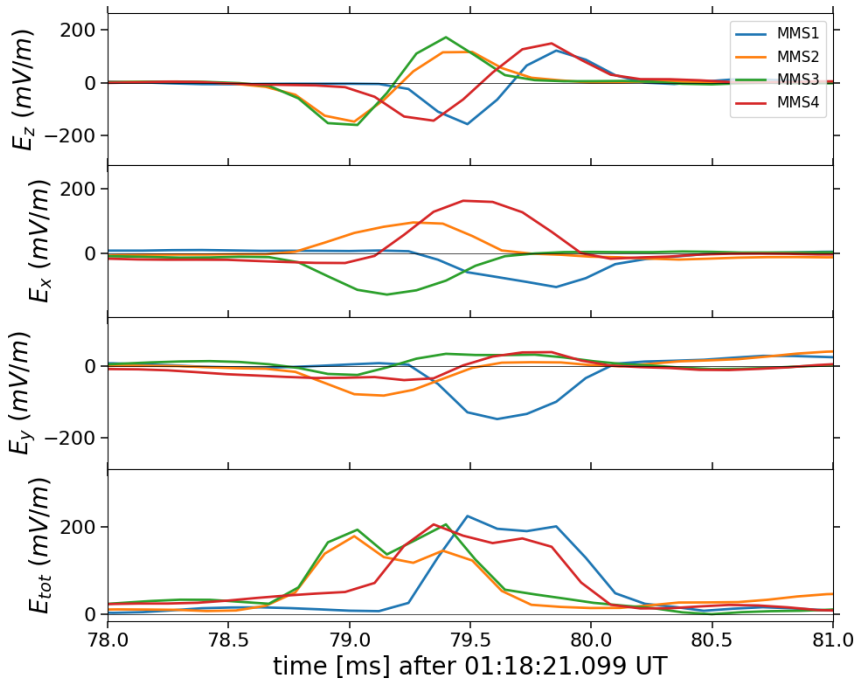

Figure B.1: An exemplary electron hole observed at four MMS spacecrafts. The three upper panels present electric fields in the field-aligned coordinate system, while the bottom panels presents the electric field magnitude.

probe paris	δt [ms]	δz [km]	$\delta z/\delta t$ [km/ms]
(1, 2)	0.46	3.82	-8.25
(1, 3)	0.49	3.21	- 6.59
(1, 4)	0.12	1.89	-15.49
(2, 3)	0.02	-0.61	24.97
(2, 4)	-0.33	-1.93	-5.87
(3, 4)	-0.37	-1.33	-3.62

Table B.1: Estimated time lag and parallel velocity by applying cross-correlation analysis to every pair of MMS spacecraft.

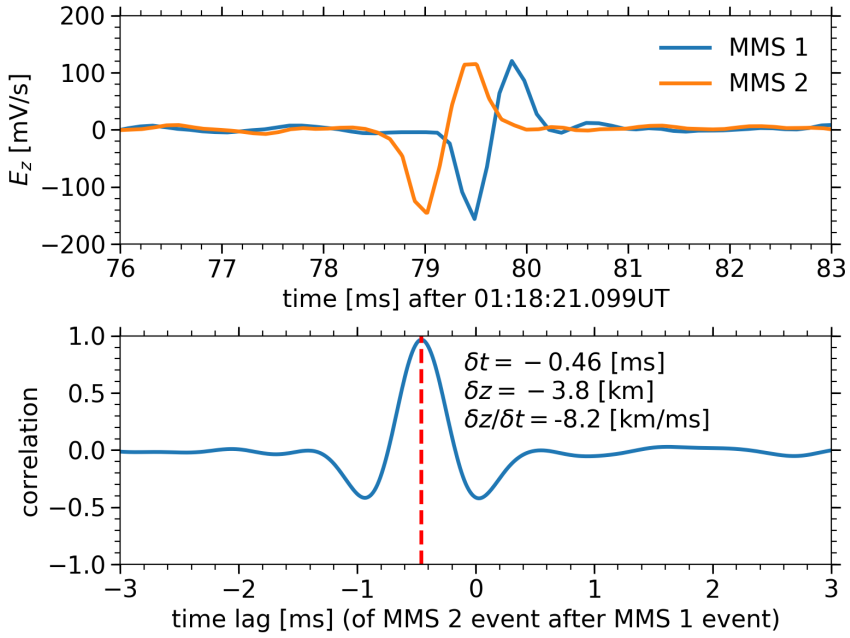

Figure B.2: Cross correlating electric fields at two spacecraft by assuming strictly parallel propagation to the magnetic field: (upper) waveforms of parallel electric fields measured by MMS 1 and MMS 2; (lower) normalized cross-correlation function versus time lag.

new approach is to relax the assumption of exact parallel propagation.

Lets denote the direction of propagation $\mathbf{k}$ and velocity v_h. Under the assumption that $E_z = 0$ in a plane propagating oblique to the magnetic field we should have

$$\begin{pmatrix} \delta x_{1,2} & \delta y_{1,2} & \delta z_{1,2} \\ \delta x_{1,3} & \delta y_{1,3} & \delta z_{1,3} \\ \delta x_{1,4} & \delta y_{1,4} & \delta z_{1,4} \end{pmatrix} \begin{pmatrix} \hat{k}_x \\ \hat{k}_y \\ \hat{k}_z \end{pmatrix} = v_h \begin{pmatrix} \delta t_{1,2} \\ \delta t_{1,3} \\ \delta t_{1,4} \end{pmatrix} \tag{B.1}$$

where $\delta x_{i,j}$, $\delta y_{i,j}$, $\delta z_{i,j}$ are spatial separations between spacecraft i and j in the field-aligned coordinates, $\delta t_{i,j}$ are time lags between spacecraft i and j. Figure B.3 demonstrates estimate of the time lags by cross-correlating $E_{tot} = |\mathbf{E}|$ that is electric field magnitudes. We use E_{tot} instead of E_z because the former is the quantity invariant to any coordinate transformations. Table B.2 presents $\delta t_{i,j}$ for all spacecraft pairs (c.f. Table B.1).

Solving Eq. (B.1) we find that the electrons hole propagates oblique to the magnetic field at $\theta_{\mathbf{kB}} = \cos^{-1}(\hat{\mathbf{k}} \cdot \hat{\mathbf{B}}) \sim 12^\circ$ with velocity $v_h = -6 \pm 1.4$ km/ms, where the minus indicates propagation opposite to $\mathbf{k}$ and, thus, opposite to $\mathbf{B}$ as well; the accuracy of this estimate (± 1.4 km/ms) is estimated from Table B.3. To verify that velocity estimate based on Eq. (B.1) is reliable, we also estimate electron hole velocity by cross-correlating electric fields $E_k = \mathbf{E} \cdot \mathbf{k}$ between different pair of spacecraft. Table B.3 shows time lags and spatial separations along $\mathbf{k}$ between different spacecraft. The ratio $\delta r_k/\delta t$ gives the velocity along

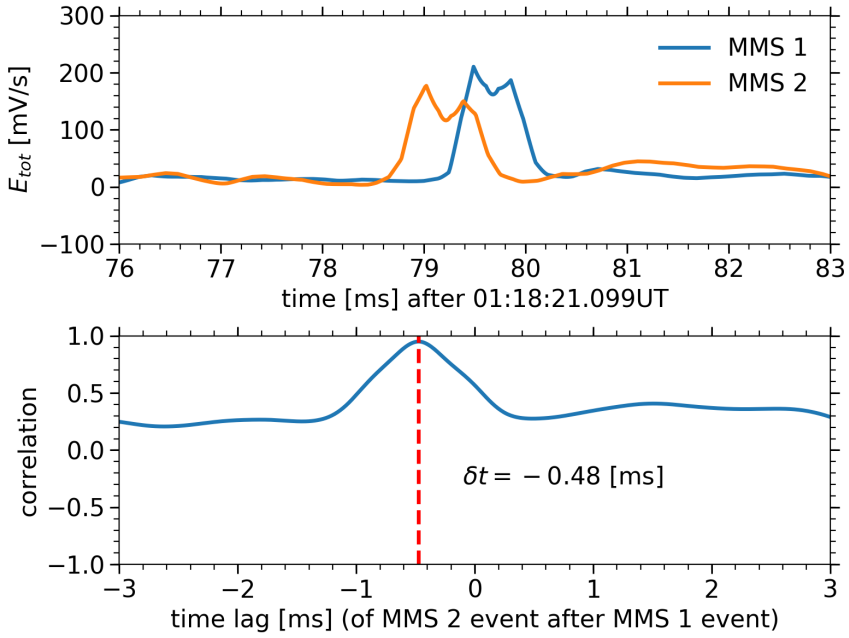

Figure B.3: The analysis of the electron hole velocity that is based in Eq. (B.1) and does not make any assumptions on the electron hole propagation direction: (upper) the electric field magnitudes $E_{tot} = |E|$ measured at MMS 1 and MMS 2; (lower) normalized cross-correlation functions versus time lag.

probe pairs	δt [ms]
(1, 2)	0.48
(1, 3)	0.49
(1, 4)	0.13
(2, 3)	0.01
(2, 4)	-0.34
(3, 4)	-0.36

Table B.2: Time lags between different pairs of spacecraft computed using the electric field magnitudes E_{tot}.

k, and the values are significantly more consistent with each other than those in Table B.1, where exactly parallel propagation is assumed.

B.3 Other diagnostics

To further validate the velocity estimate with our newly proposed approach, we have also attempted to estimate the electron hole velocity using alternative diagnostics. Two classic

probe pairs	δr_k [km]	δt [ms]	$\delta r_k/\delta t$ [km/ms]
(1, 2)	3.19	0.43	7.4
(1, 3)	3.28	0.48	6.8
(1, 4)	0.86	0.09	9.6
(2, 4)	-2.33	-0.35	6.7
(3, 4)	-2.42	-0.4	6.0

Table B.3: Analysis of consistency of the velocity estimate that is based on Eq. (B.1). Table presents time lags between $E_k = \mathbf{E} \cdot \mathbf{k}$ measured at different pairs of spacecraft, spatial separations between the spacecraft along $\mathbf{k}$ and estimates of the velocity along $\mathbf{k}$. More consistent phase speed is obtained compared to Table B.1.

single-spacecraft techniques are the probe-to-probe interferometry and analysis of magnetic field perturbations associated with electrons holes. Measurement of the electron phase space density also provides independent check on our estimation.

Single spacecraft sphere-to-sphere interferometry

Two probes of a dipole antenna would receive electric field signals of electron holes with some time lag if the propagation direction is not perpendicular to the antenna.

Figure B.4 presents voltages V3 and -V4 of two opposing voltage-sensitive spheres (voltages are with respect to the spacecraft) onboard MMS 4 during observations of the ESW presented in Figure B.1. The time lag between signals is too small to be accurately evaluated. With each antenna being 60 m long and the solitary wave velocity of 7000 km/s, the expected time lag between V3 and -V4 is at most $\delta t \sim 120\text{m}/7000\text{km/s} \sim 0.01\text{ms}$. On the other hand, the sampling rate is ~ 0.1ms. We can improve the time lag resolution by upsampling / interpolating the voltages, but the relative error is inevitably large compared to unity. We conclude that the ESW velocity is too large to be evaluated accurately by the single spacecraft sphere-to-sphere interferometry.

Lorentz transformation

According to the Lorentz transformation, a fast ESW propagating with respect to the spacecraft produces observable magnetic field fluctuations

$$\delta B = \gamma \mathbf{v} \times \mathbf{E}/c^2 \tag{B.2}$$

where γ is the relativistic factor $1/\sqrt{1 - v^2/c^2}$. Because of the quasi-parallel propagation of the ESW we expect $\delta B_\perp$ to be correlated with $E_\perp$ and their ratio provides estimate of the ESW velocity (this analysis was described, e.g., by Andersson et al. (2009)).

Figure B.5 presents the same ESW that is presented in Figure B.1. Panels (a) and (b) show the electric field and magnetic field measured by Search Coil Magnetometer (SCM) onboard MMS 1. As we already know the solitary wave propagates at a non-relativistic velocity

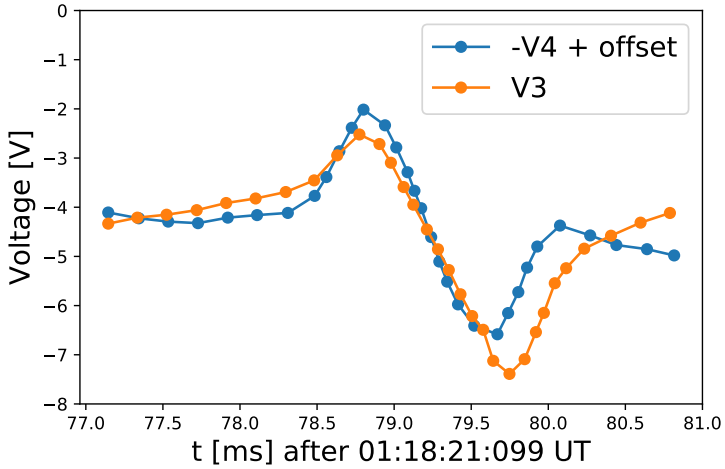

Figure B.4: Voltages V3 and -V4 of two voltage sensitive spheres aboard MMS 4 during observations of the ESW in Figure B.1.

and this results in a low signal-to-noise ratio in $\delta B_\perp$. Nevertheless, panel (c) and (d) show some order of magnitude estimate of the phase speed. Panel (c) shows the theoretical AC magnetic field due to Lorentz transformation of the observed electric field, assuming propagation opposite to the background magnetic field at velocity of $v_h = -10000$ km/s. The amplitude and shape of the theoretical magnetic field agrees reasonably well with observations in panel (b). Panel (d) uses $\delta B_\perp c^2/|E|$ to estimate the phase speed to be $|v_h| \sim 10000$ km/s. These order of magnitude estimates are more or less consistent with 7000 km/s estimated using the multi-spacecraft interferometry.

Electron phase space density measurement

Two trains of electrostatic solitary waves (ESWs) are analyzed in detail in Chapter 8, around 1:18:20 and 1:19:37 UT. Figure B.6 shows the electron pitch angle distribution (PAD) functions before (panel (a)), during (panel (b)) and after (panel (c)) ESW observation. In all panels, the distribution function of electrons with 180° pitch angles has a plateau in the energy range from about 100 eV to about 1 keV. These electrons are streaming anti-parallel to the magnetic field, i.e. parallel to the solitary waves. Using the technique described in Section B.2 above, we have found solitary waves within these time intervals to have velocities in the range 3000 - 10000 km/s.

Coincidentally, the electron distribution function of electrons co-streaming with the solitary waves plateaus in the same velocity range, indicating that the solitary wave are likely produced by an instability driven by a few hundred eV electrons streaming anti-parallel to the magnetic field. Such plateaus are observed throughout the entire event, indicating that electron holes might be generated all the time and probably not at the spacecraft location.

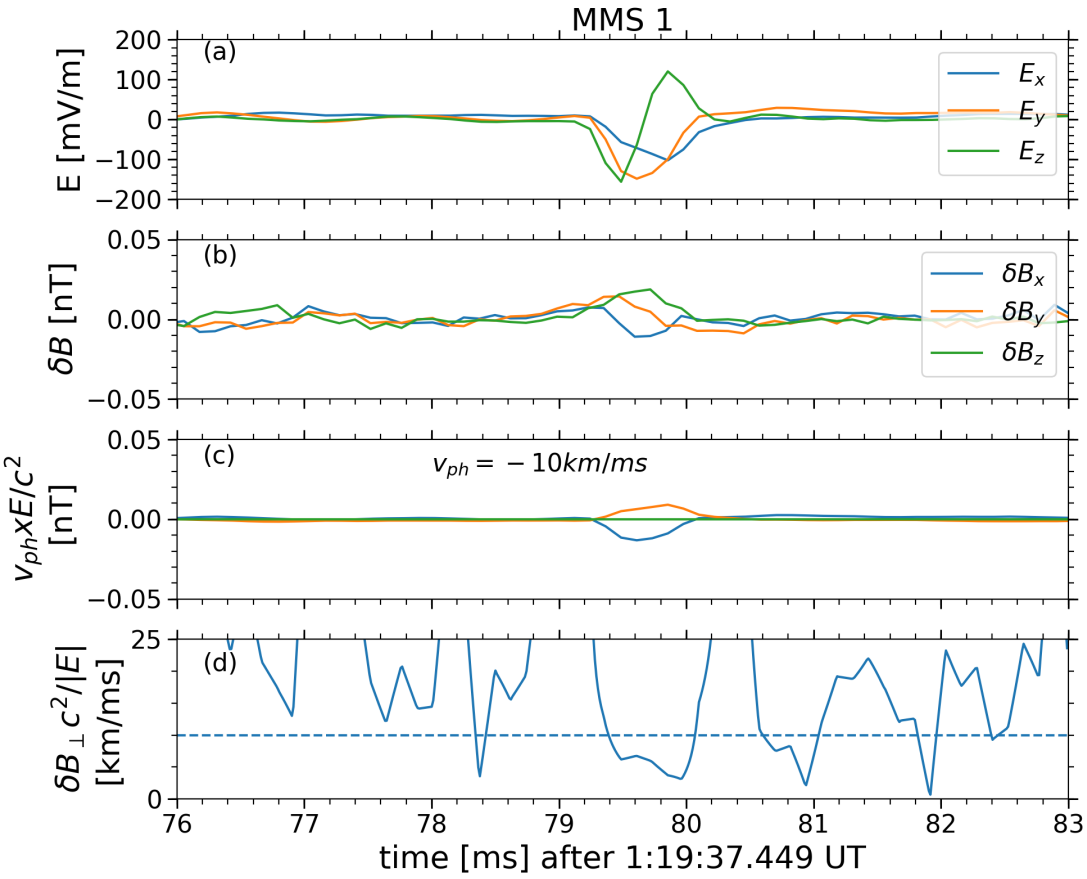

Figure B.5: (a) Electric field in the field-aligned coordinate system (FAC) measured on MMS1. (b) AC magnetic field in FAC measured by the Search Coil Magnetometer (SCM) on MMS1. (c) AC magnetic field due to Lorentz transformation of the electric field in (a) assuming parallel phase speed of $v_h = -10000$ km/s. (d) $\delta B_\perp c^2 2/|E|$.

In other words, the active phenomenon occurs in the plasma sheet and we observed only some of the electron holes that manage to propagate to the spacecraft location.

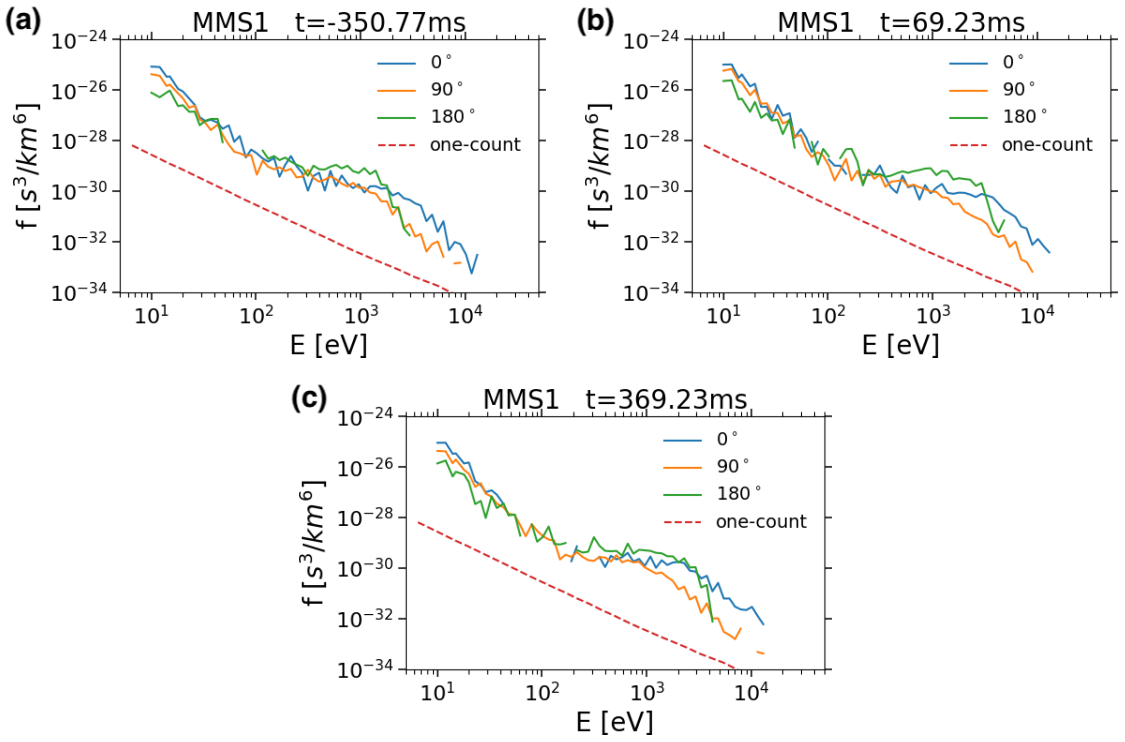

Figure B.6: The electron pitch angle distribution (PAD) function measured around 1:18:20 UT (one-count level is shown for reference). Time t is given with respect to 1:18:20.469 UT. Panel (a) - (c) shows PADs before, during and after ESW passing, which occurred over 1:18:20.470 - 1:18.20.650 UT, and correspond to the first highlighted interval that contains a train of ESWs in Figure 8.2 in Chapter 8.

Appendix C

Fitting Three Dimensional Electron Holes

C.1 Models and optimization procedures

For the observed quasi-parallel propagating electron holes we determine the best-fit parameters of a model by minimizing the following loss function

$$\text{Loss Function} \equiv \sum_{4\ SCs} \sum_{\alpha=x,y,z} \left[\max\left(E_\alpha\right) - \max\left(E_\alpha^M\right)\right]^2 \tag{C.1}$$

where $E_\alpha$and E_α^M are observed and model electric field components in the field-aligned coordinate system, while max indicate their maximum values. This loss function is essentially the sum of squared errors of the maximum electric fields. The optimization procedures using axially-symmetric and not axially-symmetric models involve four and six fitting parameters, respectively. To find the best fit parameters we use the following procedure.

We start with axial-symmetric models with $H(R) = \exp(-R)$, $\exp(-R^2/2)$ and $\cosh^{-1}(R)$ setting the distribution of the electron hole electrostatic potential in the plane perpendicular to the magnetic field (see, Section 3 in Chapter 8). The fitting parameters are Φ_0, $d_\perp$, x_0 and y_0, corresponding to the amplitude of the electrostatic potential, perpendicular scale, and locations of the electron hole center with respect to the MMS spacecrafts. We start with random initial guesses of these four parameters and minimize the loss function by gradient-descent updates to the model parameters. By taking a large number of random initial guesses, we have found what seems to be a global minimum, because the procedure always converges to the same best fit parameters. The upper panels of Figure C.2 show comparison of different axial-symmetric models for the same electron hole around 2016/09/27 1:19:37.474 UT (see Figure C.1). Each panel shows observed maximum electric field (black arrows) and model maximum electric field (red arrows) in the plane perpendicular to the background magnetic field. Black curves represent the equipotential contours. The comparison between observed and best fit model electric fields clearly demonstrate that the observed

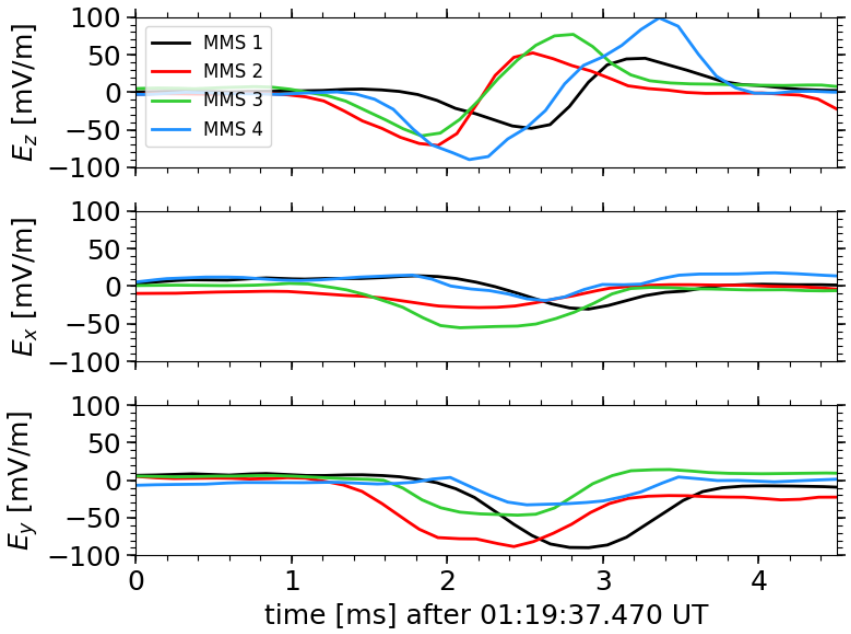

Figure C.1: Electric field of a quasi-parallel propagating electron hole in field-aligned coordinates.

electric fields are more complex than what axial-symmetric models could produce. In particular, perpendicular electric fields of an axial-symmetric model should be radial, while observed electric fields are seldom radial. This inconsistency suggests that more complex models are necessary.

Therefore, we increase the model complexity by allowing not axially-symmetric distributions of the electrostatic potential. The simplest generalization to models of electron holes is to consider elliptic cross-section with two perpendicular scales. Such models have six free parameters: on top of Φ_0, x_0 and y_0 we introduce two perpendicular scales by $d_{\min}$, $d_{\max}$ and a tilt angle ψ characterizing the orientation of the major and the minor axes of the elliptic cross-section with respect to the field-aligned coordinates (x, y). Mathematical expressions of this new model is given in Eq. (8.1).

Again we minimize the loss function (Eq. (C.1)) by gradient descent updates from random initial values. Since the optimization is now done in 6D parameter space, its harder to show that we obtain the globally optimal set of parameters. However, Figure 8.4 and the following section show that the parameters we find are sufficiently good to reproduce the observed electric fields. The lower panels of Figure C.2 show comparison of best fit electric fields versus the observed electric fields using the same format as the upper panels. While all three non-axial-symmetric models better capture electric field observations than axial-symmetric models, the non-axial-symmetric Gaussian model best fit observations among models we have considered.

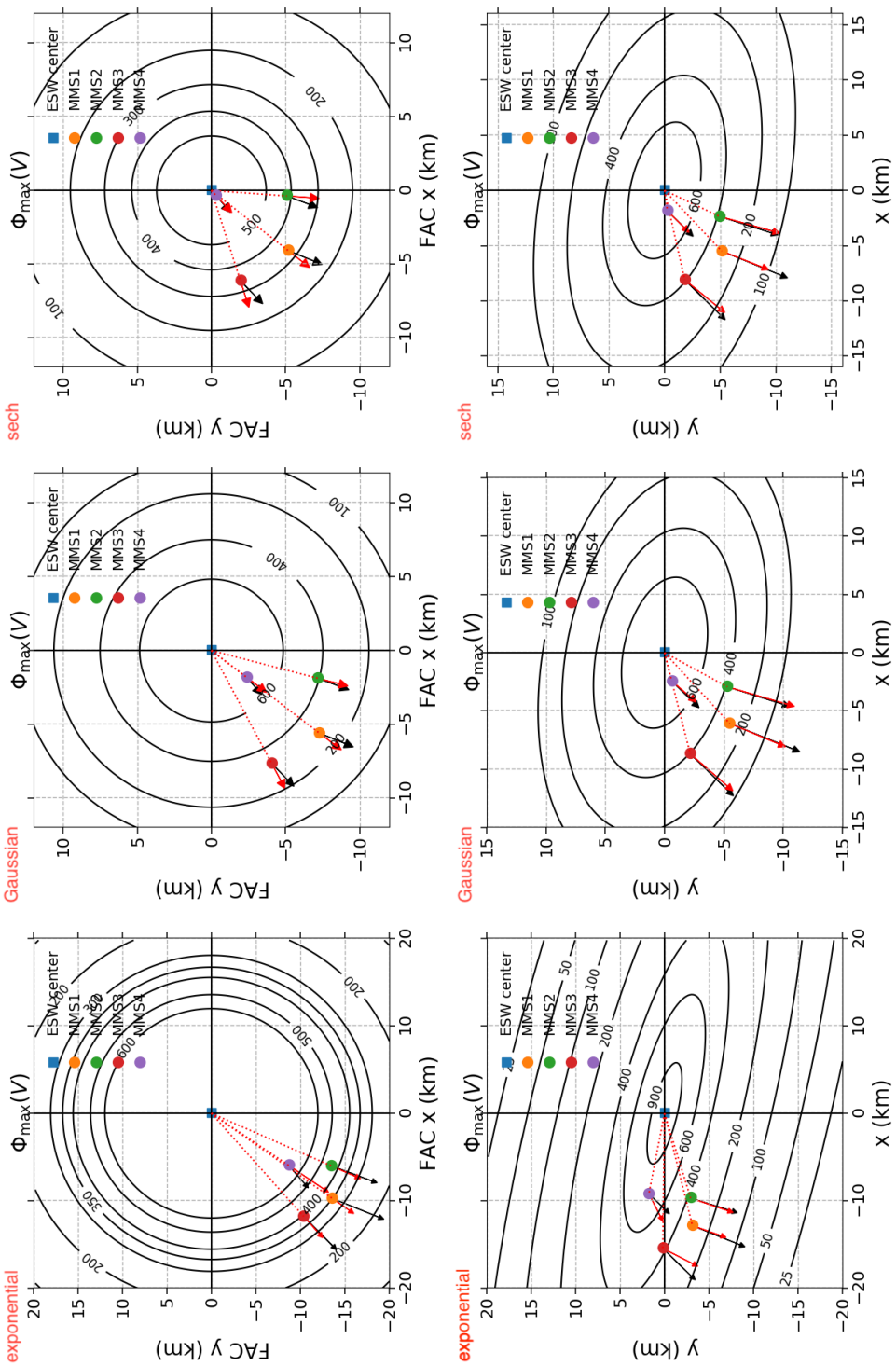

Figure C.2: Comparison of different models for the same electron hole around 2016/09/27 1:19:37.474 UT (see Figure C.1). Each panel show observed maximum electric field (black arrows) and model maximum electric field (red arrows) in the plane perpendicular to the background magnetic field. Black contours represent the equipotential contours. The upper row show three axis-symmetric models. The lower row show three non-axially-symmetric models.

For completeness, we also briefly review the method of gradient descent that we use to find best fit models. Gradient descent, also known as steepest descent, is a first order iterative optimization algorithm to find a local minimum of a function. We take a small step opposite to the gradient of the function at the current point and gradually approach a local minimum. Mathematically, one considers a multivariable and differentiable function $F(\mathbf{x})$. Start with a guess $\mathbf{x}_0$ for a local minimum of F, we consider the sequence $\mathbf{x}_0, \mathbf{x}_1, \mathbf{x}_2, \ldots$ such that

$$\mathbf{x}_{n+1} = \mathbf{x}_n - \gamma_n \nabla F(\mathbf{x}_n),\ n \geq 0 \tag{C.2}$$

where the step size $\gamma_n \in \mathbb{R}_+$ is kept small. It is possible to show that convergence to a local minimum of F is guaranteed with certain assumptions on F. When F is convex, the local minimum is also the global minimum. Gradient descent works in spaces of any number of dimensions.

C.2 Observed $\mathbf{E}(t)$ versus best fit $\mathbf{E}(t)$

Figure C.3 presents the comparison between the electric field measured at the four MMS spacecraft and the electric field of the best fit models for electron holes (A)-(D) labeled in Figure 8.2. Notice that the model parameters are determined to fit only the maximum of the electric field time series. Panels in this figure show that the models could simultaneously well reproduce the measured electric field time series at all four spacecrafts. This demonstrates that the axially-asymmetric Gaussian models are indeed capable of capturing the electric field features of the electron holes.

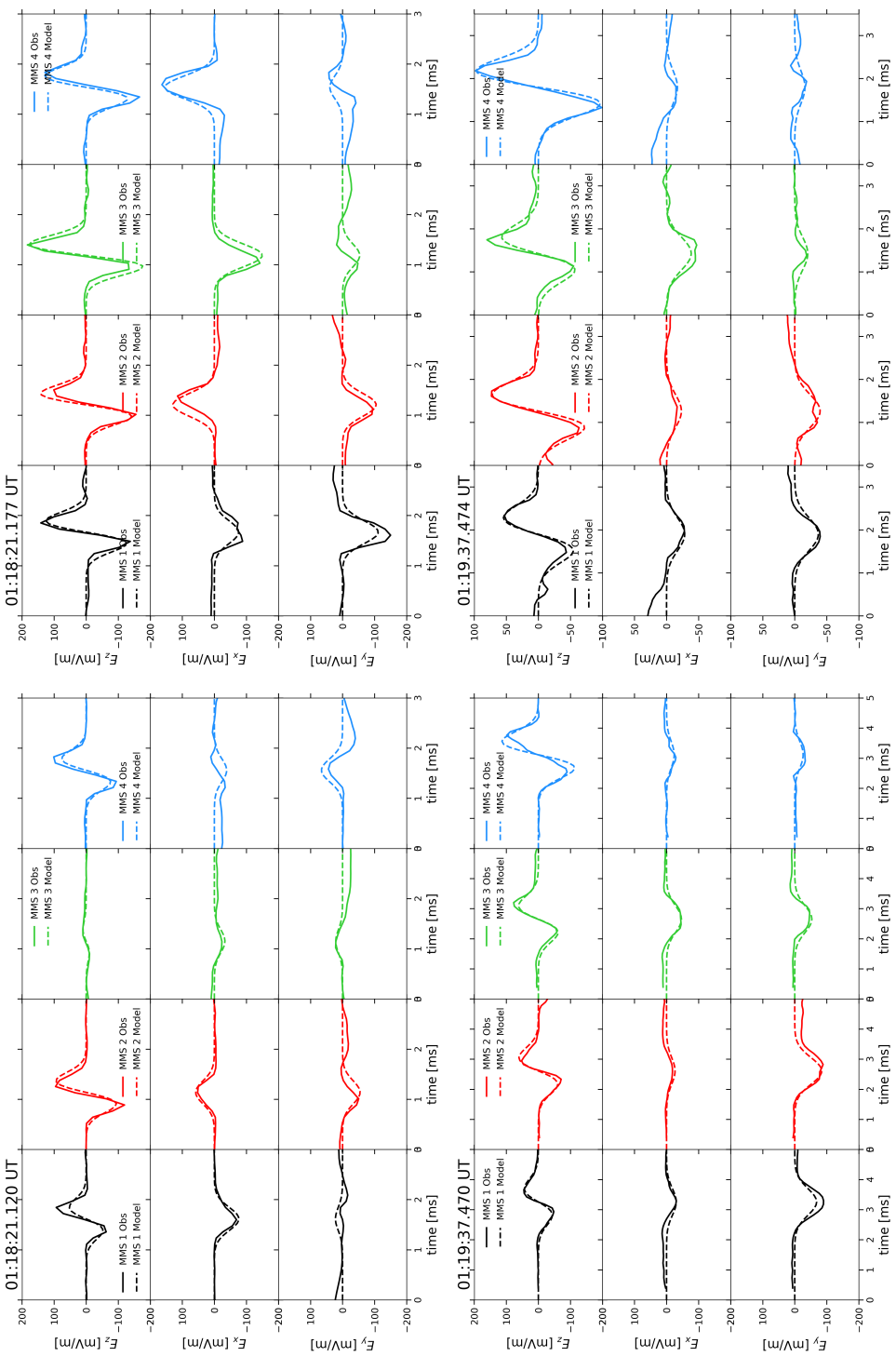

Figure C.3: Measured electric fields (solid) compared with best-fit-model electric fields (dashed) for each of the electron holes (A)-(D) presented in the Figure 4 in Chapter 8. E_x, E_y, E_z are electric fields in the field aligned coordinate system.